UNIVERSITY OF CALIFORNIA

Los Angeles

Process Operational Safety via Integrated Design of Control and Safety Systems

A dissertation submitted in partial satisfaction of the
requirements for the degree Doctor of Philosophy
in Chemical Engineering

by

Zhihao Zhang

2020

ABSTRACT OF THE DISSERTATION

Process Operational Safety via Integrated Design of Control and Safety Systems

by

Zhihao Zhang

Doctor of Philosophy in Chemical Engineering

University of California, Los Angeles, 2020

Professor Panagiotis D. Christofides, Chair

Process safety is a crucial issue in the area of process systems engineering as accident prevention is a top priority in process operations. Operational safety needs to be directly incorporated into control system and safety system to handle disturbances and device failures in the chemical processes. Motivated by the above considerations, this dissertation provides various methods and case studies to demonstrate the integration of safety considerations into controller design. First, we present the dynamic interactions between feedback control and safety systems, and elaborate on the effectiveness by showing applications to a continuous stirred tank reactor (CSTR) and a high-pressure flash drum separator with both classical and model-based controllers. Then, a Safeness Index function is developed to be utilized as a constraint in model predictive control (MPC) design to provide coordination between control and safety systems. The proposed Safeness-Index based MPC is applied to a flash drum and an ammonia production process to enhance process operational safety. Moreover, a large-scale ammonia process network is studied with respect to process operational safety with multiple model predictive controllers to avoid extremely high temperature in the presence of significant disturbances. Additionally, the 2015 explosion accident at the refinery operated by ExxonMobil in Torrance, California is analyzed. A control-based approach is presented for how the accident could have been potentially avoided

by simulating accident conditions in the fluid catalytic cracking unit (FCC). Lastly, a method for combining neural network models with first-principles models is presented. The improved performance of this hybrid model is demonstrated in both real-time optimization (RTO) and MPC of a CSTR and a distillation column. Aspen Plus Dynamics, a commercial process simulation software, is integrated with Matlab to carry out the above simulations for large-scale chemical processes to demonstrate the applicability and effectiveness of the proposed control methods.

The dissertation of Zhihao Zhang is approved.

Samanvaya Srivastava

Dante A. Simonetti

Tsu-Chin Tsao

Panagiotis D. Christofides, Committee Chair

University of California, Los Angeles

2020

Contents

List of Figures

List of Tables

ACKNOWLEDGEMENTS

First and foremost, I need to express my deep and sincere gratitude to my advisor, Professor Panagiotis D. Christofides, for his invaluable support throughout my doctoral work. It is a great privilege and honor to work and study under his guidance. He is a great role model to his students of attention to detail and excellence in his work, and also a great role model in terms of character qualities like patience, work ethic, and determination. He has made a profound impact on both my character and my career. I would also like to thank Professor Dante A. Simonetti, Professor Samanvaya Srivastava and Professor Tsu-Chin Tsao for participating in my doctoral committee.

In addition, I want to acknowledge the valuable conversations and time spent with my collaborators: Zhe Wu, David Rincon, Helen Durand, Fahad Albalawi and Anh Tran. Though it would be difficult to list all the people who have contributed to my success, I must thank Yangyao Ding, Yichi Zhang, Scarlett Chen, Yiming Ren, Carlos Garcia, Marquis Grant Crose, Andres Aguirre, Anas Wael Alanqar and Liangfeng Lao for help with my research, career and life.

Financial support from the US Department of Energy (DOE) and the US National Science Foundation (NSF) is gratefully acknowledged, and my work could not have been done without this support.

Chapters 2 and 3 contain a version of: Z. Zhang, Z. Wu, H. Durand, F. Albalawi and P. D. Christofides, "On Integration of Feedback Control and Safety Systems: Analyzing Two Chemical Process Applications", *Chemical Engineering Research and Design*, **132**, 616-626, 2018.

Chapters 4 and 5 contain a version of: Z. Zhang, Z. Wu, D Rincon, C. Garcia and P. D. Christofides, "Operational Safety of Chemical Processes via Safeness-Index Based MPC: Two Large-Scale Case Studies", *Computers and Chemical Engineering*, **125**, 204-215, 2019.

Chapter 6 contains a version of: Z. Zhang, Z. Wu, D. Rincon and P. D. Christofides, "Operational Safety of an Ammonia Process Network via Model Predictive Control", *Chemical Engineering Research and Design*, **146**, 277-289, 2019.

Chapter 7 contains a version of: Z. Zhang, Z. Wu, D. Rincon and P. D. Christofides, "Operational Safety via Model Predictive Control: The Torrance Refinery Accident Revisited",

Chemical Engineering Research and Design, **149**, 138-146, 2019.

Chapter 8 contains a version of: Z. Zhang, Wu, D. Rincon and P. D. Christofides, "Real-Time Optimization and Control of Nonlinear Processes Using Machine Learning", *Mathematics*, **7(10)**, 890, 2019.

Curriculum Vitae

Education

University of California, Los Angeles **Sep. 2016 - June 2020**

Ph.D., Chemical Engineering **Los Angeles, CA**

Advisor: Professor Panagiotis D. Christofides

University of California, Los Angeles **Sep. 2016 - June 2018**

M.S., Chemical Engineering **Los Angeles, CA**

Advisor: Professor Panagiotis D. Christofides

Thesis: "On Integration of Feedback Control and Safety Systems: Analyzing Two Chemical Process Applications"

Fachhochschule Lübeck **Sep. 2012 - July 2016**

B.S., Environmental Engineering **Lübeck, Germany**

Advisor: Professor Michael Bischoff

Thesis: "Analysis of Temperature Swing Adsorption to Extend Concentration Ranges for Economic Exhaust Gas Catalytic Combustion"

East China University of Science and Technology **Sep. 2012 - July 2016**

B.S., Chemical Engineering and Technology **Shanghai, China**

Journal Publications

1. Z. Zhang, Z. Wu, D. Rincon and P. D. Christofides, "Real-Time Optimization and Control of Nonlinear Processes Using Machine Learning", *Mathematics*, **7(10)**, 890, 2019.

2. Z. Zhang, Z. Wu, D. Rincon and P. D. Christofides, "Operational Safety via Model Predictive Control: The Torrance Refinery Accident Revisited", *Chemical Engineering Research and Design*, **149**, 138-146, 2019.

3. Z. Zhang, Z. Wu, D. Rincon and P. D. Christofides, "Operational Safety of an Ammonia Process Network via Model Predictive Control", *Chemical Engineering Research and Design*, **146**, 277-289, 2019.

4. Z. Zhang, Z. Wu, D Rincon, C. Garcia and P. D. Christofides, "Operational Safety of Chemical Processes via Safeness-Index Based MPC: Two Large-Scale Case Studies", *Computers and Chemical Engineering*, **125**, 204-215, 2019.

5. Z. Zhang, Z. Wu, H. Durand, F. Albalawi and P. D. Christofides, "On Integration of Feedback Control and Safety Systems: Analyzing Two Chemical Process Applications", *Chemical Engineering Research and Design*, **132**, 616-626, 2018.

6. Z. Wu, F. Albalawi, Z. Zhang, J. Zhang, H. Durand and P. D. Christofides, "Control Lyapunov-Barrier Function-based Model Predictive Control of Nonlinear Systems", *Automatica*, **109**, 108508, 2019.

7. Z. Wu, J. Zhang, Z. Zhang, F. Albalawi, H. Durand, M. Mahmood, P. Mhaskar and P. D. Christofides, "Economic model predictive control of stochastic nonlinear systems", *AIChE Journal*, **64(9)**, 3312-3322, 2018.

8. Z. Wu, F. Albalawi, J. Zhang, Z. Zhang, H. Durand and P. D. Christofides, "Detecting and Handling Cyber-attacks in Model Predictive Control of Chemical Processes", *Mathematics*, **6(10)**, 173, 2019 2019.

Chapter 1

Introduction

1.1 Motivation

Safety is critical in the chemical process industries due to the severe consequences involving both lives and property when safety is not maintained [105, 149]. Despite many efforts to develop, characterize, and standardize effective safe process/plant design and operation procedures, accidents continue to occur, causing significant human and capital losses [3, 4, 56]. Innovative operating strategies are required to eliminate unsafe process operations that may lead to catastrophic events. One novel perspective on process safety that has been advocated in several recent works (e.g., [6,93,101,156]) is a systems view of process safety in which accidents are seen as the result of the process state migrating to an unsafe operating region from where an accident may quickly follow (e.g., in the case of reactor runaway). Such a viewpoint is radically different from standard industrial thinking, which centers around the notion that the "safeness" of a chemical process increases as safety barriers such as individual alarms or pressure relief devices are added to the process design for each possible disturbance or equipment fault [40,104] as well as the standard risk assessment practice of individual process components [82,141]. These traditional approaches, while valuable on their own right, neglect important aspects impacting process operational safety, such as multivariable interactions of process components and variables, limited control system

authority due to limitations on the capacity of control actuators, unmonitored process state variables that incorporate valuable process safety information, and the manner in which the safety or relief system response may impact the effectiveness of the process control system [93, 166]; accounting for such aspects in the control and safety system design can be crucial to ensuring process operational safety.

Some of these issues, such as multivariable interactions, can be accounted for using model predictive control (MPC) [37, 50–52, 107, 112, 130, 133] to regulate the process, and the MPC may be augmented with state constraints to limit excursions of the process state to unsafe regions. However, current MPC designs do not incorporate metrics of process operational safeness based on the values of the process states and thus may lead to process operation in parts of the state space from which migration to an unsafe state may quickly occur. Process safeness metrics have been extensively used in the context of process design and risk assessment but have not been employed directly in the calculation of control actions by the control system. Furthermore, current MPC designs cannot deal with cases where the process state enters an unsafe operating region due to equipment faults or disturbances and the safety systems are activated [93]. In addition, the elements of the safety system such as alarms, pressure relief devices, and emergency shutdown systems should account for control actuator limitations as part of their triggering thresholds as well. Incorporating safeness metrics in the process control system and coordinating its actions with the ones of the safety systems, while maintaining their independence for redundancy purposes, would represent a significant paradigm shift in both control and safety system design that has the potential to save lives and protect the environment. In California, there have been several high-profile accidents including one explosion in an ExxonMobil refinery in Torrance, Los Angeles in 2015. In this accident, due to malfunction of the emergency systems, major flammable vapor leaks occurred from a pipe at the fluid catalytic cracker unit that sent thousands to the hospital; this is the type of accident that could have been prevented with coordination of the process control and emergency safety systems such that the control system could safely operate the plant in a limited operation regime until the emergency system is brought back on-line [42, 105]. Therefore,

the development of a systematic methodology for coordinating control and safety systems poses fundamental challenges; for example, metrics must be developed that can be shared by the control and safety systems to indicate safe or unsafe process operation, and a new MPC formulation need to be developed that incorporate safeness metrics and directly account for the impact of discrete safety system actions (like on/off behavior of relief valves) on MPC decision making to ensure operational safety.

1.2 Background and Previous Work

Though safety systems and feedback control systems are critical to safe plant operation, they act fully independently and are not integrated to yield cooperative actions to ensure both operational safety and economic performance. This has resulted in staggering profit losses for the chemical process industries; for example, it was reported that the 20 major accidents in the hydrocarbon industry from 1974 to 2015 cost over $15 billion, with the total accumulated value of the 100 largest losses at more than $33 billion (estimates in 2015 dollars) [105]. It is clear from these numbers that it is necessary to coordinate the actions of process safety and control systems from both the ethical perspective of saving lives and property, and also from an economics standpoint for the chemical process industry. Chemical process safety has traditionally been addressed through process design decisions (e.g., designing the process to be inherently safe in terms of its chemistry and physics [60, 73]) and control and safety system design decisions (e.g., adding sensors for critical process variables that trigger an alarm when a measurement outside of the desired range is obtained [104]). Inherently safer designs are achieved through four primary principles: minimize (reduce the quantity of hazardous substances used and stored by a process), substitute (utilize less hazardous process chemicals), moderate (dilute chemicals or change operating conditions), and simplify (choose designs with less complexity and less potential to create hazardous conditions when faults or errors occur) [68, 81].

It is impossible to eliminate all hazards at a plant, so a safety system, comprised of several

Figure 1.1: Control/safety system layers [104].

independent layers, should be added as shown in Fig. 1.1. Ideally, the layers of the safety system should not be activated regularly because a basic process control system (BPCS) regulates process variables to their set-points. When the BPCS fails to keep the process variables within acceptable ranges due to, for example, equipment faults or unusually large process disturbances, alarms are triggered that alert operators so that actions can be taken to prevent further unsafe deviations. If the process variables subsequently further exceed allowable values, the emergency shutdown system (ESS) is triggered, which takes automatic and extreme actions such as forcing a valve to its fully open position to bring the process to a safer state of operation. Safety relief devices such as relief valves are used on vessels that can become highly pressurized quickly to prevent an explosion. Containments are used to prevent hazardous materials from entering the environment or injuring workers when the other layers of the safety hierarchy fail to prevent release of the materials. The emergency response plan is used in severe cases that cannot be mitigated by any other layers. The layers are independent of each other and of the control system (i.e., they have separate sensors, computing elements, and actuators) to allow redundancy and improve

safety [104]. Design decisions for the location and sizing of the safety systems are aided through qualitative and quantitative studies (e.g., hazards and operability (HAZOP) studies, fault trees, event trees, what-if or worst-case scenarios, security indices, and layers of protection analysis (LOPA)) of the damage that may result from an accident (including life losses, capital equipment loss, and damage to the environment) which is evaluated to determine whether it is within an acceptable level of risk [40, 104, 108, 159].

The accidents throughout chemical plant history [85, 86, 102] have led some researchers to suggest that the philosophy used in the design of the control and safety system layers (i.e., designing barriers against specific unsafe scenarios using the safety system) is quite limited, particularly as economic considerations drive more optimized and integrated system designs [64, 71, 95, 118], and that a systems approach coordinating directly the actions of control and safety systems and analyzing closed-loop process operational safety should instead be used [8, 21, 39, 78, 93, 101, 156]. One step toward this systems approach is by incorporating safety considerations and safety system actions within the BPCS. However, the single-input/single-output controllers (e.g., proportional-integral-derivative (PID) controller) traditionally used within the BPCS cannot account for factors that are important to process safety such as multivariable interactions and state/input constraints. On the other hand, advanced model-based control methodologies such as model predictive control (MPC) can account for these factors and thus can be integrated with safety considerations [93, 107, 110, 130]. A large number of works in the MPC literature [13, 14, 46, 51, 109, 123, 135, 175]) have addressed the robustness, performance and closed-loop stability of MPC (e.g., [29, 50, 72, 76, 107, 112] and the references therein); but have not considered explicit safety considerations and safety system actions in their formulations.

Several works have looked at coordinating control with safety considerations. For example, safety in the sense of fault/abnormality diagnosis and monitoring has been addressed (e.g., [38, 58, 158]), as well as integrating fault-tolerance within process control [11, 26, 80, 90, 111, 174]; however, these methods do not address system-wide safety considerations and safety system actions in control. Furthermore, the coordination of control and safety systems through a

system-wide safety metric (while operating the systems independently) has not been performed, though this has the potential to significantly reduce unnecessary triggering of the safety system and to help in the design of triggers and appropriate actions for automated elements of the ESS and relief systems. Thresholds on a recently developed state-based Safeness Index [9] may be incorporated as triggers for safety system activation that allow the safety system to be aware of system-level safety considerations; the same metric, with different thresholds, can be utilized in MPC design to provide some coordination between the designs. This can be particularly beneficial for mitigating alarm overloading [28, 62, 166], which is the triggering of too many alarms at once, either because of poor alarm design creating frequent alarms that require no operator actions, or too many correct alarms sounding at once triggered by the same root cause. The number of alarms that sound at a chemical process plant each day can be over seven times the recommended number [49, 138], making it difficult for operators to adequately address the alarms, which can lead to environment and plant damage, danger to lives [149, 150], and reduced operator confidence in the alarm system [166]. Industry [138] and academia [12, 18, 27, 34, 114, 115, 151, 165, 166] have addressed alarm issues with techniques based on, for example, models, statistical analysis, and metrics. A recent work [2] utilizes a model predictive framework and state estimation for unmeasured states to initiate alarms when the available control action cannot ensure that state constraints related to process safety are satisfied over a prediction horizon. However, none of these methods integrates operational safety considerations and safety system actions within the control system design, paving the way for the present dissertation.

1.3 Dissertation Objectives and Structure

Motivated by the above considerations, the goal of this dissertation is to design and implement integration of control and safety system in a unified framework to achieve operational safety for chemical processes. The performances of the proposed methods are demonstrated in the context of chemical processes of industrial importance, using both explicit nonlinear dynamic models and

AspenTech dynamic models. The dissertation has the following structure:

In Chapter 2 and Chapter 3, we focus on two case studies and attempt to elucidate the dynamic interaction between feedback control and safety systems in the context of both model-based and classical control systems. In Chapter 2, the interaction of a model predictive control system with a safety system is studied in the context of the methyl isocyanate (MIC) hydrolysis reaction in a continuous stirred tank reactor (CSTR) to avoid thermal runaway. We develop a fixed control action for the MPC to take when the safety system is activated due to significant feed disturbances that lead to thermal runaway conditions. In Chapter 3, we focus on a high-pressure flash drum separator for which the temperature, level, and pressure can be regulated using proportional-integral (PI) controllers. Using a large-scale dynamic process simulator, we demonstrate that modifying the tuning parameters of one of these PI controllers based on the safety system being on or off leads to improved closed-loop performance compared to the case in which the tuning parameters of the PI controller remain the same regardless of the state of the safety system.

Chapter 4 and Chapter 5 present two applications of Safeness Index-based model predictive control schemes to improve process operational safety in safety critical chemical processes. In Chapter 4, a high-pressure flash drum separator together with pressure relief valve as safety system is used to analyze the benefits of integrating Safeness Index-based considerations in MPC. The proposed framework demonstrates that Safeness Index-based MPC can either avoid activating safety system in the presence of a small disturbance, or work together with the safety system which is activated/deactivated in the presence of a large disturbance. In Chapter 5, an ammonia process with four unit is simulated to demonstrate the application of Safeness Index to handle significant propagated disturbances to methanation unit. A Safeness Index-based MPC is developed with a feedforward disturbance compensation term, successfully ensuring process operational safety in the presence of a significant propagated disturbance to methanation unit.

Chapter 6 presents a practical application simulating multiple model predictive controllers within a multi-unit ammonia process, all of which integrate safety constraints of the process within their designs. Specifically, catalytic deactivation in the shift reactor is a common and

problematic disturbance that may trigger reaction thermal runaway in the methanator. Two controllers designed with the objective of improving operational safety are implemented on the ammonia plant under catalyst deactivation. The results demonstrate that under suitable design of the controllers, desirable closed-loop performance is achieved with high temperature extremities avoided during operation.

In Chapter 7, an accidental explosion at the refinery operated by ExxonMobil in Torrance, California occurred in 2015 during operation at the Safe Park mode is analyzed, and a control-based approach is presented to demonstrate how the accident could have been potentially avoided. Specifically, this work reproduces and tackles the accident by dynamical modeling of the fluid catalytic cracking (FCC) unit that played a key role during the accident using information extracted from the final investigation report. A model predictive controller with an offset-free mechanism is proposed and is applied to the process under two different scenarios. The first scenario is based directly on the report for the accident in Torrance, California in 2015, while the second scenario is another potentially catastrophic situation that could have occurred. The obtained results in Aspen Plus Dynamics demonstrate that the proposed safety-aware control system is able to avoid the accident under both scenarios.

Chapter 8 presents a method for combining neural network models with first-principles models in real-time optimization (RTO) and MPC, and demonstrates the application to two chemical process examples. In the first example, a continuous stirred tank reactor (CSTR) with a reversible exothermic reaction is studied. A feed-forward neural network model is used to approximate the nonlinear reaction rate and is combined with the first-principles model in RTO and MPC. The RTO is designed to find the optimal reactor operating condition balancing energy cost and reactant conversion, and the MPC is designed to drive the process to the optimal operating condition. A variation in energy price is introduced to demonstrate that the developed RTO scheme is able to minimize operation cost and yields a closed-loop performance that is very close to the one attained by RTO/MPC using the first-principles model. In the second example, a distillation column is used to demonstrate an industrial application of the use of machine learning to model nonlinearities in

RTO. A feed-forward neural network is first built to obtain the phase equilibrium properties and then combined with a first-principles model in RTO, which is designed to maximize the operation profit and calculate optimal set-points for the controllers. A variation in feed concentration is introduced to demonstrate that the developed RTO scheme can increase operation profit for all considered conditions.

Finally, Chapter 9 summarizes the contributions of this dissertation.

Chapter 2

Integration of Safety and Control Systems: MIC Reaction in a CSTR Case Study

2.1 Introduction

In the first two chapters, we will investigate how the activation of the safety system should be accounted for in the context of feedback controller design and implementation. Since the actions of the safety system change the process dynamics, they should be properly accounted for in the calculation of the feedback controller actions. Specifically, we focus on two industrially-important (from a safety point of view) case studies, a chemical reactor and a flash drum, and analyze the interaction of the control and safety systems both in the case where a model predictive control (MPC) design is employed (chemical reactor example) and in the case where a proportional-integral (PI) control design (flash drum example) is used. In this chapter, we focus on the methyl isocyanate (MIC) hydrolysis reaction in a CSTR subject to disturbances that lead to reactor thermal runaway and demonstrate how the safety and control system can work together to avoid thermal runaway. In the next chapter, we focus on valve malfunction for a flash drum to demonstrate that modifying the tuning parameters of a PI controller based on the safety system being on or off leads to improved closed-loop performance compared to the case in which the

tuning parameters of the PI controller remain the same regardless of the state of the safety system.

In this chapter, the methyl isocyanate (MIC) hydrolysis reaction in a CSTR is investigated, where MIC is the principal chemical involved in the Bhopal disaster [23]. In this case study, we will seek to coordinate an MPC formulation (for this example, a specific MPC formulation known as Lyapunov-based MPC (LMPC) [110] will be utilized to control the process) with the safety system. Section 2.2 describes the MIC hydrolysis process. Section 2.3 describes the LMPC utilized to control the process, and the results obtained under disturbances without the safety system activated. Section 2.4 completes the discussion by developing a safety system for this example and a methodology for its interaction with the LMPC to enhance process operational safety.

2.2 MIC Reaction and CSTR Process Description

The exothermic hydrolysis reaction of methyl isocyanate to the corresponding amine and carbon dioxide is given as follows:

$$CH_3NCO_{(l)} + H_2O_{(l)} \rightarrow CH_3NH_{2(aq)} + CO_{2(aq)}$$

By applying mass and energy balances, the dynamic model of the process can be described as follows:

$$\begin{aligned} m\frac{dC_A}{dt} &= -mk_0 e^{\frac{-Ea}{RT}} C_A + F(C_{A0} - C_A) \\ mC_P\frac{dT}{dt} &= (-\Delta H)mk_0 e^{\frac{-Ea}{RT}} C_A + FC_P(T_0 - T) - L(T - T_j) \end{aligned} \tag{2.1}$$

where C_A is the concentration of MIC in the reactor in units of mol/kg, m is the total mass of the mixture in the reactor, and T is the temperature of the reactor. The concentration of reactant MIC in the feed and the feed temperature are denoted by C_{A0} and T_0, respectively. The flow rates of both the CSTR feed and outlet streams are denoted by F. The reacting liquid has a constant heat

capacity of C_P. k_0, E_a and ΔH are the reaction pre-exponential factor, activation energy and the enthalpy of the reaction, respectively. The CSTR is equipped with a cooling jacket, for which the heat transfer coefficient is denoted by L, and the temperature of the cooling jacket is denoted by T_j. The reactor is simulated at the conditions reported for the Bhopal catastrophe [152]. Process parameter values are listed in Table 2.1. It is noted that the simulations of this process will assume that liquid in the CSTR can vaporize; we will continue to utilize Eq. 2.1 even when vaporization of liquid occurs because this allows key aspects of our proposed method for integrating the safety system and MPC to be explored despite the modeling approximation.

Table 2.1: Parameter values for the MIC reaction case study in a CSTR.

$T_0 = 293\ K$	$F = 57.5\ kg/s$
$m = 4.1 \times 10^4\ kg$	$E_a = 6.54 \times 10^4\ J/mol$
$k_0 = 4.13 \times 10^8\ /s$	$\Delta H = -8.04 \times 10^4\ J/mol$
$C_P = 3000\ J/(kg\ K)$	$R = 8.314\ J/(mol\ K)$
$L = 7.1 \times 10^6\ J/(s\ K)$	$C_{A_0} = 29.35\ mol/kg$
$T_{j_s} = 293\ K$	$C_{A_s} = 10.1767\ mol/kg$
$T_s = 305.1881\ K$	

2.3 LMPC Design and Thermal Runaway

2.3.1 LMPC Design

The CSTR is initially operated at the steady-state MIC concentration and temperature of $[C_{A_s}\ T_s] = [10.1767\ mol/kg\ \ 305.1881\ K]$, with steady-state jacket temperature $T_{j_s} = 293\ K$. The control objective is to stabilize the states of the reactor at their steady-state values by adjusting the manipulated input (the cooling jacket temperature T_j) subject to the bounds $280\ K \leq T_j \leq 300\ K$. The states and the input of the closed-loop process will be represented in deviation variable form from this steady-state as $x^T := [C_A - C_{A_s}\ T - T_s]$ and $u := T_j - T_{j_s}$, so that it is desired to drive x and u to the origin. In this notation, the system of Eq. 2.1 can be written in the form of $\dot{x} = f(x) + g(x)u$,

where $f(x)$ and $g(x)$ are nonlinear vector functions of the process state vector. We first design an LMPC to control the process. LMPC is an MPC formulation that utilizes stability constraints based on a Lyapunov function $V(\cdot)$ and an explicit stabilizing (Lyapunov-based) controller for the nonlinear process (denoted by $h(\cdot)$) to guarantee feasibility of the MPC and closed-loop stability of a nonlinear process operated under the MPC (in the sense that the closed-loop state is driven to a neighborhood of the origin under LMPC for all initial conditions in an explicitly characterizable region of state-space termed the stability region around the steady-state) when the disturbances and MPC sampling period are sufficiently small. Specifically, the LMPC scheme is formulated as the following optimization problem:

$$\min_{u\in S(\Delta)} \quad \int_{t_k}^{t_{k+N}} (\|\tilde{x}(\tau)\|_{Q_c}^2 + \|u(\tau)\|_{R_c}^2)\, d\tau \tag{2.2a}$$

$$\text{s.t.} \quad \dot{\tilde{x}}(t) = f(\tilde{x}(t)) + g(\tilde{x}(t))u(t) \tag{2.2b}$$

$$\tilde{x}(t_k) = x(t_k) \tag{2.2c}$$

$$u(t) \in U,\ \forall\ t \in [t_k, t_{k+N}) \tag{2.2d}$$

$$\frac{\partial V(x(t_k))}{\partial x}(f(x(t_k)) + g(x(t_k))u(t_k)) \leq \frac{\partial V(x(t_k))}{\partial x}(f(x(t_k)) + g(x(t_k))h(x(t_k))) \tag{2.2e}$$

where $S(\Delta)$ is the set of piece-wise constant functions with period Δ, and N is the number of sampling periods in the prediction horizon. The notation $t_k = k\Delta$, $k = 0, 1, \ldots$, denotes a sampling time of the LMPC at which the optimization problem of Eq. 2.2 is solved. The optimal input trajectory of the LMPC optimization problem, computed at t_k, is denoted by $u^*(t|t_k)$, which is calculated over the entire prediction horizon $t \in [t_k, t_{k+N})$. The control action computed for the first sampling period in the prediction horizon (i.e., $u^*(t_k|t_k)$) is applied at t_k for a sampling period, and the LMPC problem is re-solved at the next sampling time. The objective function to be minimized (Eq. 2.2a) is the integral of $\|\tilde{x}(\tau)\|_{Q_c}^2 + \|u(\tau)\|_{R_c}^2$ over the prediction horizon, where $||\cdot||_{Q_c}$ and $||\cdot||_{R_c}$ represent weighted Euclidean norms (weighted by matrices Q_c and R_c, respectively) utilized to penalize the deviations of the process states and manipulated inputs from their corresponding steady-state values in the objective function. The constraint of Eq. 2.2b is the deviation form

of Eq. 2.1 that is used to predict the states of the closed-loop system ($\tilde{x}$ represents the predicted process state that the LMPC computes based on this process model). Eq. 2.2c defines the initial condition $\tilde{x}(t_k)$ of the optimization problem which is the state measurement $x(t_k)$ at time t_k. Eq. 2.2d defines the input constraints applied over the entire prediction horizon. The constraint of Eq. 2.2e decreases the value of the Lyapunov function $V(x)$ such that $x(t)$ moves towards the origin at least at the worst-case rate achieved by the Lyapunov-based controller $h(x)$, the form of which will be defined below. The explicit Euler method with an integration time step of $h_c = 10^{-2}$ s was applied to numerically simulate the dynamic model of Eq. 2.1 under the LMPC. The nonlinear optimization problem of the LMPC of Eq. 2.2 was solved using the IPOPT software package [161] with the following parameters: sampling period $\Delta = 1$ s; prediction horizon $N = 10$. $Q_c = [3\ 0;\ 0\ 5]$ and $R_c = 1$ are chosen such that the term related to the states and the term related to the input are on the same order of magnitude in $\|\tilde{x}(\tau)\|^2_{Q_c} + \|u(\tau)\|^2_{R_c}$.

The Lyapunov function is designed using the standard quadratic form $V(x) = x^T P x$, where the positive definite matrix P is as follows: $[200\ 33;\ 33\ 40]$. The stability region Ω_ρ is characterized as a level set of the Lyapunov function: $\Omega_\rho := \{x \in R^2 \mid V(x) \leqslant \rho\}$. For the system of Eq. 2.1, the stability region Ω_ρ with $\rho = 8000$ was chosen. This determination was made utilizing closed-loop simulations of the nonlinear process under the above Lyapunov function V and a Lyapunov-based controller to find a region within which the closed-loop state could be driven toward the origin under the controller $h(x)$ because the time derivative of the Lyapunov function was negative under this controller along the closed-loop state trajectories. The controller $h(x)$ was formulated as follows [94]:

$$h(x) = \begin{cases} -\frac{L_f V + \sqrt{L_f V^2 + L_g V^4}}{L_g V^2} L_g V & \text{if} \quad L_g V \neq 0 \\ 0 & \text{if} \quad L_g V = 0 \end{cases} \tag{2.3}$$

where $L_f V$ signifies the Lie derivative of V along the vector field f, and L_g is the Lie derivative of V along the vector field g.

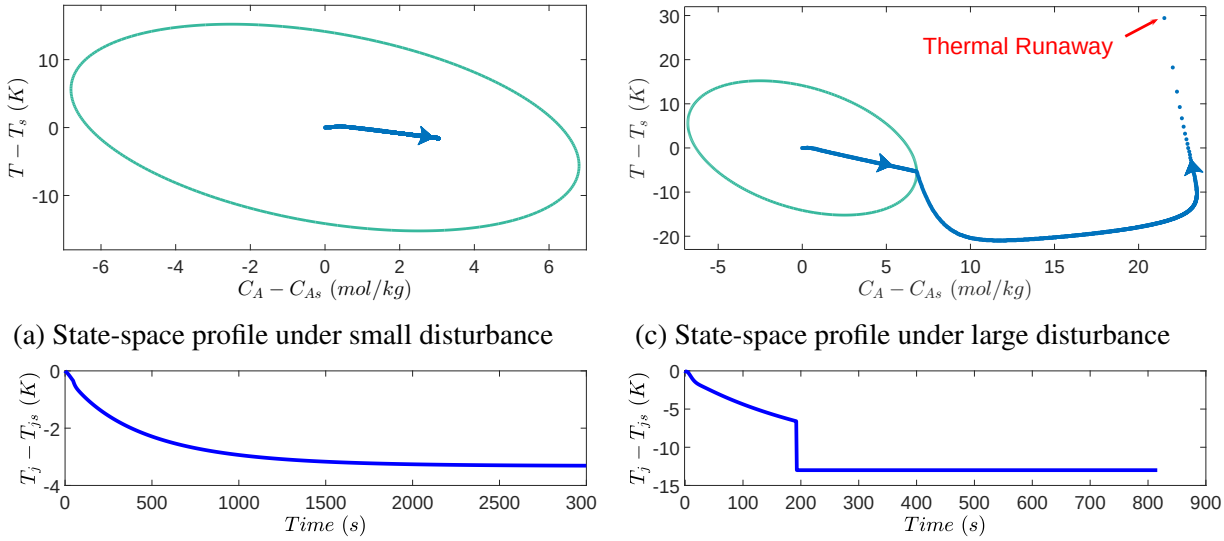

(a) State-space profile under small disturbance

(c) State-space profile under large disturbance

(b) Input trajectory under small disturbance

(d) Input trajectory under large disturbance

Figure 2.1: (a) and (b) demonstrate that the LMPC can stabilize the closed-loop state at another steady-state when there is a small disturbance. (c) and (d) demonstrate that the LMPC fails to keep the closed-loop state inside the stability region when there is a large disturbance. In Figs. 2.1a-2.1b and 2.1c-2.1d, the respective disturbances are applied from the beginning of the time of operation. The large drop in T_j in Fig. 2.1d is forced at approximately 200 s when the closed-loop state exits the stability region (Fig. 2.1c). The point labeled "thermal runaway" in Fig. 2.1c corresponds to $t = 800$ s in Fig. 2.1d. It is notable that though the same time interval is utilized between all points plotted in Fig. 2.1c, separation is only visible between the data points toward the end of the simulation as thermal runaway is approached because it is at those times that the changes in temperature become rapid between the plotting intervals.

2.3.2 Simulation Results

A small feed disturbance (i.e., change of feed concentration from 29.35 mol/kg to 35 mol/kg) is initially considered and Figs. 2.1a and 2.1b demonstrate that the closed-loop system under the LMPC is robust to the small disturbance by stabilizing the system state at another steady-state within the stability region.

However, when there exists a large disturbance (i.e., the change of feed concentration is from 29.35 mol/kg to 70 mol/kg) due to, for example, failure of the device which distributes the feed, it is shown in Fig. 2.1c that the state exits the stability region and the manipulated input hits its lower bound to cool down the reactor as much as possible. However, after 800 seconds of implementation of maximum cooling, the reactor temperature starts to increase significantly.

The reason for this increasing value of the temperature is that when the reactor temperature rises, the exothermic reaction rate also increases, causing a further increase in temperature, which is a dangerous phenomenon called thermal runaway. Therefore, it can be concluded that in the presence of large disturbances, the reactor may operate in an unsafe region due to the restriction of the control actuator, which motivates the development of a safety system to maintain reactor safety.

2.4 Integration of MPC with Safety System

In this section, the safety system for the MIC hydrolysis process is first designed using two different safety mechanisms: (a) a safety relief valve; (b) cold water injection. Then, the entire process control/safety system which integrates the safety system with the LMPC is developed to maintain closed-loop safety and stability. Finally, the MIC reaction example is used to demonstrate the application of the proposed control/safety scheme.

2.4.1 Components of Safety System

2.4.1.1 Safety Relief Valve

In the MIC hydrolysis example, we will consider the use of a valve in the reactor for which the opening is triggered by logic in the safety system (i.e., not by the process controller logic) to aid in preventing thermal runaway. The purpose of the valve in this example is to reduce the temperature of the reactor by discharging material when the temperature is high in the reactor (because the valve has this purpose and is part of the safety system, the valve in this example will be called a safety relief valve; however, it should be understood that it is not a pressure-actuated type of safety relief valve [104]). In industry, thermal runaway may occur due to different failures, such as mischarging reactant or failures in the cooling system that affect the coolant temperature or flow rate. Since the above unsafe operating conditions are unpredictable and uncontrollable and thermal runaway can vaporize liquid in a reactor, a suitable and correctly sized relief system is crucially important as a backup method to prevent fatal accidents [69]. The size of a relief valve is carefully chosen in

practice. Specifically, if a relief valve is under-sized, high pressure and equipment failure may occur; if a relief device is over-sized, the relief system may become unstable during the operation and too much material may be wasted [41].

2.4.1.2 Cold Water Injection

Direct cold solvent injection can cool down a reaction mixture's temperature. For example, [160] demonstrated in both simulation and experiment that cold water injection could rapidly lower the temperature in a reactor where an exothermic reaction took place. Cool water injection is utilized to prevent thermal runaway in this MIC hydrolysis example.

2.4.1.3 Safety System for Simulation

In our simulation, high temperature is the trigger of the opening of the relief valve. Specifically, the valve opens once the temperature is higher than 320 K. To simplify the development, we assume that all the relief discharge flow is in liquid phase. The relief valve size is 4×10^{-3} m^2 (selected based on closed-loop simulations indicating that this size allowed the closed-loop state to re-enter the stability region when the safety system is activated in the simulations performed) and the relief flow is determined by the equation in [69]:

$$G_{relief} = 0.9 \times 144 \times \frac{dP}{dT} \times (\frac{32.2}{778.16} \times \frac{T}{C_P}) \tag{2.4}$$

where G_{relief} is the mass of the mixture per area for flow through the relief valve (in kg/m^2), T is the temperature of the relief flow (in K), C_p is the heat capacity (in $J/kg\ K$), and the pressure P in the reactor (in Pa) is obtained from the Antoine equation, with parameters of this equation estimated from data in the process simulation software Aspen Plus.

Cool water is injected with a temperature of 280 K if the temperature in the reactor exceeds 320 K, and the mass flow rate of this injected cold water is the same as the mass flow rate of material leaving through the relief valve; thus, the total mass in the reactor remains unchanged

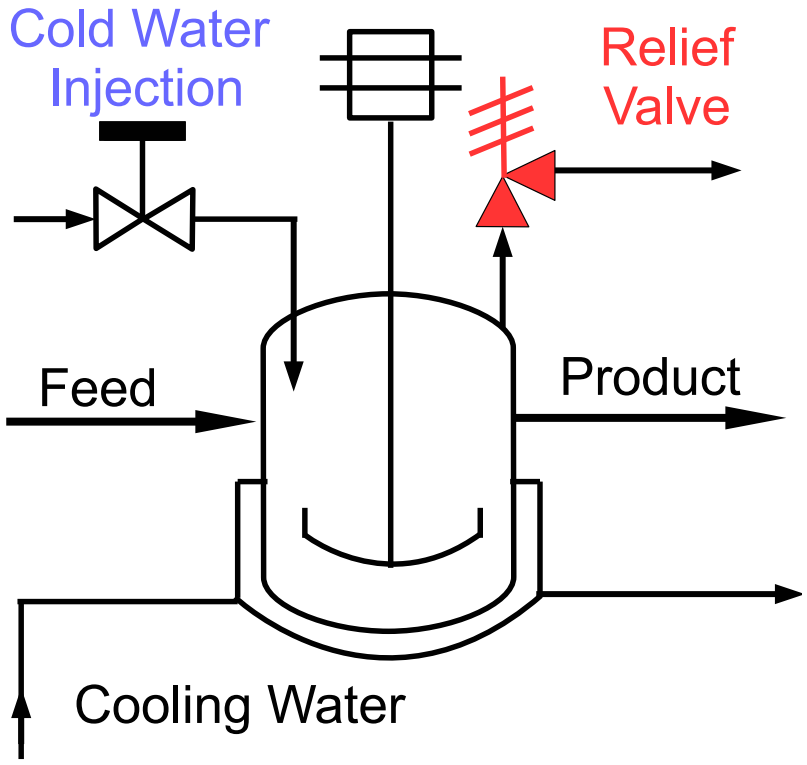

Figure 2.2: CSTR with safety system for MIC hydrolysis example. The relief valve and valve that opens to allow the cold water injection are depicted. The temperature of the cooling water is controlled by the LMPC; the positions of the two valves on the cooling water inlet and outlet for the CSTR are assumed to be fixed in this example.

when the safety system is activated. Fig. 2.2 depicts the CSTR under consideration, with the cooling water system that is manipulated using the LMPC depicted, as well as the two elements of the safety system.

2.4.2 Logic Integrating Control and Safety Systems

A methodology for integrating the LMPC with the activation of the safety system is developed to avoid thermal runaway when the LMPC fails to maintain the closed-loop state inside the stability region in the presence of large disturbances. This methodology is based on dividing the state-space into three different regions which correspond to various combinations of control and safety system actions. A schematic of these different regions and an example closed-loop state trajectory are

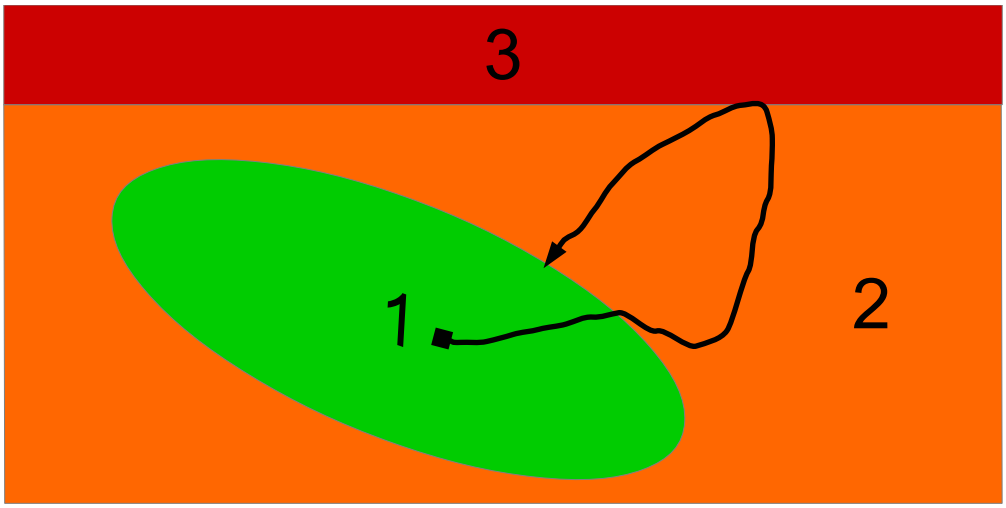

Figure 2.3: A schematic showing, in the $C_A - T$ state-space (with T considered to be on the y-axis and C_A considered to be on the x-axis), the stability region (green), unsafe operating region (orange), and the thermal runaway region (red), together with an example trajectory starting from the origin.

shown in Fig. 2.3. The different combinations of control and safety system actions in the three regions are as follows:

Region 1 (stability region): When the closed-loop state is inside the stability region, the LMPC is implemented to maintain the closed-loop state in a neighborhood of the origin even if there continuously exist small disturbances. In this region, the safety system is not activated.

Region 2 (unsafe operating region): If large disturbances are introduced to the reactor, the state may come out of the stability region. In order to enhance process operational safety, the manipulated input (i.e., T_j) is set to its lower bound, namely the lowest cooling jacket temperature, since the LMPC may not drive the closed-loop state back into the stability region once the state exits the stability region.

Region 3 (thermal runaway region): If large disturbances keep affecting the reactor and the maximum cooling is not able to lower the temperature sufficiently, then the reactor temperature may reach a high value (i.e., the lower boundary of Region 3). The safety system takes action in Region 3. Specifically, the relief valve opens immediately after the state enters Region 3 and stays open until the state goes back to Region 1. Meanwhile, cold water is injected into the reactor, cooling down the reactor. Injection stops once the relief valve is closed (state goes back into Region

1). At the same time, the jacket temperature stays at its lower bound to apply maximum cooling.

The temperature boundary between Region 2 and Region 3 was determined for this example to be a temperature at which the increase in temperature with time in the reactor was large.

2.4.3 Simulation Results

In Fig. 2.4, it is demonstrated that in the presence of a large disturbance, the LMPC integrated with the safety system via the above logic succeeds at avoiding thermal runaway and drives the state back to the origin. At the beginning of the simulation, a large disturbance (i.e., the feed concentration is changed from 29.35 mol/kg to 70 mol/kg as in Section 2.3.2) is introduced into the reactor, resulting in the failure of the LMPC to keep the system state within the stability region. After about 600 seconds, since the heat generated by the reaction is much more than the heat that the cooling system can remove, the concentration of the reactant increases to such an extent that the temperature starts to increase rapidly and reaches the safety limit of 320 K. Once the temperature exceeds the safety limit, the relief valve opens to discharge hot fluid from the reactor and an additional stream is employed to feed fresh water into the reactor. The liquid relief flow rapidly decreases the total internal energy and the reactant concentration in the reactor. Cool water promptly lowers the reactor temperature and dilutes the reactant, lowering its concentration. The safety system is activated for about 10 seconds to drive the closed-loop state back into Region 1. Once the closed-loop state goes back to Region 1, the safety system is shut off and the LMPC is utilized instead to stabilize the system state at the origin. Inside Region 1, the LMPC is guaranteed to drive the closed-loop state toward the origin when there are no disturbances and when the sampling period is sufficiently small [7, 110]. It should be noted that if the large disturbance still exists after the closed-loop system state goes back into Region 1, then the logic of Section 2.4.2 will again be implemented to avoid thermal runaway as discussed above. Because it is not desirable to have the safety system activated regularly, this indicates that some diagnostics may need to be performed after the safety system is shut off to analyze the process and determine how to prevent further activations of the safety system.

Remark 2.1. *Several points should be made regarding the MIC hydrolysis example. First, it should be noted that no attempt was made to analyze all possible combinations of control and safety system actions, encompassing all initial conditions or all possible disturbances, to ensure that the policy developed would drive the closed-loop state back to the stability region under any conditions. Rather, the example was meant to demonstrate that through careful coordination of the control and safety systems, which here was undertaken for the conditions simulated, it is possible to enhance operational safety beyond what might be achieved utilizing the control system alone. Another goal of the example was to demonstrate that the integration of the control and safety systems may aid in keeping the process on-line for economic reasons, despite the safety issues, by allowing the safety system actions to be designed such that they drive the closed-loop state back into the stability region where the controller can be utilized to regulate the process state to the steady-state. In an industrial setting, a more in-depth analysis of all potential hazardous situations should be undertaken to ensure that the control and safety system combination handles all of these and achieves the desired behavior in each case (e.g., that there are no cases where the control and safety system actions may cool the reactor but not drive the closed-loop state back into the stability region, so that the cooling does not stop under the pre-determined interaction policy for the control and safety systems). In addition, consideration would need to be given to what should happen if the safety systems are triggered, even if the closed-loop state does re-enter the stability region (for example, does any type of shut-down or correction procedure need to follow). Additionally, it should be noted that the concept of coordinating an MPC and the safety systems is not limited to LMPC. LMPC has the nice property for such coordination that an explicitly characterizable region exists from which the closed-loop state can be guaranteed to be maintained in the presence of sufficiently small disturbances and an explicitly small sampling period. This aided in the development of Region 1 in this example. However, in general, any MPC design could be utilized in conjunction with a safety system with sufficient care taken to identify all potential combinations of safety and control system actions. Third, care must be taken in disposing of any chemicals that exit through the relief valves to ensure that toxic species do not enter the environment.*

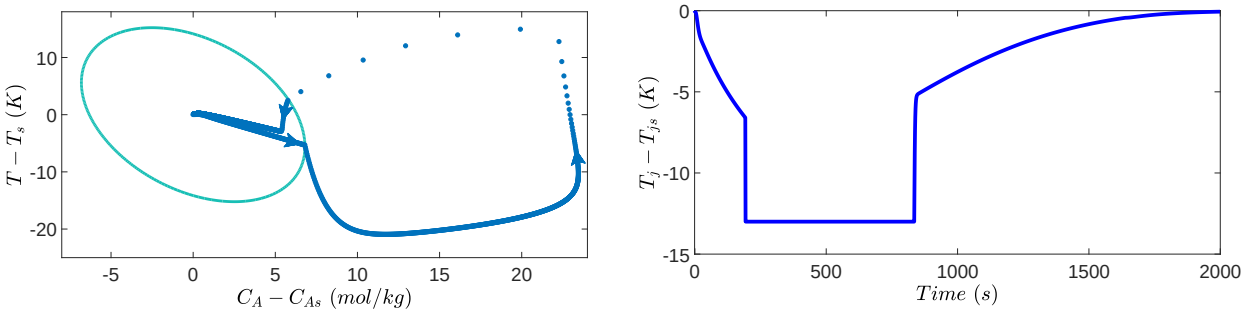

Figure 2.4: State-space plot and input plot of LMPC integrated with the safety system for the MIC hydrolysis reaction in a CSTR. The drop in the coolant temperature when the state exits the stability region is noticeable until the state re-enters the stability region and the LMPC begins to be used once again to manipulate T_j and drive the process state toward its steady-state value. The time interval is the same between the plotting of each data point in the state-space plot. Therefore, the large differences in the state between plotted points as the system approaches thermal runaway indicate rapid changes in temperature. The large differences in the state between plotted points as the state is driven back toward the stability region after the safety system is activated indicate the effectiveness of the safety system's actions to rapidly move the state back toward the stability region.

2.5 Conclusion

In this chapter, we demonstrated for the first time the integration of MPC with safety system activation. An LMPC system integrated with the activation of a safety system was developed for the MIC reaction in a CSTR to avoid thermal runaway. We first demonstrated that the closed-loop system state under the LMPC was maintained within the stability region in the presence of small disturbances. In the presence of large disturbances, it was demonstrated that an LMPC integrated with a safety system could maintain process safety in the sense of avoiding thermal runaway, and driving the process state back into the stability region even after the state exited it.

Chapter 3

Integration of Safety and Control Systems: Flash Drum Case Study

In this chapter, we continue to elucidate the dynamic interaction between feedback control and safety systems in the context of classical control, demonstrating a case study of a high-pressure flash drum used to separate a typical mixture in the chemical industry. The liquid level and the temperature in the flash drum can be regulated by two PI controllers, and this control system is integrated with a pressure relief valve. In this study, we demonstrate that in a scenario in which the valve regulating the outlet vapor stream from the drum experiences a fault that leads to a significant pressure rise inside the flash drum, modifying the tuning parameters of one of the other PI controllers when the safety system is activated leads to improved closed-loop performance compared to the case in which the tuning parameters of that PI controller remain the same regardless of the state of the safety system. Specifically, Section 3.1 describes the flash drum process under consideration, and Section 3.2 describes the tuning/re-tuning method utilized for the PI controller for which the tuning changes when the safety system is activated and demonstrates the benefits of this controller updating through closed-loop simulations.

3.1 Flash Drum Process Description and Relief Valve Design

A flash process [103], as shown in Fig. 3.1, is used to separate a mixture of methane (10%), ethane (20%), propane (30%), butane (35%) and pentane (5%) to a separation level that makes the bottom and top flash outlet streams suitable feeds for downstream distillation towers. Specifically, a liquid feed stream of flow rate F, mole fraction z_i of component i, temperature T_f and pressure P_f is initially heated by a heat exchanger with heating duty Q to a temperature T_{in} and corresponding pressure P_{in}. This heated stream passes through a throttling valve and is then separated adiabatically in the flash drum into a liquid stream of flow rate L with composition x_i and a vapor stream of flow rate V with composition y_i. Both the liquid and vapor streams exiting the flash drum have temperature T and pressure P. The five components are separated due to different vapor pressures. The feed temperature T_f is 40 $^{\circ}C$, the feed pressure P_f is 45 bar, the drum height is 4 ft and the drum diameter is 1 ft. The mole fractions of ethane, i-butane, methane, n-butane, n-pentane, and propane in the feed stream (i.e., the z_i) are 0.2, 0.15, 0.1, 0.2, 0.05, and 0.3, respectively.

To model a flash drum process, we need to apply component molar balances, an energy balance, and phase equilibrium relationships to the process to end up with a nonlinear dynamic system (i.e., systems of first-order nonlinear ordinary differential equations) with the following state variables: drum pressure P, drum temperature T, number of moles N_i of component i in the drum, mole fractions y_i and x_i of component i the in vapor and liquid phases, and the total number of moles N^V and N^L in the vapor phase and liquid phase, respectively. This model was developed within the Aspen Plus Dynamics software environment and was used to dynamically simulate the flash drum. In Aspen Plus Dynamics, the process model follows the schematic shown in Fig. 3.1. The detailed model equations are omitted for brevity but the model is readily available from the authors.

Two control loops are shown in Fig. 3.1 which are regulated by PI controllers. Specifically, PI controllers are utilized as the level controller (LC) that adjusts the liquid effluent valve to maintain the liquid level in the drum at a desired value, and as the temperature controller (TC) that adjusts the feed temperature to maintain the drum temperature T at a desired set-point value using the

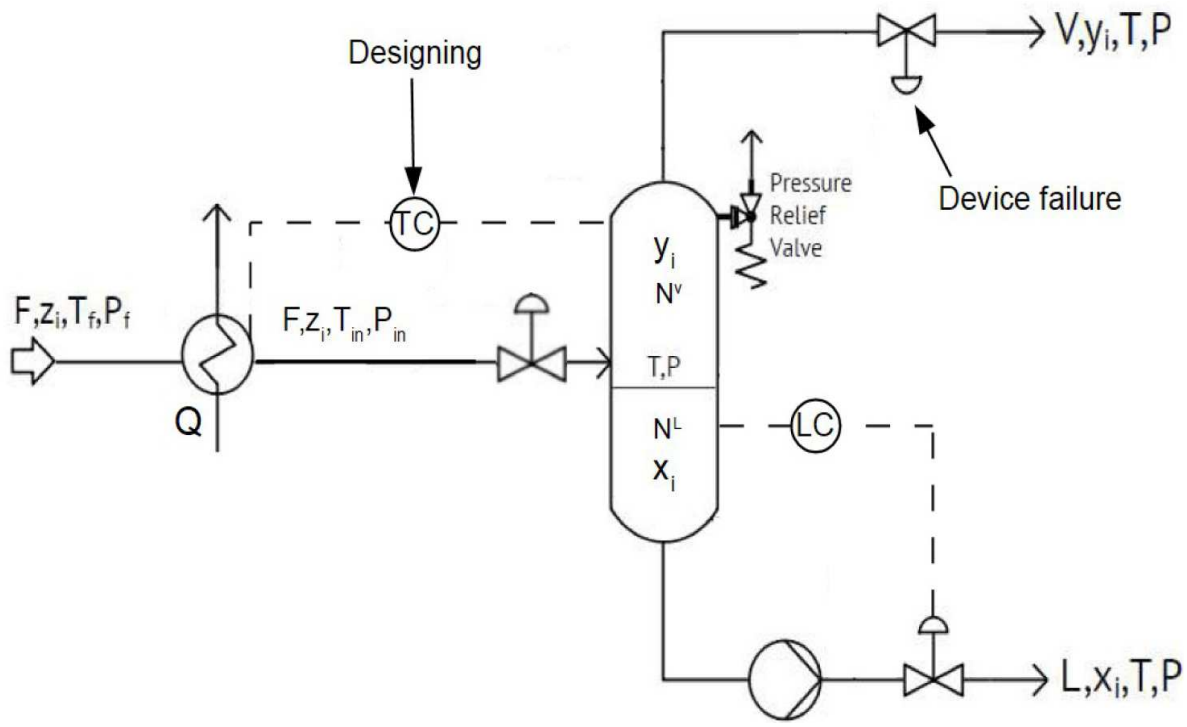

Figure 3.1: A schematic of the flash process. The temperature controller for which the tuning is changed to account for safety system activation is pointed out in the figure with the word "Designing." The vapor effluent valve experiencing the failure is pointed out in the figure with "Device failure." The three units shown in the figure besides the valves and controllers are, from left to right, a heat exchanger, flash drum, and pump.

heating duty Q as the manipulated input. Since the drum temperature and the drum pressure are related through thermodynamics, controlling the drum temperature indirectly allows manipulation of the drum pressure P.

Under normal operation, during which process equipment such as pressure sensors and valves operate properly, the two controllers can maintain the level and temperature (and indirectly the pressure) near the desired values [103]. However, a variety of fault conditions may cause an unsafe situation to occur in which an extremely high pressure may be reached in the drum (potential causes of such unsafe conditions may be faults in the top vapor effluent valve and the bottom liquid effluent valve that cause them to close). Therefore, a pressure relief valve is designed to prevent a potentially dangerous high-pressure situation by allowing pressure relief in the flash drum even if

faults occur in the vapor and liquid effluent valves.

The pressure relief valve considered in this example is a safety device designed to protect a pressurized vessel during an overpressure event and is pressure-actuated by physical means (in contrast to the type of valve termed a "safety valve" in Chapter 2, which was actuated through electrical signals based on temperature). The pressure relief valve for the flash drum in this example was designed using Aspen Plus. Since a potentially dangerous failure situation occurs when the vapor effluent valve fails, we determine the pressure relief valve parameters based on the case in which the vapor valve is totally closed. The required mass flow rate through the relief valve to quickly lower the drum pressure in such an event is calculated as the minimum mass flow rate required to keep the pressure in the drum below the maximum pressure which it can sustain; this mass flow rate is 523 kg/hr as calculated by Aspen Plus. Considering relieving conditions, fluid properties and operating conditions, a standardized orifice size of 8.303 cm^2 is used to meet the required relief flow rate.

Since the flash drum operating pressure is 10 *bar* and the highest allowable drum pressure is considered to be 12 *bar*, the opening (set) pressure of the pressure relief valve is chosen as 10.5 *bar*. The reseating pressure (at which the pressure relief valve closes) is set at 9 *bar* so that the relief valve will not close once it opens until the process equipment failure that caused the high-pressure situation is fixed. The discharge flow is considered to be only vapor. The flash calculation is based on constant enthalpy. The relief flow is considered to be a compressible fluid and the discharge coefficient is 0.96.

Remark 3.1. *The open-loop steady state of the flash drum process is an asymptotically stable one and the same is true for the closed-loop system steady-states under different relief valve settings. This conclusion was obtained by running open-loop and closed-loop simulations as the use of a large-scale simulator used to simulate the flash drum process does not allow the analytic evaluation of the eigenvalues of the Jacobian linearization of the open-loop and closed-loop process around the steady-states. With respect to the use of two PI controllers and the interaction between the loops, we carried closed-loop simulation runs in which a set-point change is requested*

in one output and the other output is requested to stay at its steady-state value and we found minimal interaction between the two control loops, thereby justifying the use of single-loop PI control.

3.2 Feedback Controller Design

3.2.1 Control Objective and Device Failure

The flash drum is initially operated at the desired operating steady-state. After the drum operates at this steady-state for 0.002 *hr*, the vapor effluent valve closes from 50% open to 0% open (i.e., it becomes fully closed) as the result of a fault. As a result of this failure, the pressure in the drum rises rapidly, reaching the opening pressure of the pressure relief valve. The pressure relief valve then opens to discharge high-pressure vapor. Both the drum temperature and drum pressure then drop. Since the pressure relief valve changes the system dynamics and PI controllers are tuned with respect to the process dynamics, more effective control of the flash drum process may be obtained during the time that the safety relief system is activated by changing the tuning of a PI controller when the pressure relief valve is open than by leaving the tuning unchanged. In the rest of this section, we explore this by developing two sets of PI control parameters for the temperature controller for the flash drum process: one which is utilized when the pressure relief valve is closed, and one which is utilized when it is open. The control objective is to maintain the drum temperature at the set-point in the presence of the failure of the vapor effluent valve, and to operate the flash drum safely before, during and after the pressure relief valve is opened (where safe operation for this example corresponds to the drum pressure remaining less than the flash drum maximum operating pressure of 12 *bar* at all times). To allow the impact of re-tuning a controller to account for safety system activation to be clearly analyzed, the tuning of the level controller ($K_c = 10$ and $\tau_I = 3600\ s$) is not adjusted when the tuning for the temperature controller is adjusted (i.e., the tuning for the level controller remains at the same value throughout the time of operation).

Table 3.1: Parameter values of the linear empirical model of Eq. 3.1 when the relief valve is closed and before any fault occurs in the pressure control loop to cause the vapor effluent valve to close (denoted by "no fault or relief valve" in the table) and after the vapor effluent valve closes and the relief valve is opened (denoted by "with fault and relief valve" in the table).

no fault or relief valve	*with fault and relief valve*
$b = 0.0202$	$b = 0.0206$
$a = 0.105$	$a = 0.113$

3.2.2 PI Controller Tuning

To develop the two sets of PI tuning parameters for the temperature controller for the cases that the relief valve is closed and when it is open, we first develop empirical linear models between the drum temperature and feed heating duty for both cases to determine the PI controller tuning parameters. Using the transient response of the drum temperature subject to a step change in the feed heating duty from its initial steady-state value, a first-order transfer function model is determined to describe the process dynamics. Specifically, data on the drum temperature T and feed heat duty Q is collected from open-loop simulations in Aspen Plus Dynamics software for a variety of step changes in Q. Then, the maximum likelihood estimation (MLE) method is applied in MATLAB to this data to identify the parameters in the following single-input-single-output model:

$$y(s) = \frac{b}{s+a}u(s) \tag{3.1}$$

where y is the drum temperature (in deviation form from its steady-state value) in $^{\circ}C$ and u is the heat duty (in deviation form from its steady-state value) in kW. The differences among the transfer functions obtained from the different step changes in Q are negligible. The model parameter values a and b for both cases are given in Table 3.1.

It needs to be mentioned that the system model identified when the relief valve is open is specific to the fault that occurred since this specific fault also impacts the dynamics of the flash drum. This means that the PI tuning parameters for the case with the fault and relief valve open are also specific to the fault that occurred because it is based on the model identified for that specific

Table 3.2: Parameter values PI controller for the flash drum inlet temperature when the relief valve is closed and before any fault occurs in the pressure control loop to cause the vapor effluent valve to close (denoted by "no fault or relief valve" in the table) and after the vapor effluent valve closes and the relief valve is opened (denoted by "with fault and relief valve" in the table).

no fault or relief valve	*with fault and relief valve*
$K_c = 4$	$K_c = 6$
$\tau_I = 14\ s$	$\tau_I = 10\ s$

scenario. In our example, the system model with the relief valve open is identified when there is a device failure corresponding to the vapor effluent valve closed from 50% to 0% open. Attempts to integrate the safety and PI control systems for an industrial system would need to account for the variety of potential fault scenarios to develop a set of PI controller tuning effective for the different possible scenarios.

Based on the above two linear system models, a PI controller is applied using the following standard form:

$$\begin{aligned} e(t_k) &= T^{set} - T(t_k) \\ u_{PI}(t_k) &= K_c \left(e(t_k) + \frac{1}{\tau_I} \int_0^{t_k} e(\tau)\, d\tau \right) \\ Q(t_k + \Delta t) &= Q(t = 0) + u_{PI}(t_k) \\ 0 &\leq Q(t_k + \Delta t) \leq Q_{max} \end{aligned} \tag{3.2}$$

where t_k and Δt are current time and sample time interval. The error $e(t_k)$ between the temperature set-point $T^{set} = 25\ ^\circ C$ and temperature measurement $T(t_k)$ at time t_k is calculated every sample interval. $Q(t = 0) = 87.2625\ kW$ is the heat duty at the initial steady-state and $Q(t_k + \Delta t)$ is the heat duty for the next sample interval. 0 and $Q_{max} = 160\ kW$ represent the lower and upper bounds on the heat duty, respectively. $u_{PI}(t_k)$ represents the control action computed by the temperature controller at time t_k. The controller gain K_c and the controller integral time τ_I used in Eq. 3.2 for the case that the relief valve is closed and the vapor effluent valve can open, and for the case that the relief valve is open and the vapor effluent valve is closed, are shown in Table 3.2. These were developed using the two different models of Eq. 3.1.

3.2.3 Simulation Results

The flash drum process including the temperature controller with a tuning that is updated when the safety system activates is dynamically simulated in Aspen Plus Dynamics. Fig. 3.2 shows that after the vapor effluent valve is closed at $t = 0.002$ *hr*, the drum temperature increases rapidly. The temperature controller reduces the heat duty such that the temperature difference between the current drum temperature and the set-point value will be decreased. However, it is observed in Fig. 3.3 that the dynamics of the temperature controller do not allow it to reduce the pressure in the drum rapidly enough to prevent the relief valve from opening, and the pressure relief valve opens when the drum pressure reaches its set pressure of 10.5 *bar*. As discussed above, different PI controller tuning parameters are utilized for the temperature controller before the vapor effluent valve closes and then after the opening of the relief valve. After the relief valve opens, the drum temperature and pressure decrease due to not only the pressure relief valve, but also the decreasing heating duty computed by the temperature controller. Eventually, after the pressure relief valve has been open for some time, the heating duty stabilizes to maintain the drum temperature at its normal operating temperature, which is the set-point temperature value used in PI controller for the heating duty.

Around time $t = 0.015$ *hr*, we assume that the fault resulting in closure of the vapor effluent valve is resolved and the vapor effluent valve returns to 50% opening. Due to the abrupt opening of the vapor valve, the drum pressure suddenly drops and reaches its reseating pressure of 9 *bar*. The pressure relief valve is closed once the drum pressure is below the reseating pressure and the parameters of the PI controller for the heat duty are changed back to their original values from before the relief valve opened. Shortly after 0.015 *hr*, after the drum temperature and pressure drop, the drum temperature increases and overshoots its set-point value. Then, the controllers drive the drum temperature back to its set-point and the system is eventually again operated at its normal operating conditions.

Fig. 3.4 shows the temperature in the flash drum (i.e., the response of the closed-loop system) over time as the vapor effluent valve is opened and closed and the relief valve is activated when

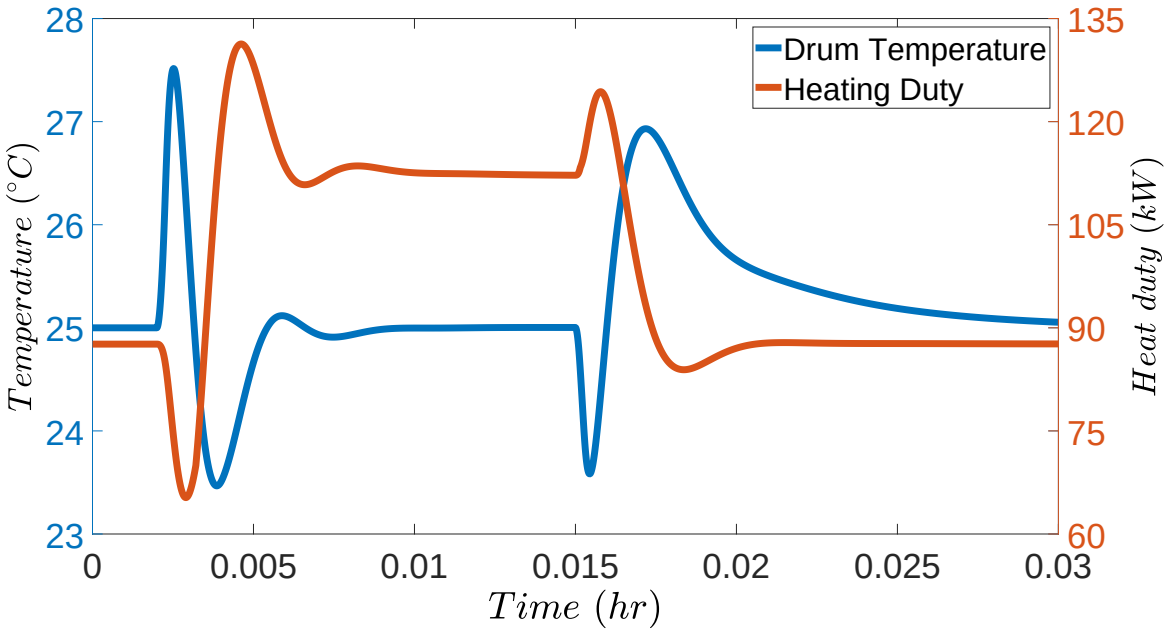

Figure 3.2: Controlled output and manipulated input for the temperature controller of the flash drum process with the tuning varying to account for the activation of the safety system.

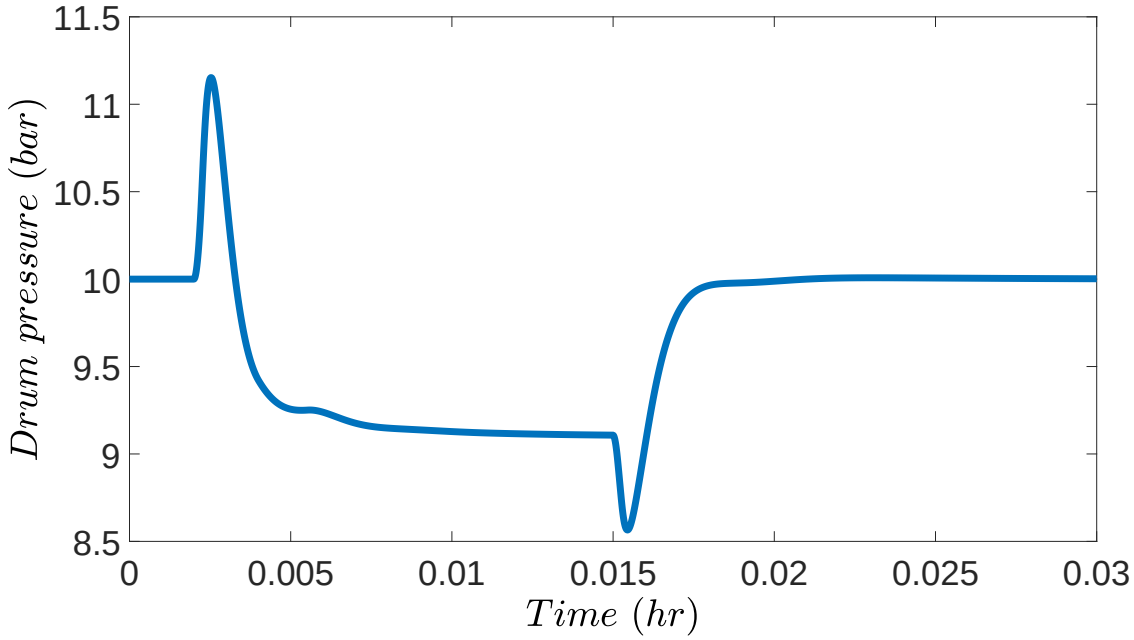

Figure 3.3: Drum pressure for the flash drum process with a varying tuning of the temperature controller to account for the activation of the safety system.

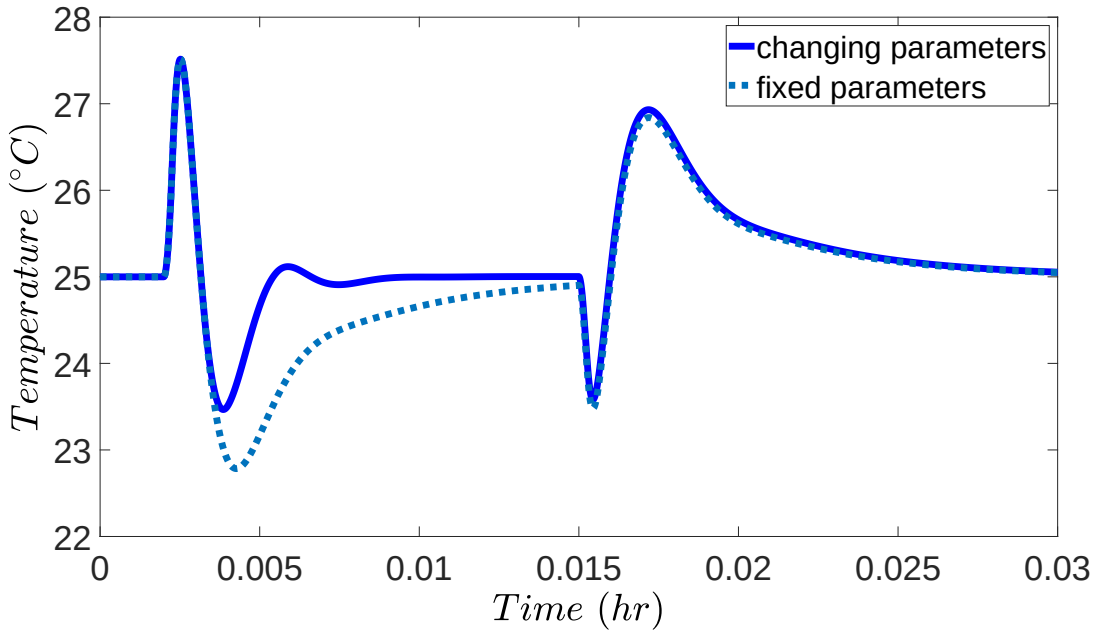

Figure 3.4: Temperature in the flash drum, with a varying tuning of the temperature controller ("changing parameters") to account for the activation of the safety system and with no change in the tuning of the temperature controller ("fixed parameters") when the safety system is activated.

the tuning of the temperature controller is fixed throughout the time of operation and when the parameters vary according to Table 3.2 based on the state of the safety system. The figure demonstrates that after the relief valve opens, the temperature controller with an updated tuning to account for the safety system activation varies the drum temperature in a smaller range compared to the temperature controller with a fixed tuning regardless of the safety system state. This temperature controller with an updated tuning also returns the temperature in the flash drum to its set-point more rapidly than the controller with the fixed tuning, leading to improved closed-loop performance.

It is worth pointing out that the pressure relief valve reseating pressure must be sufficiently low so that the relief valve will not close before the fault resulting in the closing of the vapor effluent valve has been fixed. If the pressure relief valve closed when the vapor effluent valve is still closed, the relief valve would eventually open again because the drum pressure will increase due to closure of the vapor effluent valve, and consequently, an oscillation can occur in the closure of the relief valve, which is undesirable and also has the potential to be dangerous (e.g., if it wears the

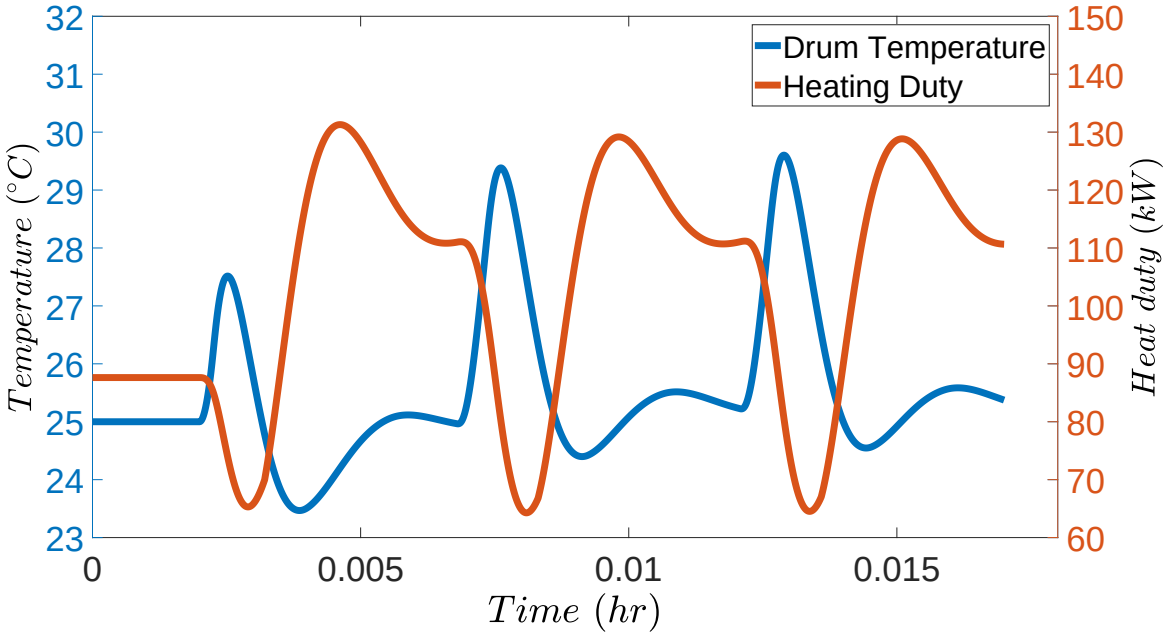

Figure 3.5: Drum temperature and heating duty for the flash drum process with a varying tuning of the temperature controller to account for the activation of the safety system when the the reseating pressure of the relief valve is set at 9.2 *bar*.

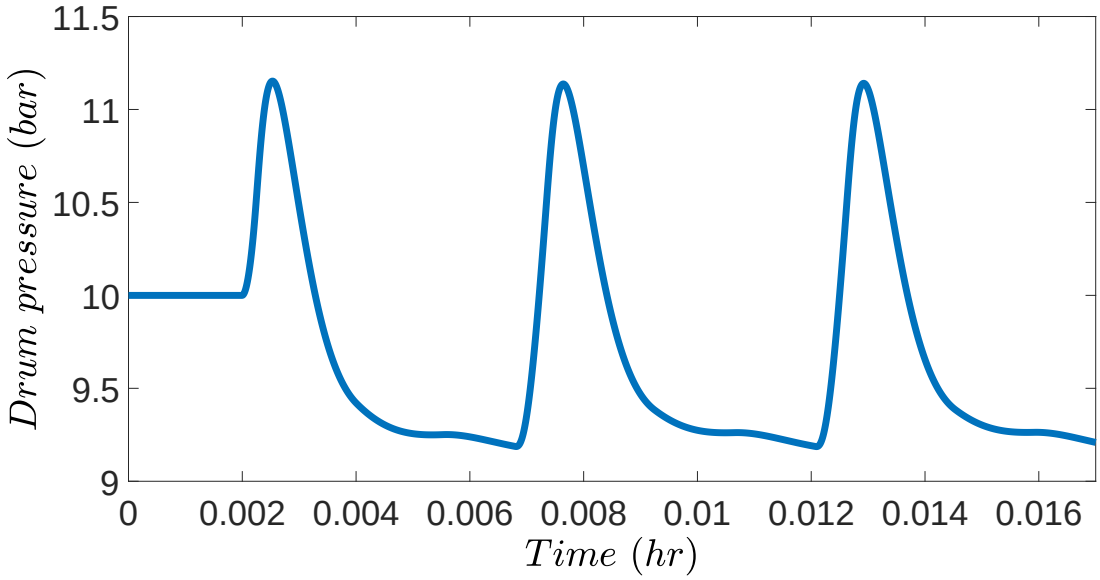

Figure 3.6: Drum pressure for the flash drum process with a varying tuning of the temperature controller to account for the activation of the safety system when the reseating pressure of the relief valve is set at 9.2 *bar*.

safety relief valve). To demonstrate this, a simulation where the reseating pressure is set at 9.2 *bar* (higher than the 9 *bar* utilized in Figs. 3.2-3.4) is shown in Fig. 3.5 and Fig. 3.6. In these figures, when the drum pressure drops to 9.2 *bar*, the relief valve is closed, and then the drum pressure increases rapidly until the relief valve opens again; this phenomenon should be avoided by using a lower reseating pressure for the safety relief valve. This indicates that to coordinate the control and safety systems effectively, it may be necessary to design these systems together (i.e., trying to determine an appropriate reseating pressure without analyzing the safety system's integration with the control system may result in too high of a reseating pressure being chosen so that the control and safety systems cannot be effectively coordinated). Furthermore, it indicates that closed-loop simulations may aid in determining an effective reseating pressure, since in general the pressure in a vessel may vary according to a nonlinear, coupled process dynamic model (where these dynamics change upon the activation of the safety system) under potentially different disturbances over time which are unknown *a priori*. It may also be helpful, when possible, to allow for manual relief valve opening and closure in the design of the valve to aid in handling issues with reseating pressure that could not be handled during the initial selection of the reseating pressure.

3.3 Conclusion

In this chapter, we focused on valve malfunction in a flash drum process under a PI controller integrated with a pressure relief valve. We demonstrated that modifying the parameters of a PI controller based on the safety system being on or off can lead to improved closed-loop performance compared to the case in which the parameters of the PI controller remain fixed regardless of the actions of the safety system.

Chapter 4

Safeness Index-based Model Predictive Control: Flash Drum Case Study

4.1 Introduction

Recently, in [9, 168, 171], a Safeness Index function was developed to provide thresholds as triggers for safety system activation that allow the safety systems to be aware of system-level safety considerations, and further can be utilized as a constraint in MPC design to provide some coordination between control and safety systems. Further development is expected for systematic methods to coordinate control and safety systems using Safeness Index functions such that the control system could reduce safety system activation to avoid unnecessarily abrupt change in operating conditions.

In this chapter, we illustrate an application of the Safeness Index-based model predictive control to improve process operational safety in a safety-critical chemical process application. A linear model is first identified from nominal process data. Then, a Safeness Index function and a Safeness Index threshold are designed to account for the key process properties and safety system characteristics. Safeness Index is integrated in MPC as a soft constraint with slack variables when the process state is outside of a safe operating region. Finally, the proposed methodology is tuned

to deal with the plant/model mismatch and certain level of disturbance attenuation. The control and safety system are validated using co-simulation of Matlab/Aspen to demonstrate that Safeness Index-based MPC can either avoid activating safety system in the presence of a small disturbance, or work together with the safety system which is activated/deactivated in the presence of a large disturbance.

The rest of the chapter is organized as follows: in Section 4.2, a flash drum process and its potential failures are introduced. In Section 4.3, the Safeness Index function is first introduced and the Safeness Index-based MPC is then developed. In Section 4.4, the proposed Safeness Index-based MPC is applied to the flash drum in the presence of disturbances with different magnitudes to demonstrate its effectiveness.

4.2 Flash Drum Process Description and Control Objective

4.2.1 Flash Drum Process Description and Relief Valve Design

As shown in Fig. 4.1, a flash process [103] is used to roughly separate a mixture of methane (10 %), ethane (20 %), propane (30 %), butane (35 %) and pentane (5 %), to a level where further distillation towers are used. A liquid feed with flow rate F, mole fraction z_i of component i, temperature T_f and pressure P_f, is heated by a heat exchanger with heating duty Q, and turned into F, z_i, T_{in}, P_{in}. Passing through a throttling valve, the feed is separated adiabatically in the drum into liquid stream L with composition x_i and vapor stream V with composition y_i. Components are separated due to different vapor pressure of different components. The feed temperature T_f is 40 $^{\circ}C$, the feed pressure P_f is 45 bar, the drum height is 4 ft and the drum diameter is 1 ft.

To model a flash process, we need to apply component molar balance, energy balance, phase equilibrium and other equations, and end up with a dynamic system with state variables of drum pressure P, drum temperature T, number of moles N_i of component i in drum, mole fractions y_i and x_i of component i in vapor and liquid phase, respectively, and total number of moles N^V and N^L in vapor phase and liquid phase, respectively. To simplify simulation, Aspen Plus Dynamics

software is used to dynamically simulate this flash drum. In Aspen Plus Dynamics, the process model is built up according to the schematic in Fig. 4.1 and the parameters above.

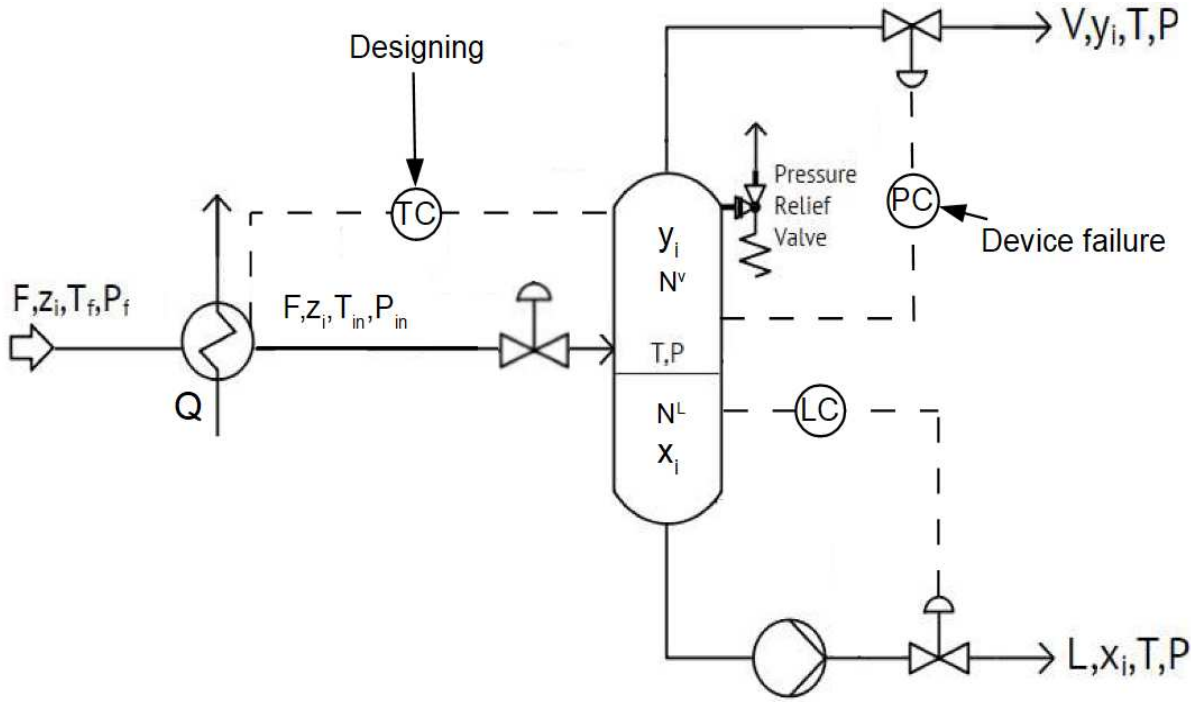

Figure 4.1: A schematic of flash process

In a safe scenario, controllers maintain the drum pressure near its desired value, relying on the proper operation of equipments such as pressure sensor and valves [103]. Two controllers are used to regulate liquid effluent valve and vapor effluent valve to maintain drum liquid level and drum pressure at desired levels, respectively. However, in an unsafe scenario where the top vapor effluent and the bottom liquid effluent valves are accidentally closed, or the broken pressure sensor causes improper control actions, an extremely high pressure will occur in the drum, which is undesired. Therefore, a pressure relief valve needs to be incorporated to handle potential dangerous situations.

Pressure relief valve is a safety device designed to protect a pressurized vessel or system in an overpressure event. In our work, Aspen Plus is used to design the pressure relief valve (e.g., size, dynamics, etc.) for this flash drum. Since the most dangerous failure situation is the vapor valve failure which normally should be directed by a controller, we design pressure relief

valve parameters based on the case that the top vapor valve is totally closed accidentally due to control failure. The required relief flow is calculated as the minimum flow required to guarantee device safety, which is 523 kg/h calculated by Aspen Plus. Considering relieving conditions, fluid properties and operating conditions, a standardized orifice size of 8.303 cm^2 is used to meet the requirement of relief flow.

Additionally, since the operating pressure is 10 *bar* and the highest device durable pressure is 12 *bar*, the opening pressure of the pressure relief valve is chosen to be 10.5 *bar*. Reseating pressure is set at 9 *bar* such that the relief valve will not close once it opens until the process failure is settled. The discharge flow is considered only vapor. Flash calculation is based on constant enthalpy. The relief flow is considered compressible fluid and the discharge coefficient is 0.96.

4.2.2 Device Failure and Control Objective

The flash drum initially operates at the desired operating steady-state under a model predictive controller. After operating the drum at the steady-state, a device failure is introduced, which causes the top vapor valve to close from 50 % opening to a smaller opening. As a result, the pressure P and temperature T in the drum rise up immediately, which leads to an unsafe operation.

Therefore, the objective of the control system is to maintain the drum temperature T at a desired set-point and to prevent the relief valve from opening in the presence of a small disturbance using the heating duty of the feed Q as the manipulated input . Specifically, the temperature T is controlled at the steady-state while the drum pressure P should remain below 10.5 *bar* when the top vapor valve has a failure. The worst case scenario for which we design the controller to deal with is that the top vapor valve is closed from 50 % opening to 35 % opening. When the top vapor valve opening is less than 35 %, the pressure relief valve may open and the controller should work safely with relief valve before, during and after pressure relief valve is turned on/off (drum pressure remains less than the device maximum operating pressure of 12 *bar*).

4.3 Safeness Index-based Model Predictive Control

4.3.1 Model Identification

The flash drum is simulated with high fidelity in Aspen Plus Dynamics, with a steady-state temperature and pressure $[T_s\ P_s] = [25\ ^\circ C\ 10\ bar]$ and a steady-state heating duty $Q_s = 87.6\ kW$. The states and the input of the process are represented in deviation variable form as $x^T = [T - T_s\ P - P_s]$ and $u = Q - Q_s$, such that the equilibrium point of the system is at the origin of the state-space. Since a process model of flash drum is needed in MPC, a linear dynamic model in the following form is identified:

$$\frac{dx}{dt} = Ax + Bu \tag{4.1}$$

where $A \in \mathbf{R}^{2\times 2}$ and $B \in \mathbf{R}^{2\times 1}$. We use Aspen simulation data to identify the matrices A and B in the model. Specifically, data on drum temperature T and pressure P is generated from open-loop simulation by pseudorandom binary sequence (PRBS) signal in heating duty Q. Then Multivariable Output Error State Space (MOSEP) algorithm is applied on this data in Matlab to identify the matrices A and B as follows:

$$A = \begin{bmatrix} -0.047453 & -0.22548 \\ -0.001111 & -0.097369 \end{bmatrix}$$

$$B = \begin{bmatrix} 0.01488 \\ 0.002277 \end{bmatrix}$$

4.3.2 Development of Safeness Index

Safeness Index is a function of process state and indicates the safeness of the plant as a whole, accounting for multivariable interactions and interactions between units [9]. Instead of typical component-by-component safety analysis (e.g., a relief valve traditionally only accounts for pressure), Safeness Index can consider interactions between states. Moreover, a state-based index

reveals that a process becomes unsafe in a gradual way [93] instead of becoming unsafe suddenly when crossing a threshold.

From fundamental process knowledge, high temperature and high pressure are the key safety issues in the flash drum. Safeness Index needs to be designed such that high temperature T and pressure P are considered unsafe operating conditions, but all the temperature T and pressure P below steady-state values are considered safe operation conditions. Therefore, in this example, Safeness Index is designed to be zero if both x_1 and x_2 are negative (e.g., below the steady-state value), and positive if either x_1 or x_2 is positive (e.g., above the steady-state value). Based on $f^+(x)$, we design the Safeness Index to be of the following form:

$$f^+(x) = \begin{cases} x, & \text{if} \quad x \geq 0 \\ 0, & \text{if} \quad x < 0 \end{cases} \tag{4.2}$$

$$S(x) = k_T \ [f^+(\frac{x_1}{T_s})]^2 + k_P \ [f^+(\frac{x_2}{P_s})]^2 \tag{4.3}$$

where k_T and k_P are the weights for temperature and pressure, respectively. Temperature and pressure in deviation form are divided by their steady-state values T_s and P_s for normalization such that potential difference in magnitude of the two terms are removed in the expression of the Safeness Index. With a quadratic form, $S(x)$ will have a significantly large value when temperature T and pressure P are far above the steady-state. Since high pressure is more dangerous than high temperature, more weight should be given to pressure P. Therefore, we choose $k_T = 1000$ and $k_P = 3000$. It is important to mention that although the Safeness Index and the Lyapunov function share similar functional forms in this case, they work to address different control objectives. Specifically, the Safeness Index is designed to indicate process safety based on measured states while the Lyapunov function is used to ensure closed-loop stability. Furthermore, the Safeness Index does not have the Lyapunov function properties. When the Safeness Index function is chosen to be a Lyapunov function, the MPC may enforce properties, such as stability and feasibility.

To avoid triggering the safety relief valve, threshold S_{TH} of Safeness Index function should be

lower than the threshold used in safety relief valve [9]. In consideration of model mismatch and sample-and-hold implementation of the controller, the actual threshold in the Safeness Index-based MPC needs to be more conservative to allow some overshoot in Safeness Index but not exceeding the threshold to trigger the safety relief valve. Therefore, we first calculate $S(x)$ when the relief valve is activated at 10.5 *bar* (i.e., $T = 25\ ^{\circ}C, P = 10.5\ bar$, and $S([0\ 0.5]^T) = 7.5$). In this case, the threshold in controller is chosen as $S_{TH} = 6$.

4.3.3 Safeness Index-based Model Predictive Control

Safeness Index-based MPC is given by the following optimization problem:

$$\min_{u \in S(\Delta), y} \quad \int_{t_k}^{t_{k+N}} (\|\tilde{x}_1(\tau)\|^2_{Q_c} + \|u(\tau)\|^2_{R_c})\, d\tau + \sum_{i=1}^{N} k_1 e^{-k_2 y(i)} \tag{4.4a}$$

$$\text{s.t.} \quad \dot{\tilde{x}}(t) = A\tilde{x}(t) + Bu(t) \tag{4.4b}$$

$$\tilde{x}(t_k) = x(t_k) \tag{4.4c}$$

$$u(t) \in U,\ \forall\, t \in [t_k, t_{k+N}) \tag{4.4d}$$

$$S(\tilde{x}(t_{k+i})) + y(i) = S_{TH}, \quad i = 1, 2, ..., N \tag{4.4e}$$

$$y(i) \geq 0,\ i = 1, 2, ..., N, \quad if\ S(x(t_k)) \leq S_{TH} \tag{4.4f}$$

where $\tilde{x}$ is the predicted state trajectory, $S(\Delta)$ is the set of piecewise constant functions with period Δ, and N is the number of sampling periods in the prediction horizon. The optimal input trajectory of the Safeness Index-based MPC optimization problem is $u^*(t)$, which is calculated over the entire prediction horizon $t \in [t_k, t_{k+N})$. The control action computed for the first sampling period in the prediction horizon $u^*(t_k)$ is applied over the first sampling period, and the MPC problem is resolved at the next sampling period. The objective function of Eq. 4.4a is minimizing the integral of $\|\tilde{x}_1(\tau)\|^2_{Q_c} + \|u(\tau)\|^2_{R_c}$ over the prediction horizon and the penalty term $\sum_{i=1}^{N} k_1 e^{-k_2 y(i)}$ of slack variables $y(i)$. It is noted that only state x_1 (instead of full state x) is included in the objective function because this controller is controlling only drum temperature T (pressure P is involved by

Safeness Index constraints in Eq. 4.4e). The constraint of Eq. 4.4b is the linear model of Eq. 4.1 that is used to predict the states of the closed-loop system. Eq. 4.4c defines the initial condition $\tilde{x}(t_k)$ of the optimization problem which is the state measurement $x(t_k)$ at $t = t_k$. Eq. 4.4d is the input constraint applied over the entire prediction horizon. The manipulated input is heating duty Q, which is bounded by: $0 \leq Q \leq 160\ kW$, namely $U = [-87.6,\ 72.4]$. Eq. 4.4e is the Safeness Index constraint, which confines $S(x)$ to be below threshold S_{TH} with slack variables $y(i)$. The soft constraint of Eq. 4.4e gradually affects the input when $S(x)$ gradually gets close to threshold S_{TH}, instead of causing an abrupt input if slack variables are not used. If $S(x(t_k)) > S_{TH}$, the constraint of Eq. 4.4e can be satisfied via the negative slack variables $y(i)$ such that Safeness Index can remain above threshold S_{TH} in the prediction horizon, even though the penalty term $\sum_{i=1}^{N} k_1 e^{-k_2 y(i)}$ in the objective function of Eq. 4.4a is large. However, if $S(x(t_k)) \leq S_{TH}$, nonnegative slack variables $y(i)$ are required by Eq. 4.4f to ensure $S(x)$ remaining below threshold S_{TH}. Additionally, it is demonstrated that the hard constraint of Eq. 4.4f can always be satisfied in this flash drum case because of the property of A matrix in Eq. 4.1. Specifically, since all four elements in A matrix are negative, there always exists an input u (e.g., $u = 0$) such that $\dot{x}_1$ and $\dot{x}_2$ are simultaneously negative. Because $S(x)$ is a monotonous function with respect to x_1 and x_2, there always exists an input u such that $S(x)$ can remain below S_{TH} if $S(x(t_k)) \leq S_{TH}$. Additionally, parameters k_1 and k_2 in the objective function of Eq. 4.4a should be carefully chosen, such that the slack variables $y(i)$ have slight effects on control actions if $S(x(t_k)) \leq S_{TH}$, and have significant effect on control actions if $S(x(t_k)) > S_{TH}$. Thus, in our simulation k_1 and k_2 are determined to be 90 and 1.6, receptively.

The explicit Euler method with an integration time step of $h_c = 10^{-3}\ s$ was applied to numerically integrate the dynamic model of Eq. 4.1 in Safeness Index-based MPC. The nonlinear optimization problem of Safeness Index-based MPC of Eq. 4.4 was solved using the solver FilterSD on OPTI Toolbox in Matlab with the following parameters: sampling period $\Delta = 0.5\ s$; prediction horizon $N = 10$. $Q_c = 1$ and $R_c = 0.0005$ are chosen such that the term related to the states and the term related to the input are on the same order of magnitude in $\|\tilde{x}_1(\tau)\|^2_{Q_c} + \|u(\tau)\|^2_{R_c}$.

Although the function $f^+(x)$ in the Safeness Index $S(x)$ in Eq. 4.4e is non-differentiable at $x = 0$, the gradient of Safeness Index constraints based on f^+ in MPC is solved via numerical methods and therefore does not create difficulties in solving the optimization problem. Additionally, in this manuscript, the states in the simulations are always positive, avoiding the non-differentiable point $x = 0$.

4.4 Simulation Results

4.4.1 Simulation without Safety System Activation

In this section, we demonstrate the application of the Safeness Index-based MPC to a flash drum process under disturbances with different magnitudes.

When the top vapor valve is closed from 50% to 45 % opening, it is demonstrated in Figs. 4.2 and 4.3 that the pressure, temperature, and Safeness Index increase initially. As a result, the input Q is decreased by the Safeness Index-based MPC of Eq. 4.4 such that both $\|\tilde{x}_1(\tau)\|^2_{Q_c}$ and $\sum_{i=1}^{N} k_1 e^{-k_2 y(i)}$ in the objective function of Eq. 4.4a are minimized. Specifically, $\sum_{i=1}^{N} k_1 e^{-k_2 y(i)}$ can be minimized with larger slack variables, which leads to a smaller Safeness Index over the prediction horizon and eventually leads to a decreasing input Q.

In the presence of a relatively small disturbance (e.g., the top vapor valve is closed from 50% to 45 % opening), the Safeness Index-based constraints of Eq. 4.4e should not constrain process operation region too much. In other words, if $S(x(t_k)) \leq S_{TH}$, small positive or zero slack variables should be utilized such that the Safeness Index is not confined to a small value according to Eq. 4.4e. To that end, a large k_2 in the objective function of Eq. 4.4a is utilized since the term $k_1 e^{-k_2 y(i)}$ is insensitive to nonnegative slack variables $y(i)$ with a large k_2. It is observed in Fig. 4.3 that Safeness Index $S(x)$ finally settles down to 3.3 with $k_2 = 1.6$. However, as shown in Fig. 4.4, if a smaller $k_2 = 1$ is used, Safeness Index $S(x)$ will finally stay much below 3.3, which is undesired.

It needs to be mentioned that the nominal steady-state ($x = 0$) is not reached at the end of the closed-loop simulation, because the disturbance value does not go back to zero and the MPC uses

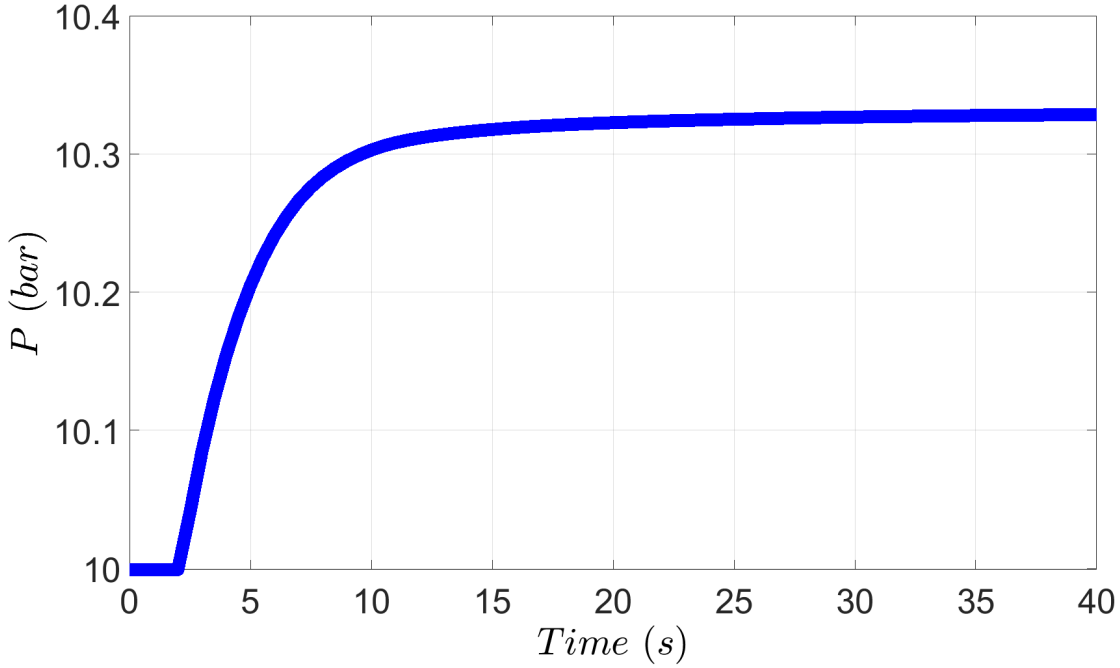

(a) Drum pressure profile

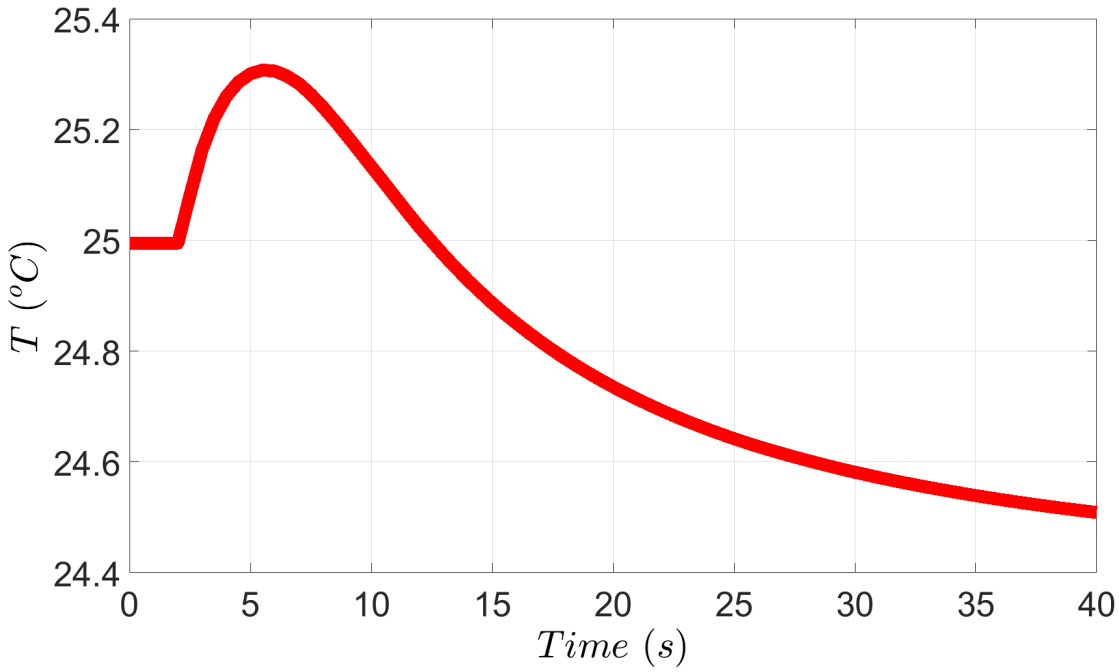

(b) Drum temperature profile

Figure 4.2: Drum pressure and temperature profiles when the top vapor valve is closed from 50% to 45% opening.

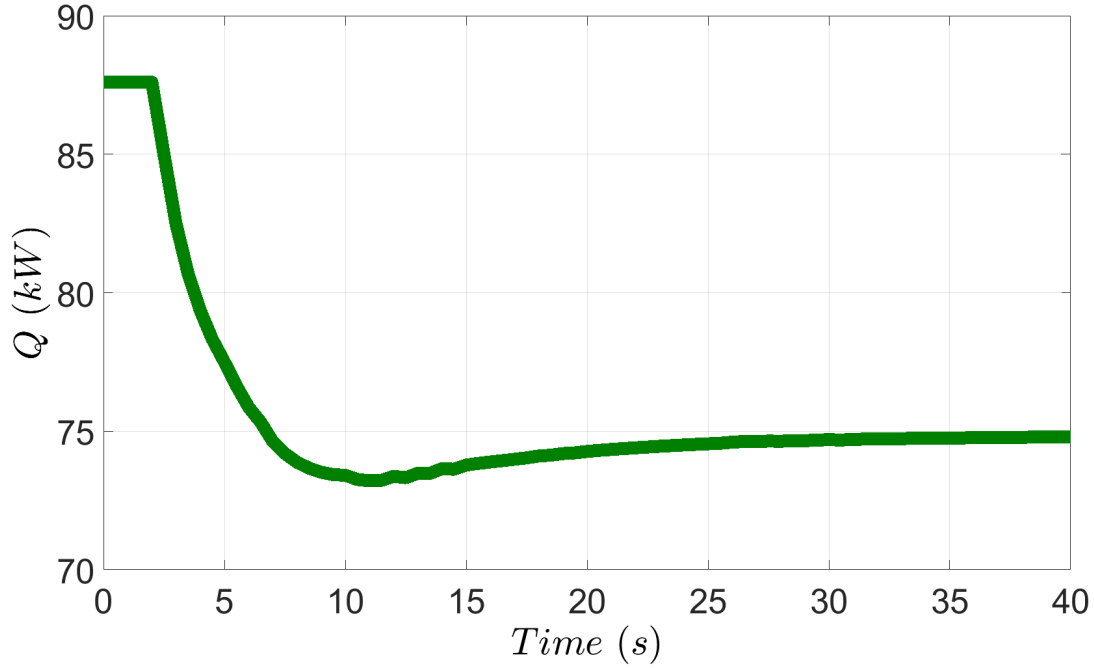

(a) Manipulated input profile

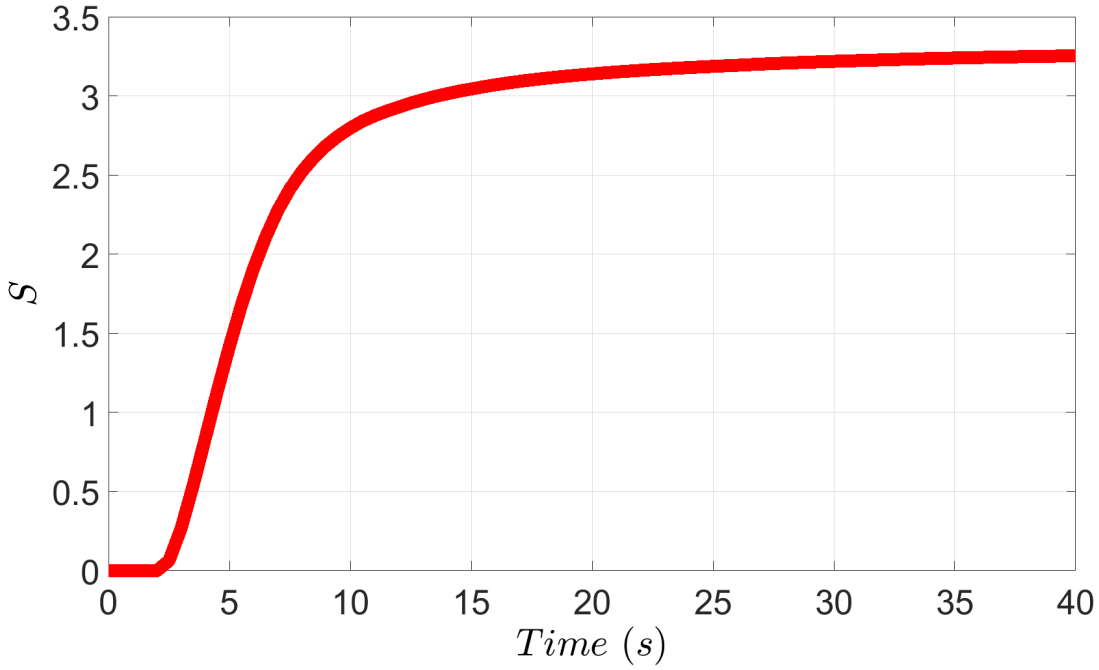

(b) Safeness Index profile

Figure 4.3: Input and Safeness Index profiles when the top vapor valve is closed from 50% to 45% opening.

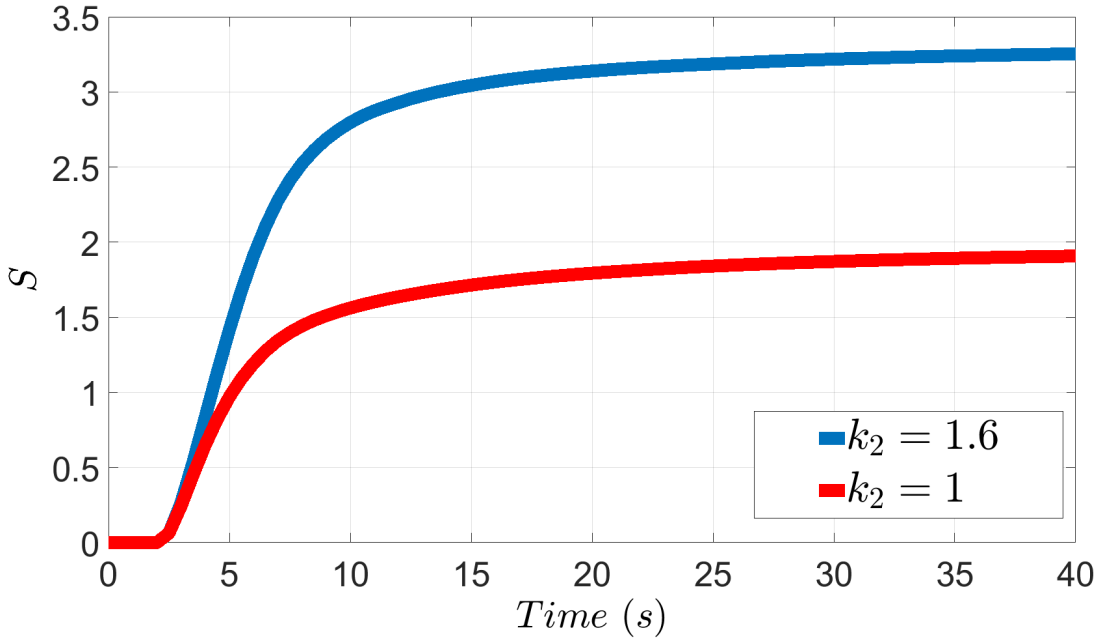

Figure 4.4: Safeness Index profiles under different k_2, from which it is shown that the small k_2 (i.e., $k_2 = 1$) results in a more conservative process operation region than the large k_2 (i.e., $k_2 = 1.6$)

the nominal process model. This offset can be removed if an integral control term is added to the MPC control action but this approach is not pursued in this work.

When the top vapor valve is closed to 35 % opening, it is demonstrated in Figs. 4.5 and 4.6 that the pressure, temperature and Safeness Index increase immediately after the disturbance occurs. When Safeness Index is getting close to the threshold S_{TH}, input Q becomes aggressive to prevent pressure exceeding 10.5 *bar*. When $S(x(t_k)) > S_{TH}$, negative slack variables $y(i)$ are utilized to satisfy the constraint of Eq. 4.4e. Since the term $\sum_{i=1}^{N} k_1 e^{-k_2 y(i)}$ dominates the objective function of Eq. 4.4a when $y(i)$ are small, MPC tends to calculate relatively large slack variables $y(i)$ to decrease future Safeness Index $S(\tilde{x}(t_{k+i}))$, which leads to aggressive input Q. In Figs. 4.5 and 4.6, it is shown that the input Q decreases to its lower bound to stop Safeness Index increasing when Safeness Index is close or above the threshold S_{TH}.

Additionally, It is noted that a larger k_2 can reduce Safeness Index faster when $S(x(t_k)) > S_{TH}$. When slack variables are negative, minimizing the objective function of Eq. 4.4a with larger k_2 leads to larger slack variables, which decreases Safeness Index faster by using more aggressive

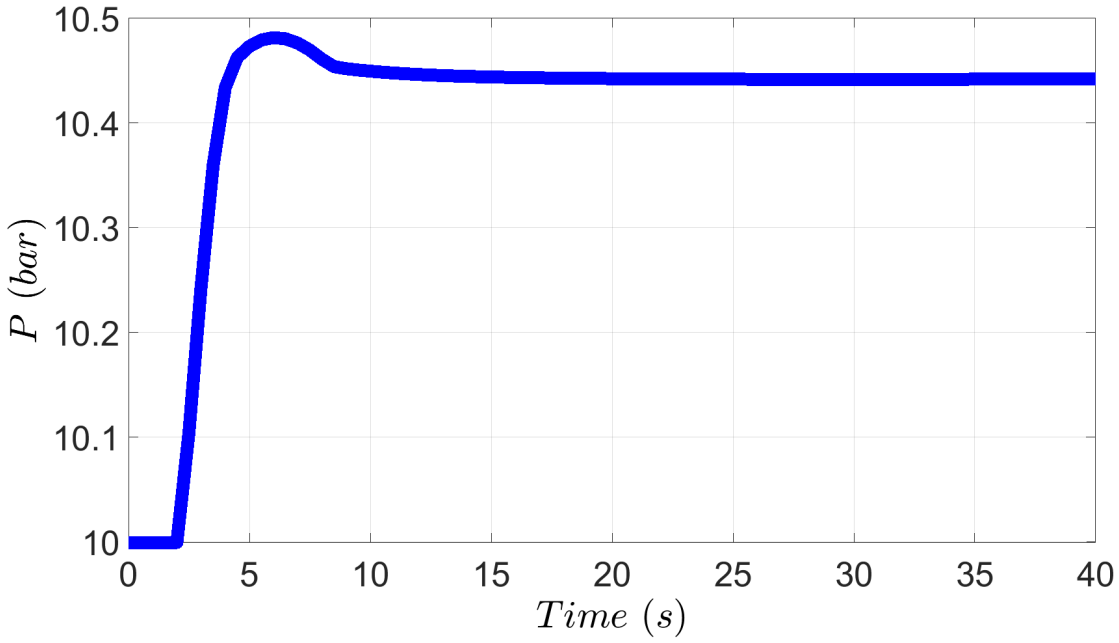

(a) Drum pressure profile

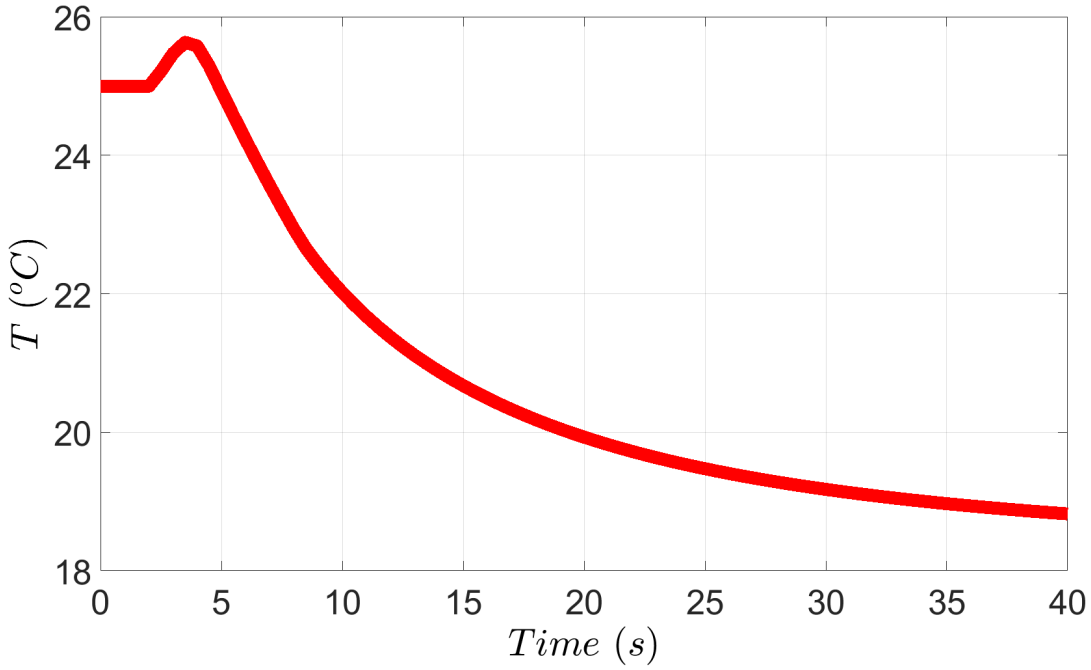

(b) Drum temperature profile

Figure 4.5: Drum pressure and temperature profiles when the top vapor valve is closed from 50% to 35% opening.

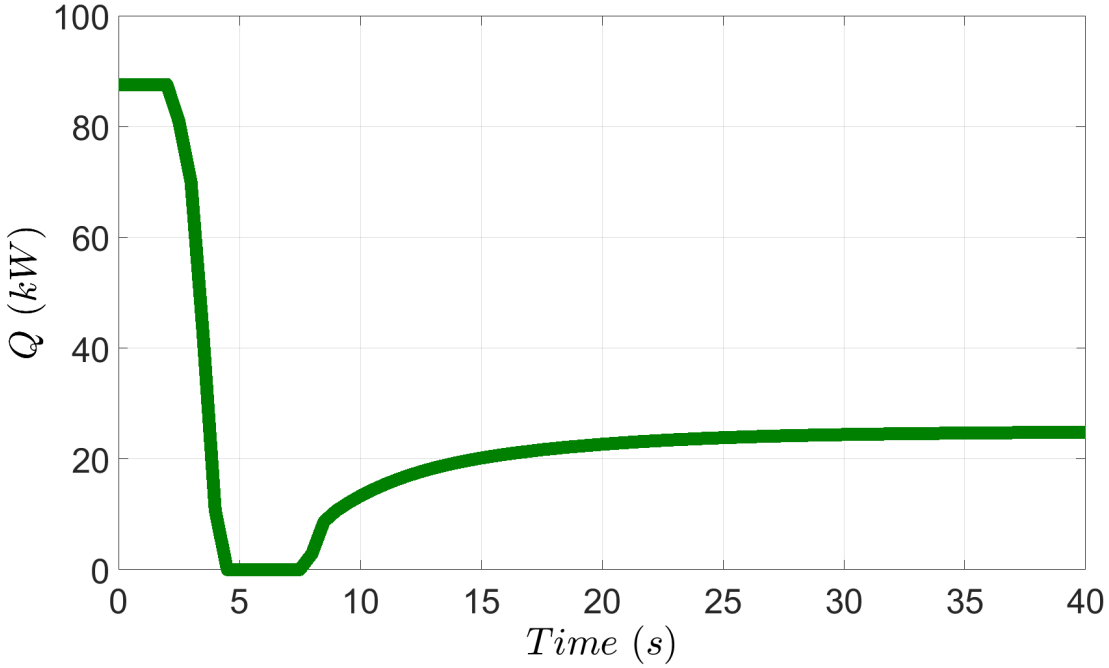

(a) Manipulated input profile

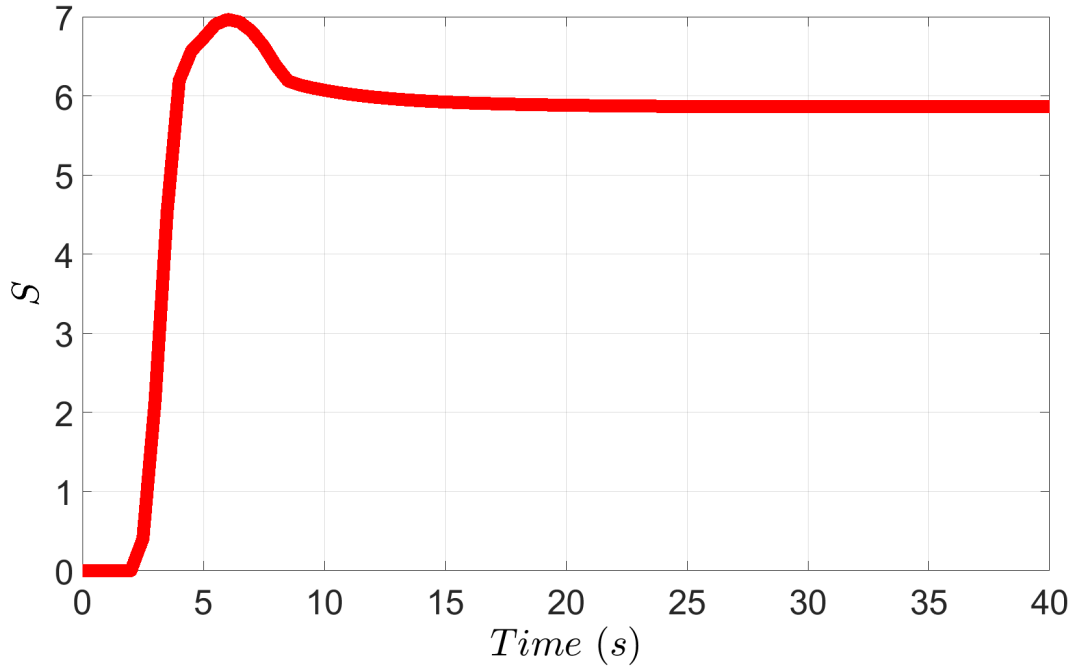

(b) Safeness Index profile

Figure 4.6: Input and Safeness Index profiles when the top vapor valve is closed from 50% to 35% opening.

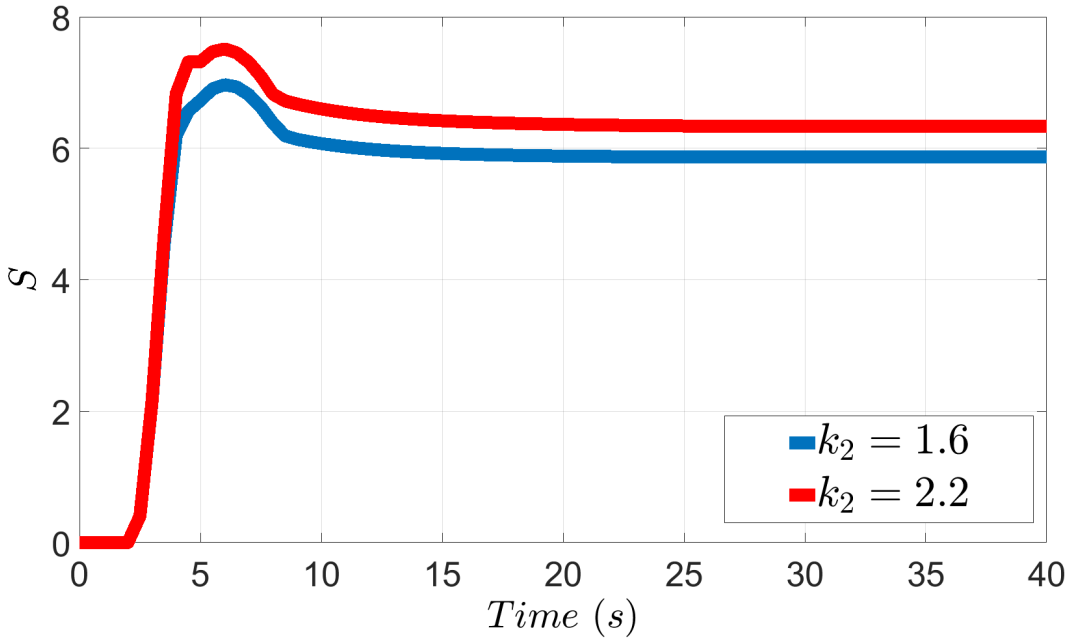

Figure 4.7: Safeness Index profiles under different k_2, from which it is shown that the large k_2 (i.e., $k_2 = 2.2$) does not reduce Safeness Index S below S_{TH}

input. However, in the case of limited input, large k_2 is not able to decrease Safeness Index faster if the input already hits its bound when using a small k_2. As shown in Fig. 4.7, a large $k_2 = 2.2$ does not reduce Safeness Index S below S_{TH} because heating duty Q already reaches its minimum value even if $k_2 = 1.6$.

Additionally, model mismatch is inevitable in all simulations because the linear model of Eq. 4.1 used in controller is identified from the nominal system simulations, but applied to the real system with disturbance. Particularly, the disturbance dramatically increases the steady-state of temperature and pressure so that temperature and pressure increase significantly with a fixed input in the presence of disturbance. Because of model mismatch, Safeness Index based on the actual states may finally exceed the threshold S_{TH}. However, a smaller k_2 in objective function of Eq. 4.4a can alleviate the adverse effect of model mismatch by calculating a conservative Safeness Index. Specifically, a small k_2 tends to calculate larger slack variables if slack variables are positive. It is demonstrated in Eq. 4.4e that larger slack variables lead to a lower and conservative Safeness Index, which can bring Safeness Index to a lower value to alleviate the adverse effect of model

mismatch.

Additionally, parameters k_1 and k_2 should be well-determined to account for how conservative the threshold S_{TH} is compared to the threshold of safety system. If the threshold S_{TH} is very conservative, a large k_2 is preferred such that the Safeness Index can keep close to the threshold S_{TH} under all disturbances. If the threshold S_{TH} is not conservative, a small k_2 is preferred so that the Safeness Index can remain below the threshold S_{TH}. Parameter k_1 should be chosen according to k_2 so that the term $\int_{t_k}^{t_{k+N}} (\|\tilde{x}_1(\tau)\|_{Q_c}^2 + \|u(\tau)\|_{R_c}^2)\, d\tau$ in the objective function of Eq. 4.4a is larger than the term $\sum_{i=1}^{N} k_1 e^{-k_2 y(i)}$ under a relatively small disturbance, and smaller under a large but handleable disturbance.

4.4.2 Simulation with Safety System Activation

In the presence of a large disturbance, the control system is unable to prevent a high pressure inside the drum due to actuator constraints. In this simulation, the top vapor valve is changed from 50 % opening to 10 % opening. As shown in Figs. 4.8 and 4.9, the drum pressure P rises above 10.5 *bar* even when the minimum heating duty Q is provided. Then, the pressure relief valve is activated to allow the pressurized fluid to flow out of the drum. MPC drives the temperature T to 0.2 $^\circ C$ below the set-point (25 $^\circ C$) because of model mismatch from vapor valve disturbance and relief valve opening. After 40 *s*, the device failure is fixed and the top vapor valve returns to 50 % opening. Then the pressure P decreases immediately after opening the vapor valve. When the pressure P decreases to 9 *bar* which is the reseating pressure, the safety relief valve is closed and the process states are driven to the steady-state by the Safeness Index-based MPC.

4.5 Conclusion

In this chapter, a high-pressure flash drum separator together with pressure relief valve as safety system was utilized to analyze the benefits of integrating Safeness Index-based considerations in model predictive control (MPC). Specifically, a Safeness Index function and a Safeness Index

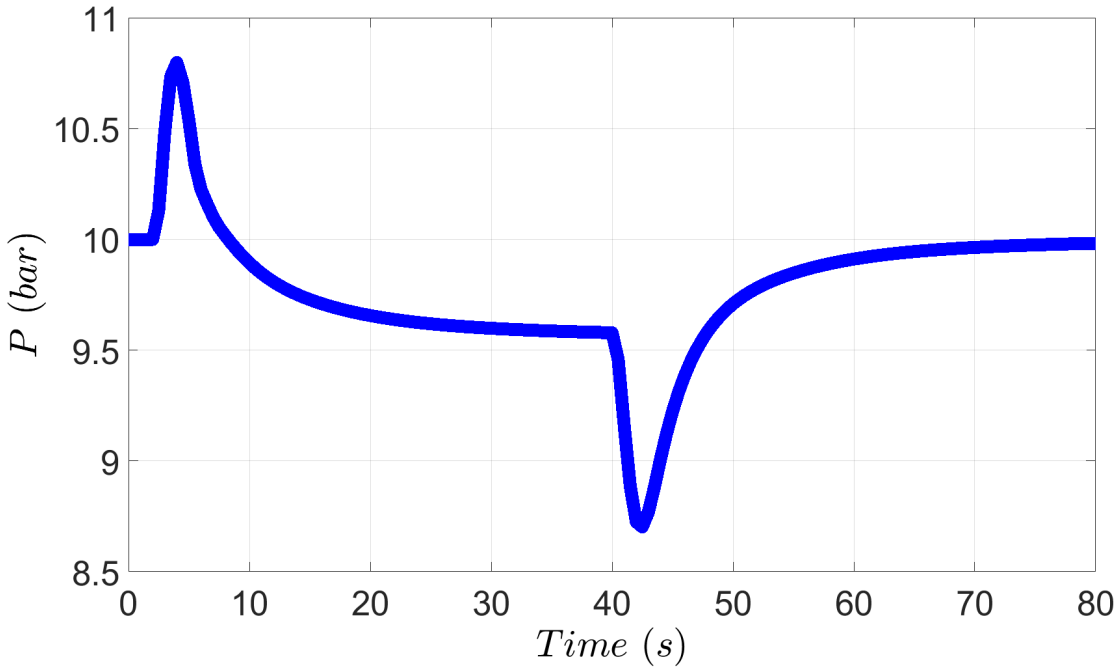

(a) Drum pressure profile

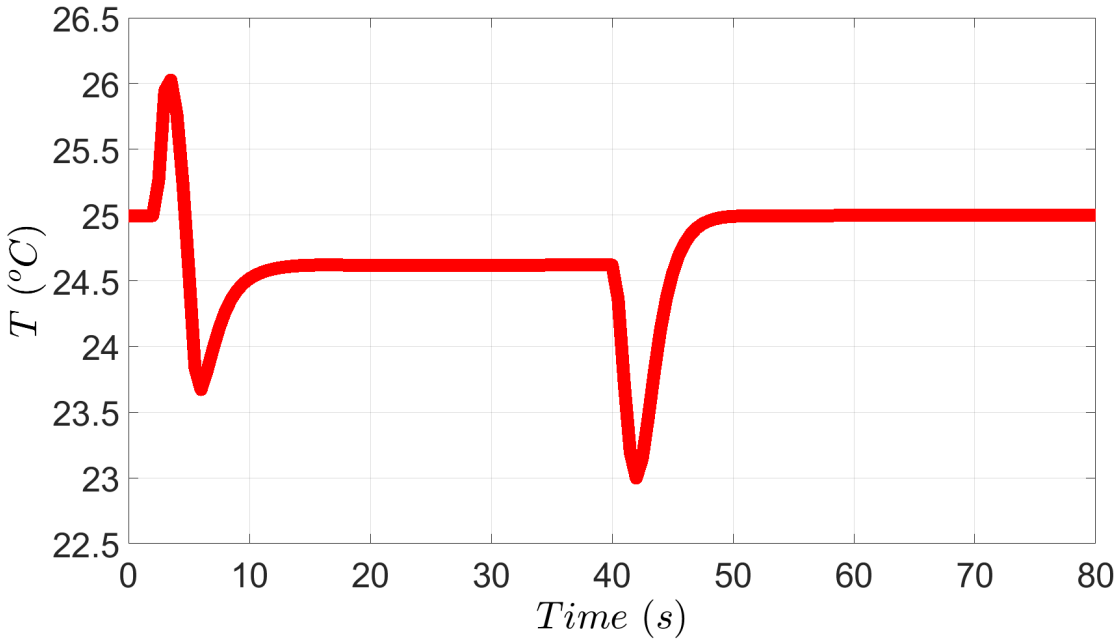

(b) Drum temperature profile

Figure 4.8: Drum pressure and temperature profiles when the top vapor valve is closed from 50% to 10% opening.

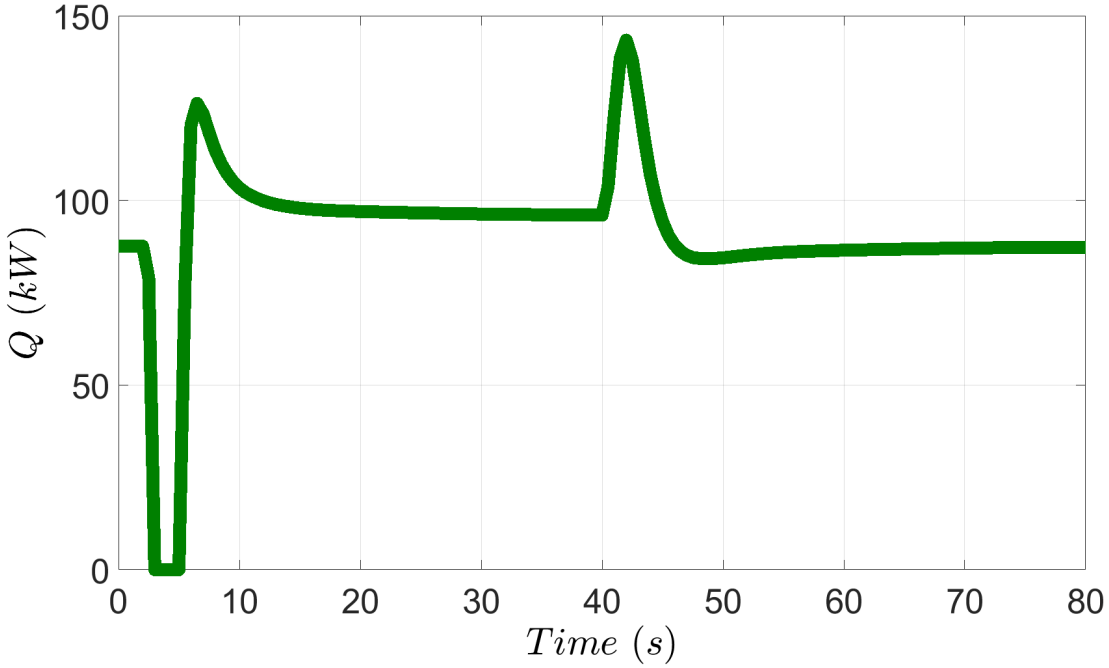

(a) Manipulated input profile

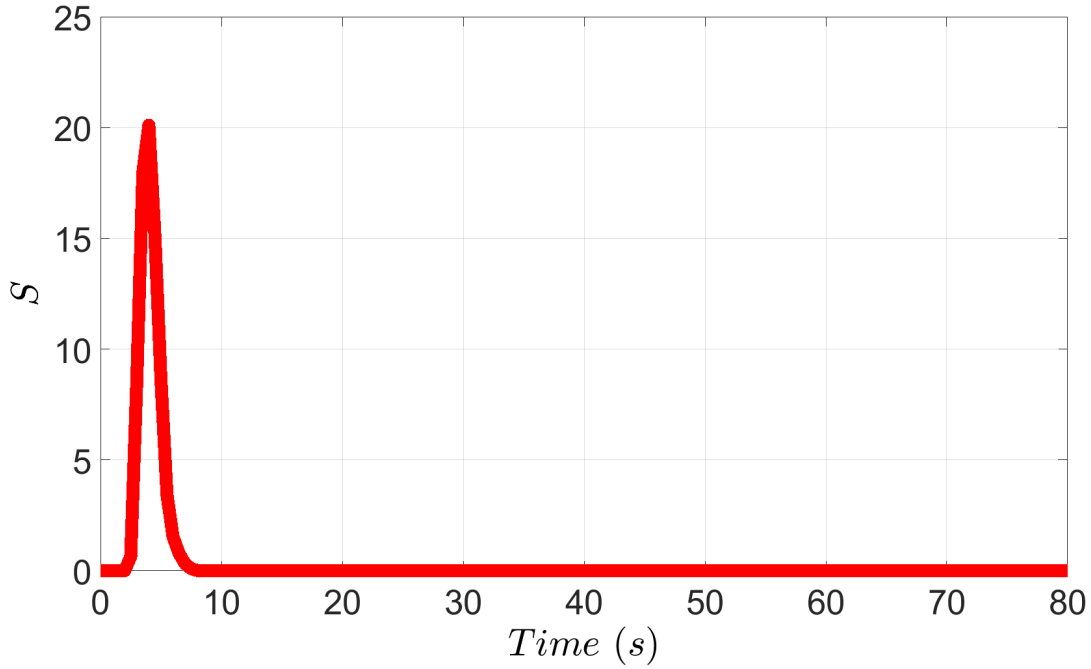

(b) Safeness Index profile

Figure 4.9: Input and Safeness Index profiles when the top vapor valve is closed from 50% to 10% opening.

threshold were developed using information collected from the process and safety system to indicate the safeness of the plant. Then, under an identified linear model, MPC was implemented with Safeness Index-based constraints and slack variables in a co-simulation of Matlab/Aspen. It was demonstrated that in the presence of a small disturbance, the drum pressure remained below the opening pressure of relief valve by Safeness Index-based MPC such that the safety system was not activated. However, in the presence of a large disturbance, the controller working together with the relief valve ensured process operational safety before, during and after the pressure relief valve was turned on/off.

Chapter 5

Safeness Index-based Model Predictive Control: Ammonia Process Case Study

5.1 Introduction

In this chapter, we apply the Safeness Index-based model predictive control to a multi-unit process to account for process operational safety in process control design. Specifically, the ammonia process is employed since it has been studied intensely from the last century in order to accommodate the ammonia demand. In a survey of major accidents that have occurred over a period of 70 years, the ammonia process has been ranked as the one of the greatest risk [83]. Accidents and problems in the ammonia process have been reviewed in the literature [121]. From the simulation point of view, the effect of various types of disturbances were studied starting in the high temperature shift converter in order to avoid thermal runaway in the methanator and poison of the catalyst [10]. Another type of risk in ammonia process can be associated with the following failures [121]: drop in activity of the catalyst, piping failure and oil leak. The analysis of an industrial accident that caused temperature oscillations in the ammonia synthesis reactor was studied in [113, 140]. From the control point of view, one of the first efforts on controlling the ammonia process is obtained relevant information of the process by modeling

and optimizing a large plant using first-principal models (e.g., [146, 147]). In [16], a plant-wide design methodology was proposed and tested with the ammonia synthesis process. In [176], a comparison between a plant-wide control approach and a methodology that relies in simulation and heuristics was performed using the ammonia synthesis process. A framework that integrates real-time optimization with zone control MPC and self-optimization control was demonstrated in an ammonia plant in [67]. Additionally, in [97], an override control structure was implemented and simulated in Aspen Plus Dynamics to handle two types of failures in an ammonia plantwide control structure: loss of coolant in the reactor and loss of cooling water in the condenser. The closed-loop performance of the ammonia synthesis process in [97] was improved by updating the control loops. However, at this stage, the integration between the control loop and the safety system has not been explored in the ammonia plant. Motivated by this, a dynamic simulation of parts of an ammonia plant is built in Aspen Plus software and Safeness Index-based MPC is applied to handle potential disturbances in ammonia plant process including catalyst deactivation and feed temperature change.

The rest of the chapter is organized as follows: in Section 5.2 an ammonia process is introduced. Then, in Section 5.3 and Section 5.4, the Safeness Index-based MPC is developed and applied to the multi-unit ammonia process to demonstrate that process operational safety is improved under the Safeness Index-based MPC.

5.2 Ammonia Process Descriptions and Simulations

5.2.1 Ammonia Process Descriptions

This case study focuses on three parts of ammonia process: shift conversion, carbon dioxide removal and methanation. As shown in Fig. 5.1, all the three parts are used to remove carbon monoxide and carbon dioxide, which are produced by the previous steam reformer. The schematic of the ammonia process implemented in this manuscript is shown in Fig. 5.2.

First, the high temperature shift reactor and the low temperature shift reactor are two adiabatic

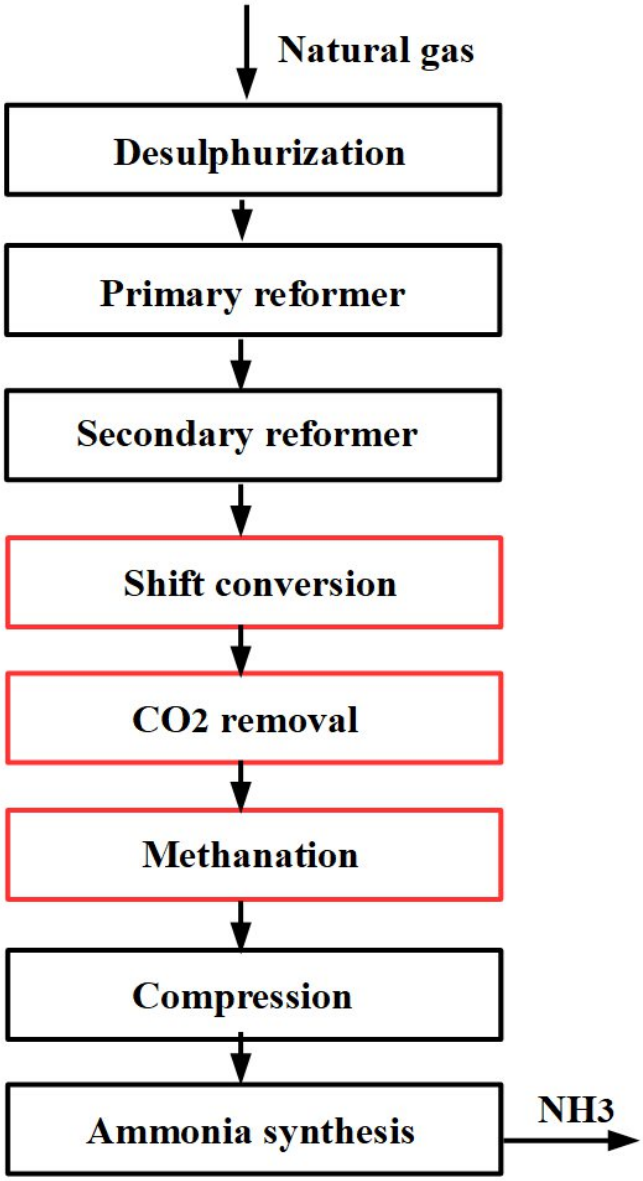

Figure 5.1: A schematic of an ammonia process.

tube reactors, converting carbon monoxide and water into carbon dioxide and hydrogen. Two-bed operation is performed in which different catalyst are utilized in each bed that is operated at different temperatures, typically at 400 $^{\circ}C$ and 200 $^{\circ}C$, respectively. Under normal operating conditions, the high temperature shift reactor is able to reduce the carbon monoxide to $2 \sim 4$ %, and the low temperature shift reactor can obtain an output of carbon monoxide between $0.1 \sim 0.3$ % [15, 53, 154].

After two shift reactors, the gas is purified in adsorption column to remove the carbon dioxide and water vapor, in order to avoid the poison of the ammonia synthesis catalysts [15].

After removal unit, methanation unit is applied to remove trace amount of carbon monoxide and carbon dioxide since even a small amount of carbon monoxide and carbon dioxide in syn-gas is poisonous to ammonia synthesis catalysts. In methanator, the concentrations of carbon monoxide and carbon dioxide are reduced to less than 5 *ppm* catalytically by exothermic methanation reaction [121, 154].

5.2.2 Simulation Settings in Aspen Plus

In our study, the simulations of all the ammonia process units are performed in Aspen plus and Aspen plus Dynamics V10.0. A dynamic simulation is developed based on the steady-state simulation provided by Aspen [20]. Detailed reaction kinetic and process parameters are discussed in this section. Specifically, reaction rates for all reactions are incorporated in Aspen plus model via the compiling and linking of the FORTRAN file with Aspen Plus software. The rate equations for all units are shown as following [20, 53]:

High temperature shift reaction: $CO + H_2O \rightleftarrows CO_2 + H_2, \Delta H = -41.2\ kJ/mol$:

$$r_{CO} = -A_c \exp(-\frac{300.69}{T} + 8.02)(P)^{1/2}(y_{CO} - \frac{y_{H_2} y_{CO_2}}{K_{eq} y_{H_2O}}),\ K_{eq} = \exp(\frac{8240}{T} - 4.33) \tag{5.1}$$

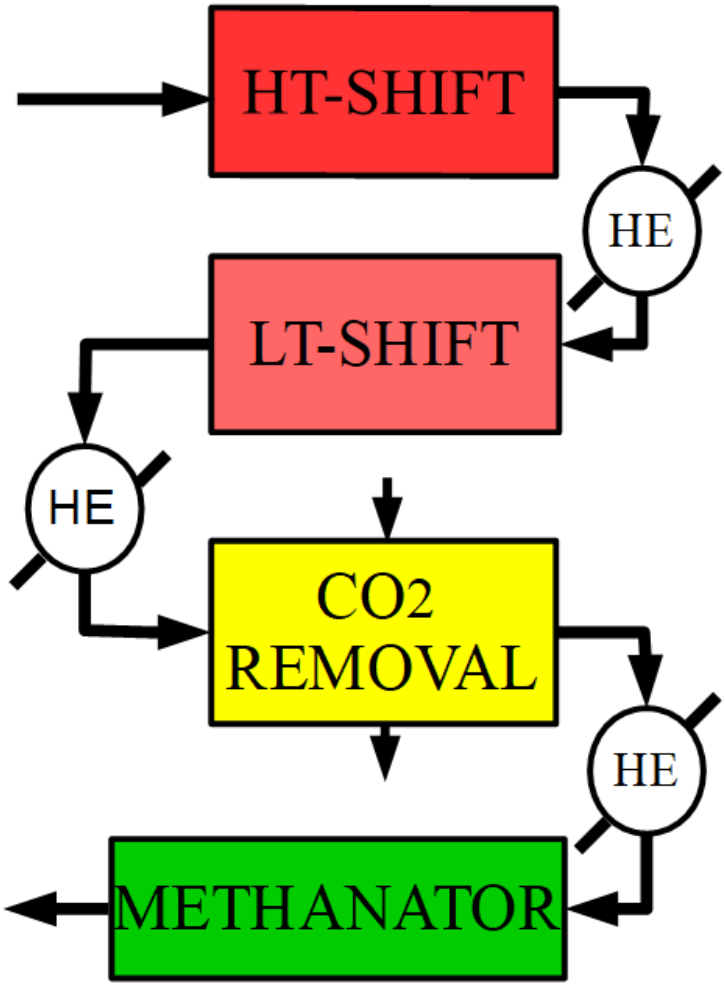

Figure 5.2: A schematic of all simulated units in this manuscript, where HT-SHIFT, HE, LT-SHIFT, CO_2 REMOVAL and METHANATOR represent the high temperature shift reactor, heat exchanger, low temperature shift reactor, CO_2 removal and methanator, respectively.

Low temperature shift reaction: $CO + H_2O \rightleftarrows CO_2 + H_2, \Delta H = -41.2\ kJ/mol$:

$$
\begin{aligned}
r_{CO} &= -A_c \frac{513.15}{T} \frac{K_L y_{CO} y_{H_2O}^{1/2} (1 - \frac{K}{K_{eq}})}{\frac{1}{P} + K_A y_{CO} + K_B y_{CO_2}},\ K = \frac{y_{H_2} y_{CO_2}}{y_{CO} y_{H_2O}},\ K_{eq} = \exp(\frac{8240}{T} - 4.33) \\
K_L &= 68.4 \exp(-3620(\frac{1}{513.15} - \frac{1}{T})),\ K_A = 4.31 \exp(-4580(\frac{1}{513.15} - \frac{1}{T})), \\
K_B &= 1.35 \exp(-1500(\frac{1}{513.15} - \frac{1}{T}))
\end{aligned}
\tag{5.2}
$$

Methanation reaction 1: $CO + 3H_2 \rightleftarrows CH_4 + H_2O, \Delta H = -206\ kJ/mol$:

$$
r_{CO} = -A_c\ 3.119\ exp(1300(\frac{1}{T} - \frac{1}{513}))\ (\frac{P}{y_{H_2}})^{1/2}\ (y_{CO} - \frac{y_{CH_4}\ y_{H_2O}}{y_{H_2}^3\ P^2\ exp(-38.4523 + \frac{2627}{T})}) \tag{5.3}
$$

Methanation reaction 2: $CO_2 + 4H_2 \rightleftarrows CH_4 + 2H_2O, \Delta H = -164\ kJ/mol$:

$$
r_{CO} = -A_c\ 3.119\ exp(1300(\frac{1}{T} - \frac{1}{513}))\ (\frac{P}{y_{H_2}})^{1/2}\ (y_{CO_2} - \frac{y_{CH_4}\ y_{H_2O}^2}{y_{H_2}^4\ P^2\ exp(-38.4523 + \frac{2627}{T})}) \tag{5.4}
$$

where r_{CO} is the reaction rate of CO in $gmol/m^3 \cdot s$; A_c is catalyst activity; T is the temperature in K; P is the total pressure in atm; and y_i is the mole fraction of component i.

In our simulation, all heat exchangers work at the fixed outlet temperature with varying heating duty. All three tube reactors are adiabatic in this simulation. CO_2 removal unit is simulated as a flash drum at 30 $^\circ C$ with feeding ammonia solution to remove CO_2 and condense water. Detailed electrolyte solution chemistry and reaction kinetic in CO_2 removal is discussed in [20]. The values of the main parameters and their steady-states are shown in Table 5.1.

5.2.3 Disturbance and Process Safety

Initially, all units are operated at the steady-states. When catalyst activity decreases in the first high temperature shift reactor, less CO is consumed in the shift reactor. Since CO_2 removal unit does not remove CO, more CO goes into methanator, which leads to a drastic increase in temperature due to the exothermic reaction of methanation occurred in the adiabatic tube reactor. Fig. 5.3 shows an

Table 5.1: Parameter values of the ammonia process simulation.

	Parameter	Value
Feed	Temperature	980 $^{\circ}C$
	Pressure	29 bar
	Mole flowrate	3435 mol/s
	Mole fraction y_{CO}	0.0839
	Mole fraction y_{CO_2}	0.0507
	Mole fraction y_{H_2}	0.355
	Mole fraction y_{H_2O}	0.353
	Mole fraction y_{N_2}	0.152
HT-shift	Reactor length	15.8 m
	Reactor diameter	4.4 m
	Loaded catalyst	9.61×10^4 kg
	Voidage	0.5
	Catalyst heat capacity	900 $J/kg\ K$
	Feed temperature	360 $^{\circ}C$
LT-shift	Reactor length	7.7 m
	Reactor diameter	3.7 m
	Loaded catalyst	3.48×10^4 kg
	Voidage	0.5
	Catalyst heat capacity	850 $J/kg\ K$
	Feed temperature	210 $^{\circ}C$
CO_2 Removal	Volume	49.09 m^3
	Temperature	30 $^{\circ}C$
	Pressure	26.9 bar
	CO_2 remove rate	98.6 %
	H_2O remove rate	99.7 %
Methanator	Reactor length	4 m
	Reactor diameter	2.5 m
	Loaded catalyst	1.57×10^4 kg
	Voidage	0.5
	Catalyst heat capacity	900 $J/kg\ K$
	Feed temperature	280 $^{\circ}C$

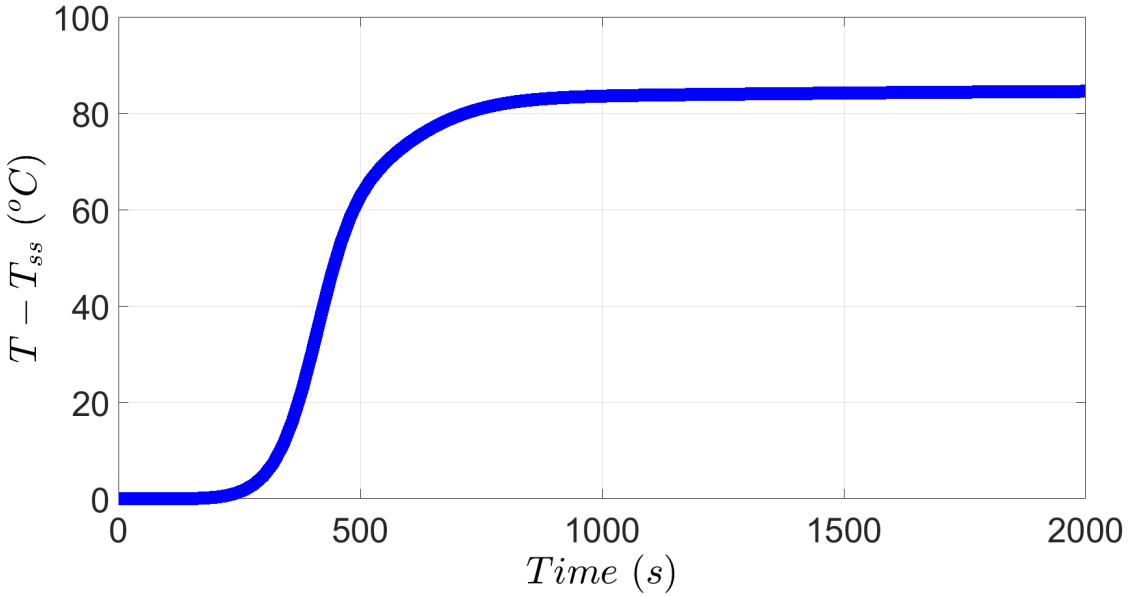

Figure 5.3: Methanator outlet temperature profile, from which it is shown that $T - T_{ss}$ increases more than 80 $^\circ C$ after the catalyst activity in high temperature shift reactor decreases from 1 to 0.1 in 300 s.

open-loop simulation with a disturbance that catalyst activity decreases from 1 to 0.1 in 300 s.

On the other hand, when feed temperature decreases in the first high temperature shift reactor, less CO is reacted in shift reactor. Similarly, since CO_2 removal unit does not remove CO, more CO goes into methanator and causes the temperature in methanator to increase drastically. Fig. 5.4 shows an open-loop simulation with a disturbance that feed temperature for high temperature shift reactor decreases from 380 $^\circ C$ to 280 $^\circ C$ in 300 s. Therefore, in order to improve process operational safety in the presence of these two types of disturbances, a controller is designed to control methanator outlet temperature by manipulating methanator inlet feed temperature.

5.3 Safeness Index-based Model Predictive Control

5.3.1 Model Identification

The methanator is initially simulated at the steady-state where feed temperature $T_{in} = 280$ $^\circ C$ and outlet temperature $T_{out} = 327.27$ $^\circ C$. Because CO concentration in the feed has a dominating

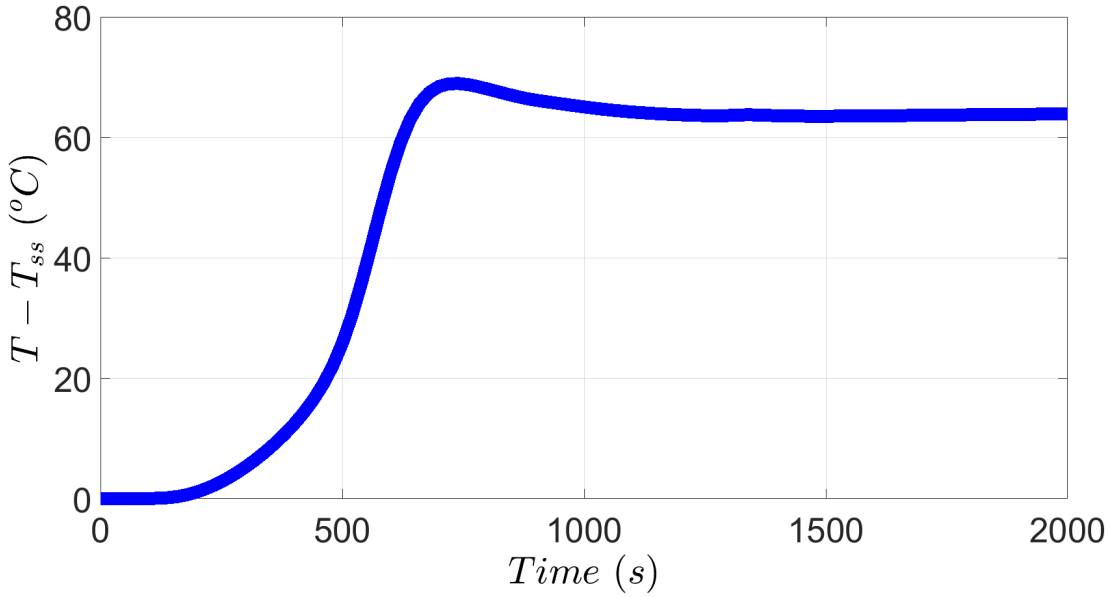

Figure 5.4: Methanator outlet temperature profile, from which it is shown that $T - T_{ss}$ increases more than 60 $^\circ C$ after the feed temperature of high temperature shift reactor decreases from 380 $^\circ C$ to 280 $^\circ C$ in 300 s.

effect on the produced heat, CO mole fraction y_{CO} is treated as a measurable disturbance with a steady-state value of 3.55×10^{-3}. The state, the input and the disturbance of the process are represented in deviation variable form as $x = T_{out} - T_{out,ss}$, $u = T_{in} - T_{in,ss}$ and $d = y_{CO} - y_{CO,ss}$, such that the equilibrium point of the system is at zero. Since there exists a time delay between the feed temperature T_{in} and the outlet temperature T_{out}, a linear dynamic model with time delay of the following form is utilized to represent the Aspen Plus model:

$$\frac{dx(t)}{dt} = Ax(t) + Bu(t - t_d) + Kd(t - t_d) \tag{5.5}$$

where t_d is the time delay in s. It is noted that the input time delay is equal to the disturbance time delay because it takes the same amount of time for the feed temperature T_{in} and the CO mole fraction of y_{CO} to affect the outlet temperature T_{out} of a tube reactor. An Aspen open-loop simulation is used to generate transient response data of outlet temperature T_{out} subject to a step change in feed temperature T_{in}, and Multivariable Output Error State Space (MOSEP) algorithm is applied in Matlab to identify the matrices A and B. Then another step change in CO mole fraction

of y_{CO} is simulated to calculate the gain K of disturbance d. The difference among the models obtained from the different step changes are negligible. The matrices A, B, K and the time delay t_d are identified as follows:

$$A = -0.005136; \quad B = 0.01207; \quad K = 32.887; \quad t_d = 100\ s$$

5.3.2 Safeness Index and Controller Design

Since temperature control plays an important role in the methanator, and high outlet temperature could lead to unsafe operations, in our work Safeness Index is designed such that high temperature T_{out} is considered unsafe operating conditions while all the temperature T_{out} below steady-state values are considered safe operation conditions. To that end, Safeness Index is design as follows:

$$S(x) = [f^{+}(x)]^2 \tag{5.6}$$

where $f^{+}(x)$ is the same function as shown in Eq. 4.2. With a quadratic form, $S(x)$ will have a significantly large value when temperature T_{out} are far above the steady-state. To avoid an extreme high temperature in methanator, the threshold S_{TH} of the Safeness Index function $S(x)$ is carefully chosen. In consideration of model mismatch, sample-and-hold implementation of the controller and the large time delay in the process, the actual threshold in the Safeness Index-based MPC should be more conservative and therefore is chosen to be $S_{TH} = 5^2 = 25$. Based on the Safeness Index function of Eq. 5.6, the controller is developed by incorporating MPC with a feedforward control action as shown in Eq. 5.7:

$$u(t_k) = u_{MPC}(t_k) + u_{forward}(t_k) \tag{5.7}$$

Specifically, the control action $u(t_k)$ consists of a feedforward term $u_{forward}(t_k)$ and an MPC term $u_{MPC}(t_k)$, where $u_{forward}(t_k)$ is calculated by Eq. 5.8 and $u_{MPC}(t_k)$ is the first control action in the

solution $u^*(t)$ to the optimization problem of Eq. 5.9.

$$u_{forward}(t_k) = -\frac{K}{B} d(t_k) \tag{5.8}$$

$$\min_{u \in S(\Delta), y} \quad \int_{t_k+t_d}^{t_{k+N}+t_d} (\|\tilde{x}(\tau)\|^2_{Q_c})\, d\tau + \int_{t_k}^{t_{k+N}} (\|u(\tau)\|^2_{R_c})\, d\tau + \sum_{i=1}^{N} k_1 e^{-k_2 y(i)}, \quad k_1, k_2 > 0 \tag{5.9a}$$

$$\text{s.t.} \quad \dot{\tilde{x}}(t) = A\tilde{x}(t) + Bu(t - t_d) \tag{5.9b}$$

$$\tilde{x}(t_k) = x(t_k) \tag{5.9c}$$

$$u(t) = u_{pre}(t),\ \forall\, t \in [t_k - t_d, t_k) \tag{5.9d}$$

$$u(t) \in U,\ \forall\, t \in [t_k, t_{k+N}) \tag{5.9e}$$

$$S(\tilde{x}(t_{k+i} + t_d)) + y(i) \leq S_{TH},\ i = 1, 2, ..., N \tag{5.9f}$$

$$y(i) \geq 0,\ i = 1, 2, ..., N, \tag{5.9g}$$

$$if\ S(\tilde{x}(t_k + t_d)) \leq S_{TH}$$

$$y(i) \in R,\ i = 1, 2, ..., N, \tag{5.9h}$$

$$if\ S(\tilde{x}(t_k + t_d)) > S_{TH}$$

where the notation follows that in Section 4 . Although the optimal input trajectory $u^*(t)$ is calculated over the entire prediction horizon $t \in [t_k, t_{k+N})$, the control action computed for the first sampling period in the prediction horizon $u(t_k)$ is applied over the first sampling period, and the MPC problem is resolved at the next sampling period. The objective function of Eq. 5.9a is minimizing the integral term $\int_{t_k+t_d}^{t_{k+N}+t_d} (\|\tilde{x}(\tau)\|^2_{Q_c})\, d\tau$ and $\int_{t_k}^{t_{k+N}} (\|u(\tau)\|^2_{R_c})\, d\tau$ and the penalty term $\sum_{i=1}^{N} k_1 e^{-k_2 y(i)}$ of slack variables $y(i)$. It is noted that state is integrated from $t_k + t_d$ to $t_{k+N} + t_d$ because state from t_k to $t_k + t_d$ is already determined by previous implemented control actions. The constraint of Eq. 5.9b is the nominal linear model of Eq. 5.5 that is used to predict the states

of the closed-loop system. Because the disturbance is mitigated by the feedforward term (i.e., $u_{forward}(t_k)$), MPC utilizes the nominal system of Eq. 5.9b for prediction. Eq. 5.9c defines the initial condition $\tilde{x}(t_k)$ of the optimization problem which is the state measurement $x(t_k)$ at $t = t_k$. Eq. 5.9d provides input trajectory calculated from previous steps, in order to predict state from t_k to $t_k + t_d$. Eq. 5.9e is the input constraint applied over the entire prediction horizon. The manipulated input is the feed temperature T_{in}, which is bounded by: $180\ ^\circ C \leq T_{in} \leq 380\ ^\circ C$, namely $U = [-100,\ 100]$. Eq. 5.9f is the Safeness Index constraints with slack variables $y(i)$. If $S(x(t_k + t_d)) > S_{TH}$, the constraint of Eq. 5.9f can be satisfied via the negative slack variables $y(i)$ such that Safeness Index can remain above threshold S_{TH} in the prediction horizon. However, if $S(x(t_k)) \leq S_{TH}$, nonnegative slack variables $y(i)$ are required by Eq. 5.9g to ensure $S(x)$ remaining below threshold S_{TH}. Additionally, parameters k_1 and k_2 in the objective function Eq. 5.9a should be carefully chosen, such that the slack variables $y(i)$ have slight effects on control actions if $S(x(t_k + t_d))$ is far below S_{TH}, and have significant effects on control actions if $S(x(t_k + t_d))$ is close to S_{TH}. Thus, in our simulation k_1 and k_2 are determined to be 10^5 and 0.2, respectively.

The explicit Euler method with an integration time step of $h_c = 10^{-1}\ s$ was applied to numerically integrate the dynamic model of Eq. 5.5 in Safeness Index-based MPC. The nonlinear optimization problem of Safeness Index-based MPC of Eq. 5.9 was solved using the solver FilterSD on OPTI Toolbox in Matlab with the following parameters: sampling period $\Delta = 20\ s$; prediction horizon $N = 30$. $Q_c = 1$ and $R_c = 0.5$ are chosen such that the terms of the states and the input have the same order of magnitude in $\|\tilde{x}_1(\tau)\|^2_{Q_c}$ and $\|u(\tau)\|^2_{R_c}$.

5.4 Simulation Results

In this section, we demonstrate the application of the proposed controller to the ammonia process in the presence of different disturbances.

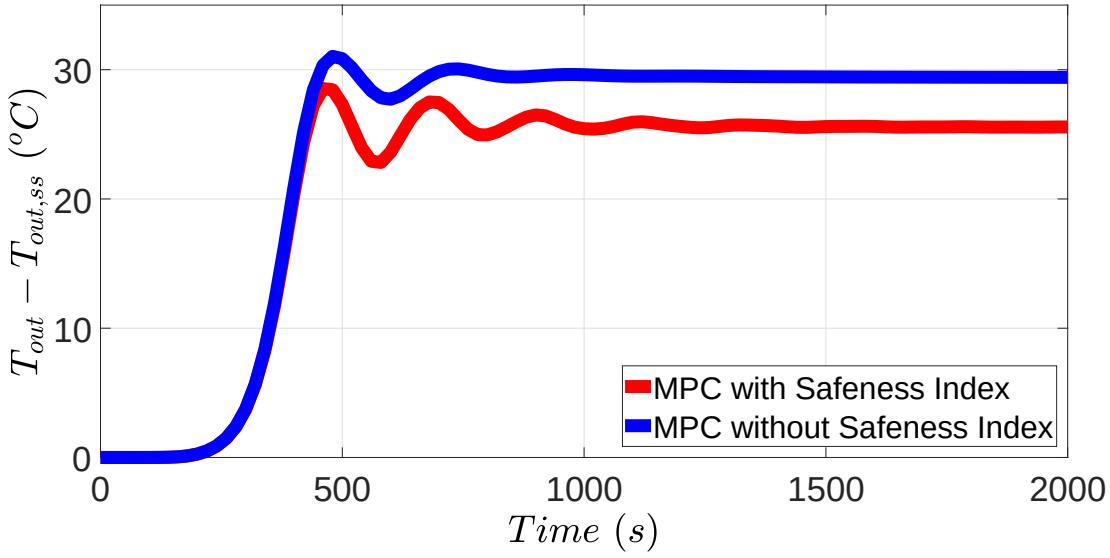

(a) Methanator outlet temperature profile

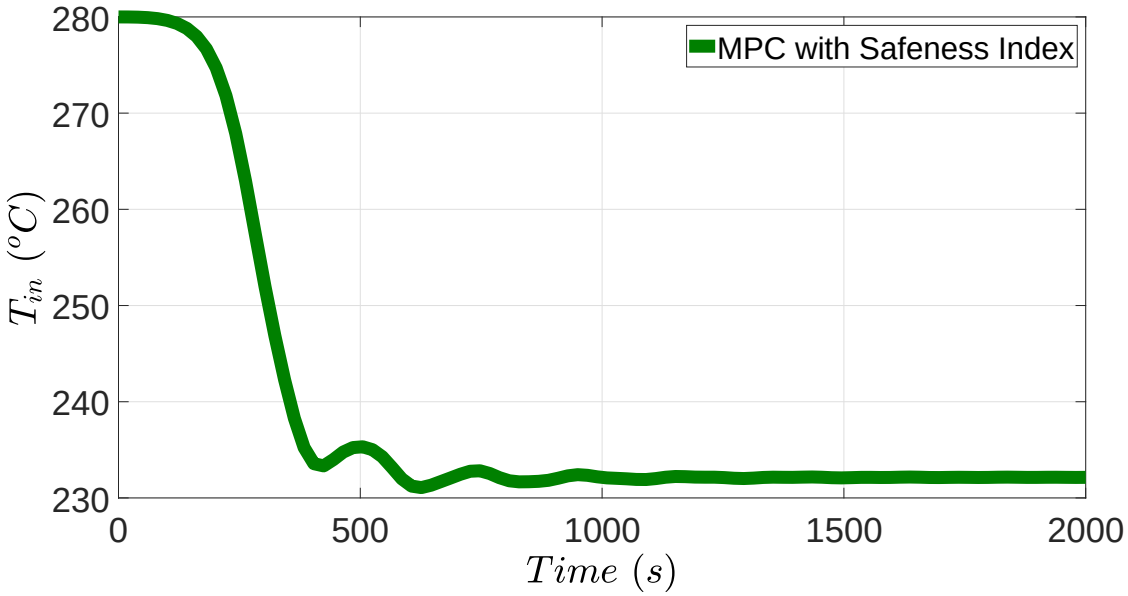

(b) Methanator feed temperature profile

Figure 5.5: Close-loop simulation results when the catalyst activity in the high temperature shift reactor decreases from 1 to 0.1 in 300 *s*.

5.4.1 Disturbance 1: Catalyst Activity

After the catalyst activity in the high temperature shift reactor decreases from 1 to 0.1 in 300 s, less CO is reacted in the high temperature shift reactor. Although the low temperature shift reactor buffers the increasing CO content, a higher concentration of CO still reaches the methanator and causes an increasing temperature. The CO mole fraction y_{CO} in the feed of methanator is measured at each sampling time t_k and sent to the feedforward controller at time t_k to account for the effect of disturbance. However, it is noted that since CO is not the only disturbance to the methanator due to catalyst deactivation, this feedforward term is not able to mitigate all the disturbances. Moreover, model mismatch still exists between the identified linear model and the actual process. As a result, the outlet temperature of the methanator increases after the disturbance is introduced and does not go back to the origin.

Fig. 5.5 shows that the outlet temperature of methanator T_{out} can increase more than 30 $^{\circ}C$ if the Safeness Index constraints are not utilized in MPC, while it increases less than 30 $^{\circ}C$ if Safeness Index constraints are utilized in MPC, which implies that the Safeness Index-based MPC can improve process operational safety of the ammonia plant.

5.4.2 Disturbance 2: Feed Temperature

After the feed temperature in the high temperature shift reactor decreases from 380 $^{\circ}C$ to 280 $^{\circ}C$, the temperature in the high temperature shift reactor starts to decrease slowly since it takes some time for a large amount of catalyst to cool down. As a result, the CO mole fraction y_{CO} in the feed of methanator increases gradually, and the temperature in methanator increases but slower than the case of disturbance 1.

Fig. 5.6 shows that the outlet temperature of methanator T_{out} can increase more than 40 $^{\circ}C$ if the Safeness Index constraints are not utilized in MPC, while it increases less than 40 $^{\circ}C$ if the Safeness Index constraints are utilized in MPC. On the other hand, by comparing Fig. 5.6 and Fig. 5.5, it is demonstrated that the temperature increases more with less control actions (i.e., lower inlet temperature) in the presence of disturbance 2. The reason is that the CO concentration

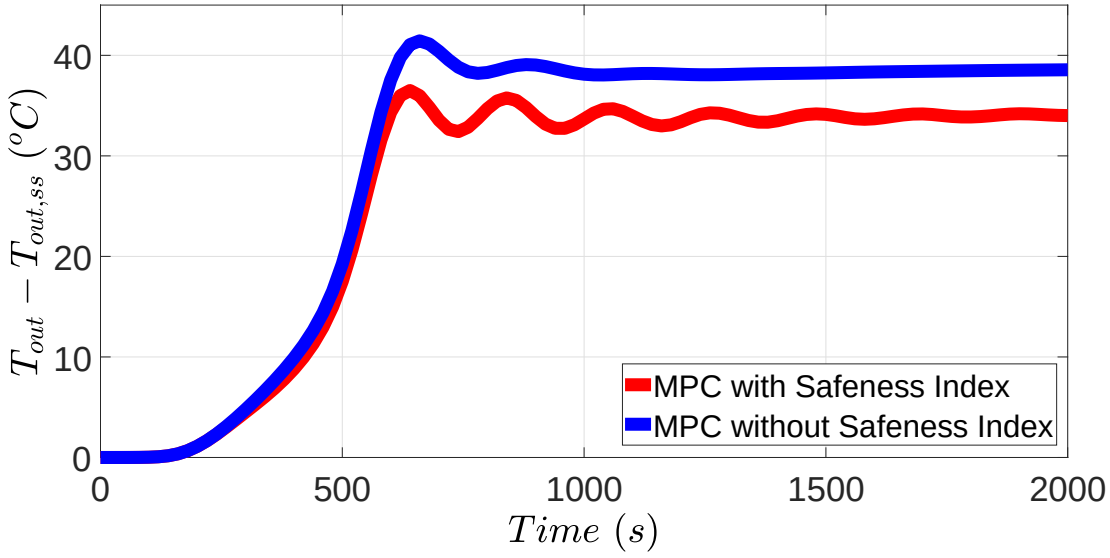

(a) Methanator outlet temperature profile

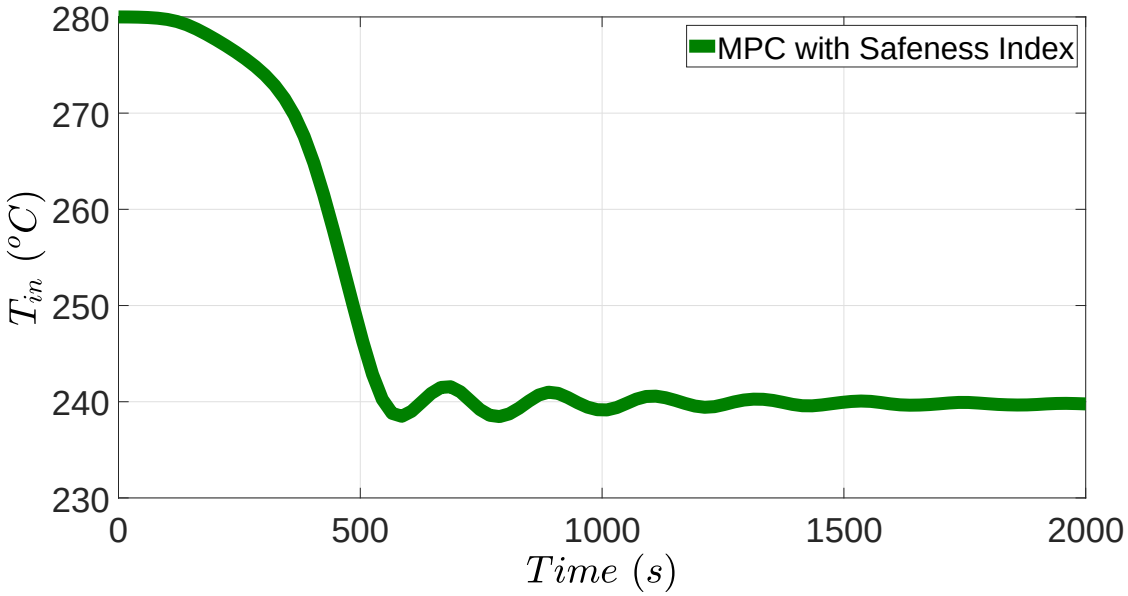

(b) Methanator feed temperature profile

Figure 5.6: Close-loop simulation results when the feed temperature of the high temperature shift reactor decreases from 380 $^\circ C$ to 280 $^\circ C$ in 300 s.

in the feed to the methanator is much less under disturbance 2 than under disturbance 1, which leads to a significantly small feedforward control action $u_{forward}$ in the presence of disturbance 2. Therefore, even though u_{MPC} is calculated to be larger in the case of disturbance 2 since the outlet temperature is further away from the steady state compared to disturbance 1, the overall control action calculated from $u = u_{MPC} + u_{forward}$ under disturbance 2 is still less than the one under disturbance 1.

It needs to be mentioned that the closed-loop state has an offset under both disturbances. Although a feedforward term is added to compensate for the measured disturbance, not all process disturbances can be measured in a multi-unit process. In future work, further offset-free feature may be implemented in MPC as discussed in [162].

5.5 Conclusion

In this chapter, four units in the ammonia process were simulated to demonstrate the application of Safeness Index-based MPC. To ensure process operational safety in the presence of a significant propagated disturbance to methanation unit in the ammonia process, a Safeness Index function and a Safeness Index threshold were developed to characterize the safeness of an adiabatic methanation tube reactor. Subsequently, a linear dynamic model with time delay and disturbance were identified for the methanator. Finally, an MPC was developed with the Safeness Index-based constraints and feedforward disturbance compensation term to improve the performance of MPC and to handle the propagated disturbance.

Chapter 6

Operational Safety via Model Predictive Control: Ammonia Process Network

6.1 Introduction

Given the intrinsic inter-connectivity of different process units in chemical industries, proper control strategies need to be carefully considered during the design phase, and rigorously practiced during regular operations, in order to maintain consistent operating conditions and high plant productivity. The ammonia plant is one example of a highly interconnected system that produces mainly chemical fertilizers to enhance food production. Due to increase of population and changing consumption patterns, the production of ammonia has increased as well [99]. For instance, the global production of ammonia is estimated to be 200 t/year [116]. However, the increase of ammonia production also brings new challenges that have not been fully tackled. For example, traditionally the safety of the ammonia plant is studied by analyzing each individual unit of the process, and then various process safety metrics and methodologies (e.g., Hazard and Operability Analysis (HAZOP), Layer of Protection Analysis (LOPA)) are implemented before the process goes online in order to avoid potential process upsets and safety hazards (e.g., [7, 126]). The traditional control methodologies are unaware of important safety conditions of the ammonia

process.

Since the ammonia plant operates under considerable high temperatures and pressures, it is well known that the variation from the operation point can damage the equipment and impact the safety and profitability of the process. For instance, failures and pitfalls in the ammonia process have been reported in the literature (e.g., [121]). It has been pointed out in [31] that operators are conscious of the impact of the die-off in the low-temperature shift reactor. The die-off has been mitigated by studying the correct selection of the catalyst and by reducing the impurities that cause the loss of activity or catalyst poisoning. Similarly, since cleaning the poisoned catalysts requires 12-24 hours in a high-temperature shift reactor, the wasted production time is an important factor to be considered [139]. In order to increase the catalyst life without stopping the process, it is usual practice to implement a small increase in pressure drop in the low-temperature shift reactor, which leads to the loss of ammonia production and to the loss of thousands of dollars. The poisoning of the catalyst and other disturbances in the high-temperature shift converter have also been associated with triggering the runaway reaction in the methanator [10]. Similarly, overheating in the methanation vessel that was caused by electrical power failure or by the failure in the heat boiler has been also reported in the ammonia industry under an already existing high-temperature protection system [120, 163]. It was detected that the high-temperature protection system failed because the fast increase of the temperature happened between measurements [163].

There are limited research efforts on process safety and control in the ammonia process. Despite the importance of real-time operational safety considerations, most works focus on the modeling and steady-state issues of safety in the ammonia plant (e.g., [16, 99, 146, 147, 176]). One research work [97] reports the introduction of two failures in an ammonia plant with a plant-wide control structure: loss of coolant in the reactor, and loss of cooling water in the condenser [97]. To tackle the above safety issues, an override control structure was implemented and simulated in Aspen Plus Dynamics. In another research work, the control performance of the ammonia synthesis process was improved by updating the control loops and implementing a multi-variable predictive control system [47].

Studies that evaluate the hazards and safety in real-time operation of a multi-unit ammonia process are also limited in the literature. For example, the ammonia process was studied in Aspen HYSYS environment with the hazard and operability (HAZOP) methodology [79]. From the HAZOP analysis of this study, it was concluded that the reaction conversion is too low when pressure and feed temperature are below 70% and 18% of the operation point, respectively. Another methodology available is the master logic diagram (MLD) technique that identifies the initiating event of a hazard. The MLD technique was implemented in an ammonia storage facility, and it was concluded that the most relevant initiating events are excess external heat, earthquakes, and loss of refrigeration capacity, among many others [125]. More recently in a different industry, an evaluation approach called multi-unit probabilistic risk assessment (MUPRA), has been proposed to account for the interaction between systems [177]. The key point of the MUPRA methodology is to assess the risk as an interacting multi-unit system rather than one single unit. However, the implementation of the MUPRA methodology is still offline.

In terms of coordinating control with safety considerations, the existing techniques usually tackle the safety problem as fault identification (e.g., [26, 90, 111]). However, the case when the safety system actions and the control actions are integrated and respond to the hazardous disturbances in real time has received attention only recently. To address the above problem, recent works have started to explore how to reduce the gap between the control system and the safety considerations. For instance, model predictive control (MPC) and economic model predictive control (EMPC) approaches were proposed to drive the process to safe operating regions using secure interior level sets [6, 7]. In order to characterize the safe region of operation, Safeness Index was proposed to indicate safeness of the process based on process state information [9]. On the other hand, the control Lyapunov-Barrier function was introduced as a constraint in the MPC formulation to avoid unsafe condition and to ensure stability [170]. Finally, the practical integration of the safety system with a control system was demonstrated in two relevant examples from literature: the MIC reactor and a high-pressure flash drum separator [178].

Motivated by the above considerations, the main contribution of this chapter is to design

a safety control scheme that integrates process operational safety and control for a multi-unit ammonia process network. Specifically, an industrial case study of a multi-unit ammonia process is studied and a control scheme is proposed and applied to an ammonia process under a disturbance that is typically encountered by engineers in practice. Under the disturbance of loss of catalyst activity in the first unit in the proposed ammonia plant, the gas temperature and concentration in the last methanation unit are affected, which could lead to unsafe operation of the whole process. To improve process operational safety in the ammonia process, two controllers on high-temperature shift reactor and methanator are designed. Specifically, the first controller is a tracking model predictive controller and the second controller is a Safeness Index-based model predictive controller. Finally, the closed-loop simulations of the ammonia plant are performed in a co-simulation between Matlab and Aspen Plus Dynamics.

The rest of this chapter is organized as follows: in Section 6.2, the implemented ammonia process, the setting in Aspen Plus Dynamics and the process disturbance are presented. In Section 6.3, the designed control scheme and the model predictive control structures are presented. In Section 6.4, the proposed controllers are applied to the ammonia plant in the presence of disturbances to evaluate the closed-loop performance.

6.2 Ammonia Process and Dynamic Simulation

In this section, a simplified description of the ammonia process is presented together with the key points of each unit in the ammonia process. Specifically, the ammonia process is generally developed based on the followings steps: feed stock pre-treatment, steam reforming, gas purification, compression, and ammonia synthesis [15]. A schematic of the entire ammonia process network is shown in Fig. 6.1. This chapter focuses specifically on the gas purification step, within which three sub-processes are simulated: shift conversion, carbon dioxide removal, and methanation. The common purpose of all three sub-processes within gas purification is to remove carbon monoxide and carbon dioxide produced by the previous steam reforming step.

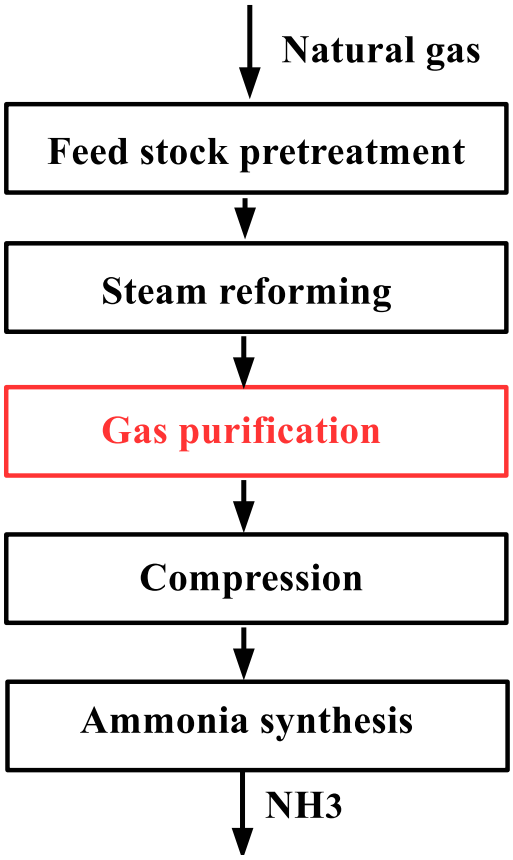

Figure 6.1: A schematic of the entire ammonia process network.

Fig. 6.2 shows the schematic of the ammonia process implemented in this chapter, where HT-shift, LT-shift, and HE stand for high-temperature shift reactor, low-temperature shift reactor, and heat exchanger, respectively.

In the shift conversion section, two-bed adiabatic operation is used to eliminate the carbon monoxide. Each bed operates at different temperatures (i.e, 400 $^{\circ}C$ and 200 $^{\circ}C$, respectively) with different catalyst components. An exothermic reaction is carried out in each reactor between carbon monoxide and water to yield carbon dioxide and hydrogen. In the high-temperature shift reactor, large amount of carbon monoxide is removed due to its high temperature and the resulting high reaction rate. In the low-temperature shift reactor, carbon monoxide is further removed by reacting at relatively low temperature because the equilibrium is preferred at low temperature in the exothermic reversible reaction. According to [15, 53, 154], the high-temperature shift

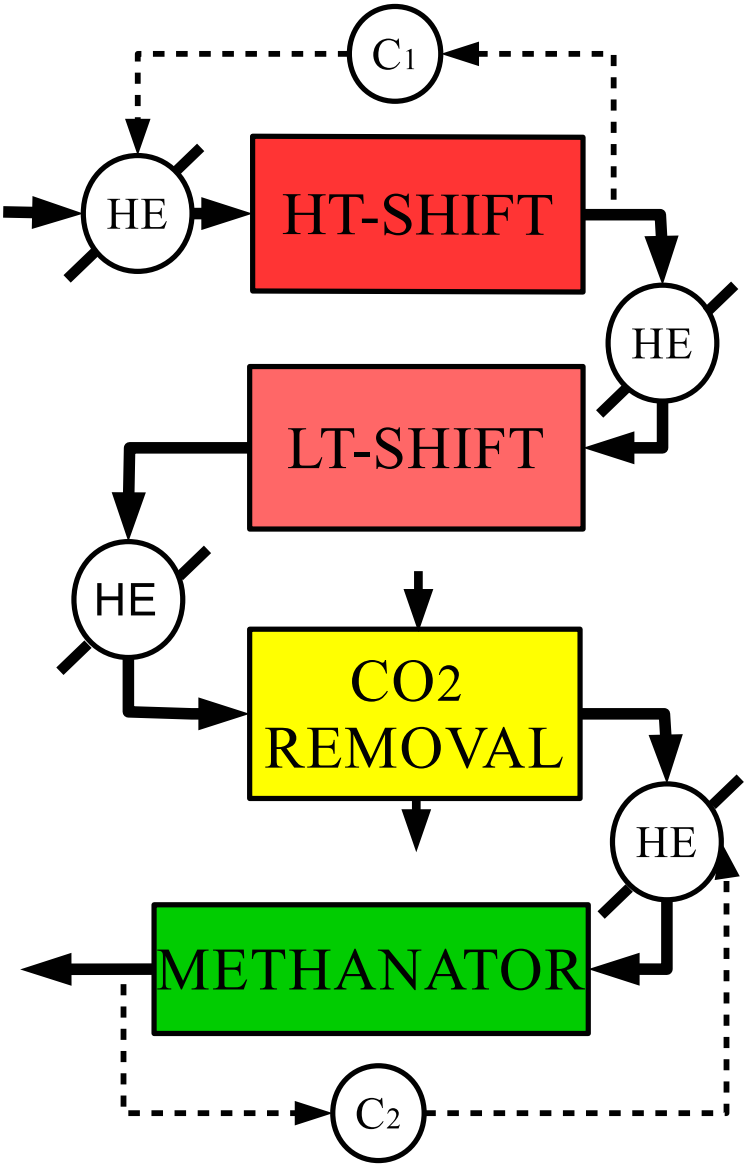

Figure 6.2: A schematic of the control structure that uses two control loops, where C_1 and C_2 represent controller 1 and controller 2.

reactor should reduce the carbon monoxide to $2-4\%$ under normal operating conditions, and the low-temperature shift reactor should further reduce carbon monoxide into the range of $0.1-0.3\%$.

In the two shift reactors, a surplus amount of water vapor is introduced into the gas stream and a large amount of carbon dioxide is produced. Water vapor and carbon dioxide are afterwards removed in an absorption column, which otherwise will poison the ammonia synthesis catalyst [15]. Additionally, the gas is purified in the absorption column by using different kinds of solvent. In general, the most typical absorption processes are classified as follows: reaction systems (e.g., Benfield), combination reaction-physical systems (e.g., Sulfinol), and physical absorption systems (e.g., Selexol) [44].

Finally, after the gas leaves the absorption column, trace amount of carbon monoxide and carbon dioxide are still present in the stream. A catalytic methanation reaction unit is used to remove the trace amount of carbon monoxide and carbon dioxide. Two exothermic catalytic reactions are carried out in the adiabatic tubular methanation reactor and transform the remaining carbon monoxide and carbon dioxide with hydrogen into methane and water [106, 137]. This methanation unit is also known for being challenging due to the high heat generation of reaction and sensitivity to the catalyst [137]. A thermal runaway can occur in methanator in the case that disturbance is introduced in upstream shift conversion reactors [10]. Finally, the methanation unit is expected to reduce concentrations of carbon monoxide and carbon dioxide to $0.0005-0.001\%$ [121, 154].

6.2.1 Simulation Settings in Aspen Plus

In order to accurately simulate the process dynamics and interaction among units, Aspen Plus and Aspen Plus Dynamics V10.0 (Aspen Technology, Inc.) are used to perform high-fidelity dynamic simulation of gas purification process within the ammonia process. Aspen Plus is a commercial software that calculates the steady-state of the process given a process design and an appropriate selection of thermodynamic models, based on the mass and energy balances of the process using a sequential modular approach. Aspen Plus Dynamics is another software that can run dynamic

simulations based on steady-state model data and additional detailed parameters. Further details about Aspen software can be found in [5, 19].

In our simulation, involved components are carefully chosen and the Redlich Kwong Soave Boston Mathias (RKS-BM) model was selected for the thermodynamic property calculation of all involved chemical components. A steady-state model is first built in Aspen Plus based on the detailed information in the example provided by Aspen [20]. Subsequently, the obtained steady-state model in Aspen Plus is exported to a dynamic model in Aspen Plus Dynamics, which is a software that can conduct dynamic process simulations. We first validate the model configuration using the Pressure Checker Tool, and then export the steady-state model to a pressure-driven dynamic file using the Dynamic Mode Tool.

Gas phase reactions in all units are modeled using the reaction rate equations from [20, 53]. Since the kinetic models available in Aspen Plus are limited, it is necessary to adopt a user-defined routine for complex kinetic models. In our work, the reaction rate equations are programmed in a FORTRAN user-kinetics subroutine file, and then the FORTRAN code is compiled into objective file and linked to the Aspen Plus software as a dynamic link library file. Specifically, the reaction rate equations for the selected three units (i.e., high-temperature shift reactor and low-temperature shift reactor, and methanator) and the relevant parameters are discussed in [180] and given as follows:

High-temperature shift reaction: $CO + H_2O \rightleftarrows CO_2 + H_2, \Delta H = -41.2\ kJ/mol$:

$$r_{CO} = -A_c \exp(-\frac{300.69}{T} + 8.02)(P)^{1/2}(y_{CO} - \frac{y_{H_2} y_{CO_2}}{K_{eq} y_{H_2O}}),\ K_{eq} = \exp(\frac{8240}{T} - 4.33) \tag{6.1}$$

Low-temperature shift reaction: $CO + H_2O \rightleftarrows CO_2 + H_2, \Delta H = -41.2\ kJ/mol$:

$$\begin{aligned} r_{CO} &= -A_c \frac{513.15}{T} \frac{K_L y_{CO} y_{H_2O}^{1/2}(1 - \frac{K}{K_{eq}})}{\frac{1}{P} + K_A y_{CO} + K_B y_{CO_2}},\ K = \frac{y_{H_2} y_{CO_2}}{y_{CO} y_{H_2O}},\ K_{eq} = \exp(\frac{8240}{T} - 4.33) \\ K_L &= 68.4 \exp(-3620(\frac{1}{513.15} - \frac{1}{T})),\ K_A = 4.31 \exp(-4580(\frac{1}{513.15} - \frac{1}{T})), \\ K_B &= 1.35 \exp(-1500(\frac{1}{513.15} - \frac{1}{T})) \end{aligned} \tag{6.2}$$

Table 6.1: Key parameters of the ammonia process.

Feed	Temperature	Pressure	Molar flowrate	y_{CO}
	980 $^{\circ}C$	29 bar	3435 mol/s	0.0839
	y_{CO_2}	y_{H_2}	y_{H_2O}	y_{N_2}
	0.0507	0.355	0.353	0.152
HT-shift	Reactor length	Reactor diameter	Loaded catalyst	Voidage
	15.8 m	4.4 m	9.61×10^4 kg	0.5
	Heat capacity	Feed temperature		
	900 $J/kg\ K$	360 $^{\circ}C$		
LT-shift	Reactor length	Reactor diameter	Loaded catalyst	Voidage
	7.7 m	3.7 m	3.48×10^4 kg	0.5
	Heat capacity	Feed temperature		
	850 $J/kg\ K$	210 $^{\circ}C$		
CO_2 Removal	Volume	Temperature	Pressure	CO_2 removal rate
	49.09 m^3	30 $^{\circ}C$	26.9 bar	98.6 %
	H_2O removal rate			
	99.7 %			
Methanator	Reactor length	Reactor diameter	Loaded catalyst	Voidage
	4 m	2.5 m	1.57×10^4 kg	0.5
	Heat capacity	Feed temperature		
	900 $J/kg\ K$	280 $^{\circ}C$		

Methanation reaction 1: $CO + 3H_2 \rightleftarrows CH_4 + H_2O, \Delta H = -206\ kJ/mol$:

$$r_{CO} = -A_c\ 3.119\ \exp(1300(\frac{1}{T} - \frac{1}{513}))\ (\frac{P}{y_{H_2}})^{1/2}\ (y_{CO} - \frac{y_{CH_4}\ y_{H_2O}}{y_{H_2}^3\ P^2\ exp(-38.4523 + \frac{2627}{T})}) \quad (6.3)$$

Methanation reaction 2: $CO_2 + 4H_2 \rightleftarrows CH_4 + 2H_2O, \Delta H = -164\ kJ/mol$:

$$r_{CO} = -A_c\ 3.119\ \exp(1300(\frac{1}{T} - \frac{1}{513}))\ (\frac{P}{y_{H_2}})^{1/2}\ (y_{CO_2} - \frac{y_{CH_4}\ y_{H_2O}^2}{y_{H_2}^4\ P^2\ exp(-38.4523 + \frac{2627}{T})}) \quad (6.4)$$

In our simulation, pressure and flow rate of each unit are carefully tuned by adjusting the feed pressure and pressure drop of each unit. All heat exchangers work at fixed outlet temperature with varying heating duty. The values of the main parameters and steady-states for all implemented units are shown in Table 6.1. Below we discuss the key design issues in the main units.

In the high-temperature shift reactor, the size and catalyst properties are designed according

to [10,20,53,154]. There exists an optimal feed temperature because high temperature can increase reaction rate while low temperature can lead to a better equilibrium in the case of exothermic reversible reaction [132,145]. In this unit, the optimal feed temperature is determined by evaluating different feed temperatures in the simulation and then selecting the one with the highest conversion of carbon monoxide. Our results are consistent with industrial data.

In the low-temperature shift reactor, the length and the diameter of the reactor, as well as the characteristics of the catalyst are found in [10, 20, 53, 154]. Due to low feed concentration, different catalyst and reactor size, the optimal feed temperature for low-temperature shift reactor can be very low. However, the limiting condition is the dew point of the gas because condensed water on catalyst is poisonous. Analysis tool for mixture in the Properties sheet in Aspen Plus is used to find the dew point to be 169 $^{\circ}C$ for the specific high pressure and high temperature gas, and 210 $^{\circ}C$ is chosen according to industrial data [10, 20, 53].

In carbon dioxide removal, an aqueous ammonia solution is used to remove carbon dioxide as well as to condense water from gas phase. In our simulation, a flash drum is chosen to represent the absorption column unit. The gas from shift reactor is cooled down to 40 $^{\circ}C$, and fed into flash drum. Meanwhile a stream of ammonia (15%) and water (85%) is also fed into the flash drum. Gas leaves flash drum with removal rates 98.6 % and 99.7 % for carbon dioxide and water, respectively. Detailed electrolyte solution chemistry properties and reaction kinetic in CO_2 removal are discussed in [20, 88].

The gas is heated up after the carbon dioxide removal, then fed into the methanation unit to apply the final purification step. Feed temperature is chosen to be 280 $^{\circ}C$ such that final outlet CO and CO_2 mole fraction is below 0.0005%. The characteristic values of the equipment and other key values of the methanator are carefully chosen according to the data from [84, 137, 154].

6.2.2 Disturbance and Process Operational Safety

One of the most common safety issues that is encountered in the ammonia plant is runaway reactions caused by catalyst deactivation in shift reactors (e.g., [10,10,17,163]). In the operation of

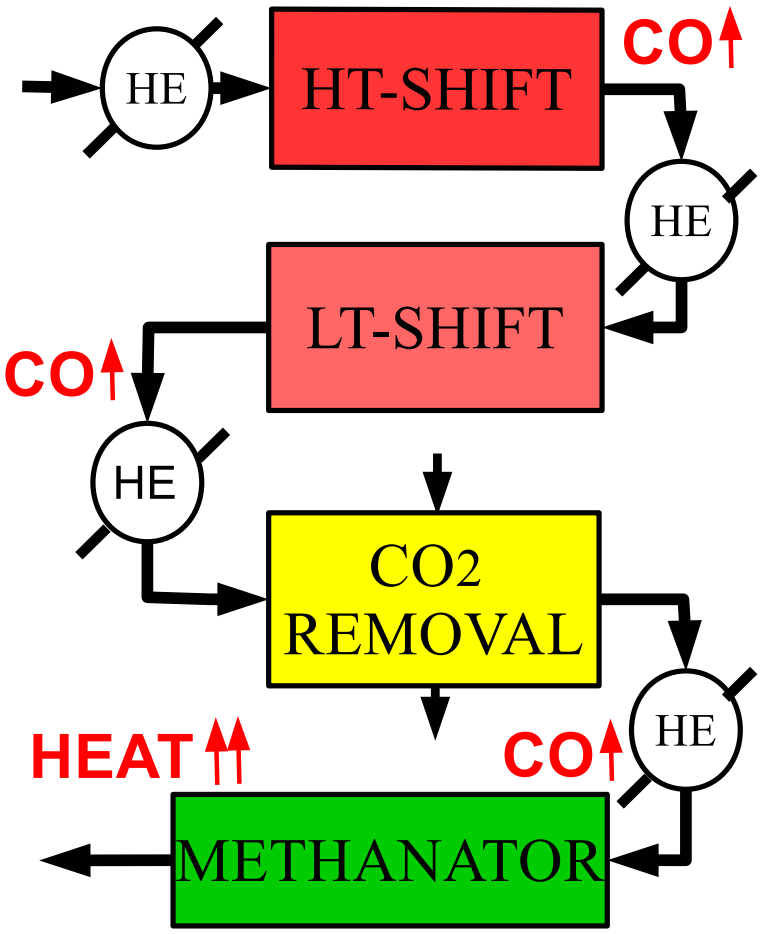

Figure 6.3: A schematic of disturbance propagation from high-temperature shift reactor to methanator, where increasing concentration of *CO* will lead to higher temperatures in the methanator that may trigger reaction thermal runaway.

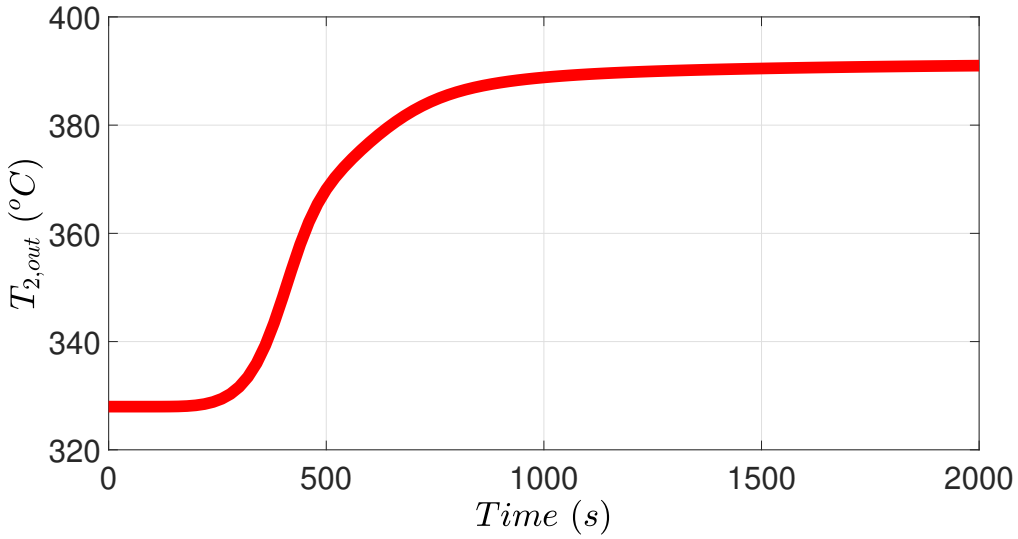

Figure 6.4: Methanator outlet temperature profile under open-loop simulation, where the temperature increases from 330 $°C$ to 390 $°C$ after catalyst activity in the high-temperature shift reactor decreases from 1 to 0.2 in 300 s.

the ammonia process, the disturbance of catalyst deactivation affects the process in the following way as demonstrated in Fig 6.3. First, the catalyst activity starts to decrease in the high-temperature shift reactor and less CO is consumed. Second, low-temperature shift reactor buffers the increasing CO content, but CO concentration still increases a lot. Third, no CO is removed in the CO_2 removal unit, and therefore more CO goes into the methanator as reactant. Finally, more CO undergoes an exothermic reaction in the methanator which leads to a drastic increase in temperature. As an example of this phenomenon, Fig. 6.4 shows an open-loop simulation of the methanator when the catalyst activity is decreasing from 1 to 0.2 in 300 s. As a result of this disturbance, the outlet temperature increases from 330 $°C$ to 390 $°C$ in the methanator.

6.3 Feedback Controller Design

6.3.1 Control Scheme

In order to avoid unsafe operation in the case of decreasing catalyst activity, a model predictive controller with feedforward term is implemented in ammonia process in [180]. In order to further

improve operational safety, in this chapter two controllers are designed for the high-temperature shift reactor and methanator, respectively. The first controller is added on the high-temperature shift reactor. The control variable of the first controller is the reactor outlet temperature and the manipulated variable is the reactor inlet temperature, which is actuated by a heat exchanger. The second controller is added on the methanator. The control variable of the second controller is the methanator outlet temperature and the manipulated variable is the methanator inlet temperature, which is actuated by another heat exchanger. It needs to be mentioned that the gas temperature inside the reactor is a crucial process variable to monitor operational safety and it increases monotonously from inlet to outlet in both high-temperature shift reactor and methanator. Therefore, outlet temperature is a reliable variable to indicate unsafe reactor operation. The described control loops in the ammonia process are demonstrated in Fig. 6.2.

6.3.2 High-temperature Shift Reactor Controller C_1

In the high-temperature shift reactor, less reaction occurs in the tube when the catalyst activity decreases, which leads to a decrease of reactor outlet temperature. In order to increase reaction rate and consume more carbon monoxide, the inlet temperature needs to be increased by adjusting the heat exchanger. To this end, a model predictive controller (MPC) is designed for the high-temperature shift reactor by manipulating the inlet temperature to control the outlet temperature. Since the process model in MPC is identified from the nominal process, to mitigate the effect of model mismatch, an integral term is added on the control action calculated by MPC to eliminate offset.

6.3.2.1 Model Identification

The high-temperature shift reactor is initially simulated at its steady-state where feed temperature $T_{1,in,ss} = 360\ ^\circ C$ and outlet temperature $T_{1,out,ss} = 429.18\ ^\circ C$. The state and the input of the process are represented in deviation variable form as $x_1 = T_{1,out} - T_{1,out,ss}$, $u_1 = T_{1,in} - T_{1,in,ss}$, such that the equilibrium point of the system is at the origin.

It is observed that there is an inverse response between the feed temperature $T_{1,in}$ and the outlet temperature $T_{1,out}$ for the high-temperature shift reactor. The reason is that for an adiabatic exothermic tube reactor, a drop in the inlet temperature causes a reduced reaction rate at the cooler upstream part of the tube reactor. Thus, the gas stream entering the downstream part of the tube reactor has a higher CO concentration, which speeds up the reaction in the downstream part of the tube reactor. This leads to a temporary increase in the local heat generation at the reactor outlet. However, the outlet temperature will decrease ultimately due to the decrease of inlet temperature [127, 155].

Since the effect of inverse response is negligible, inverse response is treated as time delay. Thus a linear dynamic model with time delay of the following form is utilized for the high-temperature shift reactor:

$$\frac{dx_1(t)}{dt} = A_1 x_1(t) + B_1 u_1(t - t_{d,1}) \tag{6.5}$$

where $t_{d,1}$ is the time delay in seconds. Aspen open-loop simulation is used to generate transient response data of the outlet temperature $T_{1,out}$ subject to a step change in feed temperature $T_{1,in}$, and Multivariable Output Error State Space (MOSEP) algorithm is applied in Matlab to identify the matrices A_1 and B_1. The matrices A_1, B_1 and the time delay $t_{d,1}$ are identified as follows:

$$A_1 = -0.015; \quad B_1 = 0.0142; \quad t_{d,1} = 360\ s$$

6.3.2.2 C_1 Design via MPC

The first controller is the MPC with an integral term. Specifically, the control action $u_1(t_k)$ consists of an integral term $u_{1,integral}(t_k)$ and an MPC term $u_{1,MPC}(t_k)$, where $u_{1,integral}(t_k)$ is calculated by Eq. 6.7 and $u_{1,MPC}(t_k)$ is the first control action in the solution $u^*(t)$ to the optimization problem of Eq. 6.8. Specifically,

$$u_1(t_k) = u_{1,MPC}(t_k) + u_{1,integral}(t_k) \tag{6.6}$$

$$
\begin{aligned}
e(t_k) &= T_{1,out}(set) - T_{1,out}(t_k) \\
u_{integral}(t_k) &= \frac{1}{\tau_I}\int_0^{t_k} e(\tau)\, d\tau
\end{aligned}
\tag{6.7}
$$

and

$$
\min_{u\in S(\Delta),y} \quad \int_{t_k+t_{d,1}}^{t_{k+N}+t_{d,1}} (\|\tilde{x}_1(\tau)\|^2_{Q_c})\, d\tau + \int_{t_k}^{t_{k+N}} (\|u_1(\tau)\|^2_{R_c})\, d\tau \tag{6.8a}
$$

$$
\text{s.t.} \quad \dot{\tilde{x}}_1(t) = A_1\tilde{x}_1(t) + B_1 u_1(t - t_{d,1}) \tag{6.8b}
$$

$$
\tilde{x}_1(t_k) = x_1(t_k) \tag{6.8c}
$$

$$
u_1(t) = u_{1,pre}(t),\ \forall\, t \in [t_k - t_{d,1}, t_k) \tag{6.8d}
$$

$$
u_1(t) \in U_1,\ \forall\, t \in [t_k, t_{k+N}) \tag{6.8e}
$$

The objective function of Eq. 6.8a requires minimizing the terms $\int_{t_k+t_{d,1}}^{t_{k+N}+t_{d,1}} (\|\tilde{x}_1(\tau)\|^2_{Q_c})\, d\tau$ and $\int_{t_k}^{t_{k+N}} (\|u_1(\tau)\|^2_{R_c})\, d\tau$ so that the system can be driven to its steady-state. The constraint of Eq. 6.8b is the nominal linear model of Eq. 6.5 that is used to predict future states. Eq. 6.8c defines the initial condition $\tilde{x}(t_k)$ of the optimization problem as the state measurement $x(t_k)$ at $t = t_k$. Eq. 6.8d provides input trajectory calculated from previous steps, in order to predict the state from t_k to $t_k + t_{d,1}$. Eq. 6.8e is the input constraint applied over the entire prediction horizon. The manipulated input is the feed temperature $T_{1,in}$, which is bounded by: $310\ ^\circ C \leq T_{1,in} \leq 410\ ^\circ C$, namely $U_1 = [-50,\ 50]$.

The explicit Euler method with an integration time step of $h_c = 10^{-1}\ s$ is applied to numerically integrate the dynamic model of Eq. 6.8b in MPC. The nonlinear optimization problem of MPC of Eq. 6.8 is solved using the solver FilterSD on OPTI Toolbox in Matlab with the following parameters: sampling period $\Delta = 20\ s$; prediction horizon $N = 30$. $Q_c = 1$ and $R_c = 0.2$ are chosen such that the terms of the states and the input have the same order of magnitude in $\|\tilde{x}_1(\tau)\|^2_{Q_c}$ and $\|u_1(\tau)\|^2_{R_c}$. The integral time constant $\tau_I = 33.3\ s$ is determined to eliminate the offset of the closed-loop system without oscillation.

6.3.3 Methanator Controller C_2

Although the low-temperature shift reactor mitigates the increase in CO concentration from the high-temperature shift reactor, a higher concentration of CO still reaches the methanator. Since more CO is fed as reactant into the methanator, the temperature increases in the methanator. To avoid potential high temperature in the methanator, a second model predictive controller (MPC) is designed to control the methanator outlet temperature by manipulating its inlet temperature.

6.3.3.1 Model Identification

The methanator is initially simulated at the steady-state where feed temperature $T_{2,in,ss} = 280\ ^{\circ}C$ and outlet temperature $T_{2,out,ss} = 327.98\ ^{\circ}C$. Because the feed CO concentration has a dominating effect on the produced heat, the CO mole fraction y_{CO} is treated as a measurable disturbance d_2 with a steady-state value of $y_{CO,ss} = 3.55 \times 10^{-3}$, where the deviation variable is $d_2 = y_{CO} - y_{CO,ss}$.

Since increasing feed CO content significantly changes the working condition of the methanator, the steady-state of the methanator changes with variation of feed CO mole fraction. Therefore, a set of steady-state values of the methanator is calculated offline as a function of feed CO mole fraction y_{CO}. Specifically, future inlet temperature and outlet temperature steady-states are expressed as a function of disturbance d_2 as follows:

$$\begin{aligned} \Delta d &= d_2(t_k) - d_2(t_{k-1}) \\ T(t_{k+N})_{2,in,ss} &= 280 - 4080.7(d_2 + \gamma\, \Delta d\ N) \\ T(t_{k+N})_{2,out,ss} &= 327.27 + 1616.3(d_2 + \gamma\, \Delta d\ N) \end{aligned} \tag{6.9}$$

where $\gamma = 0.5$ is the coefficient to regulate changing speed of future disturbance. If current disturbance $d_2(t_k)$ increases by Δd compared to the disturbance $d_2(t_{k-1})$ at the previous step, future disturbance is anticipated to increase by $\gamma\, \Delta d$ at each subsequent sampling time, and future steady-state should change accordingly with future disturbance. The above steady-state values are reasonable working conditions obtained offline, where the corresponding outlet CO content is

below 5×10^{-6} and the outlet temperature is below 340 $^{\circ}C$ if the disturbance d_2 is not large.

The state and the input of the process are represented in deviation variable form as $x_2 = T_{2,out} - T_{2,out,ss}$ and $u_2 = T_{2,in} - T_{2,in,ss}$ such that the equilibrium point of the system is at zero. Since the transient response of the outlet temperature $T_{2,out}$ has a time delay under a step-change of the feed temperature $T_{2,in}$, a linear dynamic model with time delay of the following form is utilized to represent the Aspen Plus model of the methanator:

$$\frac{dx_2(t)}{dt} = A_2 x_2(t) + B_2 u_2(t - t_{d,2}) \tag{6.10}$$

where $t_{d,2}$ is the time delay in seconds. Aspen open-loop simulations for the nominal system are used to generate transient response data of the outlet temperature $T_{2,out}$ subject to various step changes in feed temperature $T_{2,in}$, and Multivariable Output Error State Space (MOSEP) algorithm is applied in Matlab to identify the matrices A_2 and B_2. Since the disturbance of feed CO content changes only the steady-state of the methanator, and barely the dynamics of methanator (i.e., time constant, gain and time delay), the model of Eq. 6.10 is demonstrated to work well for all steady-states corresponding to different feed CO content. The matrices A_2, B_2 and the time delay $t_{d,2}$ are identified as follows:

$$A_2 = -0.005136; \quad B_2 = 0.01207; \quad t_{d,2} = 100\ s$$

6.3.3.2 C_2 Design via Safeness Index-based MPC

The methanator controller is developed to ensure process operational safety of the ammonia process since high outlet temperature above the steady-state value could lead to unsafe operations. Specifically, Safeness Index is developed and incorporated as a constraint in MPC due to safety considerations in methanator, meanwhile C_1 is a tracking MPC without explicit safety constraints since there are no critical safety issues in the high-temperature shift reactor. In our work, the Safeness Index is designed such that the process is considered unsafe when the methanator

outlet temperature $T_{2,out}$ is above the steady-state operating condition $T_{2,out,ss}$, and safe when the temperature $T_{2,out}$ is below steady-state value $T_{2,out,ss}$. To that end, we define a function $f^+(x)$ as shown in Eq. 6.11:

$$f^+(x) = \begin{cases} x, & \text{if} \quad x \geq 0 \\ 0, & \text{if} \quad x < 0 \end{cases} \tag{6.11}$$

Based on Eq. 6.11, the Safeness Index function is design as follows:

$$S(T) = [f^+(T_{2,out} - T_{2,out,initial})]^2 \tag{6.12}$$

With a quadratic form, $S(x)$ will have a significantly large value when temperature $T_{2,out}$ is far above the steady-state value. $T_{2,out,initial} = 327.98\ ^\circ C$ in Eq. 6.12 is the initial steady-state value of outlet temperature. Since the steady-state value of outlet temperature $T_{2,out,ss}$ is changing in simulation with varying disturbances d_2 as described in Eq. 6.9, Eq. 6.12 is rewritten with deviation variable x_2 as follows:

$$S(x_2(t_{k+N})) = [f^+(x_2(t_{k+N}) + 1616.3(d_2 + \gamma\, \Delta d\ N))]^2 \tag{6.13}$$

To avoid high temperature in the methanator, a threshold S_{TH} of Safeness Index function is carefully chosen. Specifically, if methanator outlet temperature $T_{2,out}$ is constrained below $340\ ^\circ C$, the threshold for $S(x_2)$ is determined to be $(340 - 327.98)^2 = 144.48$. Additionally, the actual threshold used in the controller is chosen to be a conservative value of $S_{TH} = 121$ due to a few intrinsic problems: the model mismatch between the identified model and the real plant, sample-and-hold implementation of the controller and large time delay in the process. A general method to determine the Safeness Index threshold can be found in [9]. Based on the Safeness

Index function of Eq. 6.13, the Safeness Index-based MPC is developed as follows:

$$\min_{u\in S(\Delta),y} \quad \int_{t_k+t_{d,2}}^{t_{k+N}+t_{d,2}} (\|\tilde{x}_2(\tau)\|^2_{Q_c})\, d\tau + \int_{t_k}^{t_{k+N}} (\|u_2(\tau)\|^2_{R_c})\, d\tau + \sum_{i=1}^{N} k_1 e^{-k_2 y(i)}, \quad k_1, k_2 > 0 \tag{6.14a}$$

$$\text{s.t.} \quad \dot{\tilde{x}}_2(t) = A_2\tilde{x}_2(t) + B_2 u_2(t - t_{d,2}) \tag{6.14b}$$

$$\tilde{x}_2(t_k) = x_2(t_k) \tag{6.14c}$$

$$u_2(t) = u_{2,pre}(t),\ \forall\, t \in [t_k - t_d, t_k) \tag{6.14d}$$

$$u_2(t) \in U_2,\ \forall\, t \in [t_k, t_{k+N}) \tag{6.14e}$$

$$S(\tilde{x}_2(t_{k+i} + t_d)) + y(i) \leq S_{TH},\ i = 1, 2, ..., N \tag{6.14f}$$

Although the optimal input trajectory $u_2^*(t)$ is calculated over the entire prediction horizon $t \in [t_k, t_{k+N})$, the control action computed for the first sampling period in the prediction horizon $u_2(t_k)$ is applied over the first sampling period, and the MPC problem is resolved at the next sampling period. The objective function of Eq. 6.14a requires minimizing the integral term $\int_{t_k+t_{d,2}}^{t_{k+N}+t_{d,2}} (\|\tilde{x}_2(\tau)\|^2_{Q_c})\ d\tau + \int_{t_k}^{t_{k+N}} (\|u_2(\tau)\|^2_{R_c})\ d\tau$ and the penalty term $\sum_{i=1}^{N} k_1 e^{-k_2 y(i)}$ of slack variables $y(i)$. It is noted that state is integrated from $t_k + t_{d,2}$ to $t_{k+N} + t_{d,2}$ because states from t_k to $t_k + t_{d,2}$ are already determined by the previously implemented control actions. The constraint of Eq. 6.14b is the nominal linear model of Eq. 6.10 that is used to predict the states of the closed-loop system. Eq. 6.14c defines the initial condition $\tilde{x}_2(t_k)$ of the optimization problem which is the state measurement $x_2(t_k)$ at $t = t_k$. Eq. 6.14d provides the input trajectory calculated from previous steps, in order to predict the state from t_k to $t_k + t_{d,2}$. Eq. 6.14e is the input constraint applied over the entire prediction horizon. The manipulated input is the feed temperature $T_{2,in}$, which is bounded by $180\ ^\circ C \leq T_{2,in} \leq 380\ ^\circ C$, namely $U_2 = [-100,\ 100]$. Eq. 6.14f is the Safeness Index constraint with slack variables $y(i)$. Since the penalty term $\sum_{i=1}^{N} k_1 e^{-k_2 y(i)}$ is minimized in the objective function, $y(i)$ is maximized so that the Safeness Index is restricted to be below S_{TH} as much as possible. Additionally, the parameters k_1 and k_2 in the objective function of Eq. 6.14a should be carefully chosen, such that the slack variables $y(i)$ have a small effect on control actions if $S(x_2(t_k + t_d))$ is far below S_{TH}, and have a significant effect on control actions if $S(x_2(t_k + t_d))$ is close to S_{TH} (i.e.,

approaching the threshold for unsafe operating conditions). Thus, in our simulation k_1 and k_2 are determined to be 10^3 and 0.2, respectively.

The explicit Euler method with an integration time step of $h_c = 10^{-1}$ s was applied to numerically integrate the dynamic model of Eq. 6.10 in the Safeness Index-based MPC. The nonlinear optimization problem of the Safeness Index-based MPC of Eq. 6.14 is solved using the solver FilterSD on OPTI Toolbox in Matlab with the following parameters: sampling period $\Delta = 20$ s; prediction horizon $N = 30$. $Q_c = 1$ and $R_c = 2$ are chosen such that the terms of the states and the input have the same order of magnitude in $\|\tilde{x}_2(\tau)\|^2_{Q_c}$ and $\|u_2(\tau)\|^2_{R_c}$.

6.4 Closed-loop Simulation Results

6.4.1 Simulation Results Using Both C_1 and C_2

In this section, the performance of the ammonia plant under the proposed controllers C_1 and C_2 is demonstrated. Figs. 6.5, 6.6 and 6.7a show the closed-loop simulation of the entire ammonia process in the presence of disturbance of catalyst deactivation.

As a result of catalyst deactivation from 1 to 0.2 in the high-temperature shift reactor in the first 300 s, less CO is reacting in the high-temperature shift reactor. After a small inverse response, at about 400 s the outlet temperature of the high-temperature shift reactor starts to decrease below its steady-state value as shown in Fig. 6.5a. Then, the first controller C_1 measures the decreasing outlet temperature $T_{1,out}$, hence increases the inlet temperature $T_{1,in}$ in order to react more CO in the high-temperature shift reactor, as shown in Fig. 6.5b. Under the MPC of Eq. 6.8, the outlet temperature $T_{1,out}$ of the high-temperature shift reactor returns back to its steady-state value within 1500 s. Since the catalyst activity in the high-temperature shift reactor has decreased, the reactor is not able to react as much CO as it would have under the initial nominal condition (i.e., without catalyst deactivation), thus more residual unreacted CO leaves the high-temperature shift reactor into the low-temperature shift reactor.

In the next unit of the process, the low-temperature shift reactor mitigates the increased CO

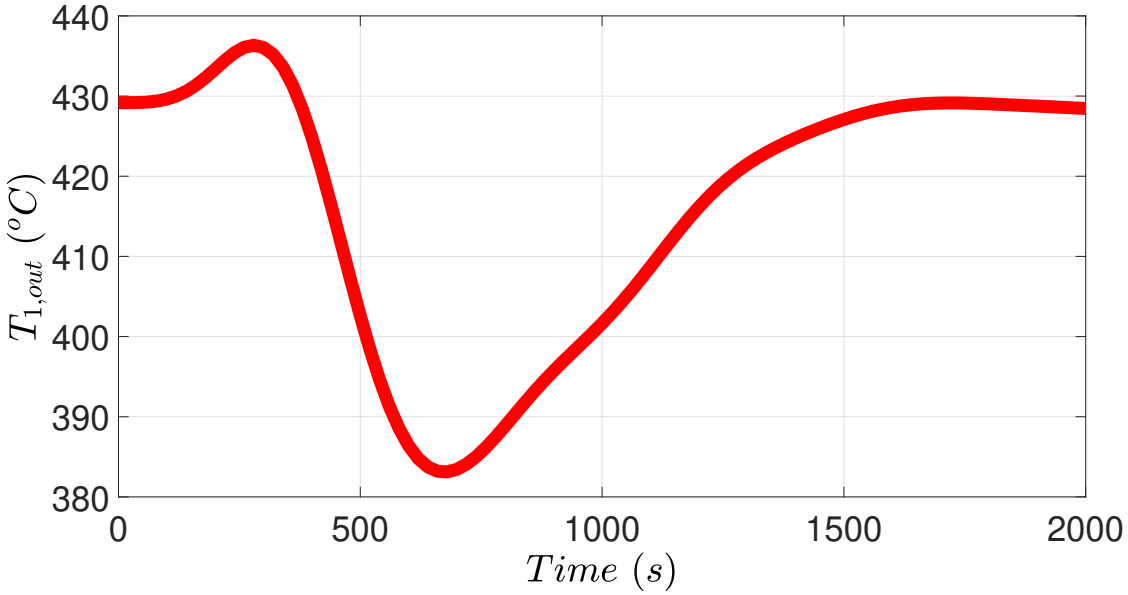

(a) Outlet temperature of the high-temperature shift reactor

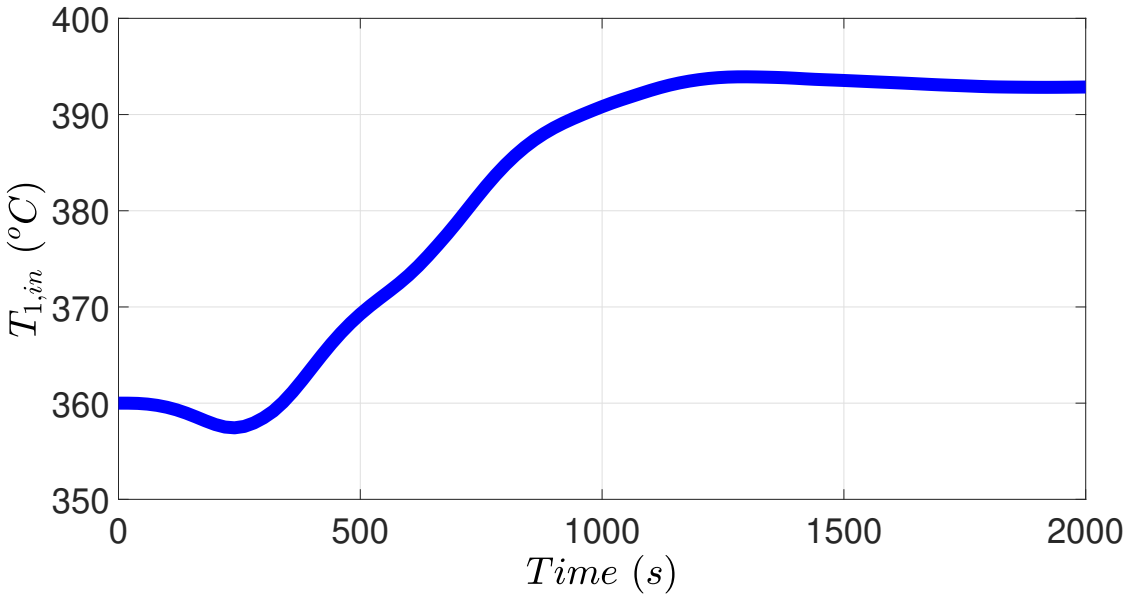

(b) Inlet temperature of the high-temperature shift reactor

Figure 6.5: Closed-loop simulation results under the control structure that uses C_1 and C_2.

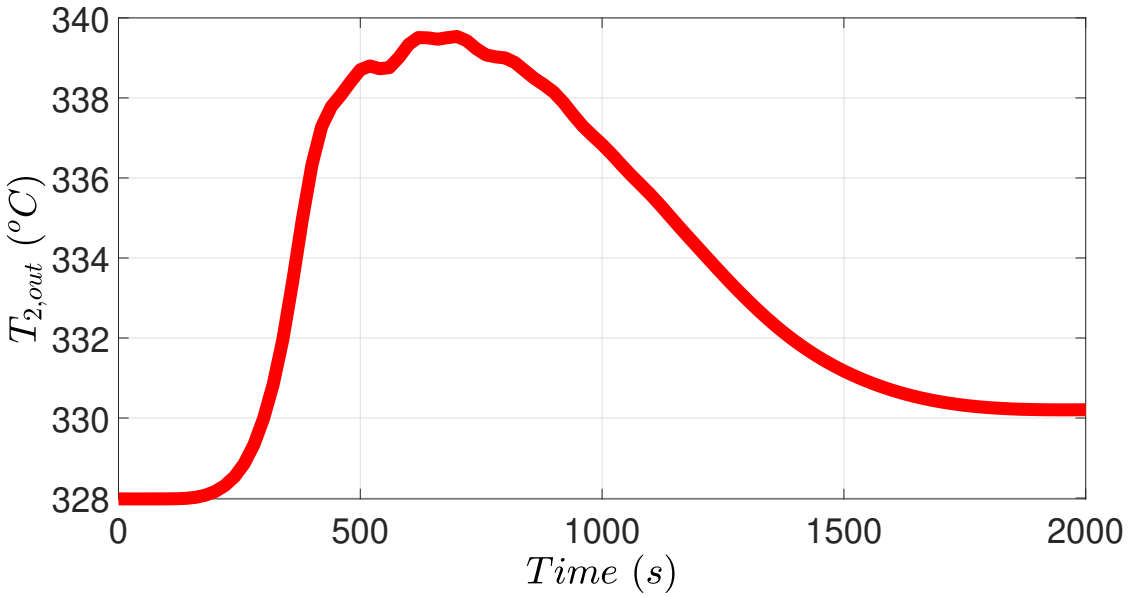

(a) Outlet temperature of the methanator

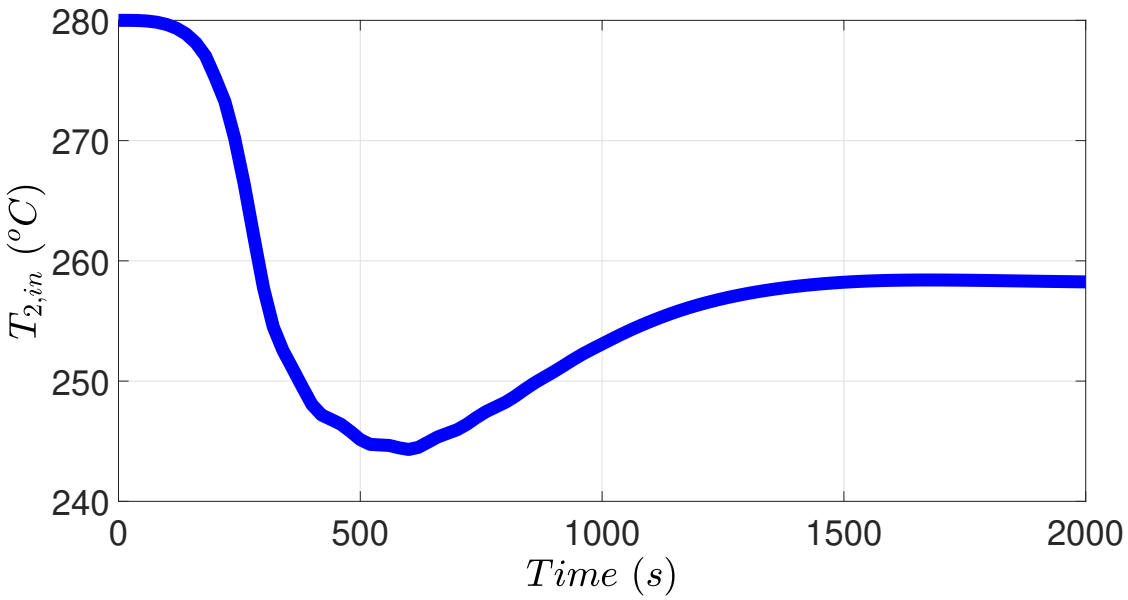

(b) Inlet temperature of the methanator

Figure 6.6: Closed-loop simulation results under the control structure that uses C_1 and C_2.

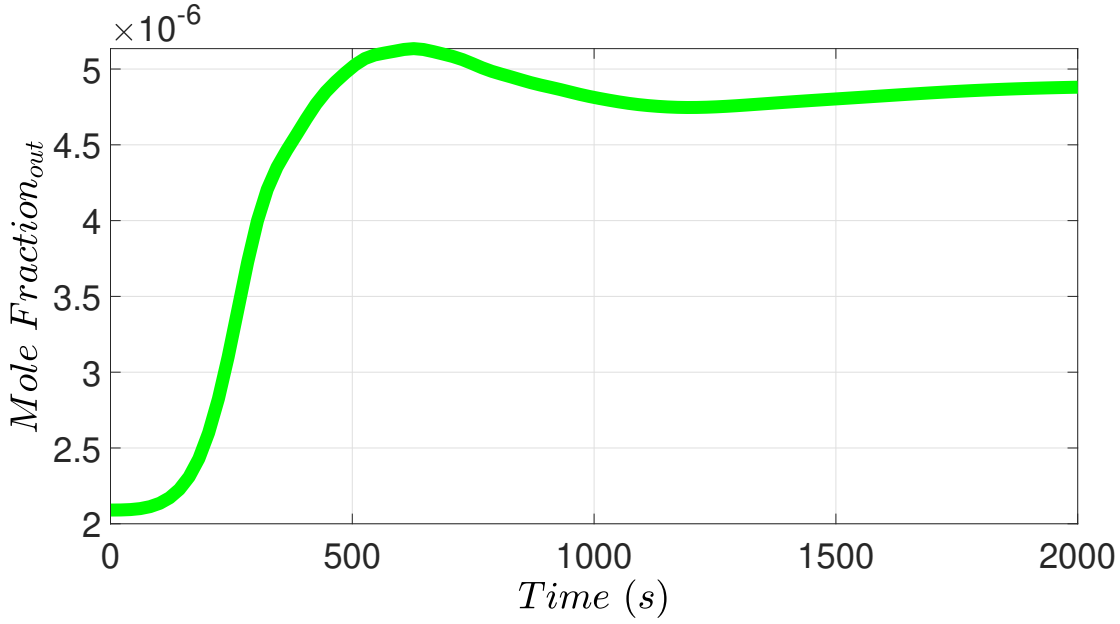

(a) Outlet mole fraction of carbon monoxide of the methanator under the control structure that uses C_1 and C_2.

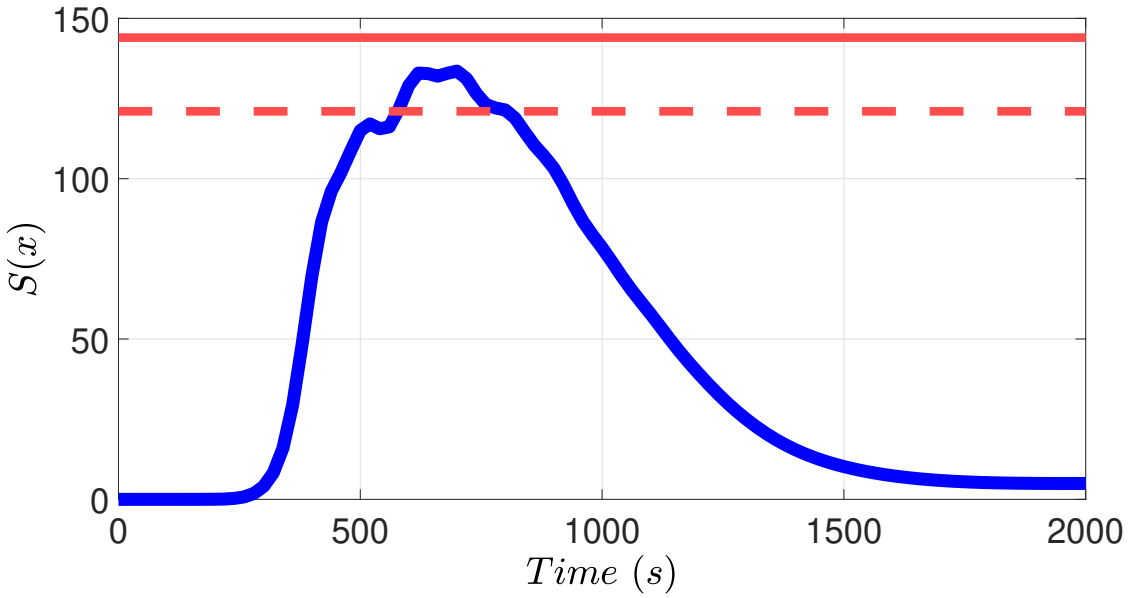

(b) Safeness Index Profile. Solid line is actual process threshold, and dashed line is threshold used in controller.

Figure 6.7: Closed-loop simulation results under the control structure that uses C_1 and C_2.

content, but a higher concentration of CO (relative to the case of no catalyst deactivation) still leaves the low-temperature shift reactor. Since more CO reaches the methanator, the outlet temperature $T_{2,out}$ from the methanator starts to increase at around 200 s, as shown in Fig. 6.6a. It is noted that the CO mole fraction y_{CO} in the feed of the methanator is measured at each sampling time t_k and a corresponding steady-state is calculated using Eq. 6.9. Then, the Safeness Index-based MPC (C_2) measures the outlet temperature $T_{2,out}$ and manipulates inlet temperature $T_{2,in}$ to drive the methanator outlet temperature $T_{2,out}$ to the new steady-state.

In order to understand the influence of the Safeness Index constraint, it is important to mention that the Safeness Index constraint of Eq. 6.14f requires all predicted Safeness Index to be below $S_{TH} = 121$ together with the slack variables $y(i)$. When the outlet temperature $T_{2,out}$ gets close to 340 $^{\circ}C$ at around 500 s as shown in Fig. 6.6a, $S(x)$ grows close to $S_{TH} = 121$. Because of the Safeness Index constraint of Eq. 6.14f, small values for slack variables $y(i)$ are used when $S(x)$ is close to S_{TH}, which makes the penalty term $\sum_{i=1}^{N} k_1 e^{-k_2 y(i)}$ dominate the objective function of Eq. 6.14a. Since the penalty term $\sum_{i=1}^{N} k_1 e^{-k_2 y(i)}$ in the objective function of Eq. 6.14a is minimized, slack variables $y(i)$ are optimized to be as large as possible, and thus to restrict the temperature $T_{2,out}$ to be as low as possible. When the outlet temperature $T_{2,out}$ gets far below 340 $^{\circ}C$ at around 1500 s as shown in Fig. 6.6a, $S(x)$ is far from $S_{TH} = 121$. Because of the Safeness Index constraint of Eq. 6.14f, large values for slack variables $y(i)$ are used when $S(x)$ is far from S_{TH}. Large slack variables make the penalty term $\sum_{i=1}^{N} k_1 e^{-k_2 y(i)}$ very small in the objective function of Eq. 6.14a, and therefore, the Safeness Index constraint of Eq. 6.14f can be easily satisfied by choosing large slack variables $y(i)$ without increasing the penalty term $\sum_{i=1}^{N} k_1 e^{-k_2 y(i)}$ in the objective function of Eq. 6.14a.

Additionally, the Safeness Index constraint of Eq. 6.14f and a state constraint are similar especially in this work, but they can be designed with different forms. In general, the Safeness Index can take any formulation that accounts for the impact of multiple process variables, and thus, become more powerful than a simple state constraint. Moreover, soft constraints may be added in the Safeness Index constraint using slack variables, instead of a hard state constraint.

Slack variables $y(i)$ are allowed to choose positive or negative values to meet the constraint of Eq. 6.14f, depending on the current measurement and the prediction of the state. The main objective of the slack variable is to ensure feasibility of the constraint $S(\tilde{x}_2(t_{k+i}+t_d)) \leq S_{TH}$ when $S(\tilde{x}_2(t_{k+i}+t_d)) > S_{TH}$ for some i. Therefore, slack variables are added in the constraint and are required to be negative when $S(\tilde{x}_2(t_{k+i}+t_d)) > S_{TH}$. The slack variables $y(i)$ allow the Safeness Index to be temporarily above S_{TH} by taking negative slack values, which can be necessary in some scenarios: (a) an abrupt large disturbance occurs so that the outlet temperature exceeds 340 $^{\circ}C$ very fast; (b) the disturbance d_2 increases very fast so that Δd is very large and the predicted outlet temperature at steady-state $T(t_{k+N})_{out,ss}$ is above 340 $^{\circ}C$. If $S(\tilde{x}_2(t_{k+i}+t_d)) \leq S_{TH}$, slack variables are still included in the constraint and are required to be positive. With the help of the slack variables $y(i)$, Fig. 6.6b demonstrates that the inlet temperature $T_{2,in}$ decreases smoothly when $S(x)$ is close to S_{TH} to avoid the unsafe region, instead of changing abruptly. If the slack variables $y(i)$ were not used in MPC, the inlet temperature $T_{2,in}$ will not start to decrease before the outlet temperature $T_{2,out}$ reaches 340 $^{\circ}C$ but will show an abrupt change when the current outlet temperature increases above 340 $^{\circ}C$.

Moreover, Fig. 6.7a shows that the outlet carbon monoxide mole fraction is around 5×10^{-6}, which satisfies the requirements and indicates that the offline calculated steady-state works well. The performance of CO removal in the methanator is not compensated too much by decreasing the methanator inlet temperature in response to the increase in its outlet temperature.

6.4.2 Comparison with Use of C_2 Only

In this section, the ammonia process is simulated under the same disturbance but with only controller C_2 implemented. Fig. 6.8 demonstrates the comparison between the simulation results under a single controller C_2 and the simulation results in Section 6.4.1.

For the scenario that both controllers C_1 and C_2 are used, the first controller C_1 increases the feed temperature $T_{1,in}$ and the reaction rate in the high-temperature shift reactor in order to reduce the effect of reduced catalyst activity. Therefore, the methanator feed CO content will first increase,

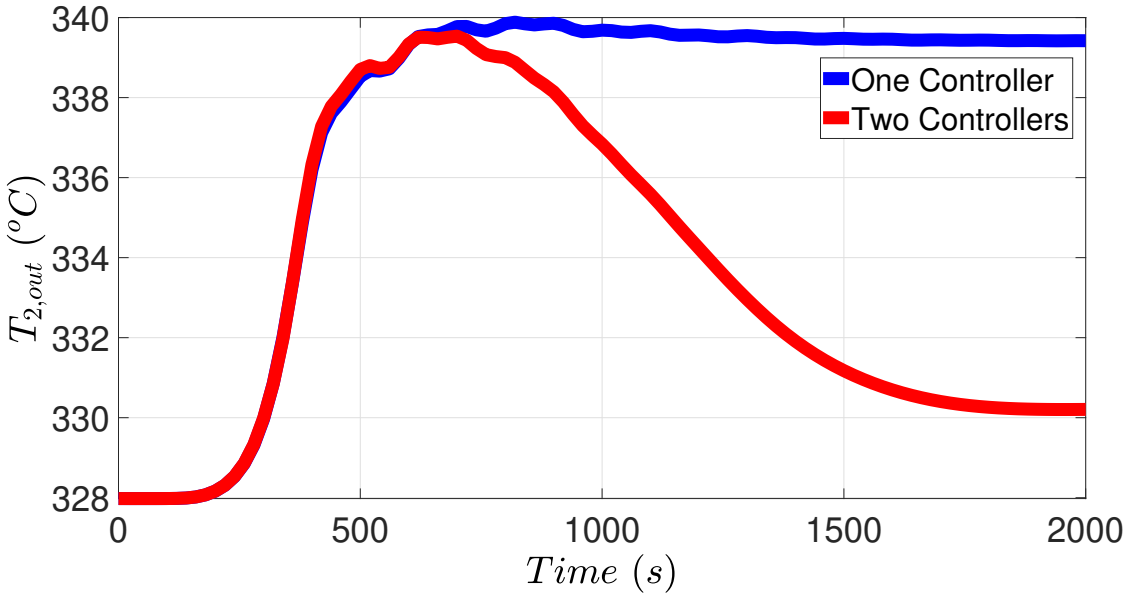

Figure 6.8: Comparison of methanator outlet temperature under two different control schemes: One scenario uses only C_2, and the other scenario uses both C_1 and C_2.

but eventually decrease after some time delay if the controller C_1 is used. Thus, the controller C_1 mitigates the disturbance d_2 and other unmeasured disturbances to the methanator and finally drives the system to a new steady-state corresponding to a smaller disturbance d_2 in Fig. 6.8.

However, when only C_2 is used in the ammonia process, the methanator feed CO content increases and remains at a very high level, which introduces a large disturbance d_2 to the methanator. Thus, the controller C_2 drives the methanator to a new steady-state corresponding to a large disturbance d_2. As shown in Fig. 6.8, the methanator outlet temperature is maintained at around 340 $^\circ C$ if controller C_1 is not used, which is the outlet temperature steady-state when methanator feed CO content is high.

In Fig. 6.8, it takes more time for two controllers to drive the methanator outlet temperature $T_{2,out}$ to the new steady-state compared to one controller. This is because the high-temperature shift reactor has a larger time delay ($t_{d,1} = 360\ s$), therefore the controller C_1 needs a long time to stabilize the high-temperature shift reactor. Then, the methanator feed CO content also decreases slowly and the methanator outlet temperature $T_{2,out}$ needs 2000 s to reach the final steady-state.

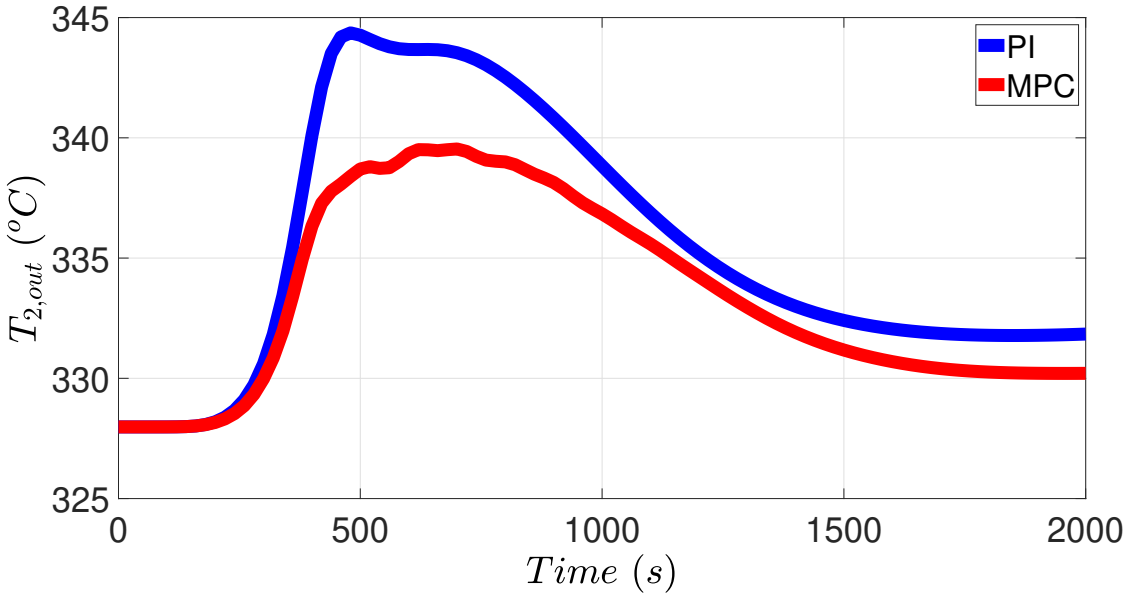

Figure 6.9: Comparison of methanator outlet temperature under PI (both C_1 and C_2) and MPC (both C_1 and C_2) control schemes.

6.4.3 Comparison with PI Controller

Since proportional-integral (PI) control is still the most popular technique for chemical industries, in this section, the ammonia process is simulated under the same disturbance but with PI controllers for both C_1 and C_2. Fig. 6.9 demonstrates the comparison between the simulation results under PI controllers and the simulation results in Section 6.4.1. Additionally, PI controllers C_2 also measure the current disturbance $d_2(t_k)$ and changes the set-point as discussed in Section 6.3.3.1

It is noted that state constraints cannot be employed in the PI controllers, but MPC can use Safeness Index constraint of Eq. 6.14f to avoid unsafe operations. Moreover, the PI controller cannot account for anticipated future potential increasing disturbance from $d_2(t_{k+1})$ to $d_2(t_{k+N})$, but MPC can consider future disturbance and future steady-state in Eq. 6.9. Therefore, the closed-loop performance of the PI controller cannot avoid extreme states in the presence of disturbance. Specifically in Fig. 6.9, the methanator outlet temperature $T_{2,out}$ under the PI controllers goes above 340 $^\circ C$ for a period of 500 s, while the proposed controllers in this chapter can avoid exceeding 340 $^\circ C$.

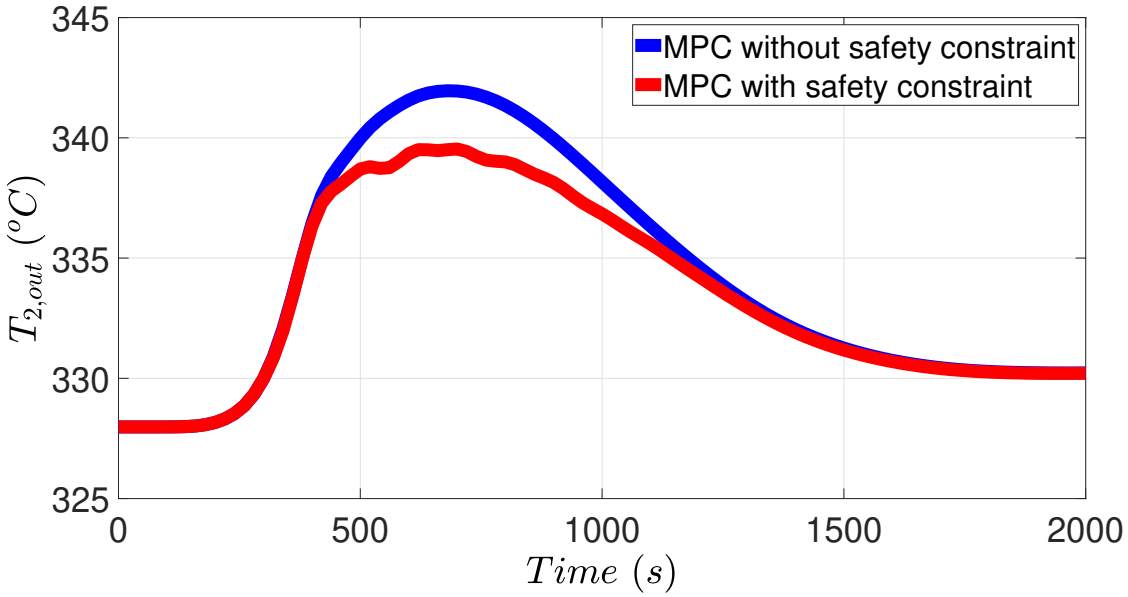

Figure 6.10: Comparison of methanator outlet temperature under MPC with and without Safeness Index constraints.

6.4.4 MPC without Safeness Index Constraint

In this section, the ammonia process is simulated under the same disturbance with both C_1 and C_2, in which the Safeness Index constraint of Eq. 6.14f is not applied. Fig. 6.10 demonstrates the comparison between the simulation results under MPC without Safeness Index constraint and the simulation results in Section 6.4.1.

The objective of controllers is to maintain the methanator outlet temperature $T_{2,out}$ below 340 $^\circ C$ in order to avoid a potential runaway reaction. However, it is observed in Fig. 6.10 that the MPC without Safeness Index constraint allows the methanator outlet temperature $T_{2,out}$ to be above 340 $^\circ C$ for 400 s. However, due to the Safeness Index constraint of Eq. 6.14f that prevents temperature from going extremely high, in the case of the MPC using Safeness Index constraint, the methanator outlet temperature $T_{2,out}$ stays in the safe region of operation for the entire simulation time. This implies that the Safeness Index-based MPC of Eq. 6.14 can improve process operational safety of the ammonia plant, compared to MPC without Safeness Index constraint.

6.5 Conclusion

In this chapter, an application was demonstrated by integrating process operational safety with multiple model predictive controllers for a multi-unit ammonia network. Aspen Plus Dynamics is a commercial process simulation software which was integrated with Matlab to run a closed-loop simulation for the ammonia process. A common and problematic disturbance, catalyst deactivation, was introduced into dynamic simulations. The disturbance was first introduced in the high-temperature shift reactor, which propagated from upstream units to downstream units and finally caused dramatic temperature increase in the methanation unit. Two controllers were designed to improve process operational safety in the entire ammonia process network. The first controller was an MPC with an integral term that controls the high-temperature shift reactor. The second controller was a Safeness Index-based MPC that controls the methanator. Closed-loop simulations demonstrated that extremely high temperature was avoided under the proposed controllers in the presence of significant disturbances.

Chapter 7

Operational Safety via Model Predictive Control: The Torrance Refinery Accident Revisited

7.1 Introduction

On Wednesday, February 18, 2015, an accidental explosion in the gasoline processing unit at the refinery operated by ExxonMobil in Torrance, California took place involving mainly the following units: a distillation column, a fluid catalytic cracking (FCC) unit, and an electrostatic precipitator (ESP). The explosion led to an economic loss, which is estimated to be from $2.4 up to $6.9 billions, and caused harm on health of operators and people surrounding the refinery [42, 65]. Based on the transcripts of the public meeting about the accident in Torrance, California [42], ExxonMobil used a methodology named operations and integrity management system (OIMS) for its process safety system, which was found to be defective in that it lacks a hierarchy inspection of control analysis and an implementation of safeguards from process hazard analysis [42]. It was further suggested by the final report from Chemical Safety Board (CSB) that a controller should be incorporated in the Safe Park mode [43]. It is worth quoting directly from that report:

"*ExxonMobil did not develop a Safe Park procedure for how to safely operate within specified safe operating limits, with specified operating parameters that could directly verify the critical Safe Park safeguards. Safe Park procedure development and improved measurement and control of critical process conditions could have prevented this incident*."

Despite the economical, the environmental, and the overall casualty rate involved in such accidents, most chemical processes still rely on process safety studies such as hazard and operability analysis (HAZOP), hazard identification (HAZID) and layer of protection analysis (LOPA) [179]. However, in a paper presented in the conference of society of petroleum engineers on health, safety, environmental, and social responsibility in 2018, the limitations of implemented safety studies in the industry and their link with the accidents were pointed out [63]. For instance, the ExxonMobil refinery in Torrance, and other involved plants investigated by US Chemical Safety Board (CSB) were used as references to show that common safety studies, such as HAZOP and HAZID, lead to the recurrent triggers of different accidents [63].

The key problem of HAZOP, LOPA and HAZID and similar process safety techniques is that they were proposed more than a half century ago, which do not adapt to the current industrial operations [63]. These process safety techniques are open-loop analysis techniques without real-time feedback, and they do not use real-time information during the operation. Moreover, process dynamics is not taken into account in these traditional techniques. Recently, some efforts have been made to investigate the disadvantages of traditional safety techniques and to improve the current practices. For example, an accident at the BP refinery in Texas in 2005 was investigated with a dynamic simulation tool to better understand the column flooding and overfilling [77, 100]. In this dynamic HAZOP approach, a dynamic simulator is integrated with the traditional HAZOP study in order to reduce the speculation while identifying the relevant events. In [89], it is argued that HAZOP has not changed at the same pace as industrial technology, which has been more integrated nowadays, especially with more frequent changes in set-point during normal operations (e.g., when using economic model predictive control). For that reason, identifying all potential events that can lead to an accident in the process becomes difficult using the HAZOP approach

only. Similarly, common process safety frameworks lack of well-known control properties in their formulations as was pointed out, for example, in the defense-in-depth strategy, which has been applied in the nuclear industry for safety studies [142].

Recently, some research works have been done on the integration of process safety systems with process control systems for real-time operation of industrial processes [179]. For instance, a high-pressure flash drum with its safety device and an MIC reactor associated with the Bhopal incident were studied using a control methodology that allows to avoid operating in unsafe regions [178]. Additionally, a multi-unit ammonia process which integrates safety constraints and model predictive control was tested under a disturbance that is associated with reaction thermal runaway in a co-simulation of Matlab and Aspen Plus Dynamics [179, 180].

In this direction, this study develops a model predictive control system for the FCC unit. Specifically, the accident in Torrence, California is studied in detail by following closely the findings and suggestions in the report from CSB. Then, after identifying the trigger events and operation conditions during the accident, the FCC unit is simulated in Aspen Plus Dynamics. In order to avoid the incident, we follow the suggestion by the CSB report and develop a model predictive controller using the recommended safeguards in the Safe Park mode. In addition, offset-free control means that the controlled variables are driven to the set-point without offset. Since any potential offset can cause severe dangers in the case of significant disturbances, offset-free methodology is employed in the controller, as discussed in [162]. Finally, two sets of disturbances are introduced into the FCC unit to demonstrate the effectiveness of the proposed safety-aware control system.

The rest of the chapter is organized as follows: in Section 7.2, the fluid catalytic cracking process is introduced with the main events that occurred during the accident at the refinery operated by ExxonMobil in Torrance, California. Then, the key aspects for dynamically simulating the refinery with the implementation of the disturbances that can cause the accidents are explained. In Section 7.3, the controller design is presented in which the model identification and the offset-free approaches are utilized in the control system. In Section 7.4, the simulation results are presented

for the FCC unit under the proposed controller and the disturbances that trigger the same accident as in the CSB report.

7.2 Accident Description and Modeling

Nowadays there are around 400 fluid catalytic cracking units operating around the world that are responsible for producing 45% of the naphtha worldwide among many other products [128, 148]. Four distinct designs have been developed for the FCC process since the first FCC unit started to operate in 1940s. Specifically, in 1947, UOP's stacked unit was the first to include the spent catalyst stripping idea in which the spent catalyst is driven by gravity [128, 148]. In 1952, FCC model IV was proposed by Standard Oil Development, in which a vessel is placed to the side of the reactor using U-bend connector for regenerating the catalyst [128, 148]. In 1979, by taking advantage of a new catalyst design and the Kellogg's Orthoflow F process (i.e., a two-step catalyst regeneration process), Exxon proposed the Flexicracking unit that uses a side-by-side concept in which the regenerator is placed in a lower position compared to the riser cracking reactor position [128, 148]. Finally, in 1981, Total Petroleum USA proposed a residue FCC unit, also named R2R unit, in which two regenerators are used allowing the reduction of the catalyst deactivation to a minimum level [55].

Following the design method in [43, 128], the following subsections describe the general FCC process, and then elaborate on the accident details in the explosion at the Torrance refinery. Aspen Plus Dynamics is used to model the FCC process with disturbances to simulate the accident conditions.

7.2.1 Fluid Catalytic Cracking Process

In this subsection, a simplified description of the FCC process is presented together with the key characteristics of each unit in the FCC process. Specifically, the FCC process involves a reactor, a riser, a catalyst regenerator, a distillation column, an expander and an electrostatic precipitator

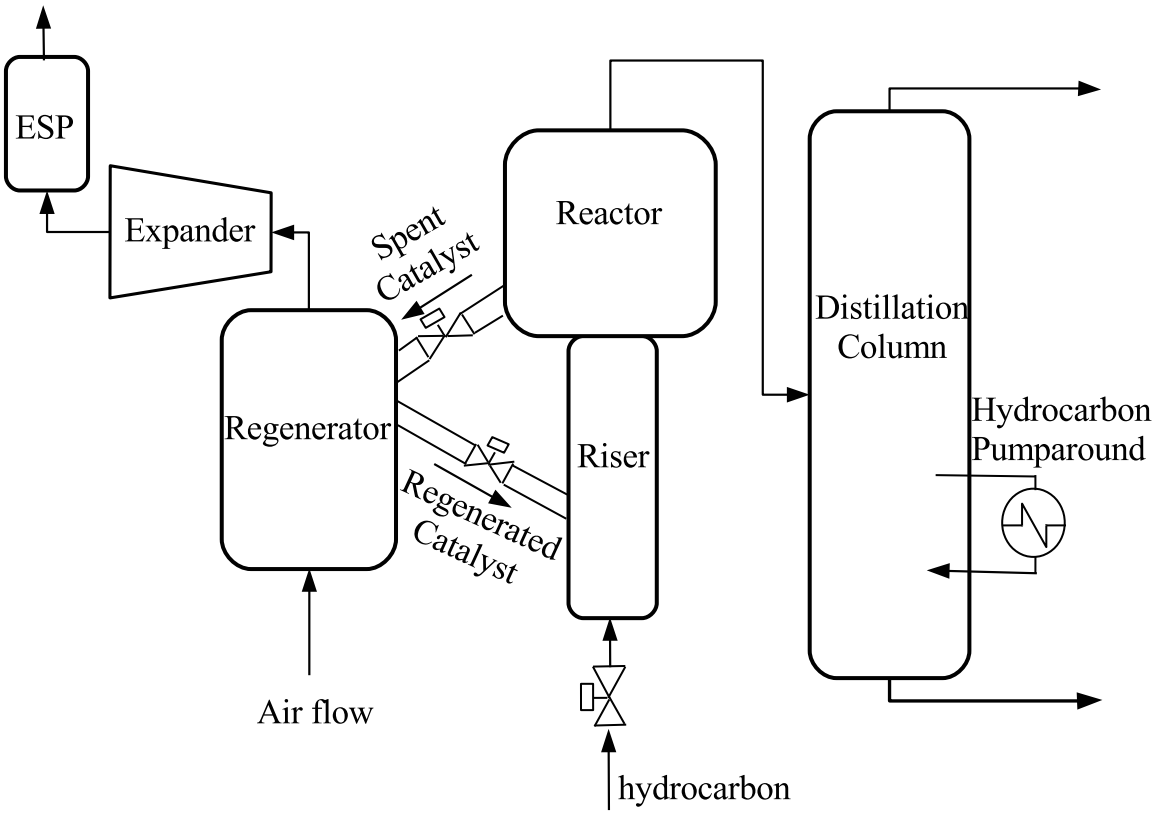

Figure 7.1: A schematic diagram of main units in FCC process under normal operation condition.

(ESP). A schematic of the FCC process network is shown in Fig. 7.1. The FCC unit cracks heavy, high boiling-point hydrocarbon molecules into smaller molecules with lower boiling points. The cracking reactions take place in the riser and the reactor. The distillation column is used to separate the hydrocarbon mixture from the reactor. The spent catalyst is regenerated in the regenerator by combustion with air. After that, the expansion of flue gas through an expander provides power to drive the air compressors. Finally, an ESP system is used to remove catalyst particles from the regenerator combustion gas to meet environmental regulations before it is discharged into the atmosphere.

In the riser, heavy hydrocarbons are mixed with hot catalyst and are cracked into smaller molecular weight components. The cracked hydrocarbon vapor then flows to the distillation column for separation. During the cracking process, coke deposits onto the catalyst, deactivating

the catalyst. Under normal operation, the catalyst circulates between the reactor and the regenerator, in which used catalyst moves from the reactor to the regenerator through the spent catalyst slide valve, while regenerated catalyst moves from the regenerator to the riser by the regenerated catalyst slide valve.

Leaving the top of the reactor, the superheated cracked hydrocarbon mixture enters the distillation column, with no additional heat added to the column under normal operation. Several pumparounds are used to remove heat from the column to cool and condense the vapor for separation. In these pumparounds, heat exchangers transfer heat to other process streams (usually hydrocarbon streams) in the refinery by reducing the temperature of the streams, and then returning to the distillation column. The distillation column separates the hydrocarbon mixture into light hydrocarbons, heavy naphtha, light cycle oil, and slurry oil.

Inside the regenerator, the coke on the surface of the hot catalyst particles burns off in a combustion reaction through contact with air. The exhausted gas leaves the top of the regenerator, containing combustion product gases with catalyst particles. Then, the flue gas flows through the gas/catalyst separator, expander, carbon monoxide boiler, and finally, the gas is routed to ESP. The expander uses expansion of gas to power other units in the process. The ESP collects most of the remaining small catalyst particles from the flue gas to meet California emissions regulations by using charged plates to attract the fine catalyst particles. This operation generates sparks, potentially leading to flame ignition inside of the ESP.

7.2.2 Accident Description

Among the many issues involved during the 2015 accident, the key events that lead to the accident are described below, followed by the main conclusions of the accident investigation and the proposed solutions to avoid this incident in the future [43]. Before the explosion, the following sequential events occurred at the Torrance Refinery: 1) The flue gas that flowed through the expander contained a small amount of catalyst particles that built up on the blades and caused vibrations in the expander. Several efforts were carried out to reduce the vibrations in the expander,

ending up without significant improvement. 2) On February 16, 2015, the vibrations reached the high limit and the control system steered the plant to a "Safe Park" mode. 3) During the Safe Park mode, the following actions were taken: the spent catalyst valve and regenerated catalyst valve were closed to prevent gas flowing from the reactor to the regenerator; the hydrocarbon feed stopped; the expander was shut down; and steam was injected to the FCC to replace hydrocarbon. 4) However, the following failures occurred: the ESP remained energized to provide potential ignition; the spent catalyst valve failed to seal and maintain the desired level of catalyst, due to an eroded valve over the years; and a leaking heat exchanger in the pumparound allowed light hydrocarbons to enter the distillation column with a higher pressure. 5) Because there was steam leaking from the expander outlet flange when the workers were trying to repair the expander, the supervisor agreed to reduce the steam flow from $20,000$ pounds per hour to $7,500$ pounds per hour, which is still higher than the minimum flow rate of $2,000$ pounds per hour reported on the safety instructions. 6) The reactor pressure was too low to prevent hydrocarbons from backflowing from the distillation column into the reactor. Around one hour later, alarms indicated that hydrocarbon was leaking and the flammable mixture ignited inside of the ESP, causing an explosion.

As shown in Fig. 7.2, the involved units in the refinery are the fluid catalytic cracking unit, the distillation column and the electrostatic precipitator. Based on the CSB final report for the distillation column, the engineers used two safeguards to prevent the backflow from the column to the FCC. The first safeguard was to maintain a positive pressure difference between the reactor and the distillation column. The second safeguard was to maintain a physical barrier between the reactor and regenerator by closing the spent catalyst valve and accumulating catalyst above the valve. Moreover, in order to monitor the above two safeguards, the engineers used indirect variables as indicators. For the first safeguard, the spent catalyst slide valve position was used to indicate that the catalyst accumulates above the valve and forms a barrier between regenerator and reactor; however, it was pointed out in the report that using a direct indicator is more effective as, for example, the catalyst level. The second indirect variable used by the engineers to check the pressure difference between the reactor and the distillation column was the steam flow rate,

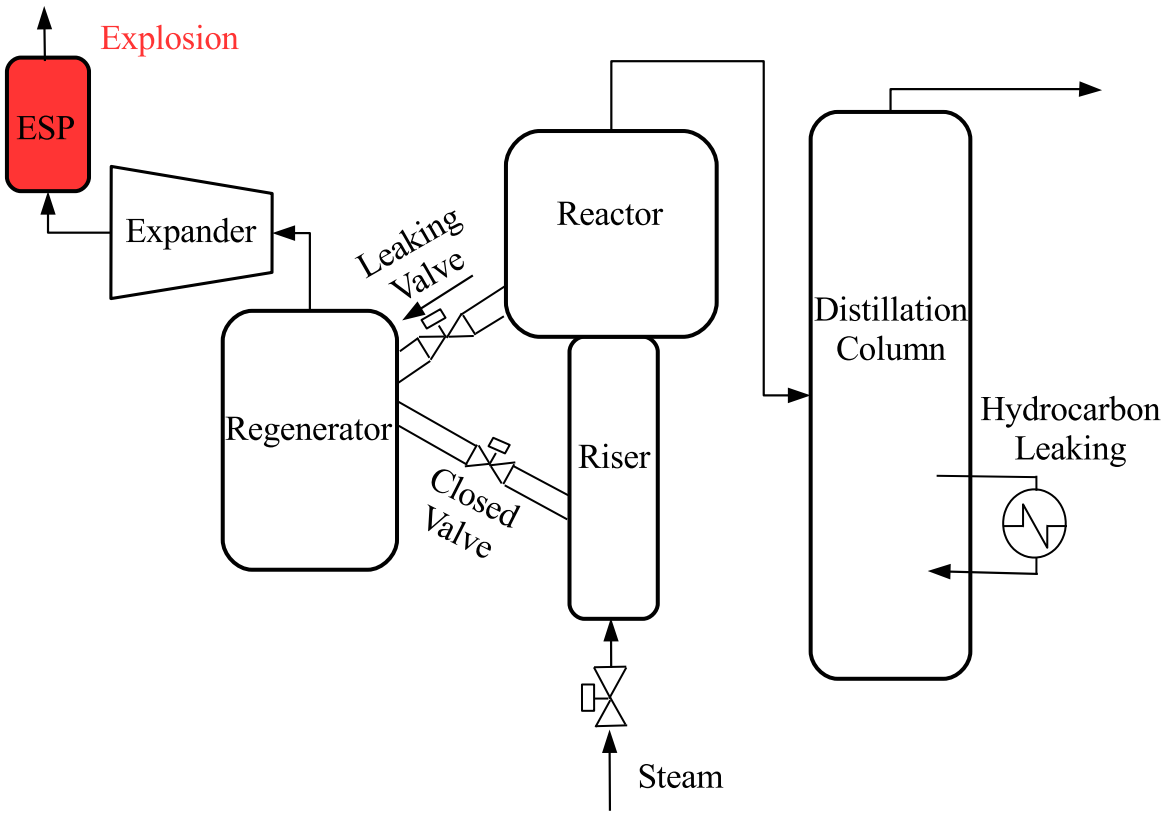

Figure 7.2: A schematic diagram of disturbances (valve leaking and hydrocarbon leaking) leading to the accident under Safe Park mode.

which was set to 2,000 pounds per hour as the minimum flow rate of the steam feed to the reactor. Similarly, it was noted by the CSB report that using a differential pressure measurement is prudent for monitoring directly this key safeguard.

One solution is to specify operation limits for all possible operation modes. By the time of the accident, engineers implemented a two-way mode that will permit to drive the process from normal operation to Safe Park mode, and vice versa. However, the implemented two-way mode did not define specific operation limits needed for maintaining the FCC safe when operating in Safe Park mode. Moreover, the CSB report went further in its suggestion to indicate the need of implementing a closed-loop (feedback controlled) operation when the process is in Safe Park mode using the direct measurement variables for the safeguards as discussed before. It is mentioned in the report that the engineers could have implemented a process control system that automatically adjusts the steam flow rate in the reactor to maintain the target reactor/distillation column differential pressure in the Safe Park mode. Process operation limits could also be involved in the controller configuration to avoid the accident.

7.2.3 Aspen Dynamic Model

In order to accurately simulate the process dynamics and interaction among the FCC units, Aspen Plus and Aspen Plus Dynamics V10.0 (Aspen Technology, Inc.) are used to perform high-fidelity dynamic simulation of the FCC process. Aspen Plus is a commercial software that calculates the steady-state of the process given a process design and an appropriate selection of thermodynamic models, based on the mass and energy balances of the process using a sequential modular approach. Aspen Plus Dynamics is another software that can run dynamic simulations based on steady-state model data and additional detailed parameters. Further details about Aspen software can be found in [5, 19].

In our simulation, the components are water and pentane. Water is the component in the vapor steam, and pentane is a typically involved hydrocarbon in the FCC unit. As shown in Fig. 7.3, the Aspen model includes a riser, reactor, regenerator, distillation column and five valves. The reactor

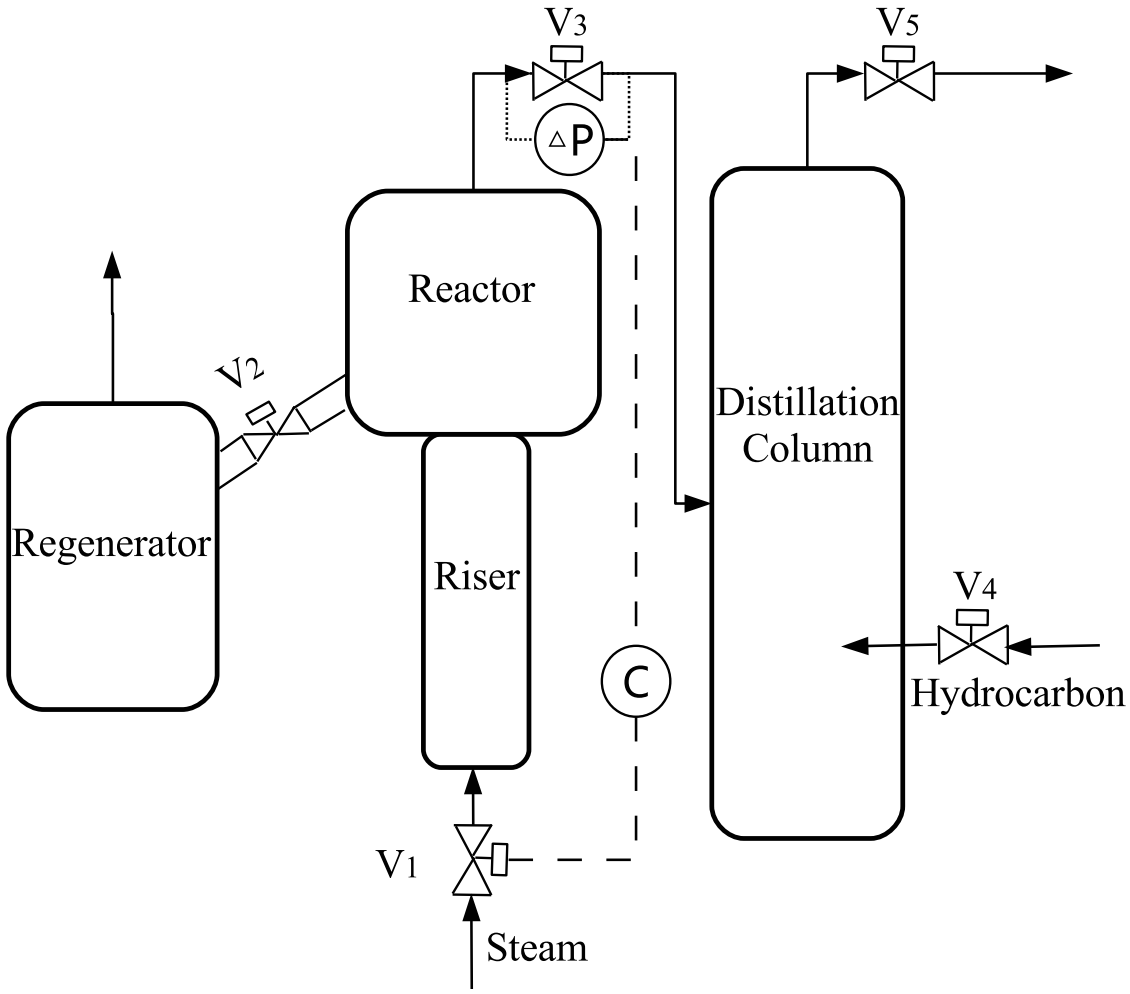

Figure 7.3: A schematic diagram of simulated units and control structure in the Aspen simulation.

riser is a tube reactor with 1 m diameter and 30 m height. The reactor is a homogeneous one with 3 m diameter and 30 m height. The distillation column in our simulation is a homogeneous reactor with 4 m diameter and 50 m height. The regenerator is a homogeneous reactor with 6 m diameter and 40 m height.

The following general forums of the mass balance, energy balance and momentum balance equations in Aspen Plus Dynamics are used to dynamically simulate the above process (without reaction in the Safe Park mode):

$$\frac{\partial}{\partial t}(\rho \omega_i) = -(\bigtriangledown \cdot n_i) \tag{7.1}$$

$$\frac{\partial}{\partial t}(\rho v) = -[\bigtriangledown \cdot \Phi] \tag{7.2}$$

$$\frac{\partial}{\partial t}\rho(\hat{U} + \frac{1}{2}v^2) = -(\bigtriangledown \cdot e) \tag{7.3}$$

where ρ is the total density, ω_i is the mass fraction of component i, n_i is the mass flux of component i, v is the velocity, Φ is the combined momentum-flux tensor, $\hat{U}$ is the internal energy per unit mass, $\frac{1}{2}v^2$ is the kinetic energy per unit mass, and e is the total energy flux. In addition to equations reflecting the mass, energy and momentum conservation laws, dynamic models also include system-dependent constitutive equations, which define the relationships between intensive variables such as thermal dynamic equation of state.

Additionally, the simulation involves 5 valves as shown in Fig. 7.3. Steam valve V_1 is the valve before the reactor riser, which is used to adjust the steam flow rate. The incoming steam to valve V_1 has a pressure of 150 $psig$ and a temperature of 300 $^{\circ}C$. Valve V_2 is the spent catalyst valve. Under Safe Park mode, valve V_2 should be able to close fully; however, it fails to seal during the accident. Valve V_3 is the valve between the reactor and the distillation column. The pressure drop of valve V_3 indicates the pressure barrier for the accident since hydrocarbon is less likely to backflow into the reactor under high positive pressure drop. The pressure drop value is usually small since this pressure drop is wasted during normal operation. Valve V_4 connects hydrocarbon and the distillation column. Valve V_4 keeps closed under normal condition and opens to simulate hydrocarbon leaking in the pumparound in the distillation column. Valve V_5 is the top valve of the

distillation column, which only closes when there is a block on top of the distillation column. The size of all valves are carefully characterized such that the pressure in the reactor and the distillation column is consistent with the data in the CSB report under different conditions [43].

Flow rate through a valve is calculated by the following equation:

$$F^2 M = \frac{1}{2}(\frac{Pos}{100} C_0^{max})^2 \rho \Delta P \tag{7.4}$$

where F is molar flow rate in $kmol/hr$, M is molecular weight in $kg/kmol$, Pos is valve position in $\%$, C_0^{max} is maximum flow coefficient in $m^{1.5} kg^{0.5} hr^{-1} bar^{-0.5}$, ρ is molar density in $kmol/m^3$, and ΔP is the pressure drop across the valve in bar.

7.2.4 Disturbances Leading to Accident

In the accident, the spent catalyst slide valve was leaking so that there was no catalyst barrier between the reactor and the regenerator. According to the final CSB report, it took about 10 minutes for the catalyst to leak in the spent catalyst valve. At the same time, it was reported that there was hydrocarbon leaking in distillation column which provides dangerous flammable hydrocarbon into the process. In order to investigate more severe unsafe scenarios in the process, the top valve in the distillation column could be used for creating another potential danger. A high pressure in distillation column can be created by a blocked top valve, which potentially causes back flow of hydrocarbon from the distillation column to the reactor.

In our simulation, there is a valve V_2 between the reactor and the regenerator, which opens from 0 % to 100 % in 200 s to simulate the spent catalyst valve leaking. If the spend catalyst valve leaks faster, then the valve V_2 opens faster and creates a more dangerous situation. It is noted that although 200 s is faster than the actual time (8 min) in the accident, it can be regarded as a reasonable disturbance. To simulate hydrocarbon leaking in the distillation column, a hydrocarbon flow is connected to the distillation column with valve V_4, which opens from 0 % to 100 % in 5 s. Another disturbance in the simulation is located in the distillation column top valve V_5, which

closes from 100 % to 50 % in 5 s in order to simulate the situation in which this top valve is blocked. If the distillation column top is blocked faster, then the valve V_5 closes also faster and requires the steam flow to increase more rapidly to maintain the desired pressure drop.

7.3 Model Predictive Controller Design

Due to the fact that the FCC is highly interconnected with other units in the refinery and dealing with dangerous operating conditions (e.g., high temperature conditions in a range between $750 - 800\ K$) and explosive substances (e.g., gasoline and naphtha), it is challenging for engineers to predict the malfunction of the plant using information from safety procedures in manuals. When the accident occurred, hydrocarbon flows back from the distillation column into the reactor, which indicates that the pressure drop of valve V_3 is negative. In order to increase the pressure drop and rebuild the pressure barrier, the steam flow rate needs to be increased, or the steam valve V_1 needs to open more. Since implementing operation limits in open-loop cannot handle disturbances that are not known a priori, a feedback controller is needed to determine the sufficient valve opening in the actuator based on feedback measurements to ensure operational safety. Therefore, to avoid the above accident and other unsafe operations, a model predictive controller is developed for the FCC process. The controlled variable is the pressure drop of valve V_3 and the manipulated variable is the steam valve V_1 position, which adjusts the steam flow rate. It needs to be mentioned that the pressure drop of V_3 can indicate the pressure barrier and the occurrence of hydrocarbon back flow, and thus, it is used as a measured state. The steam flow rate is the main operating variable during the accident, and thus, the steam valve is chosen as manipulated in this chapter. The described control loop in the FCC process is demonstrated in Fig. 7.3. It is noted that a PI controller could be used in this situation but it does not account for constraints or optimality. In our work, there is a constraint on the valve opening that is handled by MPC. Additionally, the pressure drop needs to be kept positive with an optimal performance, and thus, a model predictive controller is used. Additionally, since the process model in MPC is identified from the nominal process, in order to

achieve an offset-free performance, an augmented (additional) state is used in MPC to eliminate any potential offset.

7.3.1 Data-driven Process Model

The fluid catalytic cracking process is initially simulated at its steady-state with steam valve position $Pos_{ss} = 14.9602$ %. The pressure drop between the reactor and the distillation column at steady-state is $\Delta P_{ss} = 0.3$ *psi*. The state and the input of the process are represented in deviation variable form as $x = \Delta P - \Delta P_{ss}$ and $u = Pos - Pos_{ss}$, such that the equilibrium point of the system is at the origin. It is demonstrated that the use of a linear model in MPC with offset-free technique works well in the current work. Therefore, a nonlinear model is not necessary to be used in the MPC since it requires more calculations to identify the nonlinear model and to solve the MPC optimization problem in real-time. The following linear state-space model is used to describe the relationship between pressure drop and valve position:

$$\dot{x} = Ax + Bu \tag{7.5}$$

where x is the state variable, u is the manipulated input variable, and the parameters A and B are identified using Aspen simulation data. Specifically, data on pressure drop ΔP are generated from the nominal open-loop simulations with pseudorandom binary sequence (PRBS) signal in valve position *Pos*. Then, the Multivariable Output Error State Space (MOSEP) algorithm is applied in Matlab to identify the parameters A and B as follows:

$$A = -0.304; \quad B = 0.0102;$$

In order to handle plant-model mismatch in MPC, an additional state θ is incorporated into the model of Eq. 7.5. The additional state θ is assumed to be constant and the model is augmented as

shown in Eq. 7.6 below:

$$\begin{aligned} \dot{x} &= Ax + Bu + G_\theta \theta \\ \dot{\theta} &= 0 \end{aligned} \tag{7.6}$$

In the presence of the augmented state θ, an observer is designed to estimate the full state as follows:

$$\begin{aligned} \dot{\hat{x}} &= A\hat{x} + Bu + G_\theta \hat{\theta} + L_x(x - \hat{x}) \\ \dot{\hat{\theta}} &= L_\theta(x - \hat{x}) \end{aligned} \tag{7.7}$$

where $\hat{x}$ and $\hat{\theta}$ are the variables of the state observer and x is the actual state measurement. To apply the continuous observer in a sample-and-hold fashion, the estimated state $\tilde{x}(t_k)$ and $\tilde{\theta}(t_k)$ at sampling time t_k is calculated numerically from the last estimated state $\tilde{x}(t_{k-1})$ and $\tilde{\theta}(t_{k-1})$ using the Eq. 7.7, integrated with the explicit Euler method. The initial estimated states are set to be zero $\tilde{x}(0) = 0$ and $\tilde{\theta}(0) = 0$.

L_x and L_θ are the observer gain parameters. Observer error $e = \begin{bmatrix} x - \hat{x} \\ \theta - \hat{\theta} \end{bmatrix}$ and $\dot{e} = \begin{bmatrix} \dot{x} - \dot{\hat{x}} \\ \dot{\theta} - \dot{\hat{\theta}} \end{bmatrix} = \begin{bmatrix} A(x - \hat{x}) + G_\theta(\theta - \hat{\theta}) - L_x(x - \hat{x}) \\ -L_\theta(x - \hat{x}) \end{bmatrix} = \begin{bmatrix} A - L_x & G_\theta \\ -L_\theta & 0 \end{bmatrix} \begin{bmatrix} x - \hat{x} \\ \theta - \hat{\theta} \end{bmatrix}$. To ensure that the observer error $e(t) \to 0$ as $t \to \infty$, parameters L_x, L_θ and G_θ are chosen such that matrix $\begin{bmatrix} A - L_x & G_\theta \\ -L_\theta & 0 \end{bmatrix}$ is Hurwitz. In our simulation, the parameters are chosen to be:

$$L_x = -0.3; \quad L_\theta = 0.8; \quad G_\theta = 0.02$$

7.3.2 Offset-free MPC Design

The augmented state estimates from Eq. 7.7 are used to initialize the following offset-free MPC optimization problem:

$$\min_{u \in S(\Delta)} \quad \int_{t_k}^{t_{k+N}} (\|\tilde{x}(\tau)\|_{Q_c}^2)\, d\tau \tag{7.8a}$$

$$\text{s.t.} \quad \dot{\tilde{x}} = A\tilde{x} + Bu + G_\theta \tilde{\theta}; \quad \dot{\tilde{\theta}} = 0 \tag{7.8b}$$

$$\tilde{x}(t_k) = \hat{x}(t_k); \quad \tilde{\theta}(t_k) = \hat{\theta}(t_k) \tag{7.8c}$$

$$u(t) \in U, \ \forall\, t \in [t_k, t_{k+N}) \tag{7.8d}$$

The objective function of Eq. 7.8a requires minimizing $\int_{t_k}^{t_{k+N}} (\|\tilde{x}(\tau)\|_{Q_c}^2)\, d\tau$ so that the predicted state $\tilde{x}$ can be driven to the set-point (i.e., $x = 0$). The key reason for not minimizing u in the cost function is that $u = 0$ is no longer the steady-state corresponding to $x = 0$ in the presence of unknown disturbance and it is impossible to calculate the new steady-state u. Besides, it allows the controller to respond faster if the manipulated input is not penalized in the cost function. The constraint of Eq. 7.8b is the full-state linear model of Eq. 7.6 that is used to predict future states in the objective function. Eq. 7.8c defines the initial condition $\tilde{x}(t_k)$ and $\tilde{\theta}(t_k)$ of the optimization problem as the state observer value $\hat{x}(t_k)$ and $\hat{\theta}(t_k)$ at $t = t_k$, which are calculated by Eq. 7.7 with explicit Euler method using the measured state x and previously estimated states $\tilde{x}(t_{k-1})$ and $\tilde{\theta}(t_{k-1})$. Eq. 7.8d is the input constraint applied over the entire prediction horizon. The manipulated input is the valve position *Pos*, which is bounded by: $0\ \% \leq Pos \leq 100\ \%$, namely $U = [-14.96,\ 85.04]$.

The explicit Euler method with an integration time step of $h_c = 10^{-3}\ s$ is applied to numerically integrate the dynamic model of Eq. 7.6 in MPC optimization problem. The nonlinear optimization problem of MPC of Eq. 7.8 is solved using the solver FilterSD on OPTI Toolbox in Matlab with the following parameters: sampling period $\Delta = 5\ s$; and prediction horizon $N = 20$.

7.4 Closed-loop Simulation Results and Discussion

7.4.1 Simulation with Two Disturbances

In order to simulate the accident conditions, the following disturbances are introduced: 1) spent catalyst valve V_2 opens from 0 % to 100 % from $t = 10\ s$ to $t = 210\ s$; 2) valve V_4 opens from 0 % to 100 % from $t = 10\ s$ to $t = 15\ s$. Fig. 7.4 shows the open-loop simulation. After introducing disturbances, the pressure drop decreases from 0.3 *psi* to -0.04 *psi*. A negative pressure drop means that hydrocarbon flows from the distillation column to the reactor (i.e., backflow). Then, if the spent catalyst valve fails, hydrocarbon can flow into the regenerator and potentially causes damage in downstream units. In our simulation, when the spent catalyst fails, the obtained mole fraction of pentane in the regenerator outlet flow reaches 0.15, which is much higher than the explosion limit of pentane $(0.015 - 0.078)$. Since other components in naphtha have similar explosion limit, mole fraction of 0.15 can cause an explosion in the ESP. In order to avoid this dangerous operation condition, the designed controller is applied to this situation.

The designed controller is applied to the process and the closed-loop simulation results are shown in Fig. 7.5. The pressure drop initially decreases as a result of the disturbance. Then, the steam valve starts to open to allow more steam flow to ensure safety of the process. At each sampling time t_k, the observer estimates the states $\tilde{x}(t_k)$ and $\tilde{\theta}(t_k)$ by Eq. 7.7 using the measured state x and previously estimated states $\tilde{x}(t_{k-1})$ and $\tilde{\theta}(t_{k-1})$. Since the disturbances decrease the pressure drop, the measured state x is less than the estimated $\hat{x}$. Then, a negative value $\hat{\theta}$ is calculated from Eq. 7.7 and is used in the model (Eq. 7.8b) for prediction in the MPC. A negative θ on the right hand side of Eq. 7.8b requires a further positive input u to bring the state $\tilde{x}$ back to the steady-state, which opens the steam valve position to feed more steam into the process. The augmented state θ keeps changing until there is no difference between x and $\hat{x}$, and as a result, the MPC drives the state x back to the steady-state without offset. The use of θ makes the controller to request further opening of the steam valve in the unsafe scenario until the pressure drop comes back to its steady-state value. Therefore, as shown in Fig. 7.5, the valve keeps opening and the pressure

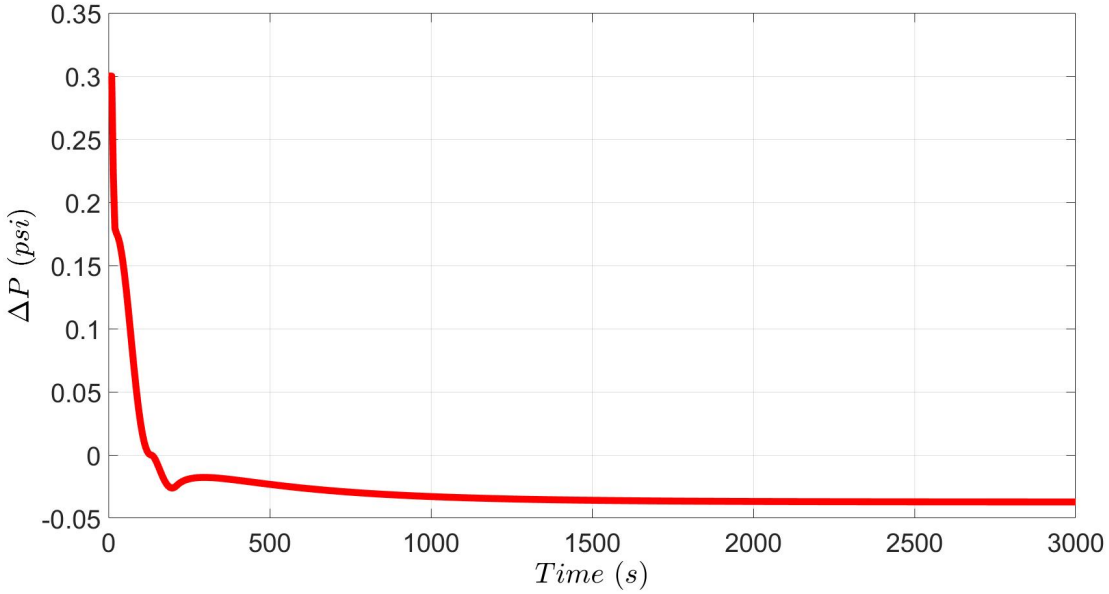

(a) Pressure drop between reactor and distillation column

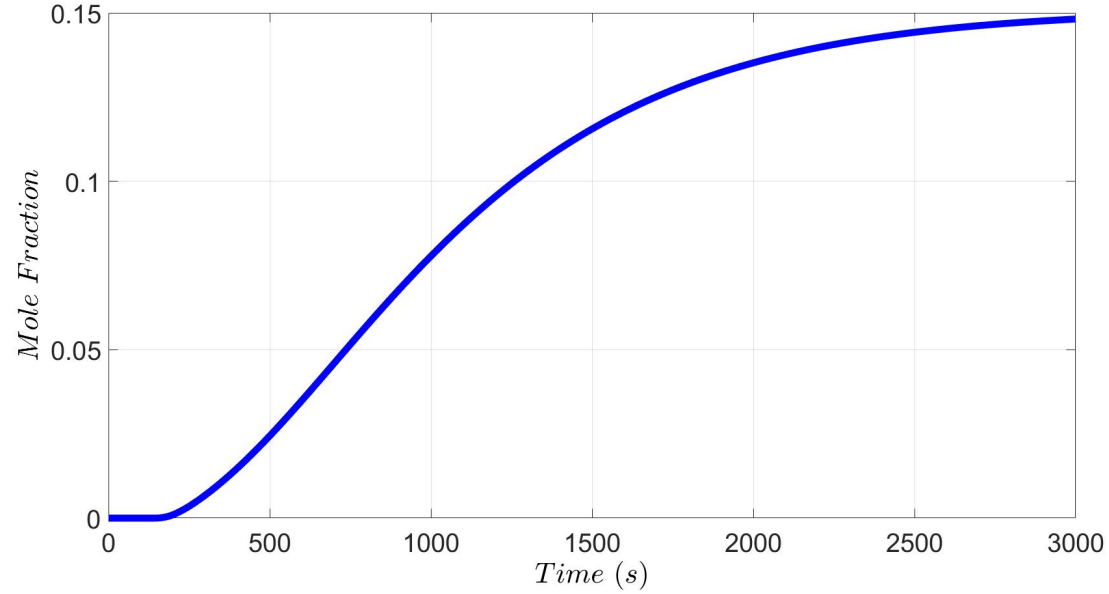

(b) Hydrocarbon mole fraction in the regenerator

Figure 7.4: Open-loop simulation results under two disturbances.

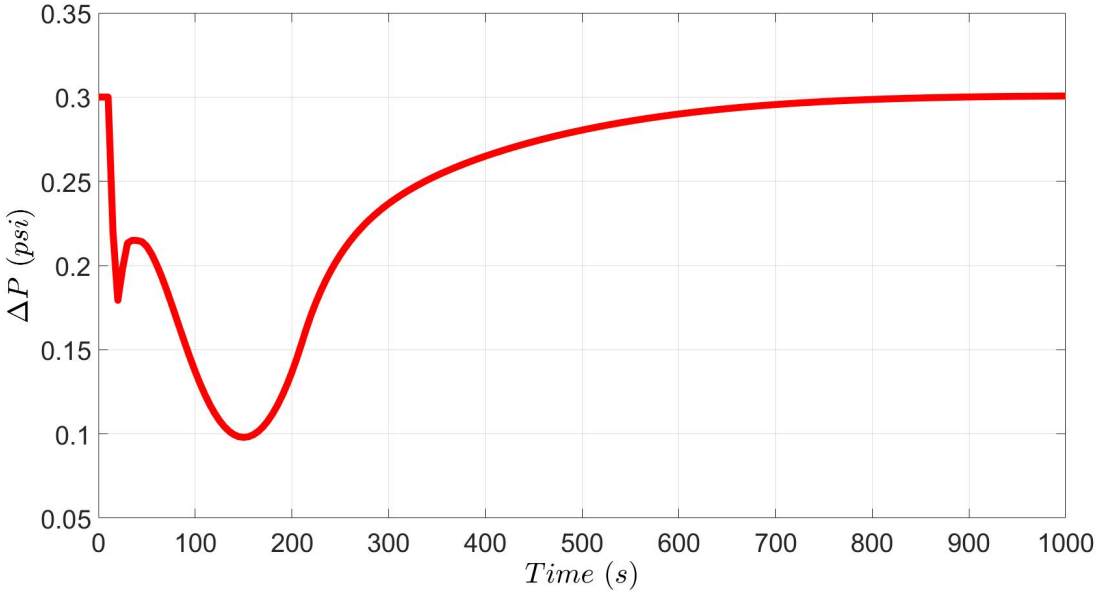

(a) Pressure drop between reactor and distillation column.

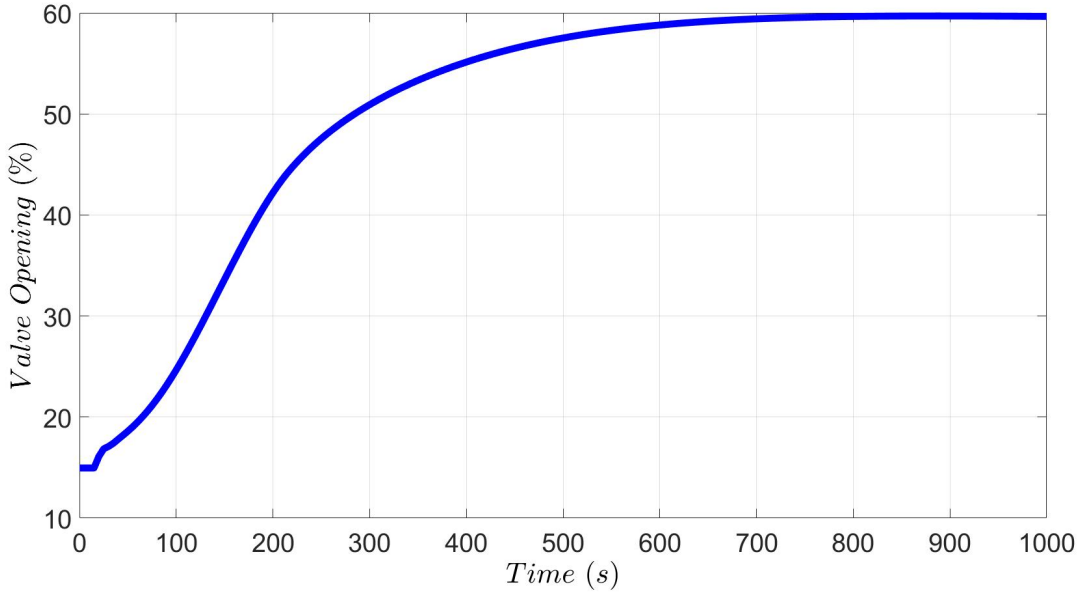

(b) Steam valve position

Figure 7.5: Closed-loop simulation results under two disturbances.

drop stops decreasing at around 150 s and goes back to 0.3 psi at the end of the simulation without offset. The pressure drop curve in Fig. 7.5a is not smooth because the introduced disturbance changes abruptly.

Additionally, it is important to note that there is not backflow under the implemented disturbances and the proposed safety-aware control system. As a matter of fact, the pressure drop has never been negative during the entire simulation, and therefore, there is no hydrocarbon flow from the distillation column to the regenerator after introducing the disturbance. The proposed controller can then be applied to the FCC process in order to operate the units safely in Safe Park mode, as suggested in the accident report in Torrence, California [43].

7.4.2 Simulation with Three Disturbances

In order to demonstrate that the designed controller can be applied in various unsafe conditions, additional disturbances are introduced as follows: 1) spent catalyst valve V_2 opens from 0 % to 100 % from $t = 10$ s to $t = 210$ s; 2) valve V_4 opens from 0 % to 100 % from $t = 10$ s to $t = 15$ s; 3) the distillation column top valve V_5 closes from 100 % to 50 % from $t = 10$ s to $t = 15$ s. Fig. 7.6 shows the open-loop simulation for these disturbances. After introducing these three disturbances, the pressure drop decreases from 0.3 psi to -0.11 psi, which is more negative than the two disturbances case. A negative pressure drop indicates that hydrocarbon flows from the distillation column to the reactor and regenerator, and potentially causes damage in the downstream units as well. In this simulation, the mole fraction of pentane in the regenerator outlet flow reaches about 0.255 in the regenerator, which is much higher than the explosion limit and can cause a potential explosion in the ESP. The proposed controller is then applied to this situation to evaluate how the controller can deal with operational safety issues under these three disturbances.

The designed controller is applied to the process and the closed-loop simulation results are shown in Fig. 7.7. The pressure drop decreases at the beginning as a response to the disturbances. Then, the controller calculates an increasing input to open the steam valve. Therefore, the pressure drop starts to increase after reaching the minimum value of 0.05 psi, and finally, goes back to

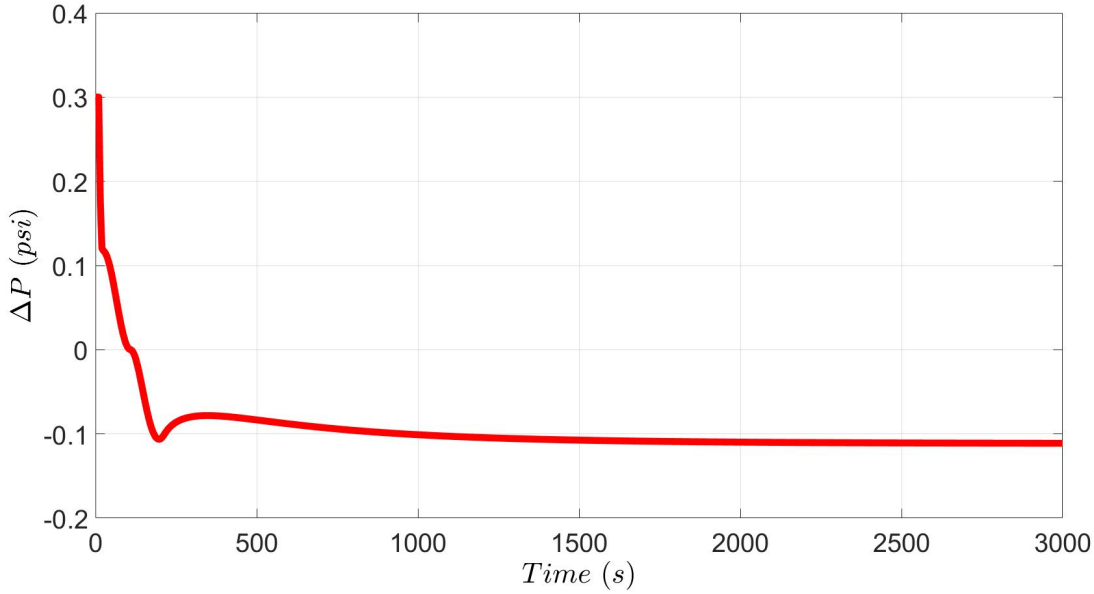

(a) Pressure drop between reactor and distillation column.

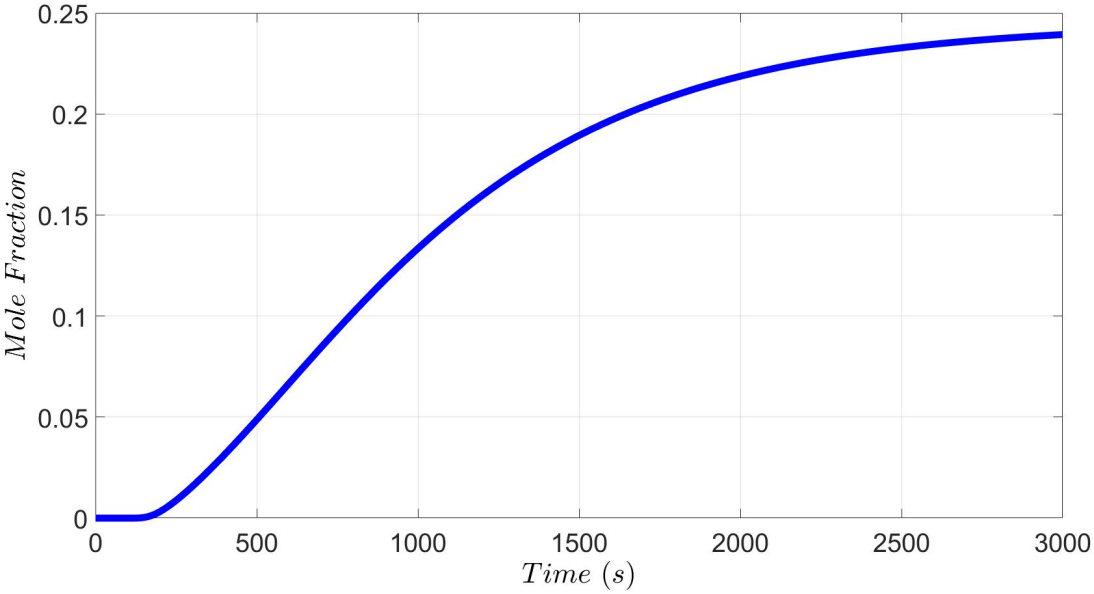

(b) Hydrocarbon mole fraction in the regenerator

Figure 7.6: Open-loop simulation results under three disturbances.

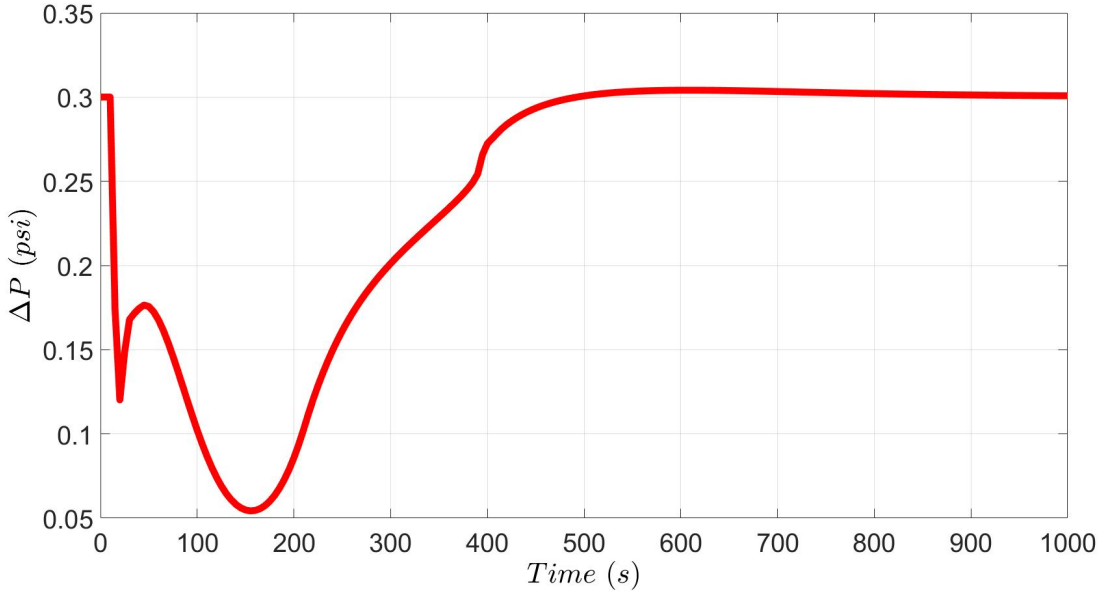

(a) Pressure drop between reactor and distillation column.

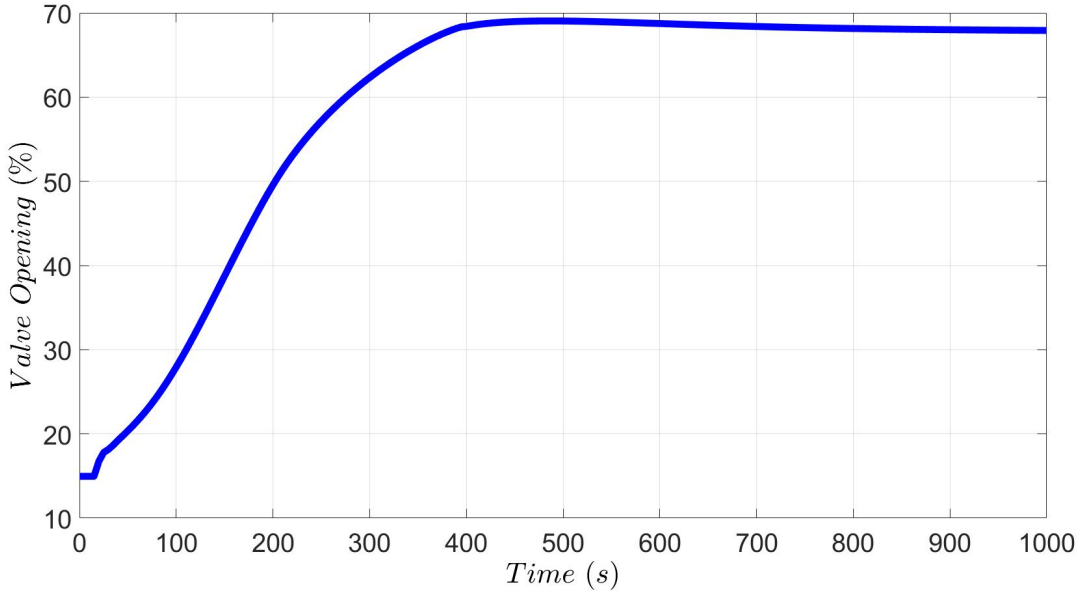

(b) Steam valve position

Figure 7.7: Closed-loop simulation results under three disturbances.

0.3 *psi* without offset. Since there are more disturbances in this situation, the steam valve opens to a larger position 68 % compared to 60 % in the two disturbance case. Again, the pressure drop has never been negative during the simulation, which implies there is no hydrocarbon backflow after introducing the disturbances. This simulation demonstrates that the proposed controller can be applied to the FCC process in the presence of unexpected additional disturbances.

7.5 Conclusion

In this chapter, we demonstrated that process operational safety was improved with an offset-free model predictive controller to avoid a fluid catalytic cracking process accident, which occurred in the refinery operated by ExxonMobil in 2015 in Torrance, California. A dynamic simulation was developed in Aspen Plus Dynamics to emulate the essential units of the fluid catalytic cracking process. Disturbances were introduced to the process to simulate the accident conditions taken from the final report of the CSB and other dangerous situations with unexpected disturbances. An MPC with augmented state to obtain offset-free performance was designed to improve the process operational safety in order to avoid the accident and other potential dangerous scenarios. Closed-loop simulations demonstrated that the accident could have been avoided with the proposed controller under the reported accident condition and other potential dangerous situations.

Chapter 8

Real-Time Optimization and Control of Nonlinear Processes Using Machine Learning

8.1 Introduction

In the last few decades, chemical processes have been studied and represented with different models for real-time optimization (RTO) and model predictive control (MPC) in order to improve the process steady-state and dynamic performance. The available models range from linear to nonlinear and from first-principles models to neural network models, among others [24]. For many applications, first-principles models are the preferable choice, especially when applied with process systems methodologies [124]. However, first-principles models are difficult to maintain due to the variation of some parameters. Furthermore, it could be difficult or impractical to obtain first-principles models for large-scale applications [131]. As a well-tested alternative, machine learning method, especially neural network models are able to represent complicated nonlinear systems [172, 173]. Neural networks fit the data in an input-output fashion using fully-connected layers within the hidden output layers [91]. However, due to their general structures, neural

networks lack physical knowledge in their formulation. To alleviate the above problem, this work integrates neural network models with first-principles models. Specifically, first-principles models are used to represent the well-known part of the process and embedding physical knowledge in the formulation, while the complex nonlinear part of the process is represented with neural networks. This proposed hybrid formulation is then applied in the context of real-time optimization and model predictive control in two chemical processes.

The machine learning method has been part of process system engineering for at least 30 years in which the feed-forward neural network is the most classical structure found in the literature [157]. For instance, neural networks have been proposed as an alternative to first-principles models for the classical problems of process engineering [157], such as modeling, fault diagnosis, product design, state estimation, and process control. The neural network model has also gained much interest in the chemical engineering field, and more comprehensive reviews with detailed information on neural networks in chemical processes are available in [74, 157]. For example, an artificial neural networks was applied to approximate pressure-volume-temperature data in refrigerant fluids [36]. Complex reaction kinetic data have been fitted using a large experimental dataset with neural networks to approximate the reaction rate and compared with standard kinetics methods, showing that neural networks can represent kinetic data at a faster pace [59]. Reliable predictions of the vapor-liquid equilibrium has been developed by means of neural networks in binary ethanol mixtures [54]. Studies on mass transfer have shown good agreements between neural network predictions and experimental data in the absorption performance of packed columns [57].

Since the applications with standard neural networks rely on fully-connected networks, the physical interpretation of the obtained model can be a difficult task. One solution is to integrate physical knowledge into the neural network model. For example, the work in [22] proposed a learning technique in which the neural network can be physically interpretable depending on the specifications. Similarly, the work in [96] designed a neural network with physical-based knowledge using hidden layers as intermediate outputs and prioritized the connection between

inputs and hidden layers based on the effect of each input with the corresponding intermediate variables. Another method to add more physical knowledge into neural networks is to combine first-principles models with neural networks as hybrid modeling [129]. For instance, biochemical processes have been represented with mass balances for modeling the bioreactor system and with artificial neural networks for representing the cell population system [122]. Similarly, an experimental study for a bio-process showed the benefits of the hybrid approach in which the kinetic models of the reaction rates were identified with neural networks [35]. In crystallization, growth rate, nucleation kinetics, and agglomeration phenomena have been represented by neural networks, while mass, energy, and population balances have been used as a complement to the system's behavior [61]. In industry, hybrid modeling using rigorous models and neural networks has also been tested in product development and process design [143]. However, most of the applications with hybrid modeling are limited to the open-loop case.

Real-time optimization (RTO) and model predictive control (MPC) are vital tools for chemical process performance in industry in which the process model plays a key role in their formulations [30, 130]. RTO and MPC have been primarily implemented based on first-principles models, while the difference is that RTO is based on steady-steady models and MPC is based on dynamical models [30, 130]. In both RTO and MPC, the performance depends highly on the accuracy of the process model. To obtain a more accurate model, machine learning methods have been employed within MPC [91] and within RTO [92], as well. In practice, it is common to use process measurements to construct neural network models for chemical processes. However, the obtained model from process operations may lack robustness and accuracy for parameter identification, as was shown in [1]. As a consequence, there has been significant effort to include hybrid models in process analysis, MPC, and process optimization (e.g., [32, 33, 87, 119, 144, 153, 164]) in order to reduce the dependency on data and infuse physical knowledge. At this stage, little attention has been paid to utilizing the full benefit of employing hybrid modeling in both the RTO and MPC layers.

Motivated by the above, this chapter demonstrates the implementation of a hybrid approach of

combining a first-principles model and a neural network model in the RTO and MPC optimization problems. Specifically, the nonlinear part of the first-principles model is replaced by a neural network model to represent the complex, nonlinear term in a nonlinear process. We note that in our previous works, we developed recurrent neural network models from process data for use in MPC without using any information from a first-principles model or process structure in the recurrent neural network model formulation [169, 172, 173]. Furthermore, the previous works did not consider the use of neural network models to describe nonlinearities in the RTO layer and focused exclusively on model predictive control. In the present work, we use neural networks to describe nonlinearities arising in chemical processes and embed these neural network models in first-principles process models used in both RTO (nonlinear steady-state process model) and MPC (nonlinear dynamic process model), resulting in the use of hybrid model formulations in both layers. The rest of the chapter is organized as follows: in Section 8.2, the proposed method that combines neural network with the first-principles model is discussed. In Section 8.3, a continuous stirred tank reactor (CSTR) example is utilized to illustrate the combination of neural network models and first-principles models in RTO and Lyapunov-based MPC, where the reaction rate equation is represented by a neural network model. In Section 8.4, an industrial distillation column is co-simulated in Aspen Plus Dynamics and MATLAB. A first-principles steady-state model of the distillation column is first developed, and a neural network model is constructed for phase equilibrium properties. The combined model is then used in RTO to investigate the performance of the proposed methodology.

8.2 Neural Network Model and Application

8.2.1 Neural Network Model

The neural network model is a nonlinear function $y = f_{NN}(x)$ with input vector $x = [x_1, x_2, ..., x_n]$ and output vector $y = [y_1, y_2, ..., y_m]$. Mathematically, a neural network function is defined as a series of functional transformations. The structure of a two-layer (one hidden-layer) feed-forward

neural network is shown in Fig. 8.1, where $h_1, h_2, ..., h_p$ are hidden neurons [25, 66]. Specifically, the hidden neurons h_j and the outputs y_k are obtained by Eq. 8.1:

$$h_j = \sigma_1(\sum_{i=1}^{n} w_{ji}^{(1)} x_i + w_{j0}^{(1)}), \quad j = 1, 2, ..., p \tag{8.1a}$$

$$y_k = \sigma_2(\sum_{i=1}^{p} w_{ki}^{(2)} h_i + w_{k0}^{(2)}), \quad k = 1, 2, ..., m \tag{8.1b}$$

where parameters $w_{ji}^{(1)}$ and $w_{ki}^{(2)}$ are weights in the first and the second layer and parameters $w_{j0}^{(1)}$ and $w_{k0}^{(2)}$ are biases. σ_1 and σ_2 are nonlinear element-wise transformations $\sigma : R^1 \to R^1$, which are generally chosen to be sigmoid functions such as the logistic sigmoid $S(x) = 1/(1+e^{-x})$ or hyperbolic tangent function $tanh(x) = 2/(1+e^{-2x}) - 1$. Each hidden neuron h_j is calculated by an activation function σ_1 with a linear combination of input variables x_i. Each output variable y_k is also calculated by an activation function σ_2 with a linear combination of hidden neurons h_i. Since the neural network models in this work are developed to solve regression problems, no additional output unit activation functions are needed. All the neural network models in this work will follow the structure discussed in this section.

Given a set of input vectors $\{x^n\}$ together with a corresponding set of target output vectors $\{\hat{y}^n\}$ as a training set of N data points, the neural network model is trained by minimizing the following sum-of-squares error function [25]:

$$E(w) = \frac{1}{2} \sum_{n=1}^{N} \|y(x^n, w) - \hat{y}^n\|^2 \tag{8.2}$$

The proper weight vectors w are obtained by minimizing the above cost function via the gradient descent optimization method:

$$w^{\tau+1} = w^{\tau} - \eta \nabla E(w^{\tau}) \tag{8.3}$$

where τ labels the iteration, $\eta > 0$ is known as the learning rate, and $\nabla E(w^{\tau})$ is the derivative of

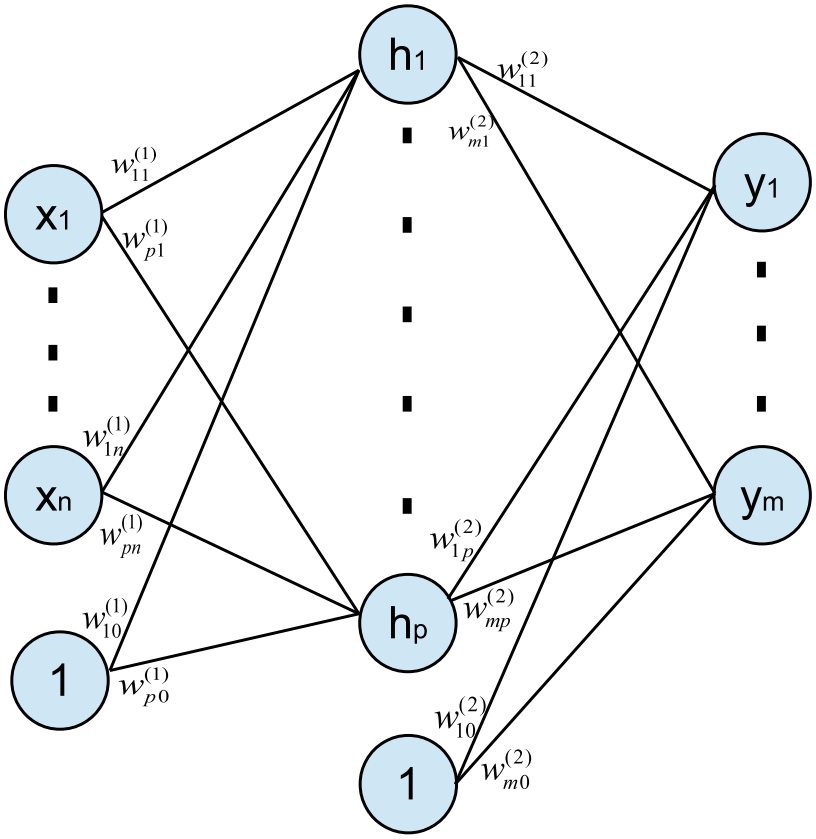

Figure 8.1: A feed-forward neural network with input $x_1, ..., x_n$, hidden neurons $h_1, h_2, ..., h_p$, and outputs $y_1, y_2, ..., y_m$. Each weight $w_{ji}^{(k)}$ is marked on the structure. Neuron "1" is used to represent the biases.

the cost function with respect to weight w. The weight vectors are optimized by moving through weight space in a succession of Eq. 8.3 with some initial value $w(0)$. The gradient of an error function $\nabla E(w)$ is evaluated by back propagation method. Additionally, data are first normalized, and then, k-fold cross-validation is used to separate the dataset into the training and validation set in order to avoid model overfitting.

8.2.2 Application of Neural Network Models in RTO and MPC

In the chemical engineering field, model fitting is a popular technique in both academia and industry. In most applications, a certain model formulation needs to be assumed first, and then, the model is fitted with experiment data. However, a good approximation is not guaranteed since the assumed model formulation may be developed based on deficient assumptions and uncertain mechanism, which lead to an inaccurate model. Alternatively, neural network model can be employed to model complex, nonlinear systems since neural networks do not require any a priori knowledge about the process and are able to fit any nonlinearity with a sufficient number of layers and neurons according to the universal approximation theorem [70]. The obtained neural network model can be used together with existing first-principles models. Specifically, the combination of the neural network model and first-principles model can be used in optimization problems, such as real-time optimization (RTO) and model predictive control (MPC).

8.2.2.1 RTO with the Neural Network Model

Real-time optimization (RTO) maximizes the economic productivity of the process subject to operational constraints via the continuous re-evaluation and alteration of operating conditions of a process [117]. The economically-optimal plant operating conditions are determined by RTO and sent to the controllers to operate the process at the optimal set-points [134].

Since RTO is an optimization problem, an explicit steady-state model is required in order to obtain optimal steady-states. First-principles models are commonly used in RTO; however, first-principles models may not represent the real process well due to model mismatch, and thus

lead to non-optimal steady-states or even infeasible steady-states. In these cases, the machine learning method becomes a good solution to improve model accuracy. Specifically, a neural network model can be used to replace the complicated nonlinear part of the steady-state model to increase the accuracy of the first-principles model.

In general, the RTO problem is formulated as the optimization problem of Eq. 8.4, where $x \in R^n$ is the state and $\hat{x} \in R^m$ is part of the state. $g(\hat{x})$ is a nonlinear function of $\hat{x}$, which is a part of the steady-state model.

$$\begin{aligned} \min_{x} \quad & cost\ function(x) \\ \text{s.t.} \quad & F(x, g(\hat{x})) = 0 \\ & other\ constraints \end{aligned} \tag{8.4}$$

Since it is difficult to obtain an accurate functional form of $g(\hat{x})$, a neural network $F_{NN}(\hat{x})$ is developed using simulation data to replace $g(\hat{x})$ in Eq. 8.4. Therefore, the RTO based on the integration of first-principles model and neural network model is developed as follows:

$$\begin{aligned} \min_{x} \quad & cost\ function(x) \\ \text{s.t.} \quad & F(x, F_{NN}(\hat{x})) = 0 \\ & other\ constraints \end{aligned} \tag{8.5}$$

8.2.2.2 MPC with Neural Network Models

Model predictive control (MPC) is an advanced control technique that uses a dynamic process model to predict future states over a finite-time horizon to calculate the optimal input trajectory. Since MPC is able to account for multi-variable interactions and process constraints, it has been widely used to control constrained multiple-input multiple-output nonlinear systems [50]. Since MPC is an optimization problem, an explicit dynamic model is required to predict future states and make optimal decisions. First-principles models can be developed and used as the prediction model in MPC; however, first-principles models suffer from model mismatch, which might lead to offsets and other issues. Therefore, machine learning methods can be used to reduce model

mismatch by replacing the complicated nonlinear part of the dynamic model with a neural network model.

In general, MPC can be formulated as the optimization problem of Eq. 8.6, where the notations follow those in Eq. 8.4 and $\dot{x} = F(x, g(\hat{x}))$ is the first-principles dynamic process model.

$$\begin{aligned} \min_{u} \quad & cost\ function(x,u) \\ \text{s.t.} \quad & \dot{x} = F(x, g(\hat{x}), u) \\ & other\ constraints \end{aligned} \tag{8.6}$$

Similar to Eq. 8.5, a neural network $F_{NN}(\hat{x})$ is developed using simulation data to replace $g(\hat{x})$ in Eq. 8.6. As a result, the MPC based on the integration of the first-principles model and neural network model is developed as follows:

$$\begin{aligned} \min_{u} \quad & cost\ function(x,u) \\ \text{s.t.} \quad & \dot{x} = F(x, F_{NN}(\hat{x}), u) \\ & other\ constraints \end{aligned} \tag{8.7}$$

Remark 8.1. *To derive stability properties for the closed-loop system under MPC, additional stabilizing constraints can be employed within the MPC of Eq. 8.7 (e.g., terminal constraints [136] and Lyapunov-based constraints [110]). In this work, a Lyapunov-based MPC (LMPC) is developed to achieve closed-loop stability in the sense that the close-loop state is bounded in a stability region for all times and is ultimately driven to the origin. The discussion and the proof of closed-loop stability under LMPC using machine learning-based models can be found in [169, 172].*

Remark 8.2. *All the optimization problems of MPC and RTO in this manuscript are solved using IPOPT, which is an interior point optimizer for large-scale nonlinear programs. The IPOPT solver was run on the OPTI Toolbox in MATLAB. It is noted that the global optimum of the nonlinear optimization problem is not required in our case, since the control objective of MPC is to stabilize*

the system at its set-point, rather than to find the globally-optimal trajectory. The Lyapunov-based constraints can guarantee closed-loop stability in terms of convergence to the set-point for the nonlinear system provided that a feasible solution (could be a locally-optimal solution) to the LMPC optimization problem exists.

Remark 8.3. *In the manuscript, the MPC is implemented in a sample-and-hold fashion, under which the control action remains the same over one sampling period, i.e.,* $u(t) = u(x(t_k))$, $\forall t \in [t_k, t_{k+1})$, *where* t_{k+1} *represents* $t_k + \Delta$ *and* Δ *is the sampling period. Additionally, one possible way to solve the optimization problems of Eqs. 8.6 and 8.7 is to use continuous-time optimization schemes. This method has recently gained researchers attention and can be found in [75, 167].*

Remark 8.4. *In this work, the neural network is used to replace the nonlinear term in the first-principles model, for which it is generally difficult to obtain an accurate functional form from first-principles calculations. It should be noted that the neural network* $F_{NN}(\hat{x})$ *was developed as an input-output function to replace only a part (static nonlinearities) of the first-principles model, and thus does not replace the entire steady-state model or dynamic model.*

8.3 Application to a Chemical Reactor Example

8.3.1 Process Description and Simulation

The first example considers a continuous stirred tank reactor (CSTR), where a reversible exothermic reaction $A \leftrightarrow B$ takes place [45, 48]. After applying mass and energy balances, the following dynamic model is achieved to describe the process:

$$\begin{aligned}
\frac{dC_A}{dt} &= \frac{1}{\tau}(C_{A_0} - C_A) - k_A e^{\frac{-E_A}{RT}} C_A + k_B e^{\frac{-E_B}{RT}} C_B \\
\frac{dC_B}{dt} &= -\frac{1}{\tau} C_B + k_A e^{\frac{-E_A}{RT}} C_A - k_B e^{\frac{-E_B}{RT}} C_B \\
\frac{dT}{dt} &= \frac{-\Delta H}{\rho C_P}(k_A e^{\frac{-E_A}{RT}} C_A - k_B e^{\frac{-E_B}{RT}} C_B) + \frac{1}{\tau}(T_0 - T) + \frac{Q}{\rho C_P V}
\end{aligned} \tag{8.8}$$

In the model of Eq. 8.8, C_A, C_B are the concentrations of A and B in the reactor, and T is the temperature of the reactor. The feed temperature and concentration are denoted by T_0 and C_{A_0}, respectively. k_A and k_B are the pre-exponential factor for the forward reaction and reverse reaction, respectively. E_A and E_B are the activation energy for the forward reaction and reverse reaction, respectively. τ is the residence time in the reactor; ΔH is the enthalpy of the reaction; and C_P is the heat capacity of the mixture liquid. The CSTR is equipped with a jacket to provide heat to the reactor at rate Q. All process parameter values and steady-state values are listed in Table 8.1. Additionally, it is noted that the second equation of Eq. 8.8 for C_B is unnecessary if C_{A_0} is fixed due to $C_B = C_{A_0} - C_A$. This does not hold when C_{A_0} is varying, and thus, the full model is used in this work for generality.

Table 8.1: Parameter values and steady-state values for the continuous stirred tank reactor (CSTR) case study.

$T_0 = 400$ K	$\tau = 60$ s
$k_A = 5000$ /s	$k_B = 10^6$ /s
$E_A = 1 \times 10^4$ cal/mol	$E_B = 1.5 \times 10^4$ cal/mol
$R = 1.987$ cal/(mol K)	$\Delta H = -5000$ cal/mol
$\rho = 1$ kg/L	$C_P = 1000$ cal/(kg K)
$C_{A_0} = 1$ mol/L	$V = 100$ L
$C_{A_s} = 0.4977$ mol/L	$C_{B_s} = 0.5023$ mol/L
$T_{A_s} = 426.743$ K	$Q_s = 40386$ cal/s

When the tank temperature T is too low, the reaction rate is maintained as slow such that the reactant A does not totally reacted during the residence time, and thus, the reactant conversion $(1 - C_A/C_{A_0})$ is low. When the tank temperature T is too high, the reversible exothermic reaction equilibrium turns backwards so that the reactant conversion $(1 - C_A/C_{A_0})$ also drops. As a result,

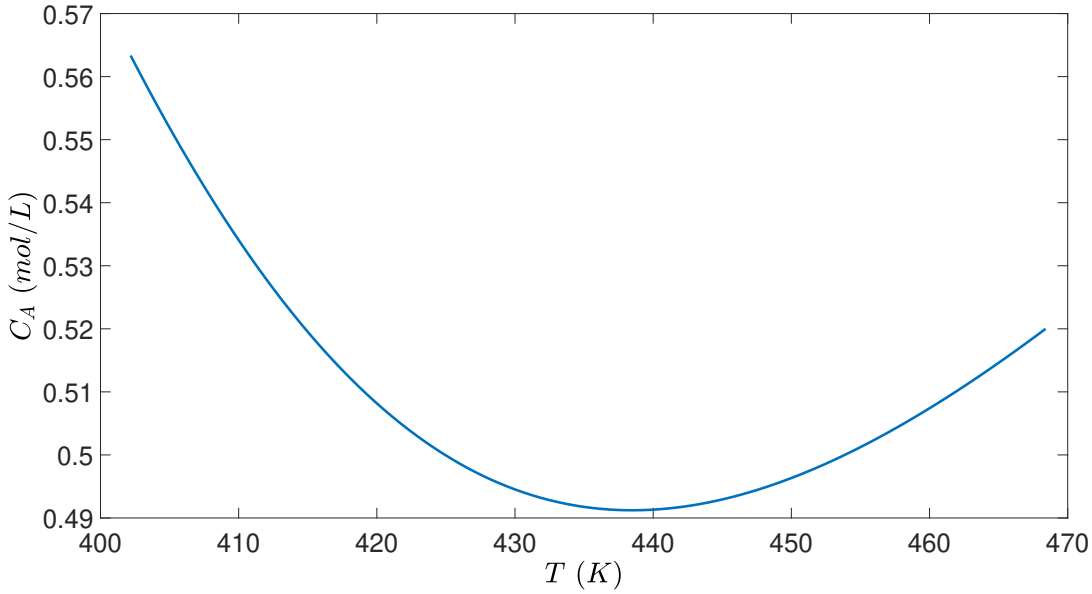

Figure 8.2: Steady-state profiles (C_A and T) for the CSTR of Eq. 8.8 under varying heat input rate Q, where the minimum of C_A is achieved at Q= 59,983 cal/s.

there exists a best tank temperature to maximize the reactant conversion. Fig. 8.2 shows the variation of the CSTR steady-state (i.e., concentration C_A and temperature T) under varying heat input rate Q, where Q is not explicitly shown in Fig. 8.2. Specifically, the minimum point of C_A represents the steady-state of C_A and T, under which the highest conversion rate (conversion rate = $1 - C_A/C_{A_0}$) is achieved. Therefore, the CSTR process should be operated at this steady-state for economic optimality if no other cost is accounted for.

8.3.2 Neural Network Model

In the CSTR model of Eq. 8.8, the reaction rate $r = k_A e^{\frac{-E_A}{RT}} C_A - k_B e^{\frac{-E_B}{RT}} C_B$ is a nonlinear function of C_A, C_B, and T. To obtain this reaction rate from experiment data, an assumption of the reaction rate mechanism and reaction rate function formulation is required. In practice, it could be challenging to obtain an accurate reaction rate expression using the above method if the reaction mechanism is unknown and the rate expression is very complicated.

In this work, a neural network model is built to represent the reaction rate r as a function of C_A, C_B, and T (i.e., $r = F_{NN}(C_A, C_B, T)$), and then, the neural network model replaces the

first-principles rate equation in the process model. Specifically, around eight million data were generated by the original reaction rate expression $r = k_A e^{\frac{-E_A}{RT}} C_A - k_B e^{\frac{-E_B}{RT}} C_B$ with different values of C_A, C_B, and T. The dataset was generated such that various reaction rates under different operating conditions (i.e., temperature, concentrations of A and B) were covered. The operating conditions were discretized equidistantly. Specifically, we tried the activation functions such as tanh, sigmoid, and ReLU for hidden layers and a linear unit and softmax function for the output layer. It is demonstrated that the choice of activation functions for the output layer significantly affected the performance of the neural network in a regression problem, while those for the hidden layers achieved similar results. $tanh(x) = 2/(1+e^{-2x}) - 1$ was ultimately chosen as the activation function for the hidden layers, and a linear unit was used for the output layer since they achieved the best training performance with the mean squared error less than 10^{-7}. Data were first normalized and then fed to the MATLAB Deep Learning toolbox to train the model. The neural network model had one hidden layer with 10 neurons. The parameters were trained using Levenberg–Marquardt optimization algorithm. In terms of the accuracy of the neural network model, the coefficient of determination R^2 was 1, and the error histogram of Fig. 8.3 demonstrates that the neural network represented the reaction rate with a high accuracy, as can be seen from the error distribution (we note that error metrics used in classification problems like the confusion matrix, precision, recall, and f1-score were not applicable to the regression problems considered in this work). In the process model of Eq. 8.8, the first-principles reaction rate term $k_A e^{\frac{-E_A}{RT}} C_A - k_B e^{\frac{-E_B}{RT}} C_B$ was replaced with the obtained neural network $F_{NN}(C_A, C_B, T)$. The integration of the first-principles model and the neural network model that was used in RTO and MPC will be discussed in the following sections.

Remark 8.5. *The activation function plays an important role in the neural network training process and may affect its prediction performance significantly. Specifically, in the CSTR example, since it is known that the reaction rate is generally in the form of exponential functions, we tried tanh and sigmoidactivation functions. It is demonstrated that both achieved the desired performance with mean squared error less than* 10^{-7}.

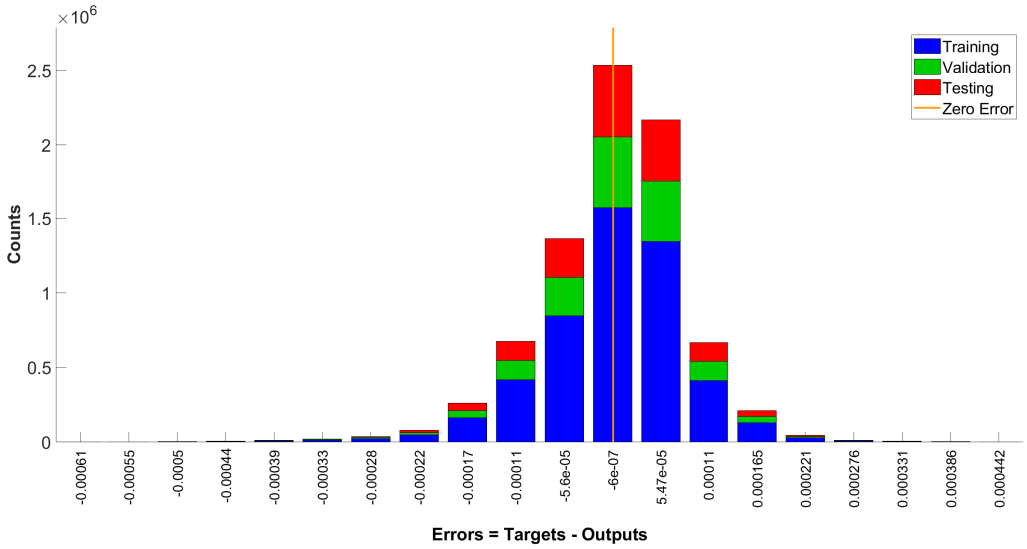

Figure 8.3: Error distribution histogram for training, validation, and testing data.

8.3.3 RTO and Controller Design

8.3.3.1 RTO Design

It is generally accepted that energy costs vary significantly compared to capital, labor, and other expenses in an actual plant. Therefore, in addition to productivity, it is important to account for energy cost in the real-time optimization of plant operation. Specifically, in this example, the heating cost was regarded as the entire energy cost since other energy costs may be lumped into the heating energy cost. The overall cost function is defined as follows:

$$total\ cost = \frac{C_A}{C_{A_0}} + heat\ price \times Q \tag{8.9}$$

Eq. 8.9 attempts to find the balance between the reactant conversion and heat cost. A simple linear form was taken between Q and C_A in this case study since it was sufficient to illustrate the relationship between energy cost and reactant conversion. The above total cost was optimized in real time to minimize the cost of the CSTR process, by solving the optimization problem of

Eq. 8.10.

$$\min_{C_A, C_B, T, Q} \quad total\ cost = \frac{C_A}{C_{A_0}} + heat\ price \times Q \tag{8.10a}$$

$$\text{s.t.} \quad 0 = \frac{1}{\tau}(C_{A_0} - C_A) - F_{NN}(C_A, C_B, T) \tag{8.10b}$$

$$0 = -\frac{1}{\tau}C_B + F_{NN}(C_A, C_B, T) \tag{8.10c}$$

$$0 = \frac{-\Delta H}{\rho C_P}F_{NN}(C_A, C_B, T) + \frac{1}{\tau}(T_0 - T) + \frac{Q}{\rho C_P V} \tag{8.10d}$$

$$C_A \in [0, 1] \tag{8.10e}$$

$$C_B \in [0, 1] \tag{8.10f}$$

$$T \in [400, 500] \tag{8.10g}$$

$$Q \in [0, 10^5] \tag{8.10h}$$

The constraints of Eq. 8.10b, Eq. 8.10c, and Eq. 8.10d are the steady-state models of the CSTR process, which set the time derivative of Eq. 8.8 to zero and replace the reaction rate term by the neural network model built in Section 8.3.2. Since the feed concentration C_{A_0} is 1 mol/L, C_A and C_B must be between 0 and 1 mol/L. The temperature constraint [400, 500] and energy constraint $[0, 10^5]$ are the desired operating conditions. At the initial steady-state, the heat price is 7×10^{-7}, and the CSTR operates at $T = 426.7$ K, $C_A = 0.4977$ mol/L and Q = 40,386 cal/s. The performance is not compromised too much since $C_A = 0.4977$ mol/L is close to the optimum value $C_A = 0.4912$ mol/L, while the energy saving is considerable when Q = 40,386 cal/s is compared to the optimum value Q = 59,983 cal/s. In the presence of variation in process variables or heat price, RTO recalculates the optimal operating condition, given that the variation is measurable every RTO period. The RTO of Eq. 8.10 is solved every RTO period, and then sends steady-state values to controllers as the optimal set-points for the next 1000 s. Since the CSTR process has a relatively fast dynamics, a small RTO period of 1000 s is chosen to illustrate the performance of RTO.

8.3.3.2 Controller Design

In order to drive the process to the optimal steady-state, a Lyapunov-based model predictive controller (LMPC) is developed in this section. The controlled variables are C_A, C_B, and T, and the manipulated variable is heat rate Q. The CSTR is initially operated at the steady-state $[C_{A_s} C_{B_s} T_s]$ = [0.4977 mol/L 0.5023 mol/L 426.743 K], with steady-state $Q_s = 40,386$ cal/s. At the beginning of each RTO period, a new set of steady-states are calculated, and then, the input and the states are represented in their deviation variable form as $u = Q - Q_s$ and $x^T = [C_A - C_{A_s}\ C_B - C_{B_s}\ T - T_s]$, such that the systems of Eq. 8.8 together with $F_{NN}(C_A, C_B, T)$ can be written in the form of $\dot{x} = f(x) + g(x)u$. A Lyapunov function is designed using the standard quadratic form $V(x) = 100{,}000x_1^2 + 100{,}000x_2^2 + x_3^2$, and the parameters are chosen to ensure that all terms are of similar order of magnitude since temperature is varying in a much larger range compared to concentration. We characterize the stability region Ω_ρ as a level set of Lyapunov function, i.e., $\Omega_\rho = \{x \in R^3 \mid V(x) \leq \rho\}$. For the system of Eq. 8.8, the stability region Ω_ρ with $\rho = 1000$ is found based on the above Lyapunov function V and the following controller $h(x)$ [94]:

$$h(x) = \begin{cases} -\frac{L_f V + \sqrt{L_f V^2 + L_g V^4}}{L_g V^2} L_g V & \text{if} \quad L_g V \neq 0 \\ 0 & \text{if} \quad L_g V = 0 \end{cases} \tag{8.11}$$

where $L_f V(x)$ denotes the standard Lie derivative $L_f V(x) := \frac{\partial V(x)}{\partial x} f(x)$. The control objective is to stabilize C_A, C_B, and T in the reactor at its steady-state by manipulating the heat rate Q. A Lyapunov-based model predictive controller (LMPC) is designed to bring the process to the steady-state calculated by the RTO. Specifically, the LMPC is presented by the following

optimization problem:

$$\min_{u\in S(\Delta)} \quad \int_{t_k}^{t_{k+N}} (\|\tilde{x}(\tau)\|^2_{Q_c} + \|u(\tau)\|^2_{R_c})\, d\tau \tag{8.12a}$$

$$\text{s.t.} \quad \dot{\tilde{x}}(t) = f(\tilde{x}(t)) + g(\tilde{x}(t))u(t) \tag{8.12b}$$

$$\tilde{x}(t_k) = x(t_k) \tag{8.12c}$$

$$u(t) \in U,\ \forall\, t \in [t_k, t_{k+N}) \tag{8.12d}$$

$$\frac{\partial V(x(t_k))}{\partial x}(f(x(t_k)) + g(x(t_k))u(t_k)) \leq \frac{\partial V(x(t_k))}{\partial x}(f(x(t_k)) + g(x(t_k))h(x(t_k))) \tag{8.12e}$$

where $\tilde{x}$ is the predicted state, N is the number of sampling periods within the prediction horizon, and $S(\Delta)$ is the set of piece-wise constant functions with period Δ. The LMPC optimization problem calculates the optimal input trajectory over the entire prediction horizon $t \in [t_k, t_{k+N})$, but only applies the control action for the first sampling period, i.e., $u(t) = u(x(t_k)), \forall t \in [t_k, t_{k+1})$. In the optimization problem of Eq. 8.12, Eq. 8.12a is the objective function minimizing the time integral of $\|\tilde{x}(\tau)\|^2_{Q_c} + \|u(\tau)\|^2_{R_c}$ over the prediction horizon. Eq. 8.12b is the process model of Eq. 8.8 in its deviation form and is used to predict the future states. A neural network $F_{NN}(x_1, x_2, x_3)$ is used to replace $k_A e^{\frac{-E_A}{RT}} C_A - k_B e^{\frac{-E_B}{RT}} C_B$ in Eq. 8.8. Eq. 8.12c uses the state measurement $x(t_k)$ at $t = t_k$ as the initial condition $\tilde{x}(t_k)$ of the optimization problem. Eq. 8.12d defines the input constraints over the entire prediction horizon, where $U = [0 - Q_s \quad 10^5 - Q_s]$. The constraint of Eq. 8.12e is used to decrease $V(x)$ such that the state $x(t)$ is forced to move towards the origin. It guarantees that the origin of the closed-loop system is rendered asymptotically stable under LMPC for any initial conditions inside the stability region Ω_ρ. The detailed proof of closed-loop stability can be found in [110].

To simulate the dynamic model of Eq. 8.8 numerically under the LMPC of Eq. 8.12, we used the explicit Euler method with an integration time step of $h_c = 10^{-2}$ s. Additionally, the optimization problem of the LMPC of Eq. 8.12 is solved using the solver IPOPT in the OPTI Toolbox in MATLAB with the following parameters: sampling period $\Delta = 5$ s; prediction horizon $N = 10$. $Q_c = \left[1\ 0\ 0;\ 0\ 1\ 0;\ 0\ 0\ 5 \times 10^{-5}\right]$ and $R_c = 10^{-11}$ were chosen such

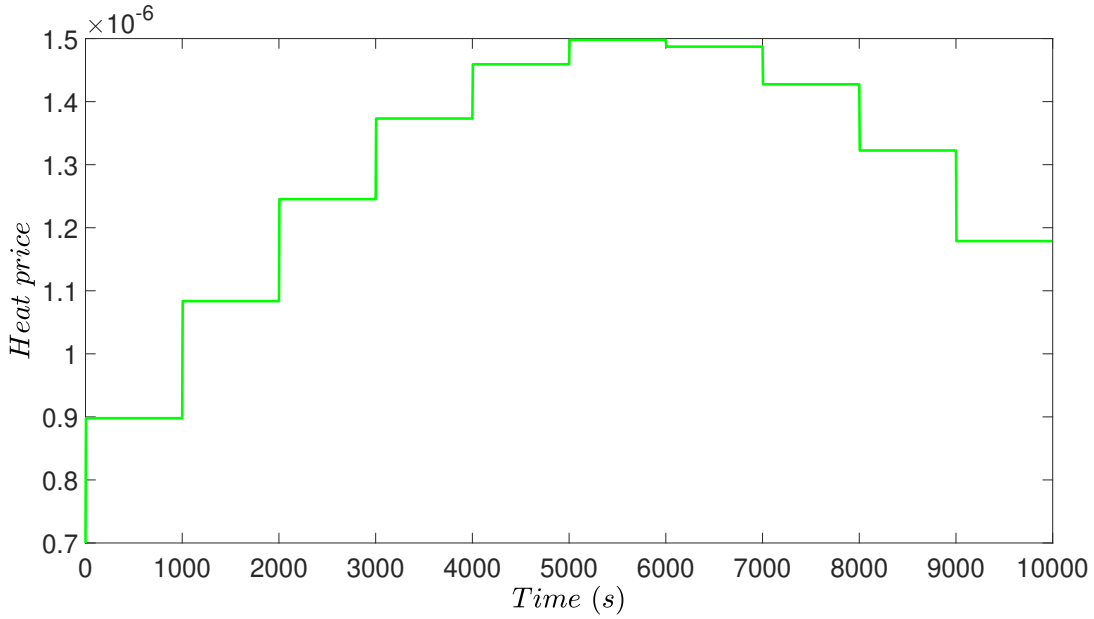

Figure 8.4: Heat price profile during the simulation, where the heat price first increases and then decreases to simulate heat rate price changing.

that the magnitudes of the states and of the input in $\|\tilde{x}(\tau)\|^2_{Q_c}$ and $\|u(\tau)\|^2_{R_c}$ have the similar order.

8.3.4 Simulation Results

In the simulation, a variation of heat price is introduced to demonstrate the performance of the designed RTO and MPC. Since the heat price is changing as shown in Fig. 8.4, the initial steady-state is no longer the optimal operating condition. The RTO of Eq. 8.10 is solved at the beginning of each RTO period to achieve a set of improved set-points, which will be tracked by the MPC of Eq. 8.12. With the updated set-points, the CSTR process keeps adjusting operating conditions accounting for varying heat price. After the controller receives the set-points, the MPC of Eq. 8.12 calculates input u to bring x to the new set-point, and finally, both state x and input u are maintained at their new steady-states. The concentration profiles, temperature profile, and heat rate profile are shown in Figs. 8.5–8.7.

During the first half of the simulation, heat price rises up to a doubled value. Considering the increasing heat price, the operation tends to decrease the heat rate to reduce the energy cost, while compromising the reactant conversion. Therefore, the energy cost and reactant conversion

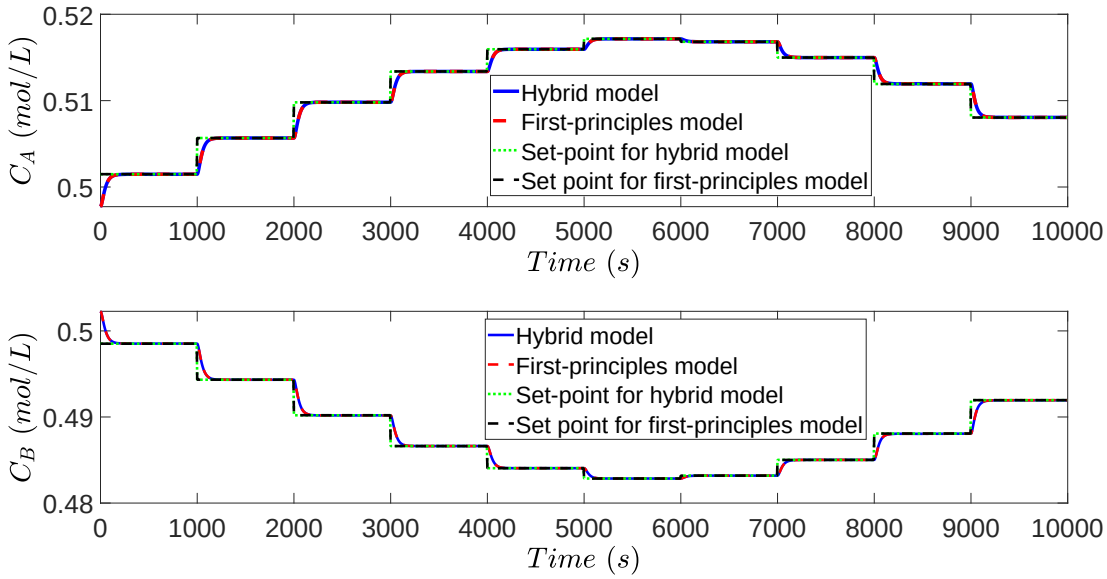

Figure 8.5: Evolution of the concentration of A and B for the CSTR case study under the proposed real-time optimization (RTO) and MPC.

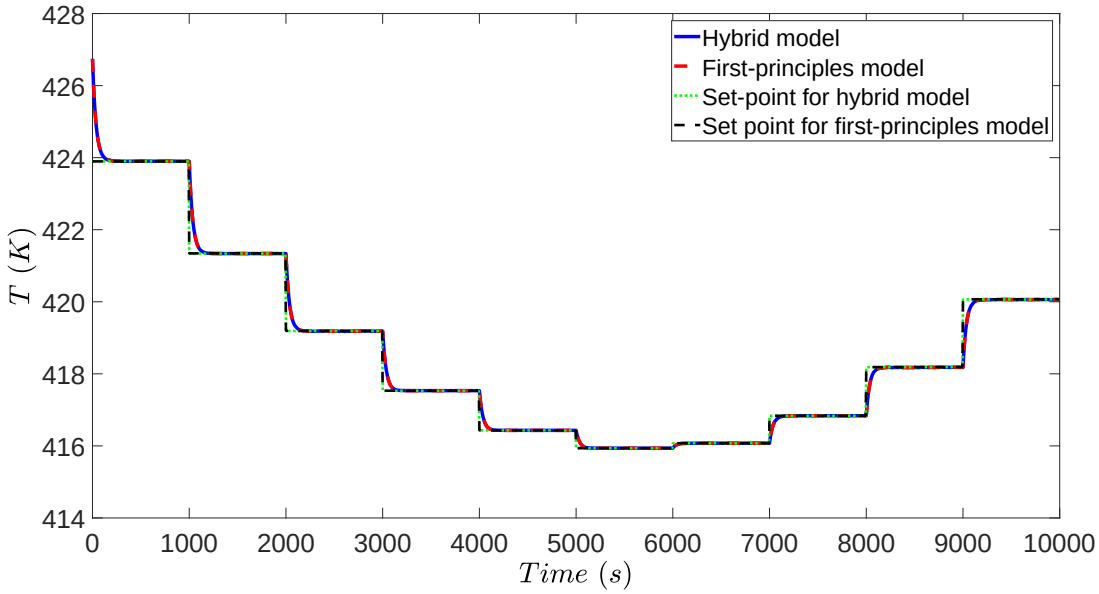

Figure 8.6: Evolution of the reactor temperature T for the CSTR case study under the proposed RTO and MPC scheme.

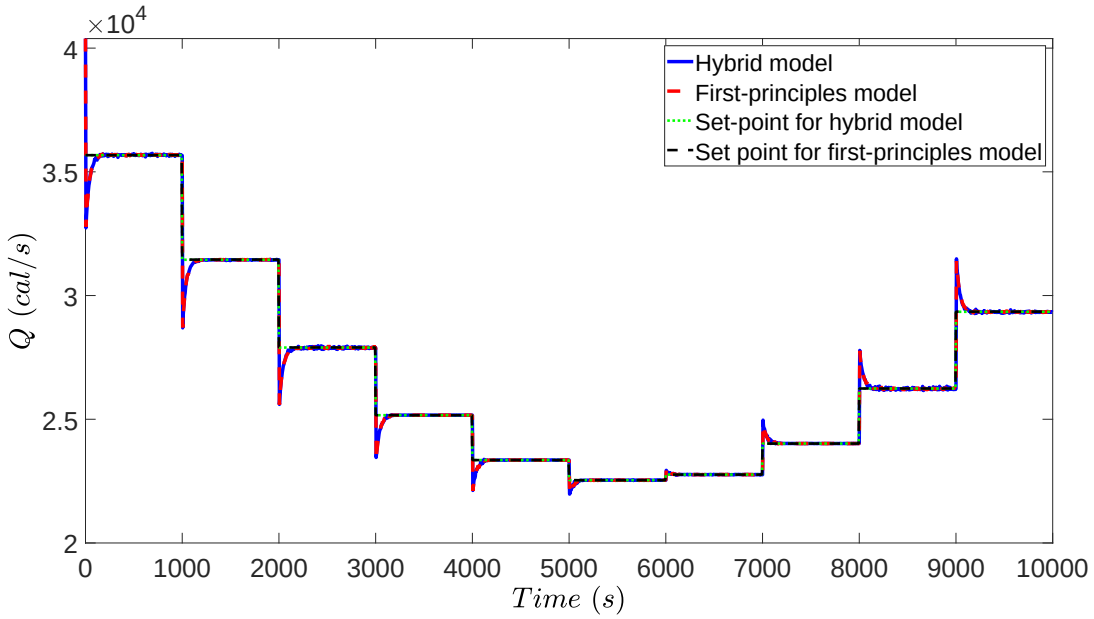

Figure 8.7: Evolution of the manipulated input, the heating rate Q, for the CSTR example under the proposed RTO and MPC scheme.

will be balanced by RTO to reach a new optimum. As demonstrated in Fig. 8.5, C_A increases and C_B decreases during the first half of simulation, which implies that less reactant A is converted to product B in the tank. The reactor temperature also drops as shown in Fig. 8.6, which corresponds to the reducing heat rate as shown in Fig. 8.7.

Total cost is calculated by Eq. 8.9 using state measurements of C_A and Q from the closed-loop simulation and is plotted in Fig. 8.8. The total cost with fixed steady-state is also calculated and plotted for comparison. After the heat price starts to increase, both total costs inevitably increase. Since RTO keeps calculating better steady-states compared to the initial steady-state, the total cost under RTO increases less than the simulation without RTO. The total cost is integrated with time to demonstrate the difference in cost increment, using Eq. 8.13.

$$cost\ increase = \int_0^{t_{final}} \|total\ cost - initial\ cost\|\ dt \tag{8.13}$$

where $initial\ cost = 0.526$ and $t_{final} = 10,000$ s. The ratio of cost increment between simulations with RTO and without RTO is $195 : 241$. Although the operating cost increases because of rising

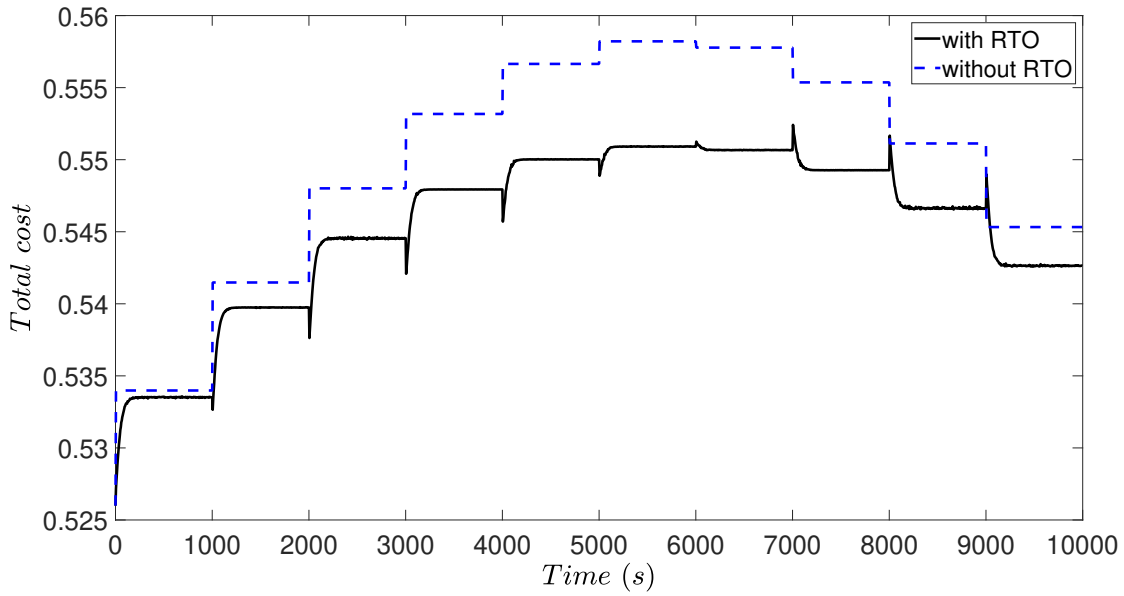

Figure 8.8: Comparison of the total operation cost for the CSTR example for simulations with and without RTO adapting to the heat rate price changing.

heat price, RTO reduces the cost increment by approximately a factor of $1/5$, when compared to the fixed operating condition without RTO.

The combination of neural network models and first-principles models works well in both RTO and MPC. Additionally, it is shown in Figs. 8.5–8.7 that the RTO with the combined first-principles and neural-network model calculates the same steady-state when compared to the RTO with a pure first-principles model. Moreover, the MPC also drives all the states to the set-points without offset when the MPC uses the combination of a neural network model with a first-principles model. In this case study, the neural network model is accurate such that the combination of neural network and first-principles model attains almost the same closed-loop result as the pure first-principles model (curves overlap when plotted in the same figure as is done in Figs. 8.5–8.7, where the blue curve denotes the solution under MPC with the combined first-principles/neural network model, the red curve denotes the solution under MPC with the first-principles model, the green curve denotes the set-points calculated by RTO with the hybrid model, and the black curve denotes the set-points calculated by RTO with the first-principles model). Additionally, we calculated the accumulated relative error (i.e., $E = \frac{\int_{t=0}^{t=10{,}000s} |T_f - T_h| dt}{\int_{t=0}^{t=10{,}000s} T_f dt}$) between the temperature curves (Fig. 8.6)

under the first-principles model (i.e., T_f) and under the hybrid model (i.e., T_h) over the entire operating period from $t = 0$ to $t = 10{,}000$ s. It was obtained that $E = 4.98 \times 10^{-6}$, which is sufficiently small. This implies that the neural network successfully approximated the nonlinear term of reaction rate. In practice, neural network could be more effective when the reaction rate is very complicated and depends on more variables and the reaction mechanism is unknown.

8.4 Application to a Distillation Column

8.4.1 Process Description, Simulation, and Model

8.4.1.1 Process Description

A simple binary separation of propane from isobutane in a distillation column was used for the second case study [98]. Aspen Plus (Aspen Technology, Inc., Bedford, MA, USA) and Aspen Plus Dynamics V10.0 were utilized to perform high-fidelity dynamic simulation for the distillation column. Specifically, Aspen Plus uses the mass and energy balances to calculate the steady-state of the process based on a process flowsheet design and carefully-chosen thermodynamic models. After the steady-state model is solved in Aspen Plus, it can be exported to a dynamic model in Aspen Plus Dynamics, which runs dynamic simulations based on the obtained steady-state models and detailed process parameters [5, 19].

A schematic of the distillation process is shown in Fig. 8.9. The feed to the separation process was at 20 atm, 322 K and 1 kmol/s, with a propane mole fraction of 0.4 and an isobutane mole fraction of 0.6. After a valve controlling the feed flow rate, the feed enters the distillation column at Tray 14. The feed tray is carefully chosen to achieve the best separation performance and minimum energy cost, as discussed in [98]. The column has 30 trays with a tray spacing of 0.61 m, and the diameter of the tray is 3.85 m and 4.89 m for the rectifying section and stripping section, respectively. At the initial steady-state, the distillate product has a propane mole fraction 0.98 and a flow rate 0.39 kmol, while the bottom product has a propane mole fraction 0.019 and a flow

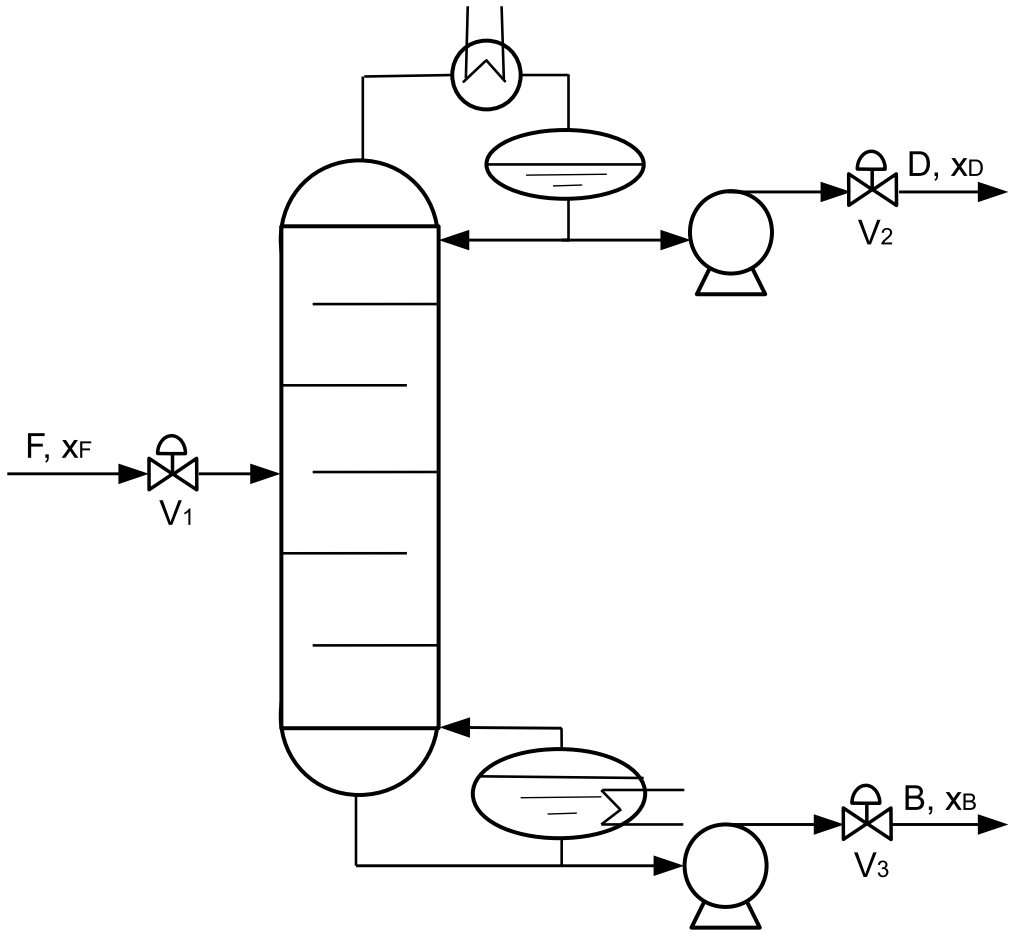

Figure 8.9: A schematic diagram of the distillation column implemented in Aspen Plus Dynamics.

rate 0.61 kmol. The reflux ratio is 3.33, together with condenser heat duty -2.17×10^7 W and reboiler heat duty 2.61×10^7 W. The pressure at the top and bottom is 16.8 atm and 17 atm. Both the top and bottom products are followed by a pump and a control valve. All the parameters are summarized in Table 8.2.

In our simulation, the involved components of propane and isobutane were carefully chosen, and the CHAO-SEA model was selected for the thermodynamic property calculation. The steady-state model was first built in Aspen Plus using the detailed information as discussed above and the parameters in Table 8.2. Then, the achieved steady-state simulation was exported to the dynamic model as a pressure-driven model, based on additional parameters such as reboiler size and drum size. After checking the open-loop response of the dynamic model, controllers will be designed in Section 8.4.3.2.

Table 8.2: Parameter values and steady-state values for the distillation column case study.

F = 1 kmol	x_F = 0.4
$T_F = 322$ K	$P_F = 20$ atm
q = 1.24	N_F = 14
N_T = 30	$Diameter_{reboiler} = 5.08$ m
$Length_{reboiler} = 10.16$ m	$Diameter_{reflux\ drum} = 4.08$ m
$Length_{reflux\ drum} = 8.16$ m	
steady-state condition:	R = 3.33
$x_B = 0.019$	$x_D = 0.98$
$P_{bottom} = 17$ atm	$P_{top} = 16.8$ atm
B = 0.61 kmol/L	D = 0.39 kmol/L
$Q_{top} = -2.17 \times 10^7$ W	$Q_{bottom} = 2.61 \times 10^7$ W

8.4.1.2 Process Model

In order to calculate the steady-state of the distillation process, an analytic steady-state model is developed in this section. Since the Aspen model cannot be used in the optimization problem explicitly, this analytic steady-state model will be used in the RTO.

The analytic steady-state model consists of five variables, which are the reflux ratio R, the distillate mole flow rate D, the bottom mole flow rate B, the distillate mole fraction x_D, and the bottom mole fraction x_B. For clarification, x is denoted as the mole fraction for the light component propane. Other parameters include feed conditions: feed molar flow rate F, feed mole fraction x_F, feed heat condition q; column parameters: total number of trays N_T, feed tray N_F; component property: relative volatility α. Three equations were developed for the steady-state model.

The first equation $F_1(D,B) = 0$ is the overall molar balance between feed and products, as shown in Eq. 8.14.

$$F = D + B \tag{8.14}$$

The second equation $F_2(D,B,x_D,x_B) = 0$ is the overall component balance of light component propane, as shown in Eq. 8.15:

$$Fx_F = Dx_D + Bx_B \tag{8.15}$$

The third equation applies the binary McCabe–Thiele method. The constant molar overflow assumptions of the McCabe–Thiele method were held in this case study: the liquid and vapor flow rates were constant in a given section of the column. Equilibrium was also assumed to be reached on each tray. The top tray was defined as the first tray. To apply the McCabe–Thiele method, the rectifying operating line (ROL), stripping operating line (SOL), and phase equilibrium were developed as follows:

Rectifying operating line (ROL):

$$y_{n+1} = \frac{R}{R+1}x_n + \frac{x_D}{R+1} \tag{8.16}$$

Stripping operating line (SOL):

$$y_{n+1} = \frac{RD+qF}{(R+1)D-(1-q)F}x_n + \frac{F-D}{(R+1)-(1-q)F}x_B \tag{8.17}$$

Phase equilibrium:

$$x_n = \frac{y_n}{\alpha-(\alpha-1)y_n} \tag{8.18}$$

where $\alpha = \frac{y_{C3}/x_{C3}}{y_{C4}/x_{C4}} = 1.79$ is the approximate relative volatility between propane and isobutane at a pressure 16.9 atm, which is the mean of the top and bottom pressure.

The third equation $F_3(R,D,x_D,x_B) = 0$ is expressed in Eq. 8.19 below:

$$y_1 = x_D \tag{8.19a}$$

$$x_n = \frac{y_n}{\alpha-(\alpha-1)y_n}, \quad n = 1,2...N_T \tag{8.19b}$$

$$y_{n+1} = \frac{R}{R+1}x_n + \frac{x_D}{R+1}, \quad n = 1,2...N_F-1 \tag{8.19c}$$

$$y_{n+1} = \frac{RD+qF}{(R+1)D-(1-q)F}x_n + \frac{F-D}{(R+1)-(1-q)F}x_B, \quad n = N_F, N_F+1...N_T-1 \tag{8.19d}$$

$$x_{N_T} = x_B \tag{8.19e}$$

The third equation $F_3(R,D,x_D,x_B) = 0$ ties the distillate mole fraction x_D to the bottom mole fraction x_B by calculating both liquid and vapor mole fractions through all trays from top to bottom. Eq. 8.19a defines the vapor mole fraction y_1 on the first tray as the distillate mole fraction x_D. Then, the liquid mole fraction x_1 on the first tray can be calculated by the phase equilibrium of Eq. 8.19b. Subsequently, the vapor mole fraction y_2 on the second tray is calculated by the ROL of Eq. 8.19c. The calculation is repeated until x_{14} and y_{14} are obtained. Then, y_{15} is calculated by the SOL of Eq. 8.19d, instead of ROL. Then, x_{15} can be calculated again by the phase equilibrium of Eq. 8.19b. The above calculations are repeated until x_{30} and y_{30} are obtained, and $x_{30} = x_B$ since the liquid on the last tray is the bottom product. In this way, all the variables (i.e., R, D, x_D, x_B) have values that satisfy $F_3(R,D,x_D,x_B) = 0$.

There are five variables R, D, B, x_D, x_B and three equations F_1, F_2, F_3, which implies that there are two degrees of freedom. In order to determine the whole process operating condition, two more states need to be fixed, potentially by RTO. It is necessary to point out that the concentrations x_i and y_i on each tray can be calculated by Eq. 8.19 if all five variables R, D, B, x_D, x_B are determined. Additionally, if the equilibrium temperature-component curve $T = f_e(x)$ (bubble point curve) or $T = f_e(y)$ (dew point curve) are provided, then the temperature on each tray T_i can also be calculated by simply using $T_i = f_e(x_i)$ or $T_i = f_e(y_i)$.

8.4.2 Neural Network Model

Phase equilibrium properties are usually nonlinear, and the first-principles models are often found to be inaccurate and demand modifications. In the above steady-state model, the phase equilibrium $x_n = \frac{y_n}{\alpha-(\alpha-1)y_n}$ of Eq. 8.19b assumes that relative volatility α is constant; however, the relative volatility α does not hold constant with varying concentration and pressure. Therefore, a more accurate model for phase equilibrium $x \sim y$ can improve the model performance. Similarly, dew point curve $T \sim y$ can be built from first-principles formulation upon Raoult's Law and the Antoine equation. However, the Antoine equation is an empirical equation, and it is hard to relate saturated pressure with temperature accurately, especially for a mixture. As a result, the machine learning method can be used to achieve a better model to represent the phase equilibrium properties.

In this case study, a neural network $(x, T) = F_{NN}(y)$ was built, with one input (vapor phase mole fraction y) and two outputs (equilibrium temperature T and liquid phase mole fraction x). One thousand five hundred data of T, x, and y were generated by the Aspen property library and were then normalized and fed into the MATLAB Deep Learning toolbox. $tanh(x) = 2/(1+e^{-2x}) - 1$ was chosen as the activation function. The neural network model had one hidden layer with five neurons. The parameters were trained according to Levenberg–Marquardt optimization, and the mean squared error for the test dataset was around 10^{-7}. It is demonstrated in Fig. 8.10 that the neural network model fits the data from the Aspen property library very well, where the blue solid curve is the neural network model prediction and the red curve denotes the Aspen model.

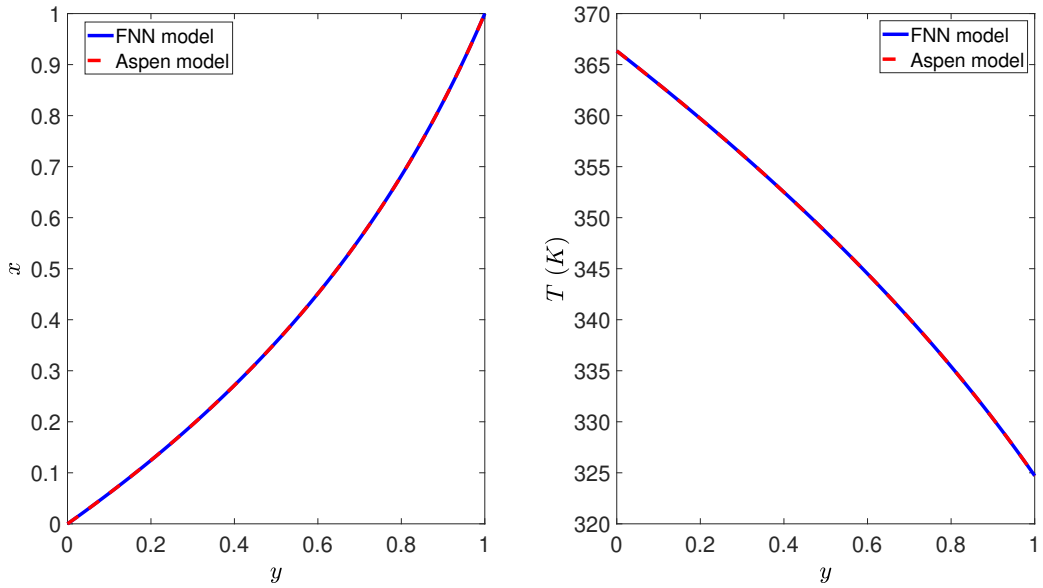

Figure 8.10: Comparison of the neural network model and the Aspen model.

Additionally, we calculated the accumulated relative error (i.e., $E = \frac{\int_{y=0}^{y=1} |T_f - T_h| dy}{\int_{y=0}^{y=1} T_f dy}$) between the temperature curves (Fig. 8.10) under the Aspen model (i.e., T_f) and under the neural network model (i.e., T_h) and $E = 2.32 \times 10^{-6}$; the result was similar for the liquid mole fraction curves. This sufficiently small error implies that the neural network model successfully approximated the nonlinear behavior of the thermodynamic properties. Additionally, the coefficient of determination R^2 was 1, and the error histogram of Fig. 8.11 demonstrated that the neural network model represented the thermodynamic properties with great accuracy.

After training the neural network model, the first-principles phase equilibrium expression $x_n = \frac{y_n}{\alpha - (\alpha - 1) y_n}$ in Eq. 8.19b is replaced by the neural network phase equilibrium expression $x_n = F_{NN,1}(y_n)$, and then, the integrated model of first-principles model and neural network model is used in RTO as discussed in the following sections. In addition, the second output of the neural network model $T_n = F_{NN,2}(y_n)$ can be combined together with Eq. 8.19 to calculate the temperature on each tray, which will be used later to calculate the set-points for the controllers.

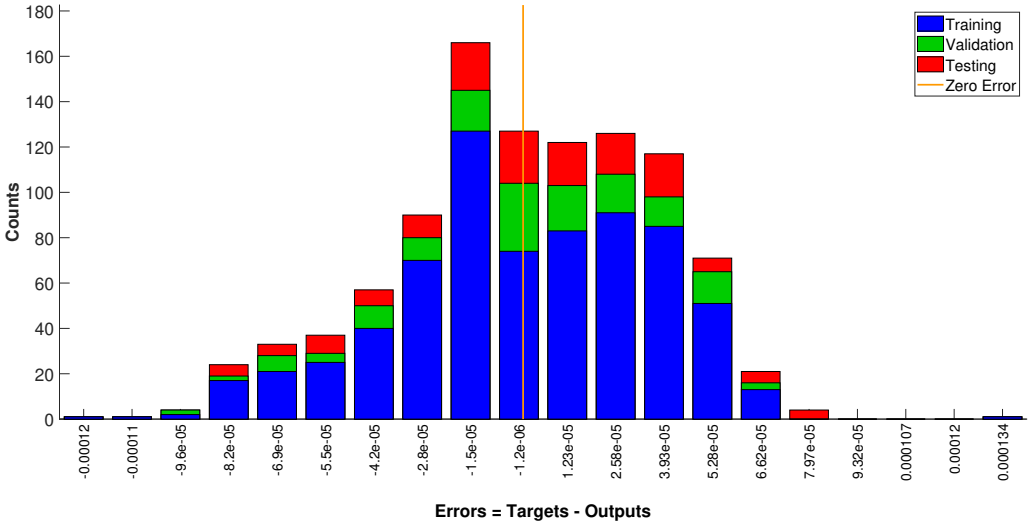

Figure 8.11: Error distribution histogram for training, validation, and testing data.

8.4.3 RTO and Controller Design

8.4.3.1 RTO Design

Since the process has two degrees of freedom, the operating condition has not been determined. An RTO was designed for the distillation process to obtain the optimal operating condition. Since RTO needs an objective function, a profit was developed to represent the operation profit. According to the products, feed, and energy price in [98], the profit is defined by Eq. 8.20.

$$\begin{aligned} Profit &= price_{top}D + price_{bottom}B - price_{feed}F - price_{energy}Q \\ &= price_{top}D + price_{bottom}B - price_{feed}F - price_{energy}(L(R+1)F) \\ &= Profit(R, D, B, x_D, x_B) \end{aligned} \tag{8.20}$$

The profit equals the profit of product subtracting the cost of feed and energy. The profit that will be used in RTO is represented as a function of R, D, B, x_D,x_B. As a result, heat duty Q of both the condenser and reboiler is approximated by $Q = L(R+1)F$, where $L = 1.29 \times 10^7$ J/kmol is the molar latent heat of the mixture. Moreover, mass-based prices are changed to mole-based prices because all flow rates are mole-based. The price of the top distillate rises linearly as the mole

fraction x_D increases in order to demonstrate that the higher purity product has a higher price.

$$\begin{aligned}
price_{top} &= (0.528 + (x_D - 0.97))\$/kg \times 44.1 kg/kmol = 23.29 + 44.1(x_D - 0.97)\ \$/kmol \\
price_{bottom} &= 0.264\$/kg \times 58.1 kg/kmol = 15.34\ \$/kmol \\
price_{feed} &= 0.264\$/kg \times 52.5 kg/kmol = 13.86\ \$/kmol \\
price_{energy} &= 6.11 \times 10^{-8}\ \$/J
\end{aligned} \tag{8.21}$$

To maximize the operation profit, the RTO problem is formulated as Eq. 8.22.

$$\min_{R,D,B,x_D,x_B} \quad -Profit(R,D,B,x_D,x_B) \tag{8.22a}$$

$$\text{s.t.} \quad F_1(D,B) = 0 \tag{8.22b}$$

$$F_2(D,B,x_D,x_B) = 0 \tag{8.22c}$$

$$F_3(D,x_D,x_B,R) = 0 \tag{8.22d}$$

$$R \in [0,\infty] \tag{8.22e}$$

$$D \in [0,1] \tag{8.22f}$$

$$B \in [0,1] \tag{8.22g}$$

$$x_D \in [0,1] \tag{8.22h}$$

$$x_B \in [0,1] \tag{8.22i}$$

Eq. 8.22a minimizes the negative profit with respective to five optimization variables R, D, B, x_D,x_B. The first three constraint Eq. 8.22b, Eq. 8.22c, and Eq. 8.22d are the steady-state model of Eq. 8.14, Eq. 8.15 and Eq. 8.19, as discussed in Section 8.4.1.2. The neural network model $x_n = F_{NN,1}(y_n)$ replaces $x_n = \frac{y_n}{\alpha-(\alpha-1)y_n}$ in Eq. 8.19. Constraints on the optimization variables are determined based on process parameters. Specifically, reflux ratio R can be any positive number; D and B should be between 0 and 1 because the feed had only 1 kmol/s; x_D and x_B should be also between zero and one because they are mole fractions. Since there are two degrees of freedom in the optimization problem, two steady-state values are sent to the controllers as set-points.

8.4.3.2 Controller Design

Six controllers were added in the distillation column, four of which had fixed set-points and two of which received set-points from RTO. The control scheme is shown in Fig. 8.12.

(1) A flow rate controller FC is controlling the feed mole flow rate at 1 kmol/s by manipulating feed valve V_1. A fixed feed flow rate helps to fix the parameters in the first-principles steady-state model.

(2) A pressure controller PC is controlling the column top pressure at 16.8 atm by manipulating condenser heat duty Q_{top}. A fixed column pressure helps to operate the process with fixed thermodynamic properties.

(3) A level controller LC_1 is controlling the reflux drum liquid level at 5.1 m by manipulating the distillate outlet valve V_2. A certain liquid level in the condenser is required to avoid flooding or drying.

(4) A level controller LC_2 is controlling the reboiler liquid level at 6.35 m by manipulating the bottom outlet valve V_3. A certain liquid level in the reboiler is required to avoid flooding or drying.

(5) A concentration controller CC is controlling the distillate C_3 mole fraction by manipulating the reflux mole flow rate. A time delay of 5 min was added to simulate the concentration measurement delay. At the beginning of each RTO period, RTO sends the optimized distillate C_3 mole fraction x_D to concentration controller CC as the set-point. Then, controller CC adjusts the reflux flow to track the mole fraction to its set-point.

(6) A temperature controller TC is controlling temperature T_7 on Tray 7, by manipulating reboiler heat duty Q_{bottom}. A time delay of 1 min was added to simulate the temperature measurement delay. Tray temperature control is common in industry, and two methods were carried out to determine the best tray temperature to be controlled. A steady-state simulation was used to obtain the temperature profile along the tube to find out that the temperature changes among Tray 6, Tray 7, and Tray 8 were greater than those among other trays. One more simulation was performed to get the gain of tray temperature as a response to a small change in the reboiler heat duty. It was also found that the temperature on Tray 7 had a greater gain than those on other

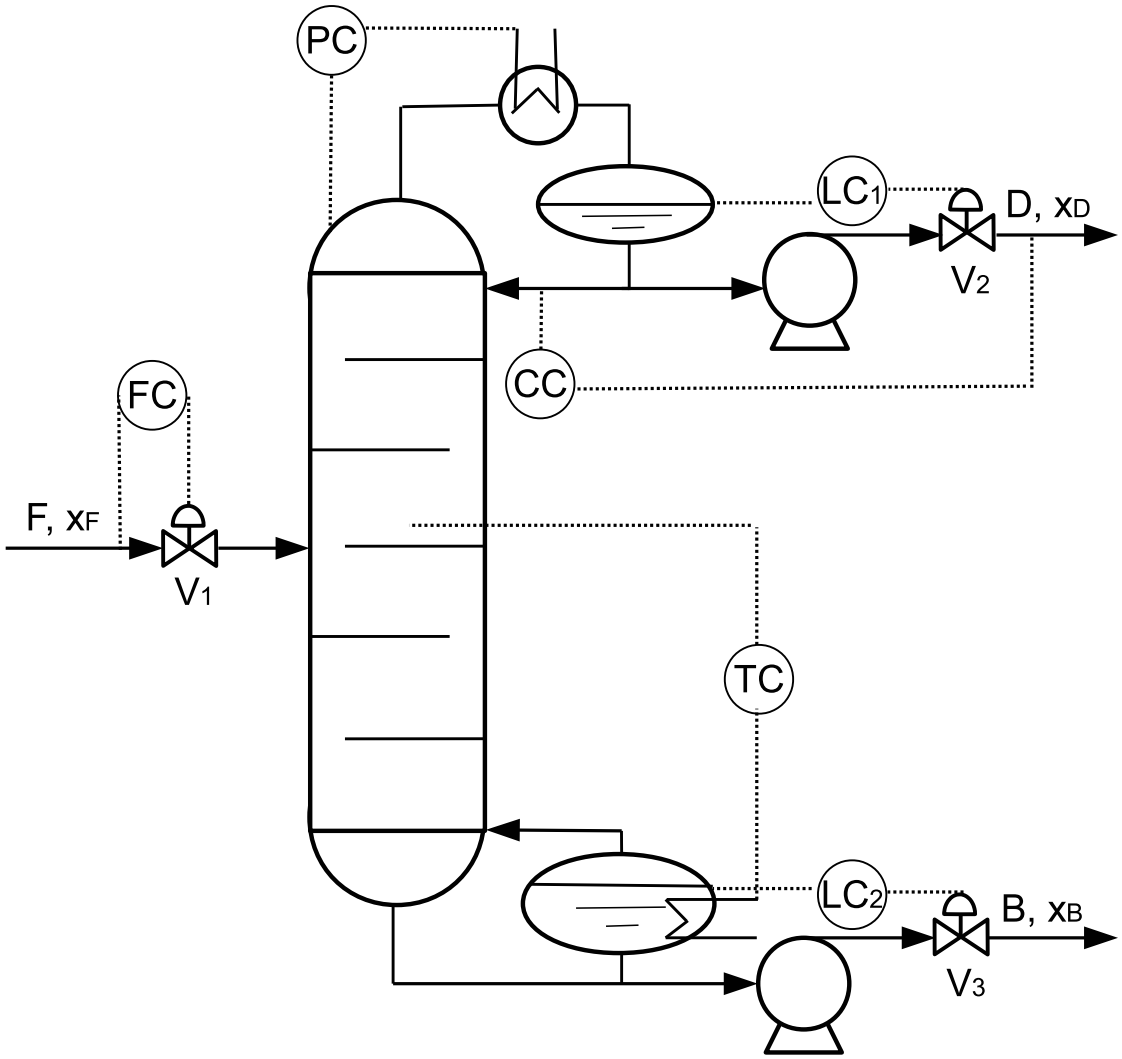

Figure 8.12: A schematic diagram of the control structure implemented in the distillation column. Flow rate controller *FC*, pressure controller *PC*, and both level controllers LC_1 and LC_2 have fixed set-points, and concentration controller *CC* and temperature controller *TC* receive set-points from the RTO.

trays. As a result, Tray 7 was chosen as the controlled variable.

At the beginning of the RTO period, RTO optimizes the profit and calculates a set of steady-states. Given the optimum value of R, D, B, x_D,x_B, the steady-state model of $F_1 = 0$, $F_2 = 0$, and $F_3 = 0$ were used again to obtain the concentration profile in the distillation column. Then, the neural network model $T_n = F_{NN,2}(y_n)$ was used to calculate the temperature on Tray 7. After that, the tray temperature T_7 was sent to the controller TC and will be tracked to its set-point by manipulating the reboiler heat duty.

Flow rate controller FC, pressure controller PC, and both level controllers LC_1 and LC_2 had fixed set-points, which stabilized the process to operate at fixed operation parameters. Concentration controller CC and temperature controller TC received set-points from RTO at the beginning of RTO period and drove the process to more profitable steady-state. All the PI parameters were tuned by the Ziegler–Nichols method and are shown in Table 8.3.

Table 8.3: Proportional gain and integral time constant of all the PI controllers in the distillation case study.

	K_C	τ_I/min
FC	0.5	0.3
PC	15	12
LC_1	2	150
LC_2	4	150
CC	0.1	20
TC	0.6	8

8.4.4 Simulation Results

To demonstrate the effectiveness of RTO, a variation in feed mole fraction x_F was introduced to the process, as shown in Fig. 8.13. At the beginning of each RTO period (20 h), one measurement

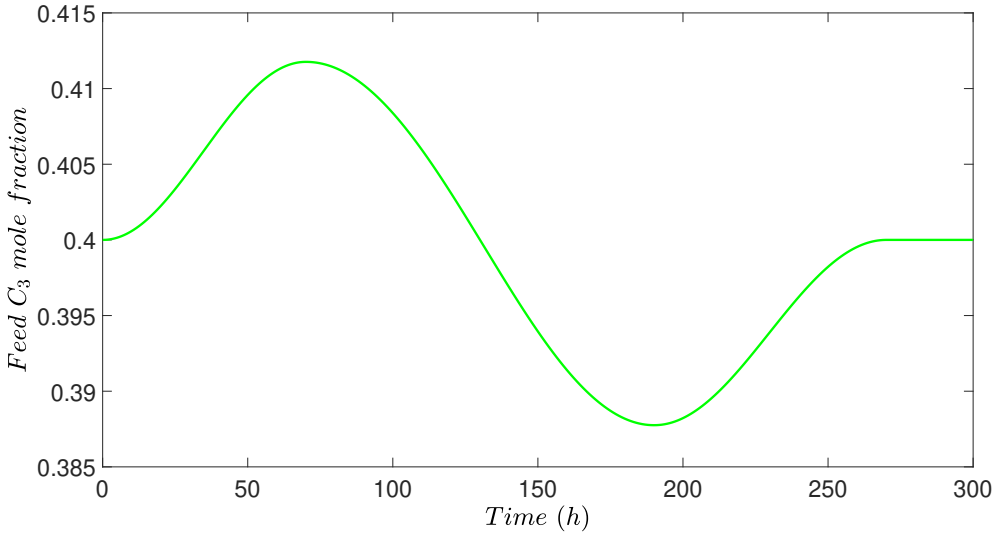

Figure 8.13: The feed concentration profile of the distillation column, which is changing with respect to time.

of feed mole fraction x_F was sent to RTO to optimize the profit. Then, a set of steady-states was achieved from RTO and was sent to the controllers as set-points.

The simulation results are shown in Figs. 8.14 and 8.15. In Fig. 8.14, the set-point of x_D increases as feed concentration x_F increases at the beginning of simulation, because higher distillate concentration is more profitable and more feed concentration x_F allows further separation to achieve a higher concentration in the distillate. The set-point for x_D also decreased later when feed concentration x_F decreased. At the beginning of the simulation, reflux flow increased to reach higher x_D set-points, and reflux flow never reached a steady-state during the whole simulation because the feed component kept changing as shown in Fig. 8.13. In some cases, the mole fraction x_D did not track exactly the set-point because of the ever-changing feed, too small set-point change, and coupled effect with other variables and controllers.

Fig. 8.15 illustrates the performance of temperature controller TC. When the feed x_F increased, the set-point for Tray 7 temperature T_7 decreased according to RTO. The controller then manipulated the reboiler heat duty to track the tray temperature with a good performance as shown in Fig. 8.15. It is noted in Fig. 8.15 that the reboiler heat duty increased as tray temperature decreased at the beginning of the simulation. The reason is that the reboiler heat duty mainly

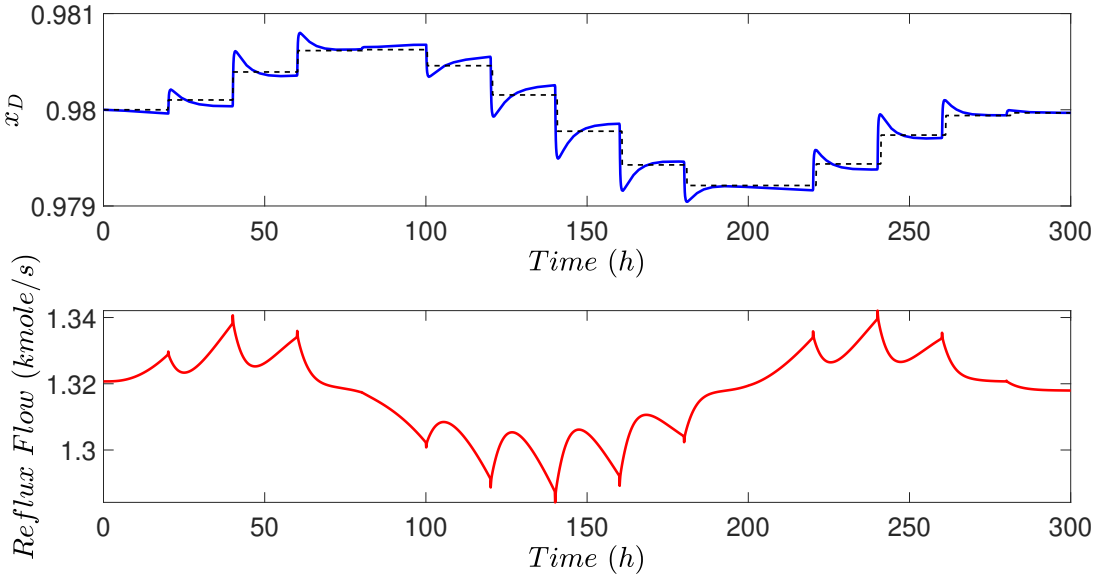

Figure 8.14: Controlled output x_D and manipulated input $reflux\ flow$ for the concentration controller *CC* in the distillation process under the proposed RTO scheme.

dependent on the liquid flow into the reboiler and the vapor flow leaving the reboiler. Since the reflux flow was increased by the concentration controller *CC* at the beginning of simulation, both the liquid flow into the reboiler and vapor leaving the reboiler increased, thus increasing reboiler heat duty.

Other controllers stayed at the fixed set-points throughout the simulation by adjusting their manipulated inputs. Therefore, we are not showing the plots for other controllers. It is demonstrated in Fig. 8.16 that the RTO increased the operation profit when distillation column had a varying feed concentration. The profit in Fig. 8.16 was calculated by the profit definition of Eq. 8.20, using the closed-loop simulation data for variables *D*, *B*, *F*, and *R*. The black line is the operation profit calculated by the closed-loop simulation where the four controllers (*FC*, *PC*, LC_1, and LC_2) had fixed set-points and the two controllers (*CC* and *TC*) had varying set-points from RTO. The blue line is the simulation where the set-points of all controllers were fixed at the initial steady-state and the controlled variables stayed at the initial set-point by adjusting manipulated variables in the presence of the same feed variation in Fig. 8.13. Although the feed concentration kept changing each second and RTO updated the steady-state only each 20 h, the profit was still

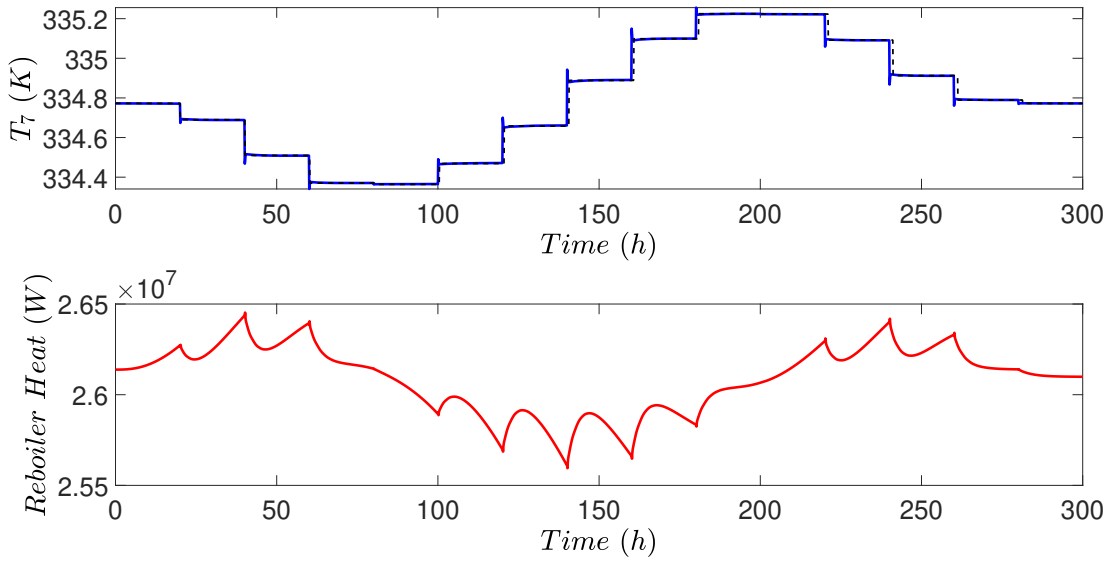

Figure 8.15: Controlled output T_7 and manipulated input *reboiler heat* for the temperature controller TC in the distillation process under the proposed RTO scheme.

improved significantly by RTO, as shown in Fig. 8.16.

In this case study, a neural network model was combined only with the steady-state first-principles model, not the dynamic model. Additionally, it was demonstrated that the steady-states calculated by RTO using a combination of models were very close to the steady-state values in the Aspen simulator, which means that the combination of the neural network model and first-principles model was of high accuracy. The neural network model was used to represent the phase equilibrium properties for RTO to calculate the optimal steady-state in this work. Neural network models can be useful when the phase equilibrium is highly nonlinear such that the first-principles model is inaccurate. Additionally, it can be used when a large number of states are included in thermodynamic equations, such as pressure or more concentrations for the multi-component case.

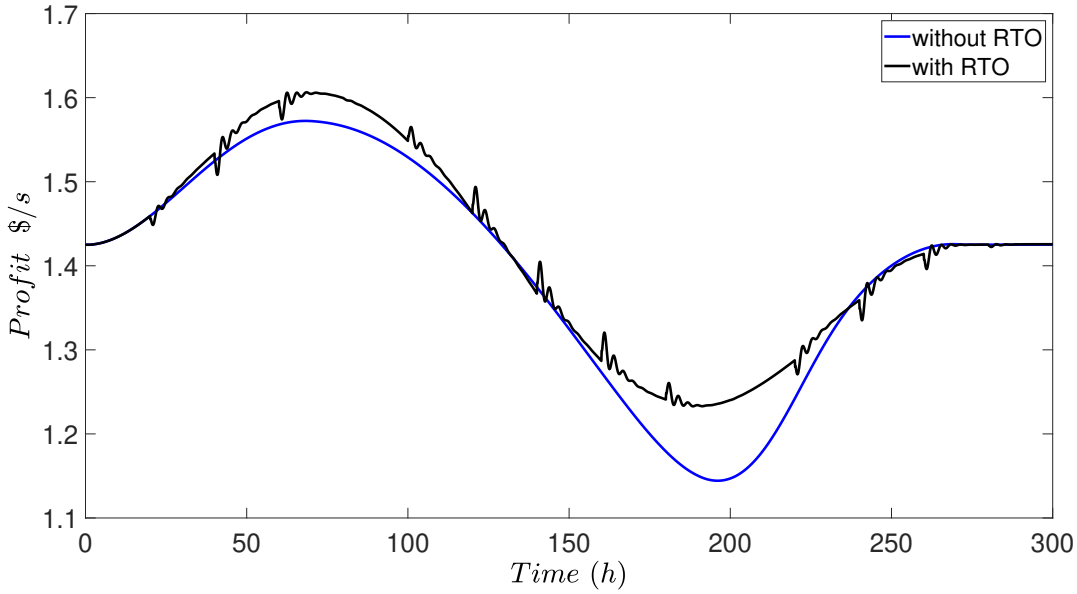

Figure 8.16: Comparison of the operation profit for the distillation process for closed-loop simulations with and without RTO adapting for change in the feed concentration.

8.5 Conclusion

In this chapter, we presented a method for integrating neural network modeling with first-principles modeling in the model used in RTO and MPC. First, a general framework that integrates neural network models with first-principle models in the optimization problems of RTO and MPC was discussed. Then, two chemical process examples were studied in this chapter. In the first case study, a CSTR with reversible exothermic reaction was utilized to analyze the performance of integrating the neural network model and first-principles model in RTO and MPC. Specifically, a neural network was first built to represent the nonlinear reaction rate. An RTO was designed to find the operating steady-state providing the optimal balance between the energy cost and reactant conversion. Then, an LMPC was designed to stabilize the process to the optimal operating condition. A variation in energy price was introduced, and the simulation results demonstrated that RTO minimized the operation cost and yielded a closed-loop performance that was very close to the one attained by RTO/MPC using the first-principles model. In the second case study, a distillation column was studied to demonstrate an application to a large-scale chemical process. A

neural network was first trained to obtain the phase equilibrium properties. An RTO scheme was designed to maximize the operation profit and calculate the optimal set-points for the controllers using a neural network model with a first-principles model. A variation in the feed concentration was introduced to demonstrate that RTO increased operation profit for all considered conditions. In closing, it is important to note that the two simulation studies only demonstrated how the proposed approach can be applied and provided some type of "proof of concept" on the use of hybrid models in RTO and MPC, but certainly, both examples yield limited conclusions and cannot substitute for an industrial/experimental implementation to evaluate the proposed approach, which would be the subject of future work.

Chapter 9

Conclusion

This dissertation provided a number of methods and case studies to demonstrate the integration of safety considerations and controller design. Dynamic interaction between feedback control and safety systems was first discussed and then illustrated with examples of both classical and model-based controllers. Following that, a Safeness-Index based model predictive control was applied to two chemical processes to enhance process operational safety. Additionally, several other large-scale industrial processes were studied to demonstrate the improvement of process operational safety by the proposed controller designs. Finally, a method for combining neural network models with first-principles models in both RTO and MPC was presented and applied to two chemical process examples to demonstrate its effectiveness.

In Chapters 2 and 3, we considered two case studies to analyze the dynamic interactions between control and safety systems. In Chapter 2, an LMPC control system was integrated with safety systems for the MIC reaction in a CSTR to avoid dangerous thermal runway phenomenon. The proposed LMPC was able to maintain the closed-loop system inside the stability region in the presence of small disturbances. In the presence of large disturbances, it was demonstrated that an LMPC integrated with a safety system could maintain process safety in the sense of avoiding thermal runaway and driving the process state back into the stability region even after exiting it. In Chapter 3, a flash drum under PI control integrated with a pressure relief valve as safety system

was investigated. In this study, we demonstrated that modifying the parameters of a PI controller based on the activation status of the safety system can lead to improved closed-loop performance compared to the case in which the parameters of the PI controller remain fixed regardless of the actions of the safety system.

In Chapters 4 and 5, two applications of Safeness Index-based model predictive control to improve process operational safety in safety critical chemical processes were demonstrated. In Chapter 4, a high-pressure flash drum separator together with pressure relief valve as safety system was utilized to analyze the benefits of integrating Safeness Index-based considerations in model predictive control. It was demonstrated that in the presence of a small disturbance, Safeness Index-based MPC ensured that the drum pressure remained below the opening pressure of relief valve such that the safety system was not activated. However, in the presence of a large disturbance, the controller working together with the relief valve ensured process operational safety before, during and after the pressure relief valve was turned on/off. In Chapter 5, an ammonia process with four units was simulated in Aspen Plus Dynamics to demonstrate the application of Safeness Index. An MPC with the Safeness Index-based constraints and the feedforward disturbance compensation term was developed to ensure process operational safety in the presence of a significant propagated disturbance to methanation unit.

In Chapter 6, a multi-unit ammonia process network was simulated to demonstrate the integration of process safety and control systems. Catalyst deactivation in shift reactor was introduced into the dynamic simulations, which propagated from upstream units to downstream units and finally caused a dramatic temperature increase in the methanation unit. Two model-based controllers were designed to improve process operational safety in the entire ammonia process network. The first controller was an MPC with an integral term that controls the high-temperature shift reactor. The second controller was a Safeness Index-based MPC that controls the methanator. Closed-loop simulations demonstrated that extremely high temperature was avoided under the proposed controllers in the presence of significant disturbances.

In Chapter 7, we demonstrated that process operational safety was improved with an offset-free

model predictive controller to avoid a fluid catalytic cracking process accident, which occurred in the refinery operated by ExxonMobil in 2015 in Torrance, California. This work reproduced and tackled the accident by dynamical modeling of the FCC process with disturbances to simulate the accident conditions and other dangerous situations. An MPC with augmented state to obtain offset-free performance was designed to improve process operational safety in the sense that the accident and other potential dangerous scenarios could be avoided. Closed-loop simulations demonstrated that the accident could have been avoided with the proposed controller under the reported accident conditions and other potential dangerous situations.

In Chapter 8, we presented a method for integrating neural network modeling with first-principles modeling in the model used in RTO and MPC. First, the proposed methodology that integrates a neural network model and a first-principles model in the optimization problems of RTO and MPC was discussed. Then, two chemical process examples were presented in this chapter. In the first case study, a CSTR with reversible exothermic reaction was utilized to analyze the performance of integrating the neural network model and first-principles model in RTO and MPC. Specifically, a neural network was first built to represent the nonlinear reaction rate. An RTO was designed to find the operating steady-state providing the optimal balance between the energy cost and reactant conversion. Then, an LMPC was designed to stabilize the process to the optimal operating condition. A variation in energy price was introduced, and the simulation results demonstrated that the RTO minimized the operation cost and yielded a closed-loop performance that was very close to the one attained by RTO/MPC using the first-principles model. In the second case study, a distillation column was studied to demonstrate an application to a large-scale chemical process. A neural network was first trained to obtain the phase equilibrium properties. An RTO scheme was designed to maximize the operation profit and calculate the optimal set-points for the controllers using a neural network model combined with a first-principles model. A variation in the feed concentration was introduced to demonstrate that RTO increased operation profit for all considered conditions.

Bibliography

[1] C. Agbi, Z. Song, and B. Krogh. Parameter identifiability for multi-zone building models. In *Proceedings of the 51st IEEE Conference on Decision and Control*, pages 6951–6956, Maui, Hawaii, 2012.

[2] T. M. Ahooyi, M. Soroush, J. E. Arbogast, W. D. Seider, and U. G. Oktem. Model-predictive safety system for proactive detection of operation hazards. *AIChE Journal*, 62:2024–2042, 2016.

[3] AIChE. *Dow's Chemical Exposure Index Guide*. AIChE, New York, New York, first edition, 1994.

[4] AIChE. *Dow's Fire and Explosion Index Hazard Classification Guide*. AIChE, New York, New York, seventh edition, 1994.

[5] K. I. Al-Malah. *Aspen Plus: chemical engineering applications*. John Wiley & Sons, 2016.

[6] F. Albalawi, A. Alanqar, H. Durand, and P. D. Christofides. A feedback control framework for safe and economically-optimal operation of nonlinear processes. *AIChE Journal*, 62:2391–2409, 2016.

[7] F. Albalawi, H. Durand, A. Alanqar, and P. D. Christofides. Achieving operational process safety via model predictive control. *Journal of Loss Prevention in the Process Industries*, 53:74–88, 2018.

[8] F. Albalawi, H. Durand, and P. D. Christofides. Distributed economic model predictive control for operational safety of nonlinear processes. *AIChE Journal*, 63:3404–3418, 2017.

[9] F. Albalawi, H. Durand, and P. D. Christofides. Process operational safety using model predictive control based on a process Safeness Index. *Computers and Chemical Engineering*, 104:76–88, 2017.

[10] F. Alhabdan and S. Elnashaie. Simulation of an ammonia plant accident using rigorous heterogeneous models: Effect of shift converter disturbances on the methanator. *Mathematical and Computer Modelling*, 21:85–106, 1995.

[11] J. T. Allen and N. H. El-Farra. A model-based framework for fault estimation and accommodation applied to distributed energy resources. *Renewable Energy*, 100:35–43, 2017.

[12] F. Alrowaie, R. B. Gopaluni, and K. E. Kwok. Alarm design for nonlinear stochastic systems. In *Proceedings of the World Congress on Intelligent Control and Automation*, pages 473–479, Shenyang, China, 2014.

[13] R. Amrit, J. B. Rawlings, and D. Angeli. Economic optimization using model predictive control with a terminal cost. *Annual Reviews in Control*, 35:178–186, 2011.

[14] R. Amrit, J. B. Rawlings, and L. T. Biegler. Optimizing process economics online using model predictive control. *Computers and Chemical Engineering*, 58:334–343, 2013.

[15] M. Appl. *Ammonia, Ullmann's Encyclopedia of Industrial Chemistry*. Wiley Online Library, 2000.

[16] A. Araújo and S. Skogestad. Control structure design for the ammonia synthesis process. *Computers and Chemical Engineering*, 32:2920–2932, 2008.

[17] M. Argyle and C. Bartholomew. Heterogeneous catalyst deactivation and regeneration: a review. *Catalysts*, 5:145–269, 2015.

[18] B. M. S. Arifin and M. A. A. S. Choudhury. An alternative approach of risk analysis for multivariable alarm system. *Journal of Chemical Engineering, IEB*, 26:75–79, 2011.

[19] Aspen Technology, Inc. *Aspen Plus user guide*. Aspen Technology, Inc., Cambridge, MA., 2003.

[20] Aspen Technology, Inc. *Aspen Plus ammonia model*. Aspen Technology, Inc., Bedford, MA., 2017.

[21] E. Bakolas and J. H. Saleh. Augmenting the traditional defense-in-depth strategy with the concept of a diagnosable safety architecture. In R. Briš, C. G. Soares, and S. Martorell, editors, *Reliability, Risk and Safety: Theory and Applications*, volume 3, pages 2113–2122. CRC Press/Balkema, Leiden, Netherlands, 2010.

[22] B. R. Bakshi, A. Koulouris, and G. Stephanopoulos. Wave-nets: novel learning techniques, and the induction of physically interpretable models. In *Wavelet Applications*, volume 2242, pages 637–648. International Society for Optics and Photonics, 1994.

[23] R. Ball. Oscillatory thermal instability and the Bhopal disaster. *Process Safety and Environmental Protection*, 89:317–322, 2011.

[24] N. Bhutani, G. P. Rangaiah, and A. K. Ray. First-principles, data-based, and hybrid modeling and optimization of an industrial hydrocracking unit. *Industrial & Engineering Chemistry Research*, 45:7807–7816, 2006.

[25] C. M. Bishop. *Pattern recognition and machine learning*. Springer, 2006.

[26] T. I. Bø and T. A. Johansen. Dynamic safety constraints by scenario based economic model predictive control. In *Proceedings of the IFAC World Congress*, pages 9412–9418, Cape Town, South Africa, 2014.

[27] R. Brooks, R. Thorpe, and J. Wilson. A new method for defining and managing process alarms and for correcting process operation when an alarm occurs. *Journal of Hazardous Materials*, 115:169–174, 2004.

[28] N. Brown. Alarm management/The EEMUA guidelines in practice. *Measurement and Control*, 36:114–119, 2003.

[29] E. F. Camacho and C. Bordons. *Model Predictive Control*. Springer-Verlag, London, England, second edition, 2007.

[30] M. Câmara, A. Quelhas, and J. Pinto. Performance evaluation of real industrial RTO systems. *Processes*, 4:44–64, 2016.

[31] J. S. Campbell. Influences of catalyst formulation and poisoning on the activity and die-off of low temperature shift catalysts. *Industrial and Engineering Chemistry Process Design and Development*, 9:588–595, 1970.

[32] D. Chaffart and L. A. Ricardez-Sandoval. Optimization and control of a thin film growth process: A hybrid first principles/artificial neural network based multiscale modelling approach. *Computers and Chemical Engineering*, 119:465–479, 2018.

[33] J. Chang, S. Lu, and Y. Chiu. Dynamic modeling of batch polymerization reactors via the hybrid neural-network rate-function approach. *Chemical Engineering Journal*, 130:19–28, 2007.

[34] Y. Chang, F. Khan, and S. Ahmed. A risk-based approach to design warning system for processing facilities. *Process Safety and Environmental Protection*, 89:310–316, 2011.

[35] L. Chen, O. Bernard, G. Bastin, and P. Angelov. Hybrid modelling of biotechnological processes using neural networks. *Control Engineering Practice*, 8:821–827, 2000.

[36] A. Chouai, S. Laugier, and D. Richon. Modeling of thermodynamic properties using neural networks: Application to refrigerants. *Fluid Phase Equilibria*, 199:53–62, 2002.

[37] P. D. Christofides, R. Scattolini, D. Muñoz de la Peña, and J. Liu. Distributed model predictive control: A tutorial review and future research directions. *Computers and Chemical Engineering*, 51:21–41, 2013.

[38] A. Çinar, A. Palazoglu, and F. Kayihan. *Chemical Process Performance Evaluation*. CRC Press, Boca Raton, Florida, 2007.

[39] R. V. Cowlagi and J. H. Saleh. Coordinability and consistency: Application of systems theory to accident causation and prevention. *Journal of Loss Prevention in the Process Industries*, 33:200–212, 2015.

[40] D. A. Crowl and J. F. Louvar. *Chemical Process Safety: Fundamentals with Applications*. Pearson Education, Upper Saddle River, New Jersey, third edition, 2011.

[41] D. A. Crowl and S. A. Tipler. Sizing pressure-relief devices. *Chemical Engineering Progress*, pages 68–76, 2013.

[42] CSB. *ExxonMobil Presentation: Transcript from 1.13.2016 Public Meeting*, 2017. https://www.csb.gov/exxonmobil-refinery-explosion-/.

[43] CSB. *ExxonMobil Torrance Refinery Final CSB Investigation Report*, 2017. https://www.csb.gov/exxonmobil-refinery-explosion-/.

[44] T. A. Czuppon, S. A. Knez, and J. M. Rovner. *Ammonia, Kirk-Othmer Encyclopedia of Chemical Technology*. Wiley Online Library, 1992.

[45] P. Daoutidis and C. Kravaris. Dynamic output feedback control of minimum-phase multivariable nonlinear processes. *Chemical Engineering Science*, 49:433–447, 1994.

[46] M. Diehl, R. Amrit, and J. B. Rawlings. A Lyapunov function for economic optimizing model predictive control. *IEEE Transactions on Automatic Control*, 56:703–707, 2011.

[47] P. D. Domanski, S. Golonka, R. Jankowski, P. Kalbarczyk, and B. Moszowski. Control rehabilitation impact on production efficiency of ammonia synthesis installation. *Industrial and Engineering Chemistry Research*, 55:10366–10376, 2016.

[48] C. G. Economou, M. Morari, and B. O. Palsson. Internal model control: Extension to nonlinear system. *Industrial & Engineering Chemistry Process Design and Development*, 25:403–411, 1986.

[49] EEMUA. *Alarm Systems - A Guide to Design, Management and Procurement*. Engineering Equipment and Materials Users Association, London, England, 2013.

[50] M. Ellis, H. Durand, and P. D. Christofides. A tutorial review of economic model predictive control methods. *Journal of Process Control*, 24:1156–1178, 2014.

[51] M. Ellis, H. Durand, and P. D. Christofides. Elucidation of the role of constraints in economic model predictive control. *Annual Reviews in Control*, 41:208–217, 2016.

[52] M. Ellis, J. Liu, and P. D. Christofides. *Economic Model Predictive Control: Theory, Formulations and Chemical Process Applications*. Springer, London, England, 2016.

[53] H. M. Ettouney, H. I. Shaban, and L. J. Nayfeh. Theoretical analysis of high and low temperature shift converters. *Chemical Engineering Communications*, 134:1–16, 1995.

[54] C. A. Faúndez, F. A. Quiero, and J. Valderrama. Phase equilibrium modeling in ethanol+ congener mixtures using an artificial neural network. *Fluid Phase Equilibria*, 292:29–35, 2010.

[55] J. L. Fernandes, J. J. Verstraete, C. I. Pinheiro, N. M. Oliveira, and F. R. Ribeiro. Dynamic modelling of an industrial R2R FCC unit. *Chemical Engineering Science*, 62:1184–1198, 2007.

[56] Center for Chemical Process Safety. *Guidelines for Hazard Evaluation Procedures*. John Wiley and Sons, Inc., Hoboken, New Jersey, third edition, 2008.

[57] K. Fu, G. Chen, T. Sema, X. Zhang, Z. Liang, R. Idem, and P. Tontiwachwuthikul. Experimental study on mass transfer and prediction using artificial neural network for CO_2 absorption into aqueous deta. *Chemical Engineering Science*, 100:195–202, 2013.

[58] S. Gajjar and A. Palazoglu. A data-driven multidimensional visualization technique for process fault detection and diagnosis. *Chemometrics and Intelligent Laboratory Systems*, 154:122–136, 2016.

[59] I. M. Galván, J. M. Zaldívar, H. Hernandez, and E. Molga. The use of neural networks for fitting complex kinetic data. *Computers and Chemical Engineering*, 20:1451–1465, 1996.

[60] M. Gentile, W. J. Rogers, and M. S. Mannan. Development of an inherent safety index based on fuzzy logic. *AIChE Journal*, 49:959–968, 2003.

[61] P. Georgieva, M. J. Meireles, and S. F. de Azevedo. Knowledge-based hybrid modelling of a batch crystallisation when accounting for nucleation, growth and agglomeration phenomena. *Chemical Engineering Science*, 58:3699–3713, 2003.

[62] G. Goble and T. Stauffer. Don't be alarmed: Avoid unplanned downtime from alarm overload, use top techniques to improve alarm management. *InTech Magazine*, 54:42–46, 2007.

[63] M. J. Godfrey. Implementing continuous improvement in hazard studies. In *SPE International Conference and Exhibition on Health, Safety, Security, Environment, and Social Responsibility*. Society of Petroleum Engineers, 2018.

[64] J. Gong and F. You. Optimal design and synthesis of algal biorefinery processes for biological carbon sequestration and utilization with zero direct greenhouse gas emissions: MINLP model and global optimization algorithm. *Industrial and Engineering Chemistry Research*, 53:1563–1579, 2014.

[65] D. Gonzales, T. R. Gulden, A. Strong, and W. Hoyle. *Cost-benefit Analysis of Proposed California Oil and Gas Refinery Regulations*. Rand Corporation, 2016.

[66] I. Goodfellow, Y. Bengio, and A. Courville. *Deep learning*. MIT press, 2016.

[67] J. E. A. Graciano, J. Jäschke, G. A. Le Roux, and L. T. Biegler. Integrating self-optimizing control and real-time optimization using zone control mpc. *Journal of Process Control*, 34:35–48, 2015.

[68] J. P. Gupta and D. W. Edwards. Inherently safer design - Present and future. *Process Safety and Environmental Protection*, 80:115–125, 2002.

[69] I. Hace. The pressure relief system design for industrial reactors. *Journal of Industrial Engineering*, 2013:1–14, 2013.

[70] S. Haykin. *Neural networks: a comprehensive foundation*. Prentice Hall PTR, 1994.

[71] C. He and F. You. Shale gas processing integrated with ethylene production: Novel process designs, exergy analysis, and techno-economic analysis. *Industrial and Engineering Chemistry Research*, 53:11442–11459, 2014.

[72] M. Heidarinejad, J. Liu, and P. D. Christofides. Economic model predictive control of nonlinear process systems using Lyapunov techniques. *AIChE Journal*, 58:855–870, 2012.

[73] A. M. Heikkilä, M. Hurme, and M. Järveläinen. Safety considerations in process synthesis. *Computers and Chemical Engineering*, 20:S115–S120, 1996.

[74] D. M. Himmelblau. Applications of artificial neural networks in chemical engineering. *Korean Journal of Chemical Engineering*, 17:373–392, 2000.

[75] M. Hosseinzadeh, A. Cotorruelo, D. Limon, and E. Garone. Constrained control of linear systems subject to combinations of intersections and unions of concave constraints. *IEEE Control Systems Letters*, 3:571–576, 2019.

[76] R. Huang, L. T. Biegler, and E. Harinath. Robust stability of economically oriented infinite horizon NMPC that include cyclic processes. *Journal of Process Control*, 22:51–59, 2012.

[77] J. Isimite and P. Rubini. A dynamic HAZOP case study using the Texas City refinery explosion. *Journal of Loss Prevention in the Process Industries*, 40:496–501, 2016.

[78] P. Jain, H. J. Pasman, S. Waldram, E. N. Pistikopoulos, and M. S. Mannan. Process resilience analysis framework (PRAF): A systems approach for improved risk and safety management. *Journal of Loss Prevention in the Process Industries*, 53:61–73, 2018.

[79] J. Janošovskỳ, M. Danko, J. Labovskỳ, and L. Jelemenskỳ. The role of a commercial process simulator in computer aided HAZOP approach. *Process Safety and Environmental Protection*, 107:12–21, 2017.

[80] M. Kettunen, P. Zhang, and S. L. Jämsä-Jounela. An embedded fault detection, isolation and accommodation system in a model predictive controller for an industrial benchmark process. *Computers and Chemical Engineering*, 32:2966–2985, 2008.

[81] F. Khan and P. R. Amyotte. How to make inherent safety practice a reality. *The Canadian Journal of Chemical Engineering*, 81:2–16, 2003.

[82] F. Khan, S. J. Hashemi, N. Paltrinieri, P. Amyotte, V. Cozzani, and G. Reniers. Dynamic risk management: a contemporary approach to process safety management. *Current Opinion in Chemical Engineering*, 14:9–17, 2016.

[83] F. I. Khan and S. Abbasi. Major accidents in process industries and an analysis of causes and consequences. *Journal of Loss Prevention in the Process Industries*, 12:361–378, 1999.

[84] K. Khorsand, M. A. Marvast, N. Pooladian, and M. Kakavand. Modeling and simulation of methanation catalytic reactor in ammonia unit. *Petroleum and Coal*, 49:46–53, 2007.

[85] K. Kidam and M. Hurme. Analysis of equipment failures as contributors to chemical process accidents. *Process Safety and Environmental Protection*, 91:61–78, 2013.

[86] T. Kletz. *What Went Wrong? - Case Histories of Process Plant Disasters and How They Could Have Been Avoided*. Elsevier, Burlington, Massachusetts, fifth edition, 2009.

[87] C. C. Klimasauskas. Hybrid modeling for robust nonlinear multivariable control. *ISA Transactions*, 37:291–297, 1998.

[88] A. L. Kohl and R. Nielsen. *Gas purification*. Gulf Publishing Co., Houston, USA, 1997.

[89] A. Kummer and T. Varga. Process simulator assisted framework to support process safety analysis. *Journal of Loss Prevention in the Process Industries*, 58:22–29, 2019.

[90] L. Lao, M. Ellis, and P. D. Christofides. Proactive fault-tolerant model predictive control. *AIChE Journal*, 59:2810–2820, 2013.

[91] M. Lee and S. Park. A new scheme combining neural feedforward control with model-predictive control. *AIChE Journal*, 38:193–200, 1992.

[92] W. J. Lee, J. Na, K. Kim, C. J. Lee, Y. Lee, and J. M. Lee. NARX modeling for real-time optimization of air and gas compression systems in chemical processes. *Computers and Chemical Engineering*, 115:262–274, 2018.

[93] N. G. Leveson and G. Stephanopoulos. A system-theoretic, control-inspired view and approach to process safety. *AIChE Journal*, 60:2–14, 2014.

[94] Y. Lin and E. Sontag. A universal formula for stabilization with bounded controls. *Systems & Control Letters*, 16:393–397, 1991.

[95] P. Liu, E. N. Pistikopoulos, and Z. Li. A multi-objective optimization approach to polygeneration energy systems design. *AIChE Journal*, 56:1218–1234, 2010.

[96] Y. Lu, M. Rajora, P. Zou, and S. Liang. Physics-embedded machine learning: case study with electrochemical micro-machining. *Machines*, 5:4–15, 2017.

[97] W. L. Luyben. Use of dynamic simulation for reactor safety analysis. *Computers and Chemical Engineering*, 40:97–109, 2012.

[98] W. L. Luyben. *Distillation design and control using Aspen simulation*. John Wiley & Sons, 2013.

[99] W. L. Luyben. Plantwide control of a coupled reformer/ammonia process. *Chemical Engineering Research and Design*, 134:518–527, 2018.

[100] D. Manca and S. Brambilla. Dynamic simulation of the BP Texas City refinery accident. *Journal of Loss Prevention in the Process Industries*, 25:950–957, 2012.

[101] M. S. Mannan, S. Sachdeva, H. Chen, O. Reyes-Valdes, Y. Liu, and D. M. Laboureur. Trends and challenges in process safety. *AIChE Journal*, 61:3558–3569, 2015.

[102] S. Mannan. *Lees' Loss Prevention in the Process Industries - Hazard Identification, Assessment and Control*. Elsevier, Waltham, Massachusetts, fourth edition, 2012.

[103] T. Marlin. *Process Control: Designing Process and Control Systems for Dynamic Performance*. McGraw-Hill, New York, 1995.

[104] T. Marlin. Operability in process design: Achieving safe, profitable, and robust process operations. *Ontario, Canada: McMaster University*, 2012.

[105] Marsh & McLennan Companies Inc. The 100 largest losses 1974-2015: Large property damage losses in the hydrocarbon industry. Technical report, Marsh & McLennan Companies Inc., 2016.

[106] I. Martínez, D. Armaroli, M. Gazzani, and M. C. Romano. Integration of the Ca–Cu process in ammonia production plants. *Industrial and Engineering Chemistry Research*, 56:2526–2539, 2017.

[107] D. Q. Mayne, J. B. Rawlings, C. V. Rao, and P. O. M. Scokaert. Constrained model predictive control: Stability and optimality. *Automatica*, 36:789–814, 2000.

[108] A. Meel and W. D. Seider. Plant-specific dynamic failure assessment using Bayesian theory. *Chemical Engineering Science*, 61:7036–7056, 2006.

[109] D. I. Mendoza-Serrano and D. J. Chmielewski. Smart grid coordination in building HVAC systems: EMPC and the impact of forecasting. *Journal of Process Control*, 24:1301–1310, 2014.

[110] P. Mhaskar, N. H. El-Farra, and P. D. Christofides. Stabilization of nonlinear systems with state and control constraints using Lyapunov-based predictive control. *Systems and Control Letters*, 55:650–659, 2006.

[111] P. Mhaskar, J. Liu, and P. D. Christofides. *Fault-Tolerant Process Control: Methods and Applications*. Springer-Verlag, London, England, 2013.

[112] M. Morari and J. H. Lee. Model predictive control: Past, present and future. *Computers and Chemical Engineering*, 23:667–682, 1999.

[113] J. C. Morud and S. Skogestad. Analysis of instability in an industrial ammonia reactor. *AIChE Journal*, 44:888–895, 1998.

[114] I. H. Moskowitz, W. D. Seider, J. E. Arbogast, U. G. Oktem, A. Pariyani, and M. Soroush. Improved predictions of alarm and safety system performance through process and operator response-time modeling. *AIChE Journal*, 62:3461–3472, 2016.

[115] E. Naghoosi, I. Izadi, and T. Chen. Estimation of alarm chattering. *Journal of Process Control*, 21:1243–1249, 2011.

[116] R. Nayak-Luke, R. Bañares-Alcántara, and I. Wilkinson. Green ammonia: Impact of renewable energy intermittency on plant sizing and levelized cost of ammonia. *Industrial and Engineering Chemistry Research*, 57:14607–14616, 2018.

[117] M. Naysmith and P. Douglas. Review of real time optimization in the chemical process industries. *Developments in Chemical Engineering and Mineral Processing*, 3:67–87, 1995.

[118] A. M. Niziolek, O. Onel, M. M. F. Hasan, and C. A. Floudas. Municipal solid waste to liquid transportation fuels - Part II: Process synthesis and global optimization strategies. *Computers and Chemical Engineering*, 74:184–203, 2015.

[119] R. M. Noor, Z. Ahmad, M. M. Don, and M. H. Uzir. Modelling and control of different types of polymerization processes using neural networks technique: a review. *The Canadian Journal of Chemical Engineering*, 88:1065–1084, 2010.

[120] R. S. Ocampo. Examination of methanation vessel after overheating—a case study. *Materials and Corrosion*, 47:392–396, 1996.

[121] M. Ojha and A. Dhiman. Problem, failure and safety analysis of ammonia plant: a review. *International Review of Chemical Engineering*, 2:631–646, 2010.

[122] R. Oliveira. Combining first principles modelling and artificial neural networks: a general framework. *Computers and Chemical Engineering*, 28:755–766, 2004.

[123] B. P. Omell and D. J. Chmielewski. IGCC power plant dispatch using infinite-horizon economic model predictive control. *Industrial and Engineering Chemistry Research*, 52:3151–3164, 2013.

[124] C. C. Pantelides and J. G. Renfro. The online use of first-principles models in process operations: Review, current status and future needs. *Computers and Chemical Engineering*, 51:136–148, 2013.

[125] I. A. Papazoglou and O. N. Aneziris. Master logic diagram: method for hazard and initiating event identification in process plants. *Journal of Hazardous Materials*, 97:11–30, 2003.

[126] V. Pattabathula and J. Richardson. Introduction to ammonia production. *Chemical Engineering Progress*, 112:69–75, 2016.

[127] P. Peng, H. Nguyen, M. P. Harold, and D. Luss. Spatio-temporal phenomena in monolithic reactors measured by combined spatially-resolved mass spectrometry and optical frequency domain reflectometry. In *Advances in Chemical Engineering*, volume 50, pages 83–130. Elsevier, 2017.

[128] C. I. Pinheiro, J. L. Fernandes, L. Domingues, A. J. Chambel, I. Graca, N. M. Oliveira, H. S. Cerqueira, and F. R. Ribeiro. Fluid catalytic cracking (FCC) process modeling, simulation, and control. *Industrial and Engineering Chemistry Research*, 51:1–29, 2011.

[129] D. C. Psichogios and L. H. Ungar. A hybrid neural network-first principles approach to process modeling. *AIChE Journal*, 38:1499–1511, 1992.

[130] S. J. Qin and T. A. Badgwell. A survey of industrial model predictive control technology. *Control Engineering Practice*, 11:733–764, 2003.

[131] A. D. Quelhas, N. J. C. de Jesus, and J. C. Pinto. Common vulnerabilities of RTO implementations in real chemical processes. *The Canadian Journal of Chemical Engineering*, 91:652–668, 2013.

[132] M. R. Rahimpour, M. R. Dehnavi, F. Allahgholipour, D. Iranshahi, and S. M. Jokar. Assessment and comparison of different catalytic coupling exothermic and endothermic reactions: a review. *Applied Energy*, 99:496–512, 2012.

[133] J. B. Rawlings. Tutorial overview of model predictive control. *IEEE Control Systems Magazine*, 20:38–52, 2000.

[134] J. B. Rawlings and R. Amrit. Optimizing process economic performance using model predictive control. In *Nonlinear Model Predictive Control*, pages 119–138. Springer, 2009.

[135] J. B. Rawlings, D. Angeli, and C. N. Bates. Fundamentals of economic model predictive control. In *Proceedings of the 51st IEEE Conference on Decision and Control*, pages 3851–3861, Maui, Hawaii, 2012.

[136] J. B. Rawlings, D. Bonné, J. B. Jørgensen, A. N. Venkat, and S. B. Jørgensen. Unreachable setpoints in model predictive control. *IEEE Transactions on Automatic Control*, 53:2209–2215, 2008.

[137] S. Rönsch, J. Schneider, S. Matthischke, M. Schlüter, M. Götz, J. Lefebvre, P. Prabhakaran, and S. Bajohr. Review on methanation–from fundamentals to current projects. *Fuel*, 166:276–296, 2016.

[138] D. H. Rothenberg. *Alarm Management for Process Control: A Best-Practice Guide for Design, Implementation, and Use of Industrial Alarm Systems*. Momentum Press, New York, New York, 2009.

[139] D. P. Rounthwaite. Improved ammonia plant catalysts. Pressure drop can be minimized using appropriately sized reforming catalysts, water-resistant high-temperature shift catalysts, and a new generation of low-temperature shift catalysts. *Process Safety Progress*, 2:127–131, 1983.

[140] M. Rovaglio, D. Manca, and F. Cortese. A reliable control for the ammonia loop facing limit-cycle and snowball effects. *AIChE Journal*, 50:1229–1241, 2004.

[141] N. Roy, F. Eljack, A. Jimenez-Gutierrez, B. Zhang, P. Thiruvenkataswamy, M. El-Halwagi, and M. S. Mannan. A review of safety indices for process design. *Current Opinion in Chemical Engineering*, 14:42–48, 2016.

[142] J. H. Saleh, R. A. Haga, F. M. Favarò, and E. Bakolas. Texas City refinery accident: Case study in breakdown of defense-in-depth and violation of the safety–diagnosability principle in design. *Engineering Failure Analysis*, 36:121–133, 2014.

[143] A. Schuppert and T. Mrziglod. Hybrid model identification and discrimination with practical examples from the chemical industry. In *Hybrid Modeling in Process Industries*, pages 63–88. CRC Press, 2018.

[144] A. M. Schweidtmann and A. Mitsos. Deterministic global optimization with artificial neural networks embedded. *Journal of Optimization Theory and Applications*, 180:925–948, 2019.

[145] Y. Seo, D. Seo, Y. Seo, and W. Yoon. Investigation of the characteristics of a compact steam reformer integrated with a water-gas shift reactor. *Journal of Power Sources*, 161:1208–1216, 2006.

[146] M. J. Shah. Control simulation in ammonia production. *Industrial and Engineering Chemistry*, 59:72–83, 1967.

[147] M. J. Shah and A. J. Weisenfelder. Control and optimization of a large ammonia plant with a digital computer. *Automatica*, 5:319–333, 1969.

[148] H. Sildir, Y. Arkun, U. Canan, S. Celebi, U. Karani, and I. Er. Dynamic modeling and optimization of an industrial fluid catalytic cracker. *Journal of Process Control*, 31:30–44, 2015.

[149] H. Smith, C. Howard, and T. Foord. Alarms management/Priority, floods, tears or gain? Introduction to the "problem". *Measurement and Control*, 36:109–113, 2003.

[150] R. Srinivasan, J. Liu, K. W. Lim, K. C. Tan, and W. K. Ho. Intelligent alarm management in a petroleum refinery. *Hydrocarbon Processing*, 83:47–53, 2004.

[151] K. Takeda, T. Hamaguchi, M. Noda, N. Kimura, and T. Itoh. Use of two-layer cause-effect model to select source of signal in plant alarm system. In R. Setchi, I. Jordanov, R. J. Howlett, and L. C. Jain, editors, *Knowledge-Based and Intelligent Information and Engineering Systems: 14th International Conference, KES 2010, Cardiff, UK, September 8-10, 2010, Proceedings, Part II*, pages 381–388. Springer-Verlag, Berlin, Germany, 2010.

[152] J. C. O. Toro, I. Dobrosz-Gómez, and M. Á. G. García. Dynamic modeling and bifurcation analysis for the methyl isocyanate hydrolysis reaction. *Journal of Loss Prevention in the Process Industries*, 39:106–111, 2016.

[153] A. Y. D. Tsen, S. S. Jang, D. S. H. Wong, and B. Joseph. Predictive control of quality in batch polymerization using hybrid ANN models. *AIChE Journal*, 42:455–465, 1996.

[154] M. V. Twigg. *Catalyst handbook*. Wolfe Publishing Ltd., London, 1989.

[155] H. Van Dijk, J. Boon, R. N. Nyqvist, and R. W. Van Den Brink. Development of a single stage heat integrated water–gas shift reactor for fuel processing. *Chemical Engineering Journal*, 159:182–189, 2010.

[156] V. Venkatasubramanian. Systemic failures: Challenges and opportunities in risk management in complex systems. *AIChE Journal*, 57:2–9, 2011.

[157] V. Venkatasubramanian. The promise of artificial intelligence in chemical engineering: Is it here, finally? *AIChE Journal*, 65:466–478, 2019.

[158] V. Venkatasubramanian, R. Rengaswamy, and S. N. Kavuri. A review of process fault detection and diagnosis: Part II: Qualitative models and search strategies. *Computers and Chemical Engineering*, 27:313–326, 2003.

[159] V. Venkatasubramanian, J. Zhao, and S. Viswanathan. Intelligent systems for HAZOP analysis of complex process plants. *Computers and Chemical Engineering*, 24:2291–2302, 2000.

[160] L. Vernières-Hassimi and S. Leveneur. Alternative method to prevent thermal runaway in case of error on operating conditions continuous reactor. *Process Safety and Environmental Protection*, 98:365–373, 2015.

[161] A. Wächter and L. Biegler. On the implementation of an interior-point filter line-search algorithm for large-scale nonlinear programming. *Mathematical programming*, 106:25–57, 2006.

[162] M. Wallace, S. S. Pon Kumar, and P. Mhaskar. Offset-free model predictive control with explicit performance specification. *Industrial and Engineering Chemistry Research*, 55:995–1003, 2016.

[163] M. Walton, T. Southerton, and P. Sharp. *Safety improvements in a Methanation reactor, Process Safety Progress*. Wiley Online Library, 2009.

[164] J. Wang, L. L. Cao, H. Y. Wu, X. G. Li, and Q. B. Jin. Dynamic modeling and optimal control of batch reactors, based on structure approaching hybrid neural networks. *Industrial and Engineering Chemistry Research*, 50:6174–6186, 2011.

[165] J. Wang and T. Chen. An online method for detection and reduction of chattering alarms due to oscillation. *Computers and Chemical Engineering*, 54:140–150, 2013.

[166] J. Wang, F. Yang, T. Chen, and S. L. Shah. An overview of industrial alarm systems: Main causes for alarm overloading, research status, and open problems. *IEEE Transactions on Automation Science and Engineering*, 13:1045–1061, 2016.

[167] L. Wang. Continuous time model predictive control design using orthonormal functions. *International Journal of Control*, 74:1588–1600, 2001.

[168] Z. Wu, F. Albalawi, Z. Zhang, J. Zhang, H. Durand, and P. D. Christofides. Model predictive control for process operational safety: Utilizing safeness index-based constraints and control Lyapunov-Barrier functions. In *Computer Aided Chemical Engineering*, volume 44, pages 505–510. Elsevier, 2018.

[169] Z. Wu and P. D. Christofides. Economic machine-learning-based predictive control of nonlinear systems. *Mathematics*, 7(6):494, 2019.

[170] Z. Wu, H. Durand, and P. D. Christofides. Safe economic model predictive control of nonlinear systems. *Systems and Control Letters*, 118:69–76, 2018.

[171] Z. Wu, H. Durand, and P. D. Christofides. Safeness index-based economic model predictive control of stochastic nonlinear systems. *Mathematics*, 6:69, 2018.

[172] Z. Wu, A. Tran, D. Rincon, and P. D. Christofides. Machine learning-based predictive control of nonlinear processes. part I: Theory. *AIChE Journal*, 65:e16729, 2019.

[173] Z. Wu, A. Tran, D. Rincon, and P. D. Christofides. Machine learning-based predictive control of nonlinear processes. part II: Computational implementation. *AIChE Journal*, 65:e16734, 2019.

[174] D. Xue and N. H. El-Farra. Actuator fault-tolerant control of networked distributed processes with event-triggered sensor-controller communication. In *Proceedings of the American Control Conference*, pages 1661–1666, Boston, Massachusetts, 2016.

[175] V. M. Zavala. A multiobjective optimization perspective on the stability of economic MPC. In *Proceedings of the 9th IFAC Symposium on Advanced Control of Chemical Processes*, pages 975–981, Whistler, Canada, 2015.

[176] C. Zhang, S. Vasudevan, and G. Rangaiah. Plantwide control system design and performance evaluation for ammonia synthesis process. *Industrial and Engineering Chemistry Research*, 49:12538–12547, 2010.

[177] S. Zhang, J. Tong, and J. Zhao. An integrated modeling approach for event sequence development in multi-unit probabilistic risk assessment. *Reliability Engineering and System Safety*, 155:147–159, 2016.

[178] Z. Zhang, Z. Wu, H. Durand, F. Albalawi, and P. D. Christofides. On integration of feedback control and safety systems: Analyzing two chemical process applications. *Chemical Engineering Research and Design*, 132:616–626, 2018.

[179] Z. Zhang, Z. Wu, D. Rincon, and P. D. Christofides. Operational safety of an ammonia process network via model predictive control. *Chemical Engineering Research and Design*, 146:277–289, 2019.

[180] Z. Zhang, Z. Wu, D. Rincon, C. Garcia, and P. D. Christofides. Operational safety of chemical processes via safeness-index based MPC: Two large-scale case studies. *Computers and Chemical Engineering*, 125:204–215, 2019.